Scintillating Metal Organic Frameworks (MOFs) for radioactive gas detection

Sharvanee Mauree

université PARIS-SACLAY

Scintillating Metal Organic Frameworks (MOFs) for radioactive gas detection

Metal Organic Frameworks (MOF) Scintillant pour la détection de gaz radioactifs

Thèse de doctorat de l'université Paris-Saclay

ED n° 573, Interfaces : matériaux, systèmes, usages
Spécialité de doctorat : Chimie
Graduate School : Sciences de l'ingénierie et des systèmes
Référent : CentraleSupélec

Thèse préparée à l'**Institut LIST** (Université Paris-Saclay, CEA)
sous la direction de **Matthieu HAMEL**, HDR, Dr, LCIM/LIST CEA Saclay,
le co-encadrement de **Guillaume BERTRAND**, Dr, LCIM/LIST CEA Saclay

Thèse soutenue à Paris-Saclay, le 23 Novembre 2023, par

Sharvanee MAUREE

Composition du Jury

Membres du jury avec voix délibérative

Isabelle LERAY Dr., HDR, ENS Paris Saclay, France	Présidente
José BUSTO Dr., HDR, Centre de Physique Particules de Marseille, France	Rapporteur
Claire HOBDAY Dr., University of Edinburgh, United-Kingdom	Rapportrice
Krasimir MITEV Dr., Sofia University "St. Kliment Ohridski", Bulgaria	Examinateur
Antoine TISSOT Dr., ENS Paris Sorbonne, France	Examinateur
Cédric BOISSIERE Dr., CNRS Paris Sorbonne, France	Examinateur

THÈSE DE DOCTORAT

NNT : 2023UPAST151

université PARIS-SACLAY | ÉCOLE DOCTORALE Interfaces: matériaux, systèmes, usages

Titre : Metal Organic Framework (MOF) Scintillant pour la détection de gaz radioactifs

Mots clés : MOF, Fluorescence, Gaz Radioactifs, Rayonnement Ionisant, Scintillation, Porosité

Résumé : La détection en ligne des gaz radioactifs est l'un des objectifs principaux pour la radioprotection. Ces gaz représentent un défi considérable en comparaison avec les solides ou les liquides radioactifs de par leur nature volatile. Les gaz radioactifs étudiés dans ce manuscrit sont le Radon-222, le Krypton-85 et le Tritium. La volatilité de ces gaz ainsi que l'énergie d'ionisation faible que certains produisent (seulement 5,7 keV en moyenne pour le Tritium) rendent leur détection par des moyens conventionnels comme les scintillateurs plastiques inefficace. Nous proposons dans cette thèse l'exploration d'une nouvelle classe de scintillateurs hybrides organiques-inorganiques poreux, les Metal Organic Frameworks (MOF). Ces matériaux sont reconnus pour leur porosité exceptionnelle et leur surface spécifique, ce qui en fait des candidats idéaux pour des interactions avec des gaz radioactifs. De précédents travaux de recherche ont montré que la synthèse de MOFs fluorescents ainsi que leur utilisation comme scintillateurs pour la détection de rayons X et de sources solides de radioactivité était possible. En se basant sur ces travaux, nous proposons de combiner les natures poreuses et scintillantes de ces matériaux pour détecter les gaz radioactifs susmentionnés. Ces MOFs seront synthétisés, caractérisés structurellement et photo-physiquement, puis testés pour la détection en ligne de gaz radioactifs sur un banc d'essai unique, couplé à un système de détection métrologique basé sur la méthode du Rapport des Coïncidences Triples à Doubles (RCTD) permettant de compter les photons de lumière.

Title: Scintillating Metal Organic Framework (MOF) for radioactive gas detection

Keywords: MOF, Fluorescence, Radioactive Gas, Ionising Radiation, Scintillation, Porosity

Abstract: The online detection of radioactive gases is of the utmost importance in the field of radioprotection. They represent a considerable challenge compared to solid or liquid sources of radioactivity due to their volatile nature. The radioactive gases under scrutiny here are Radon-222, Krypton-85 and Tritium. Due to the volatility of those gases as well as the low energy of its ionising radiation some of them produce (only 5.7 keV on average for Tritium), the detection of those gases via conventional detectors such as plastic scintillators are ineffective. We propose here to explore a new class of porous hybrid organic-inorganic scintillators, Metal Organic Frameworks or MOFs. These materials are known for their outstanding porosity and specific surface area making them ideal candidates for interaction with radioactive gases. Past research has demonstrated the possibility of synthesising fluorescent MOFs as well as their use as scintillators for the detection of X-rays and solid sources of radioactivity. With that in mind, we propose combining the porous and scintillant nature of these materials to detect the aforementioned radioactive gases. These MOFs will be synthesised, structurally and photophysically characterised to then be tested for online radioactive gas detection using a unique homemade gas bench fitted with a Triple-to-Double Coincidence Ratio (TDCR) metrological device which allows for photon counting.

Résumé en Français

La détection en ligne des gaz radioactifs est l'un des objectifs principaux pour la radioprotection. Ces gaz représentent un défi considérable en comparaison avec les solides ou les liquides radioactifs étant donnée leur nature volatile. Les gaz radioactifs étudiés dans ce manuscrit sont le Radon-222, le Krypton-85 et le Tritium. La volatilité de ces gaz ainsi que l'énergie d'ionisation faible que certains produisent (seulement 5,7 keV en moyenne pour le Tritium) rendent leur détection par des moyens conventionnels comme les scintillateurs plastiques inefficace. Nous proposons dans cette thèse l'exploration d'une nouvelle classe de scintillateurs hybrides organiques-inorganiques poreux, les Metal Organic Frameworks (MOF). Ces matériaux sont reconnus pour leur porosité exceptionnelle et leur surface spécifique allant jusqu'à 7000 $m^2 \cdot g^{-1}$, ce qui en fait des candidats idéaux pour des interactions avec des gaz radioactifs. De précédents travaux de recherche ont montré que la synthèse de MOFs fluorescents ainsi que leur utilisation comme scintillateurs pour la détection de rayons X et de sources solides de radioactivité était possible. En se basant sur ces travaux, nous proposons de combiner les natures poreuses et scintillantes de ces matériaux pour détecter les gaz radioactifs susmentionnés. Ces MOFs seront synthétisés, caractérisés structurellement et photo-physiquement, puis testés pour la détection en ligne de gaz radioactifs sur un banc d'essai unique, couplé à un système de détection métrologique basé sur la méthode du Rapport des Coïncidences Triples à Doubles (RCTD) permettant de compter les photons de lumière.

L'usage théorique des MOFs pour la détection des gaz radioactifs a été étudiée auparavant. Ces études montrent que le MOF peut absorber et concentrer le gaz à l'intérieur de ses pores tout en absorbant le rayonnement ionisant émis par le gaz pour ensuite émettre des photons par un procédé dit de scintillation.

Ce projet est issu d'un financement « Horizon 2020 Research and Innovation Programme » de l'Union Européenne, No 899293 pour le projet SPARTE. SPARTE (Scintillating Porous Architectures for RadioacTivE gas detection) est un consortium Européen dont l'objectif et la détection et les mesures d'activité métrologique des traceurs relatifs à l'activité nucléaire.

Cette thèse a été effectuée au Commissariat à l'Énergie Atomique et aux Énergies Alternatives (CEA, Saclay) de 2020 à 2023 au sein du Laboratoire Capteurs et Instrumentation pour la Mesure (LCIM), appelé Laboratoire Capteurs et Architectures Électroniques (LCAE) au début de la thèse. Les expériences de détection de gaz radioactifs ont été effectuées au Laboratoire National Henri Becquerel (LNHB, Saclay).

Ce travail de thèse se place à l'intersection de 3 axes de travail, principalement les chimies inorganiques et organiques, la photophysique et la physique nucléaire. Ce manuscrit a été divisé en 5 chapitres détaillés ci-dessous :

- Le chapitre I pose les bases qui permettent de comprendre ce manuscrit interdisciplinaire. Il explique la base de la radioactivité et des rayonnements ionisants et le besoin de les détecter. La base de l'interaction lumière-matière/rayonnement-matière et les concepts fondamentaux de luminescence et de scintillation y sont discutés. L'historique et les protocoles de synthèse des MOFs dans la littérature sont examinés. L'exploration de ces MOFs pour la détection des gaz radioactifs est justifiée en passant en revue la relation structure-propriétés, plus précisément en dressant une revue non-exhaustive des MOFs fluorescents et luminescents. Un récapitulatif des objectifs de la thèse est présentée à la fin de ce chapitre.
- Le chapitre II présente les aspects expérimentaux de cette étude. Il détail d'abord les protocoles de synthèse et d'activation utilisées dans le cadre de cette thèse. Il liste également et explique les différentes techniques de caractérisation utilisées pour identifier les MOFs synthétisés et déterminer leurs structure et propriétés photophysiques. Les propriétés structurelles ont été caractérisées par Diffraction à Rayons X (DRX), mesures d'absorption de N_2 (BET), Analyse thermogravimétrique (ATG), Spectroscopie Infrarouge par Transformée de Fourier (FT-IR), Microscopie Électronique à Balayage (MEB) et Résonnance Magnétique Nucléaire (RMN) du ^{13}C, ^{1}H et ^{129}Xe. Les techniques de caractérisation photophysiques incluent les expériences de photoluminescence, Time-Correlated Single Photon Counting (TCSPC), rendement de fluorescence, et de radioluminescence. Le système expérimental de détection de gaz radioactifs et le Ratio de Coïncidence Triple-à-Double (RCTD) sont détaillés dans ce chapitre.
- Le chapitre III explore la synthèse, caractérisation et tests de 4 MOFs à base de Zn, IRMOF-1/MOF-5, IRMOF-7, IRMOF-9 et MOF-205. Les MOFs à base de ZN ont d'abord été explorés à cause des nombreuses publications et de leur synthèse relativement simple. Nous nous sommes focalisés sur les mécanismes de fluorescence et la surface spécifique de chaque MOF. Le rendement de scintillation a été calculé puis comparé entre tous les MOFs. Chaque MOF a été testé pour la détection de ^{85}Kr. Nous avons conclu que l'IRMOF-9 et le MOF-205 sont des scintillateurs efficaces pour la détection de ^{85}Kr, le MOF-205 montrant les meilleurs résultats. Nous avons démontré par des calculs mathématiques et des simulations un effet de pré-concentration du ^{85}Kr dans le MOF-205 ce qui avait été auparavant théorisé. Le MOF-205 a aussi été testé pour des mesures de reproductibilité et des mesures à différentes activités de ^{85}Kr. Pour terminer, le MOF-205 a été testé pour la détection de ^{222}Rn et ^{3}H, et pour la première fois, le temps de demi-vie du ^{222}Rn a été mesuré avec un MOF.
- Le chapitre IV présente les tentatives de passer de structures à base de Zn connues pour s'effondrer dans des environnements humides vers des MOFs à bases de Zr. Ce chapitre

explore les synthèses avec modulateur où une compétition entre le ligand du MOF et le modulateur est nécessaire pour ralentir le taux de nucléation et tenter de cristalliser le MOF. Ces MOFs ont été caractérisés pour la photophysique et la structure et ont été testés pour la détection de ^{85}Kr. Le meilleur résultat a été obtenu avec l'UIO-67 qui a ensuite été testé pour la détection de ^{222}Rn et ^{3}H. Le rendement de scintillation de chaque MOF a été calculé puis comparé avec les MOFs à base de Zn (chapitre III).

- Le chapitre V explore les stratégies de dopage où certains MOFs des chapitres III et IV ont été dopés avec des ligands anthracène fortement fluorescents. Ceci a pour but de décaler la longueur d'onde d'émission de ces MOFs, ce qui permet une meilleure détection par le système et un meilleur rendement de scintillation. Les MOFs sont synthétisés avec une concentration de dopant de 1,38% et 5,5%. L'effet du dopage sur la structure et les propriétés physiques et photophysiques a été étudié. Nous avons conclu que le dopage d'un MOF décale non seulement la longueur d'onde d'émission mais augmente aussi le rendement de photoluminescence. Nous avons évalué un seuil de dopage au-dessus duquel un effet d'auto-absorption de l'anthracène limite le rendement de photoluminescence. L'effet du dopage sur la détection des gaz radioactifs a aussi été analysé. Le MOF-5 + 1,38% d'anthracène propose des performances largement meilleures que le MOF-5 non dopé.

Ce manuscrit se termine par une comparaison entre la performance des MOFs à travers les 3 chapitres, une conclusion et les perspectives ouvertes par ce projet. Nous avons remarqué qu'un équilibre entre la surface spécifique et les propriétés photophysiques était nécessaire. Nous observons que les performances de détection du ^{85}Kr augmentent lorsque la surface spécifique du MOF augmente. Cependant, quelques exceptions subsistent. Par exemple, le MOF-5 a l'une des plus grandes surfaces spécifiques mais elle n'est pas suffisante pour contrebalancer ses mauvaises performances photophysiques, c'est-à-dire les émissions a des courtes longueurs d'ondes et un rendement de scintillation relativement faible. Nous avons également conclu que le MOF-205 présente les meilleures performances en termes de production de photons sur les 3 gaz testés. Néanmoins, un matériau stable dans l'humidité étant requis pour des applications dans la réalité, le meilleur candidat serait l'UIO-67, qui montre des performances proches du MOF-205.

TABLE OF CONTENT

Acknowledgements

The well-known proverb “It takes a village to raise a child” could easily be applied to the world of research and, more specifically, to the many people who contributed in one way or another to my PhD journey. It is with immense pleasure that I get to thank them all for making this milestone possible.

First and foremost, I would like to acknowledge the SPARTE European Project for funding this thesis.

I would like to thank my thesis director, Matthieu Hamel and my supervisor, Dr. Guillaume Bertrand, for their guidance, expertise and feedback throughout those three years. I want to express my gratitude to them for their moral support during the more challenging times, whether professionally or personally, and for their unwavering patience.

I would also like to thank Dr. Vincent Villemot for paving the way to scintillating MOFs at the LCIM laboratory. I am incredibly grateful to him for showing me the ins and outs of this field and all the necessary experimental knowledge, without which I could have never had gotten a good start on my PhD.

I am also greatly indebted to Dr. Benoît Sabot for his guidance, insights and explanations of the world of metrology and the TDCR device. I would like to further thank him and Sylvie Pierre for their immense help with last-minute radioactive gas bench experiments needed to complete this PhD.

I want to express my deepest gratitude to everyone who has trained me or helped me carry out the characterisation experiments in this manuscript, namely Mr. Charles Rivron and Jonathan Bachir for the BET measurements at NIMBE and ILV laboratory, respectively. I would also like to thank Mr. Vincent Mertens for the training and booking of the PXRD experiment at the NIMBE laboratory.

My sincere thanks should also go to Prof. Christophe Dujardin and Pavlo Mai of the University of Lyon 1 (also members of the SPARTE project) for their help with the radioluminescence experiments.

I am also profoundly indebted to the research group at the University of Milano-Bicocca for welcoming me among them for three weeks in Milano. So, I thank Prof. Angiolina Comotti, Prof. Angelo Monguzzi, Dr. Jacopo Perego, Dr. Matteo Orfano and Silvia Bracco for their immense help characterising a few of the MOFs presented in this manuscript.

Thankyous should also be attributed to Dr. Francesca Belloni for her work on the MCPN simulations and explanations for this manuscript.

I want to acknowledge my thesis follow-up committee of Prof. Yves Dumont, Dr. Thierry Loiseau and Dr. Clémence Sicard for their very useful feedback halfway through my PhD.

I would like to extend a big thank you to everyone at the LCIM laboratory, formerly LCAE. Thank you for the warm welcome and the dynamic and pleasant work environment over the years. I want to extend some special thanks to some members of the laboratory. Firstly, to the two heads of the laboratory over the last three years, Dr. Frédérick Carrel and Vincent Schoepff, for their assistance and managerial help. To Dr. Dominique Tromson, the head of the chemistry pole, thank you for always lending a listening ear and being as involved as you were. An immense thank you to Chrystele Dehe-Pittance for always ordering laboratory equipment when I ran out and keeping this laboratory in good working conditions. Thank you also for all your wise emotional support over the years. I would like to extend my thanks to Hans Grigaut-Desbrosses for all the informatics support over the three years. I would also like to thank Céline Gesset for the MEB experiments. I would also like to extend my gratitude to two interns who have come and gone namely Alix Desjonqueres and Pauline Vergnory, for their help in synthesising and washing some MOFs.

I would like to acknowledge also the help of Camille Patron at Mission Handicap CEA and everyone at the health service of CEA Saclay for their help in accommodating my work environment to my handicap.

On a more personal note, I would like to thank Aya Kanj for being the best office partner and for being with me since day one of this thesis. I would also like to extend a particular thanks to Quentin Gendre, Pauline Vergnory and Caitline Morais De Moura for their friendship and support specially in the last months of this thesis.

I would be remiss not to mention my parents, without whom I would not have had the education, upbringing and resilience necessary to be here today. I thank my brothers, friends and other family members for their unwavering encouragement and support.

Lastly, I thank my partner, Clément Eliat, for always believing in me. I am grateful for his practical as well as emotional support. Thank you for always making me laugh, even in the most challenging moments we have faced during those last three years.

General Introduction

Metal Organic Frameworks (MOFs) are hybrid organic-inorganic materials mainly exploited due to their porosity and high surface area, the most significant being reported around 7000 $m^2 \cdot g^{-1}$. MOFs also became attractive due to their chemical versatility, i.e. they can be "infinitely" tuned by changing the organic or inorganic component at will, which then affects their physical properties. This chemical tunability, or "Lego chemistry", brought about the discovery that fluorescent MOFs with different fluorescence mechanisms could be synthesised.

Since plastic scintillators, which are at the heart of our laboratory's research, are not effective for detecting some radioactive gases, we decided to position ourselves to combine those two properties of MOFs, porosity and fluorescence, for the online/real-time detection of radioactive gases. Some fluorescent materials can also emit light, when excited by an ionising particles or ray. This is the scintillation phenomenon, and we would like to explore its feasibility on fluorescent MOFs.

The theoretical use of MOFs for the detection of radioactive gases has been proposed before, whereby the MOF can absorb and concentrate the gas within its pores along with absorbing the ionising radiation emitted by that gas to then emit photons in a process known as scintillation.

This project received funding from the European Union's Horizon 2020 research and innovation programme under grant agreement No 899293 for the SPARTE project. SPARTE (Scintillating Porous Architectures for RadioacTivE gas detection) is a European consortium, which focuses on the detection and activity measurement metrology of tracers related to nuclear activity.

This thesis was done at the Commissariat à L'Energie Atomique et aux Energies Alternatives (CEA) in Saclay from 2020 to 2023. The host laboratory was the Laboratoire Capteurs et Instrumentation pour la Mesure (LCIM), previously known at the start of this thesis as the Laboratoire Capteurs et Architectures Electroniques (LCAE). The radioactive gas detection experiments were conducted at the Laboratoire National Henri Becquerel (LNHB).

This work finds itself at a crossroad between three main fields of study, namely organic and inorganic chemistry, photophysics and nuclear physics. This manuscript has been divided for maximum clarity into the five following sections:

- Chapter I lays down the foundation for comprehending this interdisciplinary manuscript. It explains the basis of radioactivity and ionising radiation and the need for their detection. The premise for the light-matter/radiation-matter interaction and the fundamental concepts of luminescence and scintillation are also discussed. The history and synthesis protocols of Metal Organic Frameworks from the literature are examined. The exploration of said MOFs for the detection of radioactive gases are justified by reviewing their structure-properties relationship, more precisely, by canvassing a non-

exhaustible literature review of fluorescent and scintillating MOFs. An overview of the objectives for this thesis is also presented at the end of this chapter.

- Chapter II present the experimental aspects of this study. It first details the synthesis and activation protocols used throughout this thesis. It also lists and explains the different characterisation techniques used to identify the synthesised MOFs and determine their structural and photophysical properties. The structural properties were characterised by X-ray diffraction, N_2 adsorption measurements, Thermogravimetric Analysis (TGA), Fourier-Transform Infrared Spectroscopy (FT-IR), Scanning Electron Microscopy (SEM) and ^{13}C, ^{1}H and ^{129}Xe Nuclear Magnetic Resonance (NMR). The photophysical characterisation techniques include photoluminescence experiments, Time-Correlated single photon counting, photoluminescence light yield, and radioluminescence experiments. The radioactive gas detection experimental setup and the Triple-to-Double Coincidence Ratio (TDCR) detection system are also outlined in this chapter.
- Chapter III explores the synthesis, characterisation and testing of four Zn-based MOFs, namely, IRMOF-1/MOF-5, IRMOF-7, IRMOF-9 and MOF-205. Zn-based MOFs were explored first due to the large array of publications on them and their ease of synthesis. A particular focus on the fluorescence mechanism and surface area is put forward for each MOF. The scintillation yield of each MOF was calculated and compared to one another. Each MOF was tested for ^{85}Kr detection. The MOF with the most promising result was tested for reproducibility measurements and measurements at different activities of ^{85}Kr and lastly also for ^{222}Rn and ^{3}H detection. For the first time, the half-life of ^{222}Rn was also measured using a MOF and is reported in this chapter.
- Chapter IV attempts to move away from Zn-based whose structures are known to collapse with moisture towards more stable Zr-based MOFs. This chapter explores the modulated synthesis approach whereby a modulator competes with the ligand present in the MOF to slow down the nucleation rate and attempt to crystallise the respective MOFs. These MOFs underwent structural and photophysical characterisation and were tested for ^{85}Kr detection. Results for ^{222}Rn and ^{3}H detection using the most promising MOF are also shown in this chapter. The scintillation yield of each MOF was calculated and compared to one another. The results were compared to those in Chapter III.
- Chapter V explores a doping strategy whereby some of the MOFs explored in Chapters III and IV are doped with a highly fluorescent anthracene ligand. This aims to shift the emission wavelength of some of those MOFs and increase their scintillation yield. The MOFs were synthesised with a 1.38% and 5.5% anthracene dopant concentration. The effect of doping on the structure and physical and photophysical properties were studied. The effect of doping with respect to radioactive gas detection was also analysed.

This manuscript draws to a close with a conclusion and the perspectives in this field.

Chapter I: Bibliography

I. Bibliography

1. Radioactivity

The discovery of radioactivity as we know it started with the discovery of radiation by Wilhelm Röntgen in 1895 when he took the first iconic photo of his wife's skeletal hand (Figure I-1) and coined the term X-Rays for the first time[1].

Figure I-1: Showing the first X-ray image.

Fascinated by this discovery, Henri Becquerel immediately started studying a material he possessed, potassium-uranyl sulphate, to see it also emitted radiation. Pierre and Marie Curie further pursued the study on uranium ores and the rays they emitted. The latter was the first to coin the term radioactivity. She was awarded the Nobel Price twice, once for her work in Physics with radioactivity/spontaneous radiation and years later in Chemistry for the discovery of radium and polonium.

To understand why these scientists dedicated their lives' work to radioactivity, we must first understand the term ourselves.

The nucleus of an atom is composed of protons and neutrons. The number of protons define the nature of the elements and the proportion of neutrons defines the isotopes of the elements.

The nuclei of most atoms naturally present are stable nuclei with the right ratio of neutron to proton. Some atoms, however, have too much proton, and/or an unbalanced neutron to proton ratio, making them unstable. Those are termed radionuclides or radioisotopes. Radioactivity is the physical phenomenon by which radionuclides spontaneously transform into other unstable

or stable nuclei by disintegration[2]. In doing so, the atom loses energy in the form of radiation. This is known as radioactive decay. Some radionuclides have to undergo a series of transformations to reach a stable state; this is known as a decay chain. The radiation emitted during radioactive decay is ionizing radiation, i.e., it has sufficient energy to ionise atoms or molecules of matter by which it passes, that is, detach electrons from them[3]. It is this ionization power that make them both useful but also dangerous to biological life.

There are three main types of ionising radiation:

-Alpha particles (α)

Alpha particles were discovered by Ernest Rutherford in 1899[4]. Alpha particles consist of two protons and two neutrons bound together but deprived of two electrons. An alpha particle is identical to the nucleus of a helium atom and is often represented as $^{4}_{2}He^{2+}$. Atoms having a radioactive nucleus with too many protons and neutrons often emit alpha radiation, for example, uranium-238 and radon-222. Alpha particles are doubly positive, heavy (6.645×10^{-27} kg), and therefore more probable to interact with matter compared to other forms of nuclear radiation. These properties make them highly ionising radiations, but cannot penetrate matter very far. Thus, a few centimetres of air or a thin sheet of paper efficiently stops alpha particles. Alpha particles are emitted with discrete energies (4 to 9 MeV) characteristic of the particular decay from which they originate.

-Beta particles (β)

Beta particles are high energy/high-speed electrons (β^-) or positrons (β^+) ejected during a radioactive decay known as a beta decay[5]. Electrons are emitted by radionuclides heavily loaded with neutrons, for example, thorium-234. Conversely, positrons are emitted by radionuclides with too many protons, such as iodine-122. A beta particle has a small mass (9.1×10^{-31} kg) and can be released with high energy, which means it can reach relativistic speeds. Unlike alpha particles, they are emitted with a continuous range of energies up to a maximum that is characteristic of each radionuclide. They are less ionising than alpha particles and can travel up to tens of centimetres in air and a few mm in certain materials. When the beta particle ejected does not entirely eliminate the nuclei's excess energy, gamma-ray emission often accompanies the beta emission to get rid of the remaining excess energy.

-Gamma rays and X-rays

Gamma and X-rays are both electromagnetic waves, just like visible light but with higher energy. Electromagnetic radiation can be described as a stream of photons, each with a specific energy, travelling in a wavelike pattern and moving at the speed of light[6]. Gamma-ray photos have the highest energy and, therefore, the shortest wavelength of the electromagnetic spectrum, as shown in Figure I-2. This high energy allows gamma rays to pass through materials such as paper, steel, and even human tissue. High density material such as lead is often used to stop or slow down gamma rays. Gamma rays are produced from the de-excitation of the nucleus of an excited atom after the disintegration of an unstable radionucleus and often accompany alpha and beta decays. X-rays, on the other hand, are produced from the relaxation of an electron

from a higher energy level in the electron cloud of an atom to a lower energy level, thereby releasing the excess energy as X-rays[7].

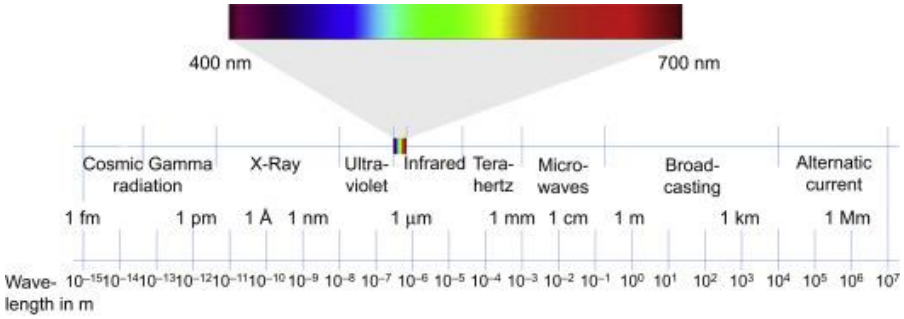

Figure I-2: Illustrating the electromagnetic spectrum[8].

The becquerel (Bq) [9] is official SI unit used to measure the radioactivity of species. The activity of a radioactive sample is the number of disintegrations its radioactive nucleus undergoes per second, hence the following definition of a Becquerel:

1 Bq = 1 disintegration per second

With every disintegration, the radioactivity of the sample decreases. At the end of the time $t_{1/2}$, known as the half-life, the activity of the sample would have reduced by half. The activity follows the decay trend shown in Figure I-3.

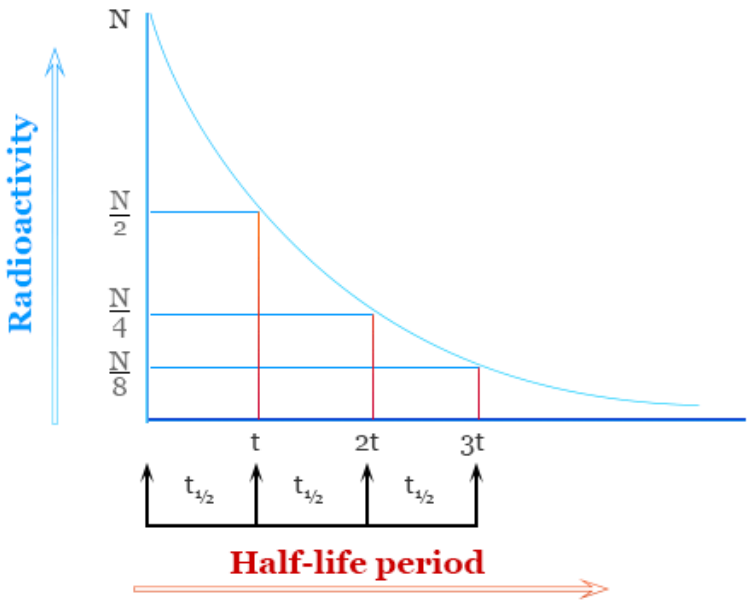

Figure I-3: Figure illustrating the half-life of a radionucleus[10].

If N_0 is the number of atoms present at a time $t = 0$ and N is the number of atoms present after the time t, the radioactive decay formula is as follows:

$$N = N_0 e^{-\lambda t}$$

Equation I-1

where λ is the decay constant.

Radioactive matter can present itself in solid, liquid or gaseous forms. Gaseous sources of radioactivity are trickier to detect than solid and liquid sources of radioactivity, as gases are volatile and hence challenging to contain. This challenge is what drives forward our motivation for gas detection experiments. A wide array of radioactive gases exists. For this thesis, we will consider the following sources of radioactivity are gases: ^{222}Rn, ^{85}Kr and ^{3}H.

2. Radioactive gases

2.1 Radon-222 or ^{222}Rn

Radon-222 or ^{222}Rn, is a colourless and odourless radioactive gas. It is generated from the decay chain of naturally occurring ^{238}U found in the earth's crust and hence in rocks and soils all around us. Radon is the second leading cause of lung cancer, just after tobacco consumption[11,12]. In France, 3000 fatalities per year are registered due to radon exposure[13]. In the open air, the concentration of radon gets diluted, and the risk remains very low. The gas accumulates in enclosed spaces such as basements, cellars, and buildings, leading to higher risk concentrations. The World Health Organisation and European Commission have determined a safe concentration level for radon to be 400 Bq·m^{-3} for existing houses and 200 Bq·m^{-3} for further constructions[14].

The naturally occurring uranium decays to thorium into radium. ^{222}Rn is then obtained from the alpha decay of Radium-226, as seen in Figure I-4. Radon-222 itself undergoes an alpha decay into Polonim-218 with a half-life of 3.8232 days[15]. The alpha emitted has an energy of 5.59 MeV. The rest of the decay chain is shown in Figure I-4, along with the half-lives of each decay process.

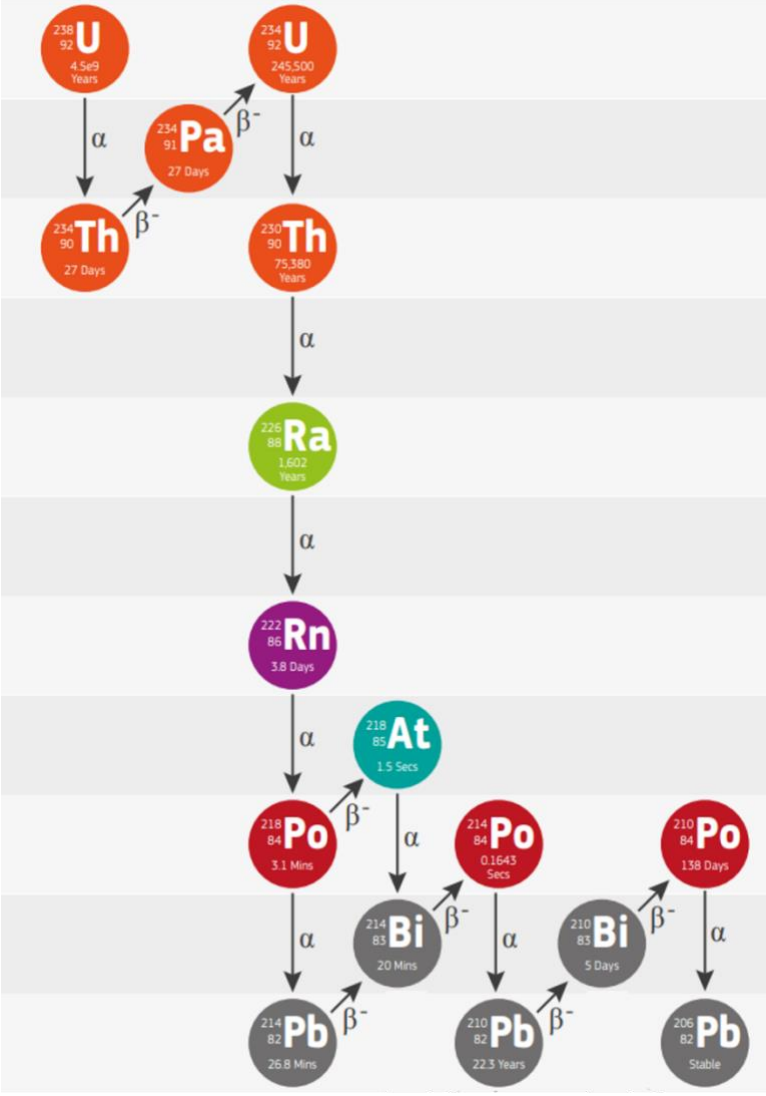

Figure I-4: Illustrating the decay chain of Radon-222 (shown in purple) with the mode of disintegration[16].

As we can see, Polonium-218, Lead-214 and Bismuth-214 decay happen within minutes and Polonium-214 within seconds. These short-lived progenies make the interpretation of a measurement of Radon-222 decay quite challenging, because the addition of these various decay. However, the decay chain shown in Figure I-4 is known to achieve a secular equilibrium when the gas is contained in a closed environment like a vial. A secular equilibrium is when the measured activity of ^{222}Rn equals the activity of its descendants, i.e. when the production rate of ^{222}Rn is equal to its decay rate. This has been calculated using the Bateman mathematical model[17] and, according to the Decay Data Evaluation Project[18], estimated to be 4 h for ^{222}Rn.

Several ^{222}Rn detection system have been developed over the years. Some of them allow for an online/real-time detection while some have a relatively long measurement time or need processing post measurement. Older detection methods for radon include charcoal detectors[19]. The charcoal is exposed to ^{222}Rn gas, and latter is mixed with a liquid scintillation cocktail[20,21]. This technique does not give very accurate measurements as the radon absorbed at the exposure

stage decays and is partially desorbed from the surface of the charcoal. Gamma spectroscopy can also be performed with the charcoal since ^{214}Pb and ^{214}Bi are gamma emitting progenies[22].

Current commercially-available detection devices already exist for detecting radon, for example, Radon Eye's RD200[23]. Radon Eye's device is based on a pulsed ionisation chamber technology. It gives a reading every 10 minutes, is compact, and only costs around 250 € to 450 € depending on the options. Other instruments include Alphaguard from Bertin Technologies[24] and several devices from the company Airthings. Inexpensive track detectors[25] (30 €) also exist and are perfectly adapted to public use. These devices are shown in Figure I-5.

Figure I-5: Illustrating the different commercially available devices for radon detection a) – Radon Eye; b) – Alpha guard; c) – track detector.

Another method of detection, especially for ^{222}Rn, is based on Passivated Implanted Planar Silicon Detectors (PIPS), which use semiconductors for alpha spectrometry and hence the identification of radon and its descendants[26].

An innovative technique studied is the use of compact disk (CD) method for radon measurements studied by D. Pressyanov *et al.*[27]. However, this technique does not allow for online detection.

2.2 Krypton-85 or ^{85}Kr

Krypton-85 or ^{85}Kr, is the radioactive gas most produced by anthropogenic activities. It is a fission product from ^{235}U and is produced and rejected by nuclear reactors. It is also produced by nuclear fuel reprocessing plants. The two reprocessing plants that have quantified their ^{85}Kr emission are La Hague in France (379 PBq/year in 2019) and Sellafield in the United Kingdom (95 PBq/year reported for 1999)[28,29]. By law, these reprocessing plants are allowed a specific concentration of gas rejection into the environment, making this monitoring of utmost importance. The target ambient radioactivity in these facilities is 1 $kBq \cdot cm^{-3}$ at the mouth of the evacuation chimney and 1 $Bq \cdot cm^{-3}$[30] at the ground level of the facility.

The core of a reactor confines a large amount of fission gases. However, less than 1% of the krypton generated by fission in nuclear reactors manage leave the fuel cladding, making nuclear reactors a minor source of ^{85}Kr. However, they need to be monitored in case of accidental rejection. The European Commission and the French electricity provider (EDF) recommend a detection limit of 1.8 $Bq \cdot cm^{-3}$ in the atmosphere of nuclear power plants[30]. The Chernobyl (1986) and the Fukushima-Daiichi (2011) accidents rejected 33 and 44 PBq of ^{85}Kr, respectively[29,31].

The impact of rare gases emitted during nuclear weapon testing is negligible due to the altitude at which those tests were conducted. They have of course contributed to the background radiation but the amount has continuously decreased overtime.

^{85}Kr decays into stable Rubidium-85. Its most common emission is β^- particle (99.57% of the emission) with a maximum energy of 687.1 keV and an average of 251.4 keV. The other 0.43% possible emission is by a beta particle emission with a maximum energy of 173 keV followed by gamma-ray emission of 513.99 keV. The most effective way to detect ^{85}Kr is by the detection of the pure β^- particle as it represents the majority of the emission. The half-life of ^{85}Kr is of 10.756 years[31].

The detection of ^{85}Kr using liquid scintillation is not adapted because of the poor solubility of ^{85}Kr. However, proportional gas counters are, to this date, the most efficient method for ^{85}Kr detection. However, they sometimes use heavy gas carrier bottles such as Argon and Xenon, which means the detection system cannot be portable and require several minutes to reach reliable detection rate.

2.3 Tritium or ^{3}H

Tritium or ^{3}H, is naturally produced at very low concentrations in the upper atmosphere. In the mid-1950s and early 1960s, man-made tritium was widely produced to be further used during nuclear weapons testing to create fusion bombs. The quantity of tritium due to these tests peaked in 1963 and has ever since been decreasing[32]. Its detection and monitoring are, however,

imposed by the French Nuclear Safety Authority (ASN). Tritium is also a by-product of nuclear power plants, due to activation of water by escaping neutron, estimated at approximately 68 PBq per year per reactor[32]. The use of tritium and hence the production of tritiated waste is bound to increase in the upcoming years with the implementation of fusion reactors by the ITER project. It is estimated that 300 g of tritium (100 mol or an activity of 107.1 PBq) will be necessary to produce 800 MW of electricity per day[33].

^{3}H is the radioactive isotope of hydrogen. It is a pure beta emitter with a maximum energy of 18.59 *keV and an average of 5.7 keV. Its half-life is 12.312 years. Of all three gases of interest, tritium emits the particle with the lowest energy, making it the most challenging to detect. The beta particles lose their energy very quickly and therefore have a very small penetration depth. For example, beta particles emitted by tritium can only travel 6 mm in air and 6 µm in water.

Liquid scintillation counting is the most efficient detection system for tritium due to the direct contact of the ionising radiation with the scintillating cocktail. However, the liquid scintillation method is very time-consuming and does not allow for the online measurement as the tritium gas needs to be bubbled in water first. The protocol for tritium detection is as follows: bubbling through water for 1 week, withdrawing a bubbled sample and mixing it into a scintillating cocktail, measurement in a scintillation counter for 1 h. This method yields a detection limit of 15 $kBq \cdot m^{-3}$[34].

Another method studied is helium mass spectrometry, which is very sensitive but relatively expensive[34].

2.4 Detection characteristics

Table I-1 summarises the different characteristics of existing detection methods for radioactive gases with the last column listing the targets we wish to achieve with our own detection system.

Table I-1: Comparison of the leading technologies in literature used for radioactive gas detection[14].

	Liquid scintillation	**Proportional gas counter [Air]**	**Proportional gas counter [Sealed Xe]**	**Laboratory Target**
Limit of Detection	0.005 Bq·cm^3	0.01 Bq·cm^3	0.5 Bq·cm^3	1 Bq·cm^3
Decision threshold	0.002 Bq·cm^3	0.002 Bq·cm^3	0.1 Bq·cm^3	0.5 Bq·cm^3
Measurement time range	1 h – 1 day	20 min – 1 h	> 1 h	1 min
Active volume	1 L	8 L	11 L	-
Final detector mass	> 100 kg	50 kg	220 kg	< 1kg
Operational practicality	Offline, fixed, mixed chemical and radioactive waste	Online, fixed	Online, fixed	Online

3. Photoluminescence and Scintillation

3.1 Photoluminescence

We have seen that ionising radiation and even radioactive gases, more specifically, can be detected using scintillation, namely liquid and plastic scintillators. To fully understand scintillation, we need to jump back to the concept of luminescence.

The IUPAC definition of luminescence is the spontaneous emission of radiation from an electronically or vibrationally excited species not in thermal equilibrium with its environment. There are different types of luminescence: photoluminescence, radioluminescence, chemiluminescence, and electroluminescence, among many others. We will be focussing in this manuscript on photoluminescence and radioluminescence.

Photoluminescence is the emission of light or photons from matter after the absorption of photons from electromagnetic radiation roughly in the 1 to 10 eV energy range. One photon is absorbed and one photon is emitted for a successful fluorescence event.

Radioluminescence is also the emission of photons from matter but this time after the absorption of ionising radiation. Many ionized and excited state molecules are produced during the ionization of the medium. These molecules decay to lower energy excited state and some of

them emit photon. This is the same as scintillation; the different name is often due to the experimentation.

In quantum mechanics, four quantum numbers can be used to describe an electron in an atom: The principal quantum number (n), the azimuthal quantum number (l), the magnetic quantum number (m_l), and the spin quantum number (m_s).

The spin quantum number is the most important one to understand electronic transitions, which are necessary for photoluminescence to occur.

The spin quantum number (m_s) describes the intrinsic angular momentum or spin of an electron. It can take the value of $\pm\frac{1}{2}$ with $+\frac{1}{2}$ being a "spin up" electron and $-\frac{1}{2}$ a "spin down" electron. Each electron in an orbital must have different quantum numbers due to the Pauli Exclusion Principle. For a transition to occur, there must be an overlap between the orbitals involved in the transition. For this, the transition must occur between two states with the same spin S where S is the sum of all the spin quantum numbers.

We will also often encounter the term singlet and triplet state, which refers to the spin multiplicity of a state, M, where $M = 2S + 1$. When the multiplicity is equal to 1, this state is termed as a singlet state. The electronic ground state is typically a ground singlet state S_0. Electronically excited states are usually S_n singlet states where $n \geq 1$. However, it happens that an electron in an excited singlet state undergoes a spin inversion which causes the multiplicity to be equal to 3 and termed as a triplet state, T_n where $n \geq 1$. Each electronic state is accompanied by several vibrational energy levels. All their energy levels are represented in the Perrin-Jablonski diagram in Figure I-6, together with the possible energy transitions that can occur.

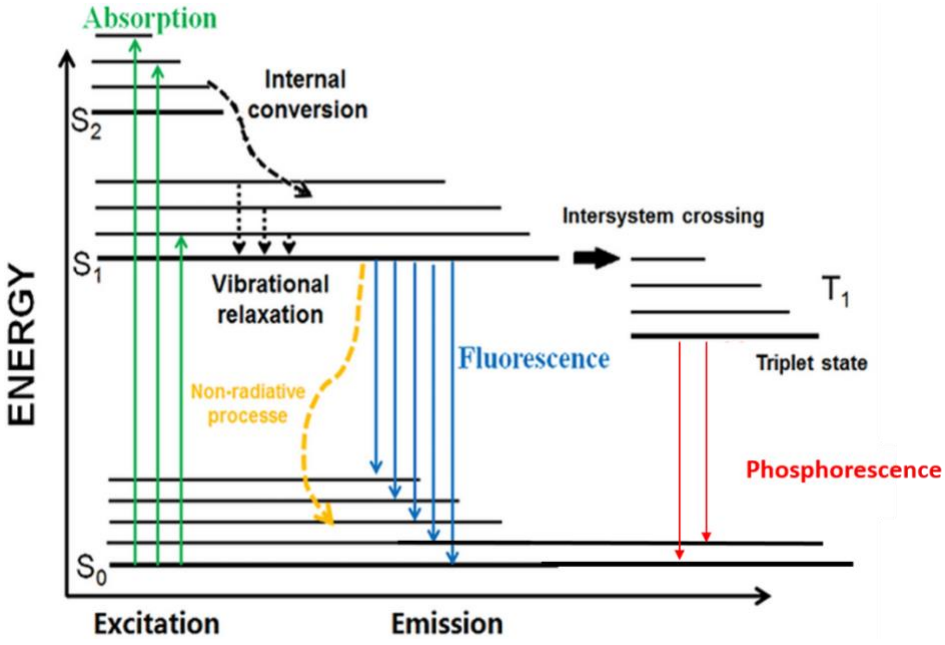

Figure I-6: Illustrating the Perrin-Jablonski diagram. Modified from IBS website[35].

As seen in Figure I-6, the absorption of energy leads to the promotion of an electron from the ground state energy level with the lowest vibrational level to the excited state energy level. The use of ultraviolet or visible light is necessary for such transitions. Light of lower energy, such as infrared, is not energetic enough to cause such a promotion but can, however, cause the excitation of an electron from a lower vibrational state to a higher vibrational state in the electronic ground or excited state.

To get the complete picture of the electronic transitions happening here, be it excitation or emission, we need to consider the Frank-Condon principle together with the Perrin-Jablonski diagram. Figure I-7 shows a more accurate illustration of electronic states as a potential well or potential energy surface (PES) with the vibrational states within the well. As we can see here, the absorption and emission transitions are "vertical", i.e. they are happening at fixed molecular configuration. This is because the absorption of a photon occurs in around 10^{-15} s, whereas structural reorganisation of atoms is slower around 10^{-12} to 10^{2} s. The Frank-Condon principle states that for the emissions to occur through a "vertical" transition, they should occur from the lowest possible vibronic excited state.

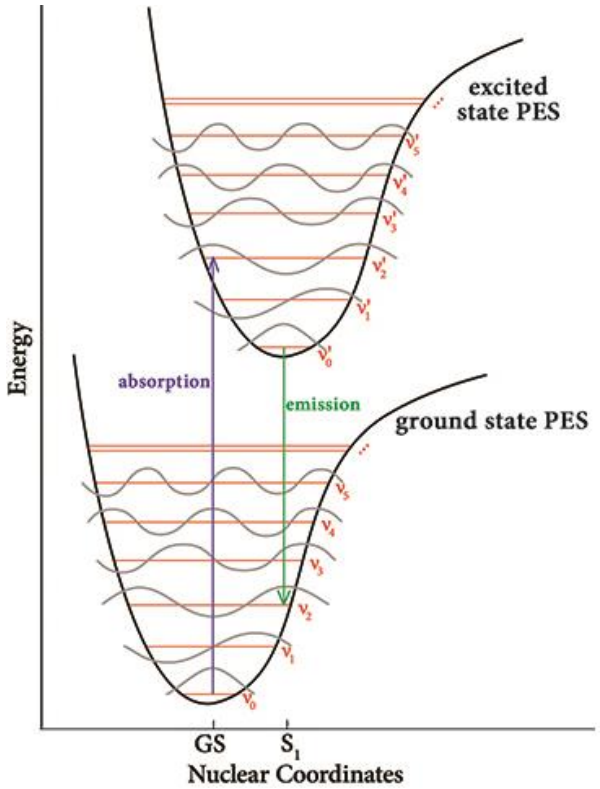

Figure I-7: Illustrating the Frank-Condon principle[36].

After the transition of an electron to an excited state, the electron will be in a metastable state. It would proceed to return to its fundamental ground state by different mechanisms, as seen in Figure I-6.

It will first begin to lose excess vibrational energy through vibrational relaxation, by a non-radiative process in which the electron goes from a higher to a lower vibrational state of the same electronic state. After that, another non-radiative process called internal conversion can happen between electronic states of the same multiplicity. Together, vibrational relaxation and internal conversion will bring the electron to the lowest vibrational state of the lowest electronic state, where it can undergo relaxation by three possible mechanisms.

The first one is a non-radiative mechanism. However, this mechanism is not possible in systems where the bandgap between the lowest vibrational excited state of the excited electronic state and the ground vibronic states is too large. For these systems, the excess energy will be lost through a spin-allowed radiative transition known as fluorescence from the lowest vibrational level of the excited electronic state to the ground electronic state. This transition is always lower in energy than the energy absorbed due to the electron going through internal conversion and vibrational relaxation before reaching the lowest vibrational state of the excited electronic state. This lower energy, therefore, means an emission at a higher wavelength. The difference in wavelength between the absorption maxima, λ_a^{max}, and the emission maxima, λ_f^{max}, is known as the Stokes Shift (see Figure I-8). The latter is often reported in wavenumber, $\tilde{\nu}$ in cm^{-1} and is calculated using Equation I-2 and Equation I-3.

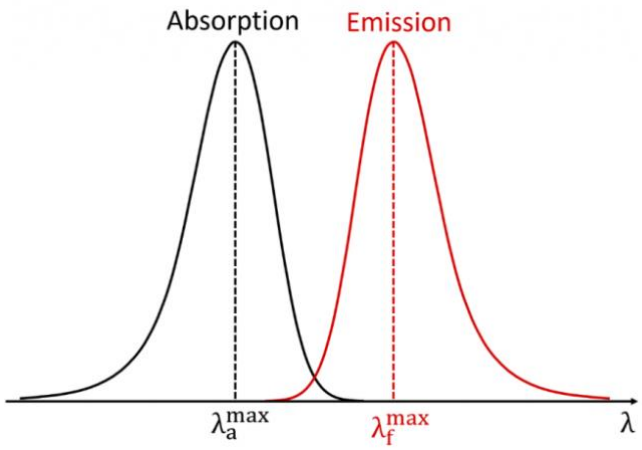

Figure I-8: Illustrating the Stokes shift[37].

$$\Delta\lambda = \lambda_f^{max} - \lambda_a^{max}$$

Equation I-2

$$\Delta\tilde{\nu} = \tilde{\nu}_a^{max} - \tilde{\nu}_f^{max} = \frac{1}{\lambda_a^{max}} - \frac{1}{\lambda_f^{max}}$$

Equation I-3

The last possible mechanism is an intersystem crossing followed by a spin-forbidden radiative emission known as phosphorescence. Even though this transition is spin forbidden, it is possible due to spin-orbit coupling[38]. Similar to fluorescence, the phosphorescence emission happens at a higher wavelength than the absorption.

Another concept essential to understanding luminescence is the concept of the lifetime (τ) of an excited state. This lifetime is the average time a molecule exists in the excited state before it relaxes back to the ground state. The typical fluorescence lifetime for organic molecules is around 10^{-11} to 10^{-7} s, while for phosphorescence, the lifetime is longer (10^{-4} to 10^{0} s) because of the spin-forbidden transitions[39].

The quantum efficiency of fluorescence (ϕ) is also an indicator in the field of luminescence. It is defined as the ratio of the number of photons emitted to the number of photons absorbed, as describe by Equation I-4 and takes a value between 0 and 1.

$$\phi = \frac{N_{emitted\ photons}}{N_{Absorbed\ photons}}$$

Equation I-4

3.2 Scintillation

As we have seen, fluorescence occurs because of the absorption of a UV-Visible photon. A visible photon has an energy between 1.6 to 3.2 eV, and an ultra-violet photon can range from 4 eV to 300 eV. Scintillation is a type of fluorescence where ionising radiation is the incident-absorbed radiation. Ionising radiation, for example, beta particles from the disintegration of ^{85}Kr have a maximum energy of 687.1 keV and an average energy of 251.4 keV, as seen in section 2.2. This difference in energy with respect to UV-Visible photons in fluorescence will have different consequences on the material the radiation interacts with.

Scintillation occurs in the three consecutive stages mentioned below[40]:

- Conversion

Conversion is the process during which a material absorbs the energy of the incident radiation, and consequently, electrons and holes are created in this material. The energy absorption pathway depends on the type and energy of the incident radiation. For highly energetic incident photons, the conversion process can happen by photoelectric absorption, Compton scattering, and pair production.

- Compton scattering: The most prevalent mechanism in organic scintillator when exposed to gamma radiation. It is the transfer of a partial amount of energy to a recoil electron that will, in turn, deposits its energy in the dense medium.
- Photoelectric effect: It is the total transfer of energy from a gamma to an electron. The recoil electron will deposit its energy in the dense medium.

- Pair production: At very high energy (> 2.1 MeV) photon can interact with nucleus and create an electron positron pair. This to particle are most likely to recombine and create two gamma ray or a various array of subatomic particles.

For beta and gamma particles, the conversion step is always the full deposition on its energy in the dense medium.

These processes all have different cross section interaction, which characterise how easily photons can interact with the material. This attenuation coefficient is dictated by the nature energy of the incident radiation, the atomic number of the material, and its density.

- Charge transport

In this process, the electrons and holes created in the conversion process migrate inside the material. Loss of scintillating efficiency occurs due to trapping or non-radiative recombination during this process. This loss is often due to impurities in the scintillating material, making purity crucial. Inorganic centre and other polarized molecules are known to be exciton trap and favour non-radiative decay. Many other factors such as quenching exist but won't be discussed for the purpose of this manuscript.

- Luminescence

Lastly, the electrons and holes recombine radiatively. The mechanisms of luminescence have already been discussed in this chapter. This phase is highly dependent on the scintillator used during the process.

A material that emits photons when excited by ionising radiation is known as a scintillator. Different properties are desirable for scintillators, such as high scintillating efficiency, transparency, short decay times, good linearity over a range of energies, high stopping power, radiation hardness and low cost. Different types of scintillators exist, including organic crystals, organic liquids, plastic scintillators, inorganic scintillators, glasses, and perovskites. Plastic scintillators are a scintillating material in which the primary fluorescent emitter is dissolved in a solid polymer matrix. K. Mitev and P. Cassette [41] demonstrated the detection of radon using plastic scintillators. They however stated that for the detection of other noble gases the adsorption inside the plastic could be a drawback leading to a memory effect. Plastic scintillators are, however, ineffective for detecting radioactive gases emitting low energy ionising radiation. This is because plastic scintillators are generally quite dense and low energy particles can only penetrate the surface of the scintillator as they quickly lose energy while travelling in matter. Plastic scintillators are, therefore, surface scintillators, i.e. the photon production is limited to the surface. To detect low-energy ionising radiation, we will be turning to porous/volumic scintillators. The porous scintillator will be able to adsorb the radioactive gas, maximizing the contact between the ionising radiation and the scintillating material, therefore, optimising the photon production. One such example of a porous scintillator is the Metal-Organic Frameworks (MOFs).

4. Metal Organic Frameworks (MOFs)

Metal organic frameworks are hybrid organic-inorganic crystalline materials with the highest known surface area, making them ideal materials for gas applications. MOF-like structures, known as coordination polymers, have been reported as early as the 1960s by Tomic *et al.*[42]. But MOFs started to become a material of interest only in the early 90s through the work of the pioneer in the development of MOF chemistry, Omar Yaghi. He and his co-workers first worked on the iconic and now well-known IRMOF-1, also known as MOF-5[43,44]. To this date, more than 100,000 MOF-like structures exist, according to the Cambridge Structural Database (CSD). One would think that with such a comprehensive database of MOFs, a worldwide nomenclature for MOFs would have been put in place. However, this is not the case. In the beginning, MOFs were named in chronological order of discovery. Later, however, they were named after the university where they were first synthesised. Some examples are listed herein: UIO (University of Oslo), CAU (Christian-Albrechts-Universität), HKUST (Hong Kong University of Science and Technology), MIL (Materials Institut Lavoisier), and so many more.

4.1 Structure

Metal Organic Frameworks are made up of inorganic clusters forming the node of the structure linked together by organic ligands through strong iono-covalent bonds. To understand the structure of a MOF more clearly, let us consider the structure of the most iconic MOF-5 shown in Figure I-9. We can see that one node of the cube is made up of 4 blue tetrahedra of zinc atoms bonded together by a red oxygen, as shown in the middle inset. This Zn_4O is decorated with the carboxylates from the organic ligand (1,4-Benzenedicarboxylic acid), as shown on the inset on the far right. This shows 6 carboxylates connectivity for one node, leading to a final $Zn_4O(CO_2)_6$. The yellow sphere represents the largest Van der Waals sphere that can fit inside the structure without touching the framework[45] it represents the porosity MOF-5 has to offer.

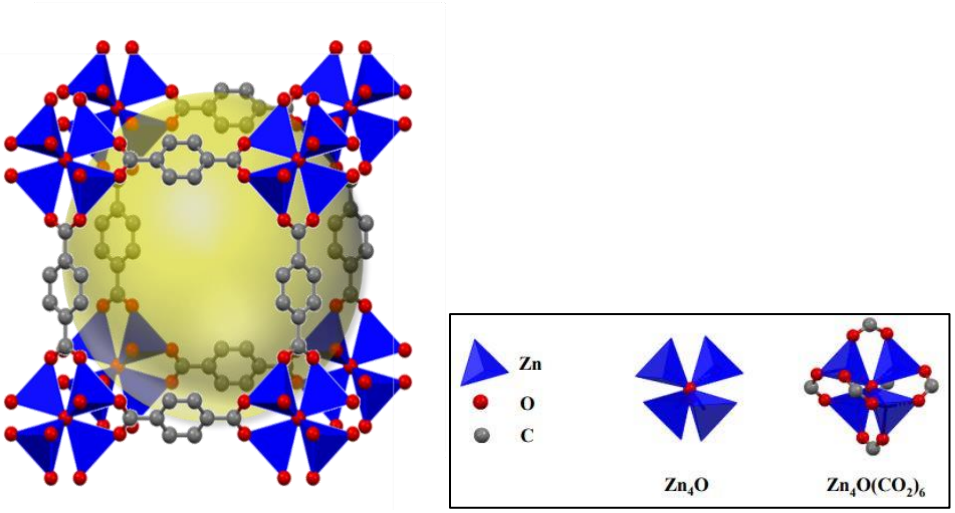

Figure I-9: Illustrating the structure of MOF-5.

MOF materials form 1D, 2D and 3D crystalline structures. One such 3D crystalline structure is shown in Figure I-10.

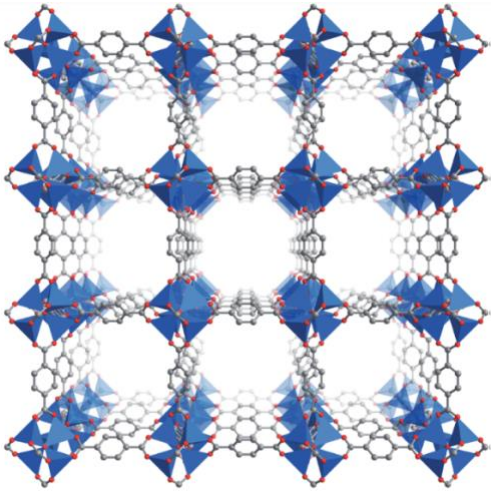

Figure I-10: Illustrating the extended lattice of MOF-5[46].

One of the most attractive properties of Metal Organic Frameworks is their "infinite" structural diversity. By changing the identity of the metal cluster and/or ligand, we obtain a different MOF with different properties. In other words, the structure and hence properties are "infinitely" tuneable.

Let us consider what happens when we keep the Zn inorganic cluster and change the organic ligand. For the MOF to assemble, the ligand must have at least two functional groups able to bond to the metal cluster. Several functional groups exist, such as carboxylates, phosphonates, sulphates, and nitrogen donors with a lone pair of electrons. The carboxylates ligands are the

most commonly used, as they form a bond with the metal strong enough to synthesise a stable MOF but weak enough to allow for a slow and reversible bonding essential to form crystalline structures. The ligand in MOF-5 above is said to have a ditopic ligand, i.e. with two functional groups, in this case, carboxylates. MOFs can also have tritopic and tetratopic ligands, as shown in Figure I-11.

DITOPIC

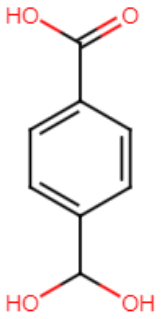

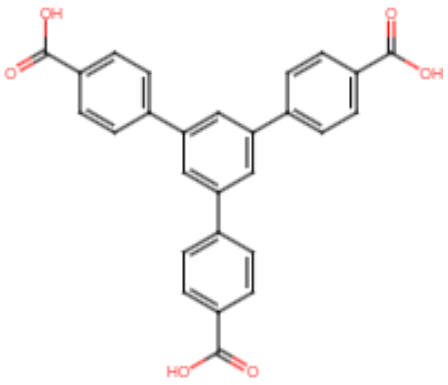

TRITOPIC

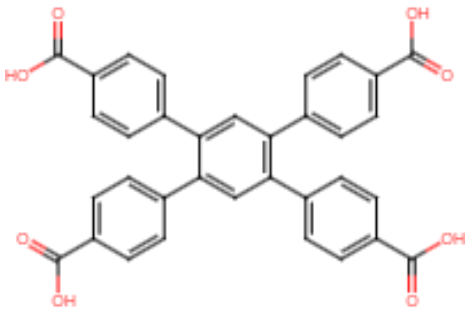

TETRATOPIC

Figure I-11: Illustrating examples of ditopic, tritopic and tetratopic ligands.

We can see in Figure I-12 that changing the ligand can influence the pore size. Generally, increasing the length of the organic ligands increases the pore size, as seen in Figure I-13[47]. The names of the respective MOFs are isoreticular MOF or IRMOF-X, with X being the number shown next to the structure.

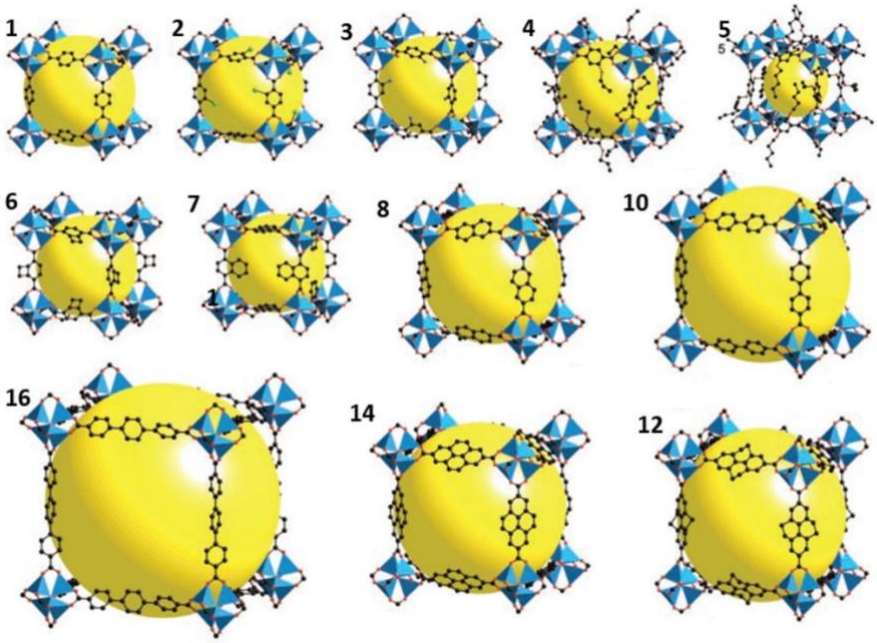

Figure I-12: Illustrating different isoreticular MOFs with a Zn cluster and different ligands[48].

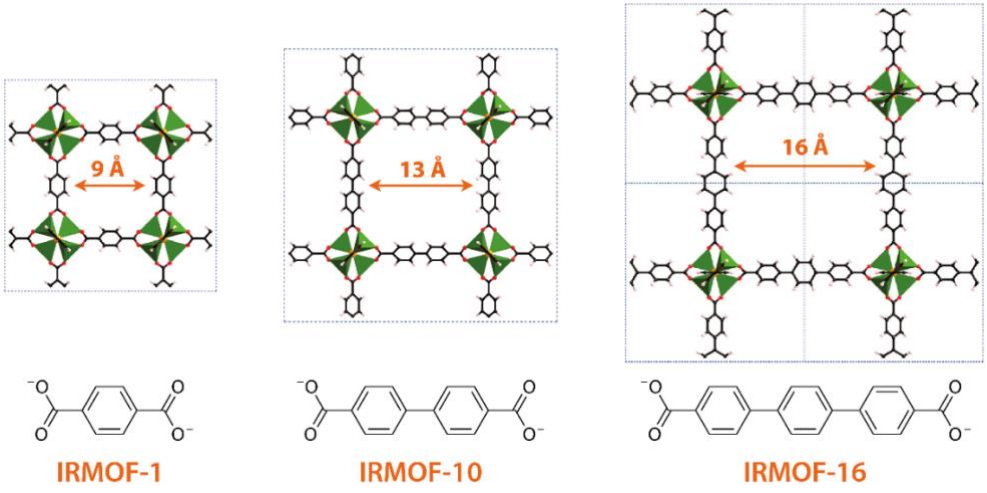

Figure I-13: Illustrating the pore size of some isoreticular MOFs[47].

As shown in Figure I-12, certain numbers are not shown, for example, 9 and 11. These MOFs are known as interpenetrating MOFs. MOFs with large spaces in a single network can form interpenetrating structures with each other to reduce the space, as shown in Figure I-14. The interacting forces that make up interpenetrating MOFs are not chemical bonds but supramolecular interactions such as hydrogen bonding, π–π stacking and van der Waals forces[49]. Interpenetrating structures have been shown to have structural flexibility compared to

their non-interpenetrating counterpart. However, interpenetration does not necessarily mean lower surface areas. Figure I-15 now shows the previously missing interpenetrating MOFs.

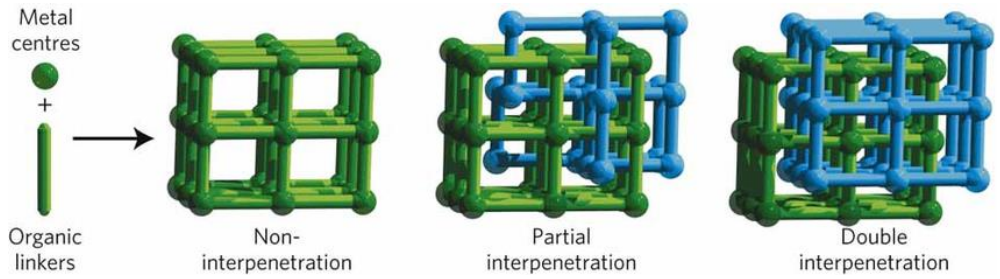

Figure I-14: Illustrating interpenetration in MOFs[50].

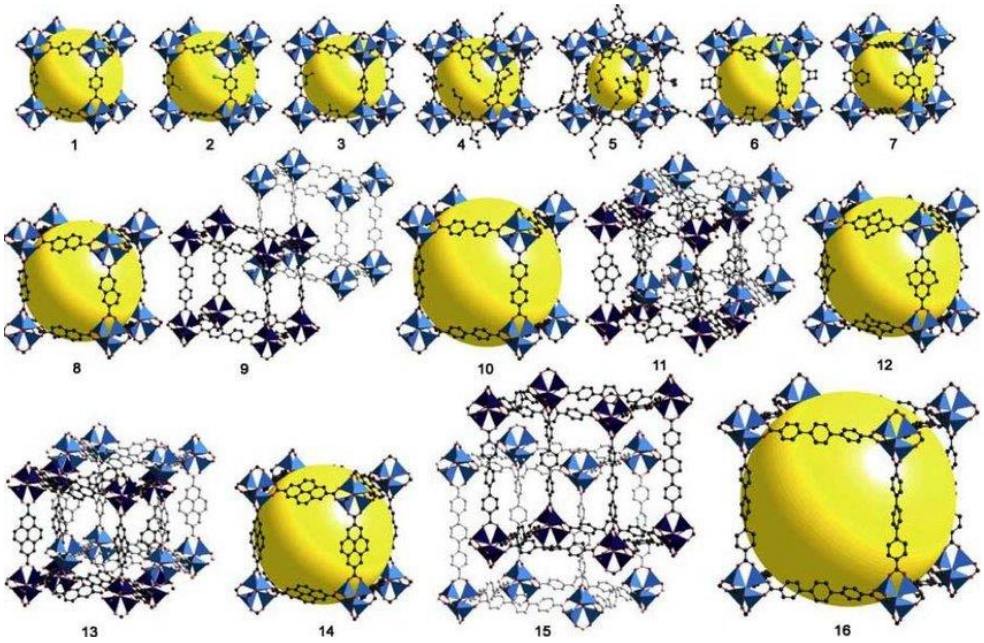

Figure I-15: Illustrating different isoreticular MOFs with a Zn cluster and different ligands and the corresponding interpenetrating structures.

Now let us look at what happens if we change the identity of the metal cluster. The inorganic/metallic clusters are also known as the secondary building units (SBU). The geometry of the SBU is governed by the coordination number and coordination geometry of the metal ion or cluster and the nature of the functional groups[51]. Different metals hence lead to different SBU geometries, as shown in Figure I-16. For a given ligand, changing the metallic cluster affects the pore size and surface area of the MOF. It is also important to note that a MOF can have one, two or more metal clusters[52–55].

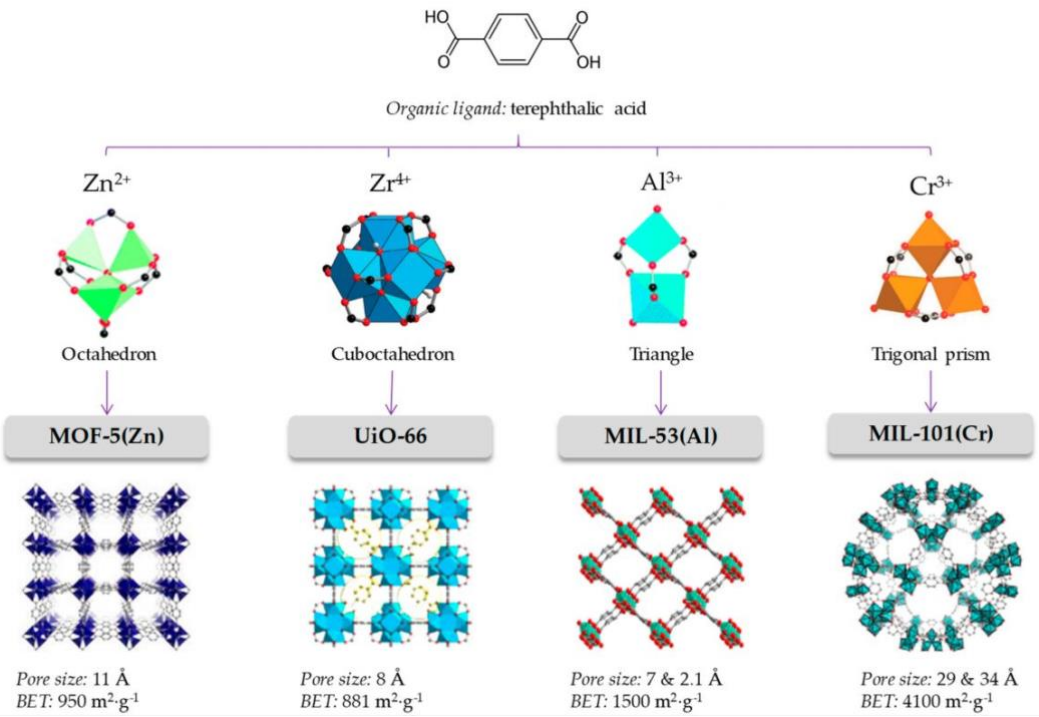

Figure I-16: Illustrating different metal nodes for some metal organic frameworks[56].

4.2 MOF Stability

Since MOFs are made of strong C-C, C-H, C-O and Metal-O bonds, they exhibit a high thermal stability of up to 300°C to 500°C depending on the MOF[57]. Some MOFs, however, show poor chemical and mechanical stability. Chemical stability refers to the resistance of MOF against moisture, solvents, acids and bases[58]. One of the main disadvantages of Zn-based MOFs is how they are affected by humidity. It has been shown that water interact with the carboxylate-zinc bond, leading to the cleavage of the Zn-O bond and hence the partial or complete collapse of the MOF structure[59]. This mechanism in shown for MOF-5 in Figure I-17 where the initial state is the structure of MOF-5 as we know is surrounded by water molecules. At the transition state, the water molecules migrate towards the Zn atoms and finally the Zn-O bonds break via the insertion of a water molecule. This drawback complicates the use of MOFs in practical applications since a structure collapse causes a partial or complete loss in porosity.

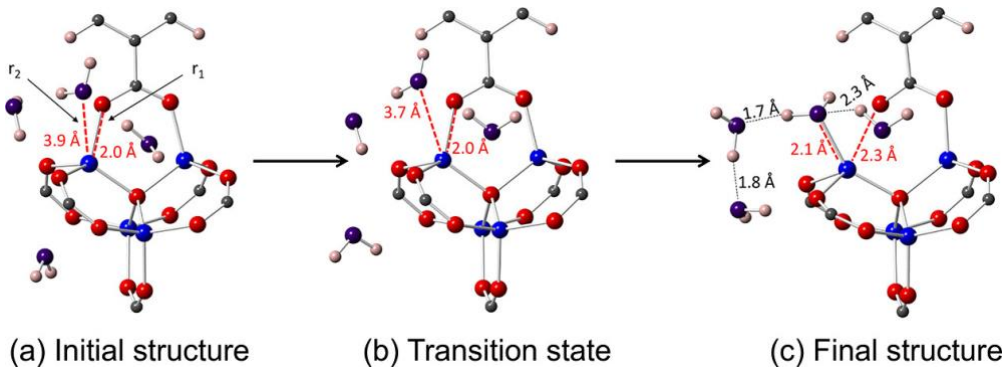

Figure I-17: Illustrating a) Initial MOF-5 structure, b) transition state and c) the final structure with Zn-O bonds. O atoms in the water molecules are purple to distinguish them from oxygen in the MOF (red). Black dashed lines indicate hydrogen bond lengths between adjacent water molecules. Red dashed lines illustrate Zn−O bond distances. r_1 is the Zn−O (MOF) distance, whereas r_2 is the Zn−O (inserted water) distance[59].

The mechanical stability can be affected by the process used for the activation of the MOF, i.e. the method to remove solvent from the pores of the MOF. As we will see in section 4.5 of this chapter as well as in Chapter II, certain activation processes cause excessive capillary tension within the MOF which eventually leads to its partial or complete collapse.

The metal-ligand bond in a MOF determines its thermodynamic stability. Therefore, a compatible pair of metal-ligand is necessary before attempting any synthesis. This stability is generally governed by Pearson's hard/soft acid/base principle[60,61]. This principle states that ligands with relatively high pK_a, known as soft Lewis bases, for example, azoles, tend to produce robust frameworks with low-valent metal ions. On the contrary, ligands with relatively low pK_a, known as hard Lewis bases, such as carboxylates, tend to produce robust frameworks with high-valent metal ions.

4.3 Synthesis

Figure I-18 shows the discovery of the different synthesis methods for metal organic frameworks.

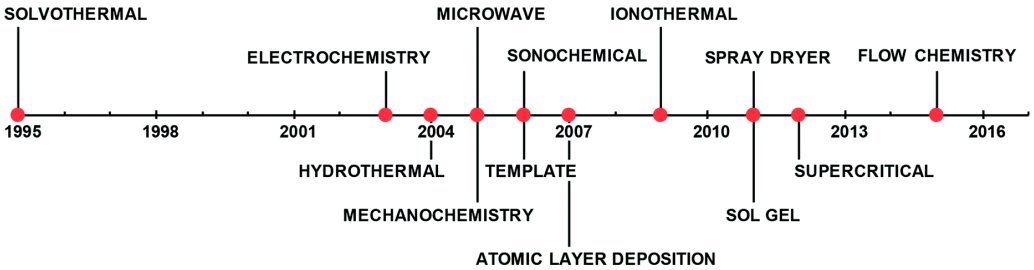

Figure I-18: Illustrating different synthesis methods discovered for MOF over years of research[62].

The synthesis method chosen for this thesis was the solvothermal synthesis method for the simplicity of the setup. Solvothermal synthesis has also been widely studied to synthesise pure crystals and is known to have a better synthesis yield than the other methods[63]. The metallic salt and organic ligand are dissolved in a suitable solvent. Figure I-19 illustrates the self-assembly of the MOFs by a solvothermal method. This synthesis method and its details will be further discussed in Chapter II.

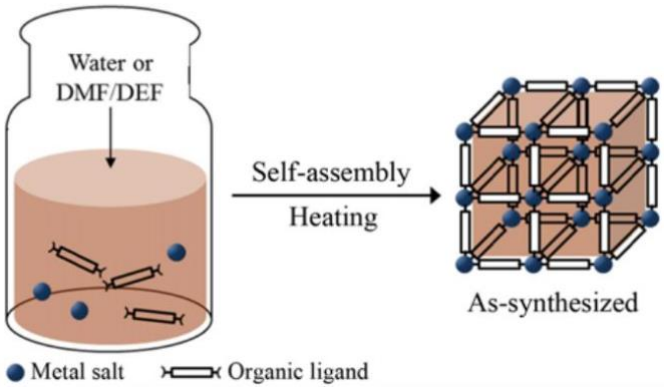

Figure I-19: Illustrating solvothermal synthesis[64].

Since the purity of MOFs greatly affect its photophysical properties, as we will see in section 5.1, one of the aims of this thesis was to synthesise pure millimetric single crystals of MOF. Big transparent single crystals also allow more light to diffuse out than powder, which is an immense advantage for the detection of low-energy ionising radiation to boost photon detection.

For the synthesis of single crystals of MOF, one must start with a supersaturated solution. Aside from that, the two phases that govern the successful synthesis of a single crystal of any material, including MOFs, are nucleation and growth. Both of these processes are governed by the laws of thermodynamics, more precisely, the Gibbs Free energy[65] illustrated in Figure I-20, along with the equation below.

$$\Delta G_{nucl} = \Delta G_{vol} + \Delta G_{surf}$$

Equation I-5

where ΔG_{nucl} is the total Gibbs free energy for nucleation, ΔG_{vol} is the volume free energy, and ΔG_{surf} is the surface free energy.

Nucleation refers to the formation of a new thermodynamic phase or nuclei from a solution, liquid or gas phase. As we can see in Figure I-20a, this can occur after a certain concentration, C_{nuc}. Above this concentration, a thermodynamically unstable supersaturated solution with a

higher Gibbs free energy is formed. In order to reduce the total Gibbs free energy, solute particles are separated from the solution by forming a nucleus. The formation of these nuclei is therefore accompanied by the reduction of the volume energy and the increase of the surface energy, reported as ΔG_{vol} and ΔG_{surf} in Figure I-20b. The small nuclei then act as a template for the growth of the crystal. Before the critical nuclei radius r_{crit} shown in Figure I-20b, the small nuclei can dissolve back into the solution in order to reduce the total Gibbs free energy by reducing the surface free energy. After the critical radius, the nuclei can start to grow; the Gibbs free energy is reduced by reducing the volume free energy. With this comes the concept of reversible bonds which considerably slows down the nucleation rate and reduces the defects present in the final crystal.

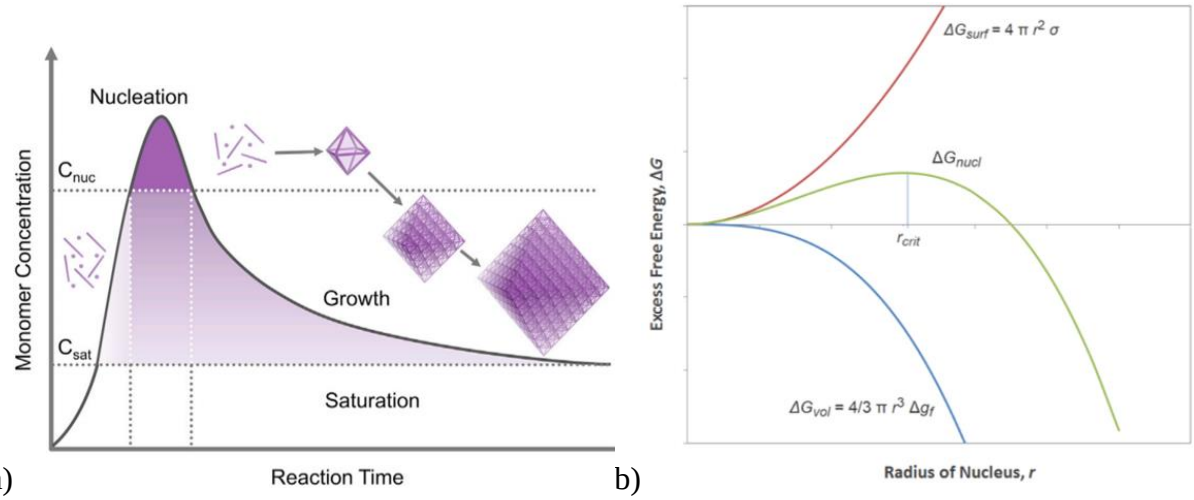

Figure I-20: Illustrating a) the structural evolution of MOF crystals[66] b) the relationship between Gibbs free energy and radius of a nuclei during crystal formation.

Since the growth stage is particularly difficult to control, controlling the early stage of nucleation allows to control the size of the MOF. Generally, at higher supersaturation, crystal nucleation tends to be more rapid than growth and hence many smaller crystals are obtained. In our case, in order to obtain millimetric single crystals of MOFs, slow nuclei formation should be encouraged. At low supersaturation, crystals can grow faster than they nucleate, leading to larger crystals.

4.4 Modulated Synthesis

Certain MOFs, such as Zr-based MOFs, have shown to be particularly tricky to synthesise. Typical hydrothermal synthesis of those MOFs has shown the fast precipitation of the metal and ligand forming products with low crystallinity and surface area[67]. A slightly modified synthesis method known as the modulated synthesis approach has been shown to produce crystalline MOFs as well as have an effect on the particle size[67–71]. A modulated synthesis is

the addition of a ligand with one coordination site to the initial precursor solution needed for a MOF synthesis. This ligand is usually an organic acid such as benzoic acid or acetic acid. The modulator acts as a competing molecule which coordinates with the metal cluster forming an intermediate complex. This modulator molecule then undergoes an exchange with the ligand molecule meant to be present in the MOF structure. This competition, therefore, slows down the rate of nucleation and prevents rapid precipitation of a non-crystalline product. Figure I-21 shows the XRD pattern and SEM images produced with the addition of a molar equivalent of benzoic acid modulator molecule with respect to the number of moles of Zirconium(IV) Chloride. It can be seen that when no benzoic acid is used, a broad peak is obtained in the XRD pattern, showing that the product form is not crystalline. The crystallinity of the product increases as the amount of benzoic acid increases. This study also shows that increasing the amount of benzoic acid has an effect on the crystallite size. Bigger crystals are obtained with higher amounts of benzoic acid as the latter further slows down the nucleation rate; therefore, fewer nuclei then grow into larger crystals.

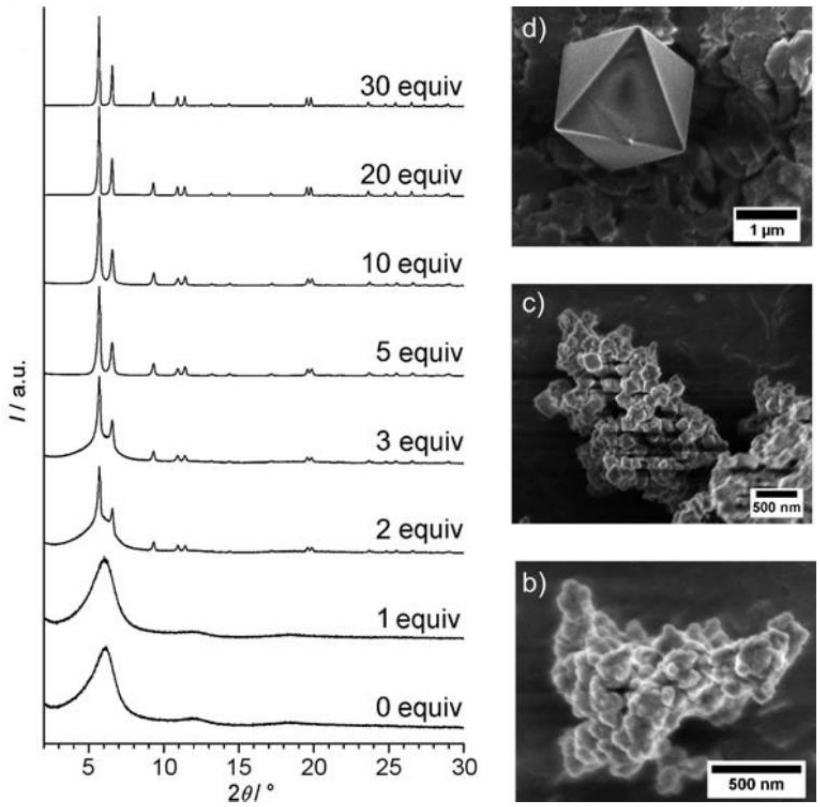

Figure I-21: Illustrating the effect of modulated synthesis on UIO-67[68].

4.5 Gas interaction in MOF

As we have seen one of the most attractive properties of a MOF is its porosity and surface areas. Porous materials are often classified according to their pore size, as illustrated in Table I-2[72]. Microporous materials can be further subdivided into ultramicroporous materials with a pore size of 0.7 nm and supermicroporous between 0.7 nm and 2 nm.

Table I-2: Illustrating the classification of porous materials.

Porous classification	Pore size
Macroporous	> 50 nm
Mesoporous	2 – 50 nm
Microporous	< 2 nm

Most MOFs exhibit microporosity. However, mesoporous and mixed microporous-mesoporous MOFs have also been reported[73].

Adsorption in MOFs is mainly due to physisorption. Physisorption in MOFs is usually attributed to London dispersion forces where no chemical bonding takes place. Chemisorption only take place when the MOF has reactive functional groups, unsaturated metal sites and reactive gases such as CO, NO and CO_2[73] .

As seen in section 4.3, MOFs are often synthesised using a solvent. After the synthesis process, the pores of the MOF are filled with the solvent used. In order for the gases to access those pores, the MOF needs to be activated, i.e. the solvent removed from the pores. One of the most commonly used techniques is the activation by supercritical CO_2. The synthesis solvent is replaced by liquid CO_2 at high pressure. The MOF/CO_2 is then brought above the supercritical temperature of CO_2, which lies around 31°C at 73.7 bar. The supercritical CO_2 is converted to the gas phase directly without passing through the liquid phase and is evaporated from the pores of the MOF, leaving a stable porous structure[74]. Activation by supercritical CO_2 has shown to produce MOFs with higher surface areas compared to other conventional activation techniques and solvent exchange techniques[75]. This is because of the very low capillary forces acting upon the MOF during the removal of the solvent and CO_2 from the pores, hence maintaining the structural integrity. Another activation process is benzene freeze drying whereby the MOF is left in benzene and the sample frozen at 0°C and brought back to room temperature several times. For the last freeze cycle, the sample is heated under vacuum to a temperature and pressure below the solvent's triple point, which causes the benzene to sublime. This avoids the liquid-gas transition and reduces the capillary forces known to cause MOF collapse[76].

An important property of porous materials is their specific surface area, that is, the surface area per unit mass of material. A widely used technique to determine the specific surface area of a porous material is by the adsorption of N_2 gas at 77 K. The uptake of N_2 by the material is

monitored at constant temperature and by varying the pressure. Different mathematical models can then be used to calculate the surface area of a porous material from these data. The simplest model is the Langmuir model, where the adsorption of the gas is limited to one monolayer before achieving an equilibrium. Another popular model is the Brunauer, Emmett et Teller (BET) which expand on the Langmuir model with multi-layer adsorption. Figure I-23 illustrates the gas uptake in the pores of materials. A MOF can have different pore sizes within the same structure. Figure I-22 shows the two pore sizes present in MOF-5. In this case, the smaller pores are filled first, at lower gas pressures and larger pores are filled at higher pressures[77].

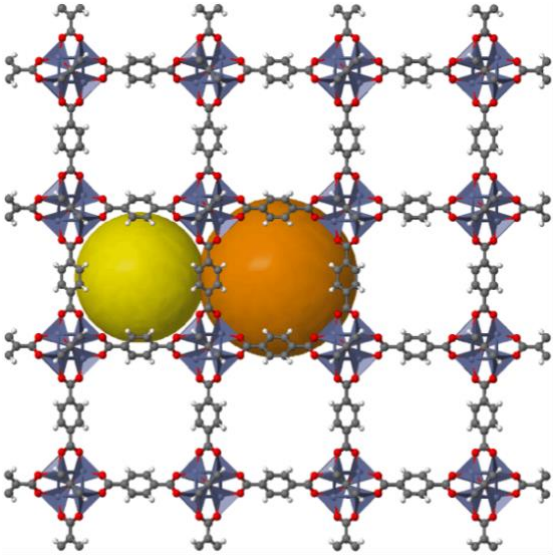

Figure I-22: Illustrating the two pore sizes present in MOF-5[78].

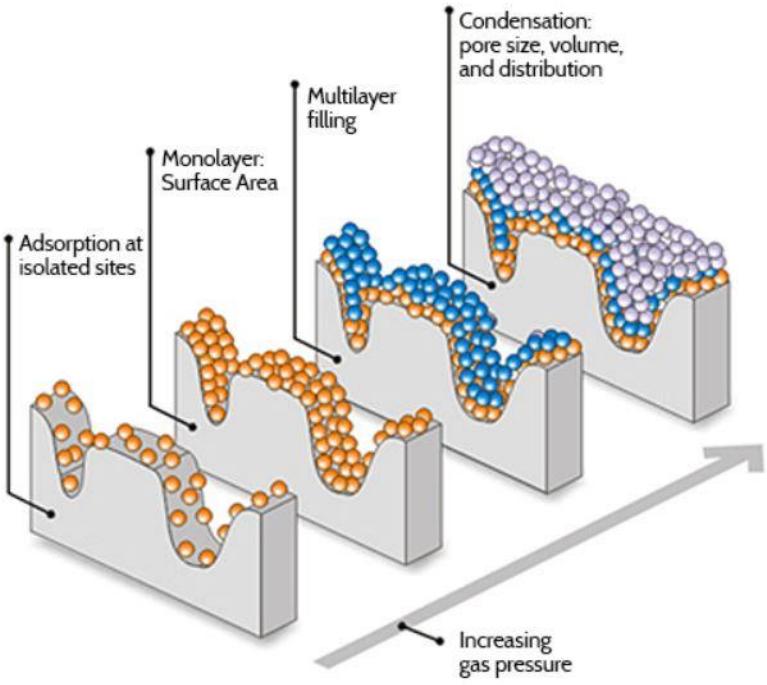

Figure I-23: Illustrating the uptake of gas in a porous material[79].

Aside from the specific surface area, we can also determine the pore size, pore volume and pore size distributions, among others. The nature of the porous classification in Table I-2 can be determined by the N_2 adsorption isotherms obtained from the gas adsorption experiments. The different types of adsorption isotherms are shown in Figure I-24. MOFs generally display Type I isotherms typical for microporous materials but have been shown to also display Type II isotherms. Type IV and V isotherms can be displayed by MOFs due to poor activation, changes in the structure due to humidity or capillary condensation within the pores.

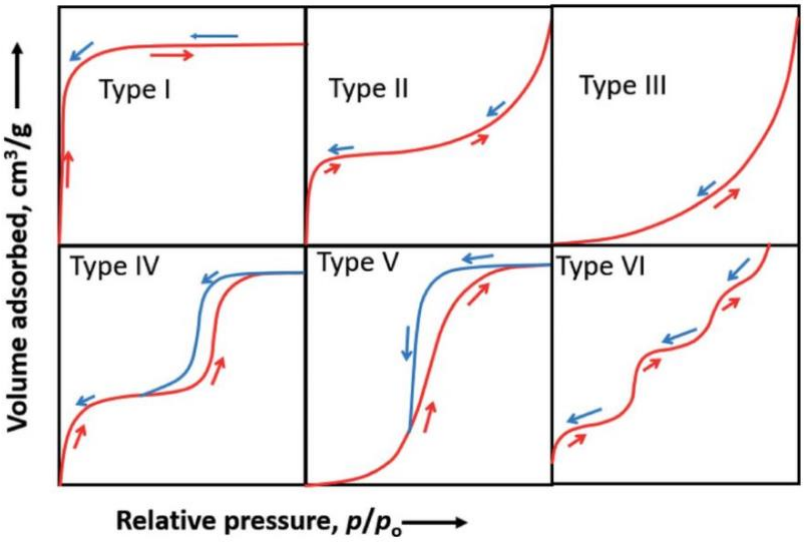

Figure I-24: Illustrating different adsorption isotherms of porous materials[80].

The surface area of a porous material can be determined from these adsorption measurements, by the Brunauer, Emmett et Teller (BET) mathematical model which will be further detailed in Chapter II. The pore size and pore size distribution can also be evaluated. It is important to note that the BET surface area should not be regarded as an absolute value[73] as some assumptions made in the BET model are oversimplified, especially for materials like MOFs which can have multiple pores and heterogeneous pore surfaces. The BET values should be regarded as apparent surface areas and not precise values. The BET surface areas of several MOFs are shown in Figure I-25 as compared to conventional porous materials.

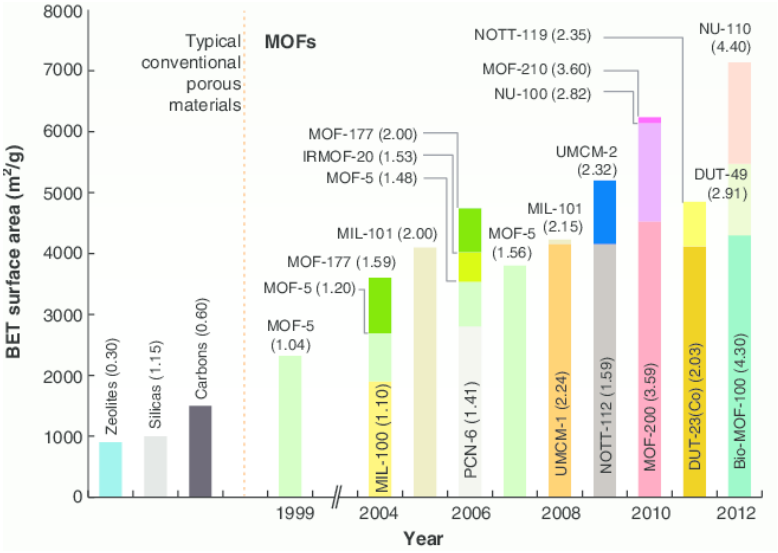

Figure I-25: Illustrating the surface area of several MOFs compared to other porous materials[57].

4.6 MOF applications

In this section, we will cover a number of MOF applications in an arbitrary order of importance.

One of the most researched applications for MOFs is catalysis[61,63,81]. MOFs have been used as photocatalyst for hydrogen and oxygen production from water splitting and CO_2 reduction. Electrocatalysis is also possible in MOFs after the addition of electronically conducting nanoparticles. They have shown excellent results for oxygen reduction reactions as well as hydrogen evolution reaction.

MOF have been used as a part of surface acoustic wave sensors (SAW) which are piezoelectric sensors to detect greenhouse gases such as CO_2 or methane[82] and volatile organic compounds (VOCs) such as hexane or toluene[83]. Other than CO_2 detection, MOFs have also shown outstanding ability for CO_2 capture[84]. The capture of any gas by a MOF is closely related to the selectivity of the gas over other gases and its overall gas intake. The selectivity of a MOF depends on the size and shape of the pore and the interaction between the surface of that pore and the molecule being adsorbed. The size/shape dependency, also known as the molecular sieve effect dictates that only molecules having a kinetic diameter compatible with the diameter of the pores of the MOF can pass through the latter[85]. HKUST-1[86] and MOF-177[87] have been the most studied MOF in this field. Studies on the selectivity of a MOF towards gases, have also been applied to rare gases, more specifically Xe/Kr selectivity[88,89]. This is particularly interesting since we are working on the detection of an isotope of Kr. As discussed in section 2.2 ^{85}Kr is released by nuclear reprocessing plants and so is ^{135}Xe. The half-life of ^{85}Kr (10.7 years) being much longer than ^{135}Xe (9.14 hours), the Kr must be captured and removed from the air and gases released by nuclear reprocessing processes, as its uncontrolled release can be dangerous. The separation of these two gases is of utmost importance since Xe is used in many applications such as commercial lighting, propulsion, anaesthesia and insulation,

among others. Several MOFs have been studied for Kr/Xe separation, namely, HKUST-1, SBMOF-2 and PCN-14 among others[90].

In the same aspect, MOFs have been widely studied for H_2 storage and hydrogen fuel cell technology[46,91]. Understanding the adsorption and storage of H_2 in MOFs gives us an idea of the behaviour of those MOFs towards tritiated dihydrogen (one of our targeted radioactive gases) which is the structural equivalent of hydrogen. Using MOFs to store hydrogen offer the possibility to do so at non-cryogenic temperatures and lower pressures than other existing methods. However, research is still ongoing to maximise the uptake of H_2 by MOFs at room temperature. MOFs with ultrahigh surface areas are also recommended, since according to Chahine's rule there is a 1 wt.% H_2 uptake every 500 m^2g^{-1} increase in surface area[92]. Qualitative activation techniques are therefore required for this application. MOF with metal oxides centres have shown to form a crystalline framework with permanent porosity and strong binding energy with the hydrogen. Zr and Hf MOF-525 have displayed a high dipole moment which allowed them to trap hydrogen on their surfaces. HKUST-1[93], UIO-66 and Mg-MOF-74 have been intensely scrutinised and have displayed promising results for hydrogen storage capacity as well. Furthermore, interpenetrating MOFs have shown to have stronger interaction with guest molecules. For example, they have been shown to assist CO_2 uptake and H_2 storage and separation.

MOFs are also materials of interest in the biomedical field, especially in drug delivery. MOF are biodegradable and their high surface area have resulted in a high loading capacity for different drugs. Their adjustable pore sizes are also desirable to determine which drug molecules would fit into them. Their open architectures also make the interaction between the biomolecule and the external environment more efficient[94]. The MOF NU-1000 and MIL-100 have been tested for oral insulin delivery by imitating stomach conditions. They both showed resistance to stomach acidity and hence protected the insulin to then degrade upon entering the blood stream[95]. MOFs have also been studied in the field of biomedical imaging where imaging contrast agents can modify MOFs for use in magnetic resonance imaging (MRI) and X-ray tomography imaging (CT).

Another field of where MOFs have been gaining terrain is electrochemical energy storage devices[96–98], for example in batteries and supercapacitors. These devices are obviously necessary for technological advancement in the field of hybrid or electric vehicles as well as portable electronic devices. MOFs are ideal candidates as their porosity boosts the electron/ions transfer and their hollow structures can withstand the volume changes of electrodes during cycling. The hydrophobicity of certain MOFs also improves the stability of the batteries. MOFs can also be functionalised to improve their inherent low conductivity.

The study of the use of MOFs in microelectronics are also steadily increasing. ZIF-8 films for example have been found to be potential future insulators in microelectronic chip devices with a strong elastic modulus, good adhesion to the support as well as low k dielectric value[99].

We will discuss further in this chapter MOF application related to their interaction with light, more specifically luminescent and scintillating MOFs.

5. Luminescent MOF

5.1 Luminescent MOFs

Aside from MOFs attractive porosity, some also have shown interesting fluorescence and scintillating properties. These properties are essential for the detection of radioactive gases by scintillation that we target in this thesis.

Different luminescence mechanisms can be exhibited by MOFs as shown in Figure I-26.

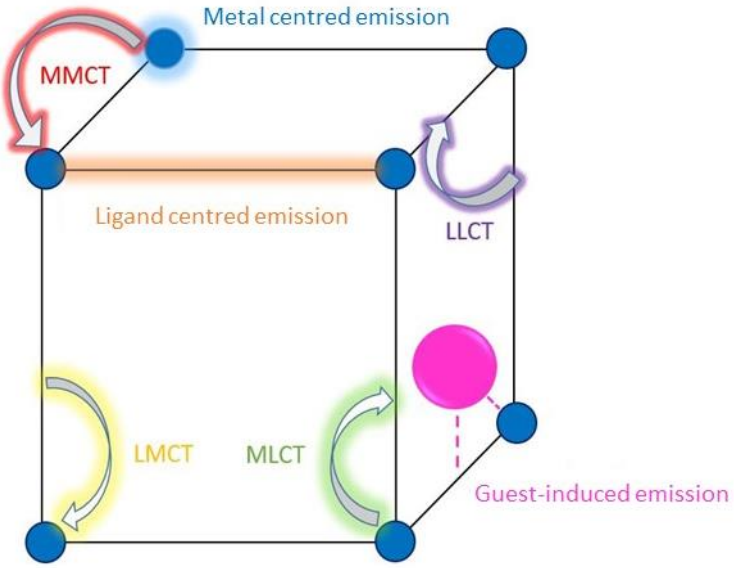

Figure I-26: Illustrating the luminescence mechanisms present in MOFs with the blue circles representing the inorganic metal clusters and the lines representing the organic ligand.

Metal centred emissions are exhibited by MOFs containing metals with partially empty orbitals. All of lanthanide trivalent ions except for La^{III} and Lu^{III} are luminescent. They exhibit narrow emissions with long lifetimes. A weak absorbance is often observed with lanthanides. A low brightness is also observed due to certain forbidden electronic transitions dictated by the parity selection rule (Laporte rule) where the transition between which two symmetric states with respect to an inversion centre is not allowed[100,101].

For this reason, the scientific community started looking at pairing these metals with absorbing organic molecules. When efficient vibronic coupling exists between an organic molecule and a metal ion, energy transfer is possible from the organic ligand's existed state and the metal ion's higher energy levels, this is known as Ligand-to-Metal Charge Transfer (LMCT). This increases the luminescence intensity of the material[39] and is known as an antenna effect. The most common lanthanide MOFs consist of Eu^{III} and Tb^{III} metal clusters which have been reported to

exhibit luminescence properties and emit in the red and green emission in the visible range[39], respectively. Serre *et al.*[102] synthesised a series of MOFs using lanthanoid elements with 1,3,5-BTC linker. Three Yttrium-based MOF were synthesised using Tb, Dy and Eu to partially substitute for the Y. Although no spectra were reported, Figure I-27 shows the change in fluorescence upon changing the metal centre.

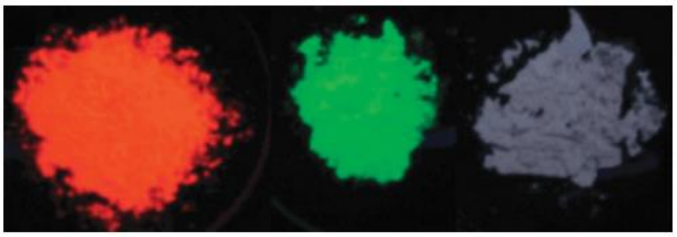

Figure I-27: Luminescence from MIL-78(Y/Eu)-red, MIL-78(Y/Tb)-green, and MIL-78(Y/Dy)-blue under 252 nm irradiation[102].

Another LMCT is observed in the famous MIL-101, which is made up of a Cr^{III} metal ion with a d^3 electronic configuration and a benzene dicarboxylic acid ligand (BDC). The BDC ligand has a relatively low quantum yield of fluorescence on its own as it consists of only one conjugated ring. But when it is coordinated to a metal in a MOF, the latter undergoes a LMCT and the MOF has an emission around 485 nm[103]. Figure I-28 shows three MOFs with the same BDC ligand but three different metal centres and the effect on the emission wavelength.

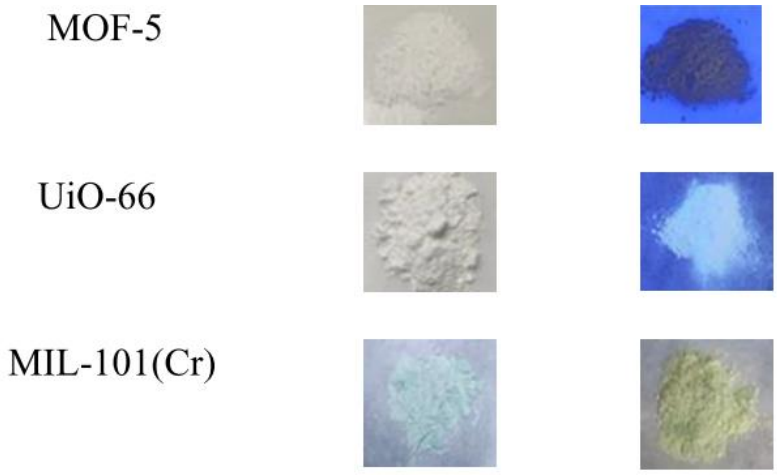

Figure I-28: Showing a photograph of three MOFs under white light (left) and UV light at 365 nm (right)[103].

Metal-to-Metal Charge Transfers (MMCTs) have also been reported in MOFs. Sticking to the lanthanide MOFs, a Eu and Tb mixed-metal MOF has been reported[104] where the luminescence from the Tb^{III} was nearly fully quenched and leaving the luminescence centred on the Eu^{III}. An increase in the quantum yield compared to the MOF only with Eu^{III} was also observed, where they concluded and antenna effect between the metal centres or a MMCT.

Now that we have explored all the possible scenarios involving the metal centre, let us move on to the ligand centred emission in a MOF. Ligand centred emission is present in structures with the metal ion exhibiting no d-d or f-f transitions, typically d^{10} metal ions such as Ag^{I} and Zn^{II} and d^{0} metal ions such as Zr^{II} and Hf^{II}. Often, the ligand-centred emission of the MOF resembles that of the ligand in a dilute solution. This is due to the rigidification of the ligand in the MOF structure, which keep the ligands quite far away from each other, and therefore mimics ligands in a diluted solution. It has been shown that for the IRMOF series, the effect of increasing the ligand conjugation decreases the π- π^{*} energy gap, making the transfer to the metal even less probable and centring the emission on the ligand. An advantage of this rigidification is also the decrease in non-radiative transitions that happen via intramolecular rotation or intermolecular phonons which are more difficult in a rigidified and spaced structure[39,105] Reducing non-radiative emissions has a tendency to increase fluorescence lifetimes and quantum yield of a molecule.

In interpenetrated structures of IRMOFs, charge transfer can happen. It has been shown that the emission of IRMOF-15 exhibits a red shift compared to the non-interpenetrated counterpart IRMOF-16[106] This is due to the interpenetrating structure that might cause smaller ligand-ligand distances, thereby making interpenetrated structures more probable for LLCT.

Metal-to-Ligand Charge Transfer (MLCT) is one of the least reported luminescence mechanisms in MOFs. It is observed in d^{10} Cu^{I} and Ag^{I} MOFs where there exists the probability of a d-electron transfer to lower empty states[39].

The mechanism we are left with to discuss are guest-induced emission. Different scenarios are possible here. One where a luminescent guest is incorporated in a non-luminescent MOF and therefore gives its luminescent properties to the MOF+Guest material. Another scenario is the inclusion of a luminescent guest inside a luminescent MOF where MOF-Guest interaction/charge transfer may occur leading to new luminescent properties different to that of the MOF or the guest when not combined. It is also possible to enhance or quench the luminescence of a MOF by incorporating certain guest molecules. Figure I-29 illustrates a study showing the effect of different lanthanide molecules on the fluorescence wavelength of a MOF.

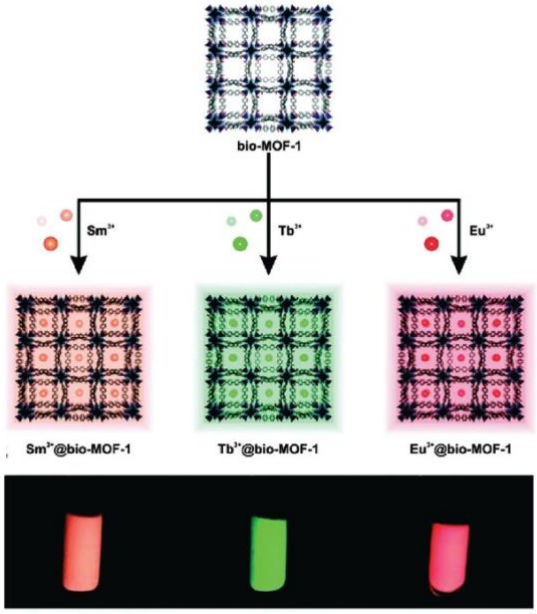

Figure I-29: Illustrating guest-induced luminescence in MOF by different lanthanide molecules[107].

Assigning a luminescence mechanism can be tricky. Literature has shown some discrepancy in the past, namely on the luminescence mechanisms assigned to IRMOF-1. It has been assigned at 525 nm through LMCT[108] and also as a green emission through trapped ZnO particles in the MOF[109]. A study carried out at our laboratory, helped unravel the true luminescence of MOF-5 by synthesising pure millimetric single crystals of this MOF[110]. The luminescence was assigned to a ligand centred emission. The effect of the solvent on the emission, also known as solvatochromism, was also studied and the different spectra shown in Figure I-30. This study is also an example of the similarity of ligand centred emission with the free ligand in solution. In the last image of Figure I-30, we can notice the broadening of the emission of the activated MOF attributed to the partial collapse of the structure. We can also observe an emission and excitation maxima of the activated MOF at shorter wavelength than the respective ligand. This is the consequence of the increased band gap in the framework due to the stabilisation of the linker and the absence of solvent. The emission wavelength is consistent with DFT calculations where the band gap is calculated at 3.56-3.46 eV, which corresponds to an emission between 348 nm and 358 nm[111].

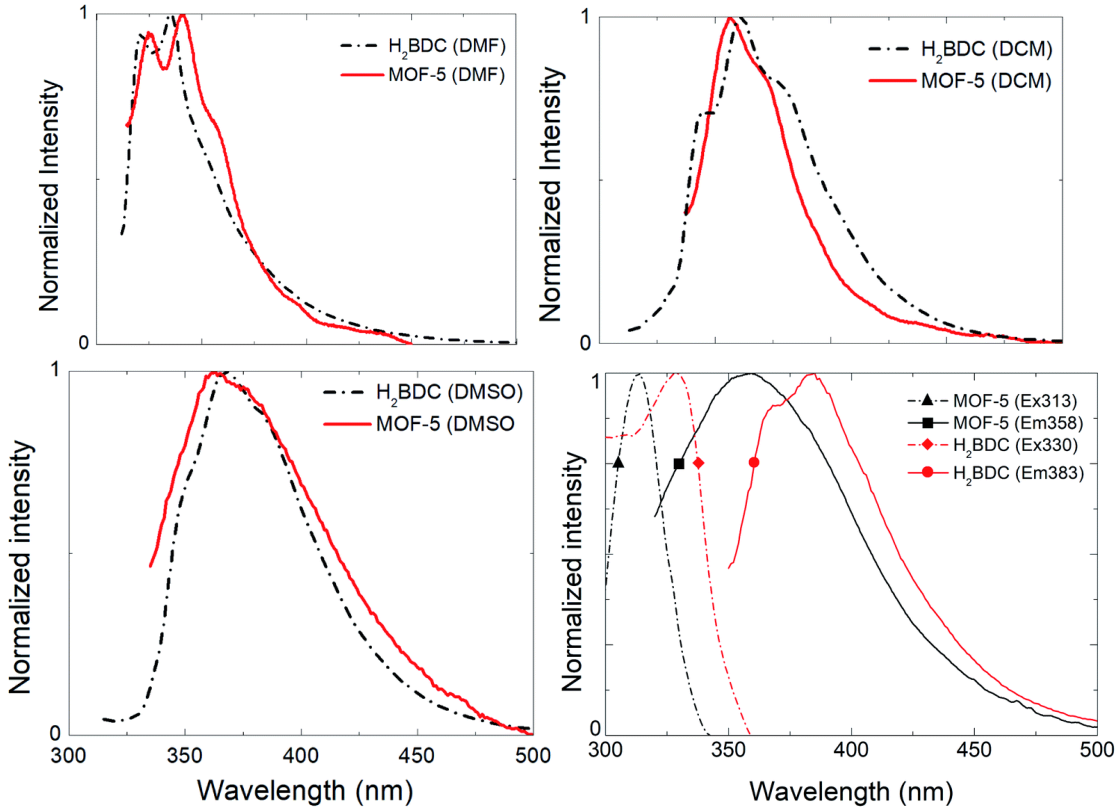

Figure I-30: Illustrating the effect of a solvent on MOF emission and the emission of the activated MOF[110].

The ability of MOFs to adsorb molecules in its pores can sometimes be detrimental to its luminescence. A foreign molecule or impurity can easily embed itself in the MOF sometimes leading to wavelength shifts, fluorescence quenching, or simply poor interpretation of the luminescence mechanisms involved.

5.2 Luminescent MOF applications

Luminescent MOFs can be used for sensing application. Gutiérrez et al[112] have recently shown that they can transform a non-luminescent MOF to a highly luminescent MOF for sensing acetone production in diabetic patients' breath.

As seen in section 5.1, MOFs can present different fluorescence wavelengths with different metal guests and can therefore be used for environmental and biological control of these metals[113]. MOFs which are stable in water can also be used to detect heavy metal pollutants in water[114].

The characteristic luminescence of certain MOFs can be quenched in the presence of certain molecules. This quenching method can also be used for sensing applications. For example $[Eu_2(3,5\text{-bct})(phen)_2(ox)_2(H_2O)]\cdot H_2O$ emits at 622 nm and this peak is quenched in the

presence of colchicine, a water-soluble drug that causes serious pollution to the environment, as shown in Figure I-31[115].

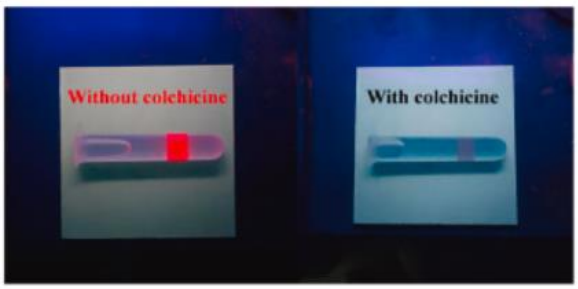

Figure I-31: A photograph of a film of the Eu-MOF without colchicine and with colchicine[115].

Mixed Eu^{3+} and Tb^{3+} luminescent MOFs can also be used as temperature sensors. There exists a difference in energy for Eu^{3+} and Tb^{3+} and hence an energy transfer from Tb^{3+} to Eu^{3+} is possible. This energy transfer changes with temperature and hence also the ratio of luminescence intensity of Eu^{3+} and Tb^{3+}. For example, MOF ($[(CH_3)_2NH_2]Eu_{0.036}Tb_{0.964}BPTC$) has been studied as a temperature sensor between 220 K and 310 K[116].

Luminescent MOFs have also been studied as pH sensors. A Tb-based MOF showed an emission intensity gradually decreasing with acidity. This MOF contained pyridyl groups whereby the protonation of those groups alters the electronic absorption capacity of the MOF and hence reduced its luminescence intensity at low pH[116].

Luminescent MOFs can also be combined to Pb to targeted luminescent properties. For example, HPU-14 was used as a platform to grow ZIF-8 MOFs on the outer later. This combined two emission centres namely that of anthracene and that of lanthanide ions. This composite MOF material can exhibit reversible photoswitching behaviour under 365 nm and has been successful in anticounterfeiting application[117].

The research for making Solid State light emitting diode (LED) safer, energy efficient and environmentally friendly has been ongoing for years. C. Sun *et al.*[118] has shown the effect of applying a MOF on a LED device as illustrated by Figure I-32. It shows that LED alone projects a blue tinge (a) while when coated with a thin layer of 3.5 wt% $[Ir(ppy)^2(bpy)]^+$ MOF, a bright white light is observed.

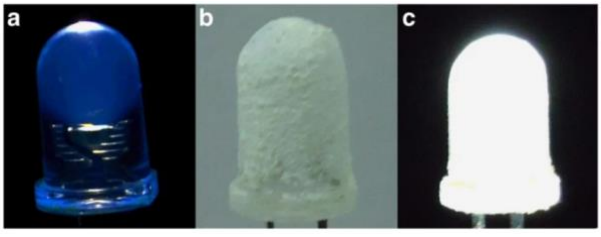

Figure I-32: (a) An illuminating 3 mm reference ultraviolet LED, (b) The same LED coated with a thin layer of sample of 3.5 wt% [Ir(ppy)2(bpy)]+@1 (not turned on), (c) The coated LED was turned on[118].

6. Scintillating MOFs

The research group of F.P. Doty *et al.*[119] first started to explore MOFs as potential scintillating materials with the idea that their structural diversity will help control factors that affect the efficiency of a scintillator such as structural composition, electronic structure, crystal symmetry and atomic density. They started by studying MOFs with a full d^{10} electronic configuration, to restrict the optical UV-Vis transitions from the metal and hence centre the scintillation on the organic ligand. Conjugated organic molecules that present fluorescent properties, also often present scintillating properties. They went on to synthesise a MOF based on a stilbene organic ligand as shown in Figure I-33. Stilbene can usually undergo a non-radiative light-induced *trans-cis* isomerisation, which significantly decreases its quantum yield of luminescence. However, they have shown that its incorporation in a MOF lattice causes a rigidification which supresses the isomerisation. They managed to demonstrate the increase in the fluorescence lifetime due to the rigidification. Even though they theorised an increase in the quantum yield of fluorescence, they were could not study it due to variations in the crystal size and shape which can introduce significant uncertainties in the measurements.

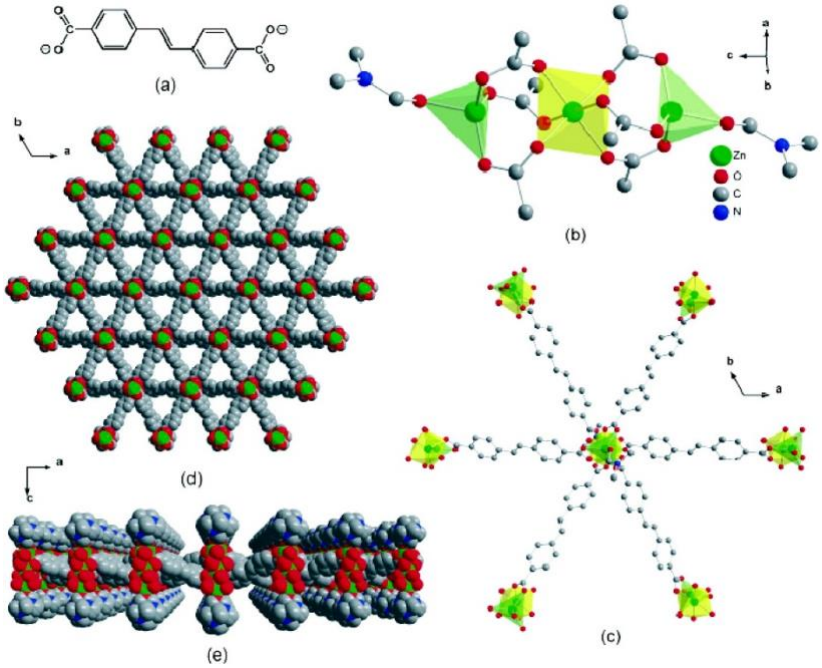

Figure I-33: Illustrating a) trans-4,4'stilbenedicarboxylate ligand, b) $Zn_3(RCO_2)_6(DMF)_2$ SBU along the c-axis, c) the SBU hexagonal pinwheel connections from the top, d) space filling model looking down the c axis[120].

Two stilbene MOFs were synthesised: an interpenetrated $Zn_4O(SDC)_3$ with a 3D topology similar to isoreticular MOFs discussed in section 4.1 of this chapter (MOF-S1) and 2D sheets of $Zn_3(SDC)_3(DMF)_2$, (MOF-S2). These single crystals of MOFs were exposed to high-energy protons (3 MeV). Figure I-34 shows the results using ion-beam-induced luminescence (IBIL) spectroscopy on the organic ligand and the two MOFs. The shape of the IBIL spectrum of the ligand is different to the ones of the MOFs but they still lie in the same wavelength range.

Distinctive vibronic bands can also be seen for the 3D MOF-S2 compared to the MOF-S1. The large stokes shift in the IBIL results of the MOFs with respect to their fluorescence excitation maxima are relatively large so that little overlap exists between the absorption and the IBIL emission and hence self-absorption is considerably reduced.

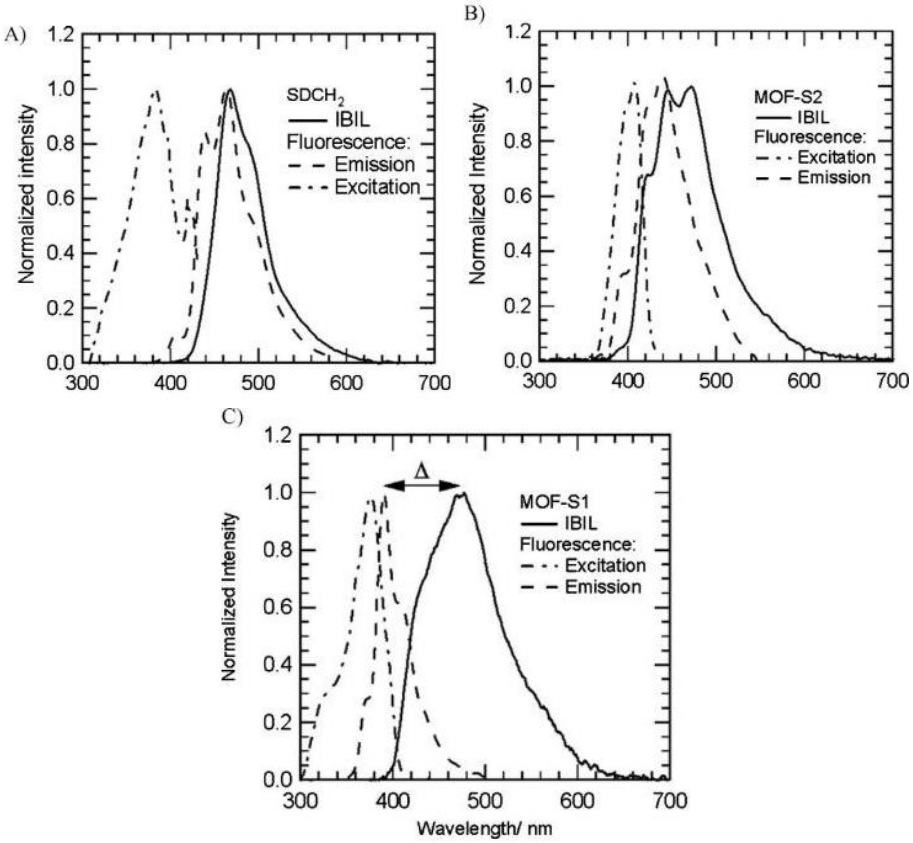

Figure I-34: Illustrating the IBIL and fluorescence results of the A) Stilbene ligand B) MOF-S2 and C) MOF-S1[119].

This study also concluded that compared to commercial organic scintillators, these MOF scintillators showed more resistance to radiation damage. They attributed this resistance to the spatial separation of the organic linkers in the MOF. In a densely packed material, the defects formed by the radiation damage are recombined with the delocalized excitons and are quenched. However, in an open framework such as a MOF, the mobility of the excitons are considerably reduced.

The MOFs were also exposed to a source of alpha particles (^{241}Am) and the results showed that time-dependence of luminescence varied from one MOF to the other meaning that varying the ligand's environment by crystal structure design varies the scintillating properties.

For a limited range of energy and application, organic scintillators can see some application in X-ray detection. But for > 40 keV X-ray organic scintillators are ineffective for X-ray detection due to their low X-ray scattering cross section, an opening for another novel material for X-ray detection was available. MOFs with a first-row transition metal with a low atomic number Z would also have a relatively small X-ray scattering cross section. Therefore, the research turned

towards high Z MOFs such a as Zr and Hf which serve as efficient X-ray absorbers. C. Wang *et al.*[121] showed that the metal centres served as antennas, whereby their outer shell electrons are ejected and undergo inelastic scattering thereby transferring their energy to the ligand of the MOF. The ligand is then in an excited state and relaxes by emitting photons. Logically, Hf MOFs display higher X-ray induced scintillation than Zr because of its higher atomic number and hence better interaction with X-rays.

A more recent study by J. Lu *et al.*[122] showed a similar antenna effect with four different lead-based MOFs: $[Pb(1,4\text{-ndc})(DMF)]_n$ referred to as (SMOF-1), $[Pb(1,4\text{-ndc})(DMA)]_n$ referred to as (SMOF-2), $[Pb_2(2,6\text{-ndc})2(H_2O)]_n \cdot nDMF$ referred to as (SMOF-3) and $[Pb_4(2,6\text{-ndc})_3Cl_2]n$ referred to as (SMOF-4). They chose Pb to achieve an even higher scattering cross-section as it has a higher atomic number than Zr and have a high X-ray attenuation coefficient. The four Pb MOFs were exposed to an X-ray of energy around 18.9 keV and they all exhibited scintillating properties as seen in Figure I-35.

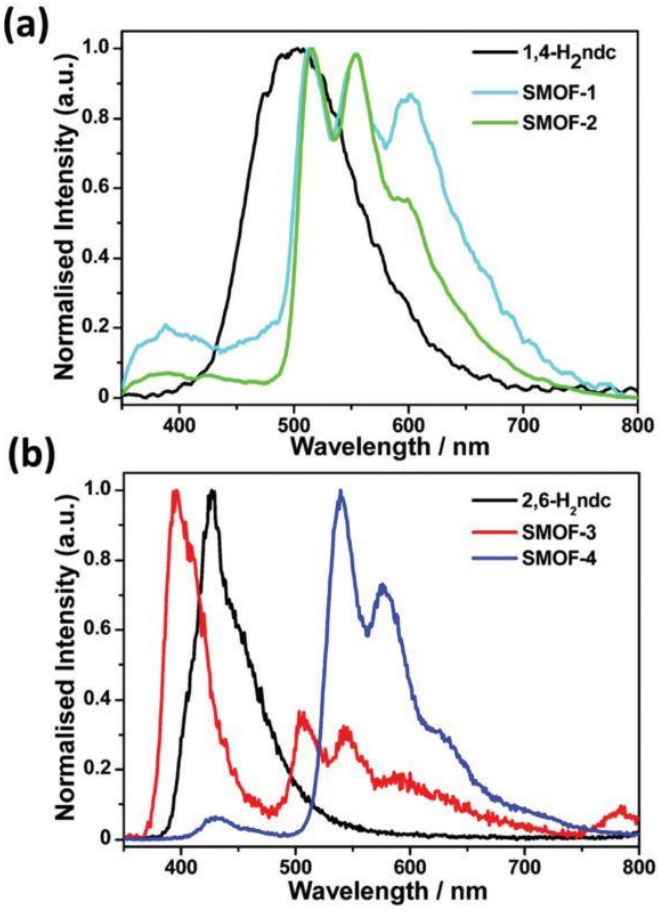

Figure I-35: Illustrating the X-ray stimulated luminescence of a) SMOF-1 and SMOF-2 and b) SMOF-3 and SMOF-4[122].

SMOF-4 reveals the largest stokes shift minimising the self-absorption in this MOF and hence making it a better scintillating candidate. Indeed, when examining the luminosity of the four

MOFs, their corresponding ligands and mixture of a molar equivalent of the metal and ligand that composes the MOF, they found that SMOF-4 emits a higher light output. The results are illustrated in Figure I-36 and compared to a fast inorganic scintillator, namely BaF_2. Furthermore, the density of SMOF-4 (3.154 $g \cdot cm^{-3}$) was higher than the other MOFs studied here (2.193, 2.187 and 2.380 $g \cdot cm^{-3}$) meaning that its stopping power for X-rays was higher than the other MOFs.

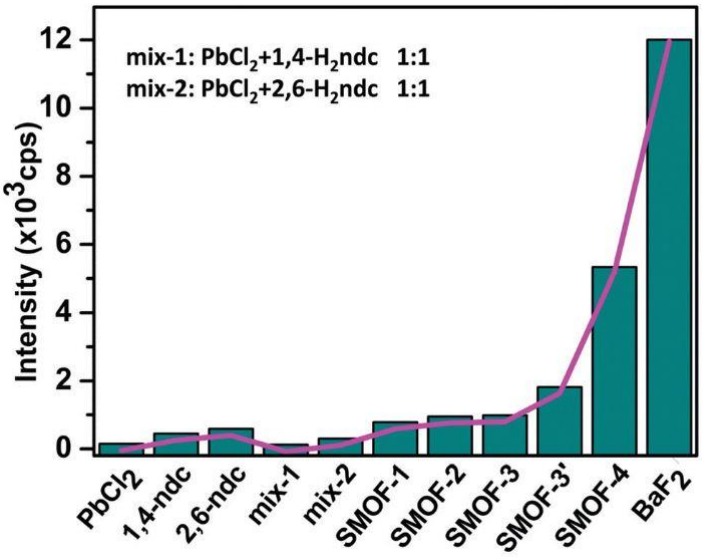

Figure I-36: Illustrating the intensity of the light output of the four different MOFs, ligands and mixtures of ligand and metals[122].

Another more recent study on a Pb-based MOF was carried out by W. Wang *et al.*[123]. A $[Pb(adda)(DMF)]_n$ MOF was synthesised, where H_2adda=(2E,2′E)-3,3′-(anthracene-9,10-diyl)diacrylic acid). The metal-to-ligand antenna effect was also exploited in this MOF. This MOF is referred to as 1 in Figure I-37, which illustrates the results of a radioluminescence (RL) experiment with an X-ray source. In Figure I-37 (a), we can notice that the RL intensity increases along with the dose rate, showing an efficient X-ray response. This response is shown to be linear in Figure I-37 (b) and we can observe that the MOF 1 has a larger slope than the reference scintillators which shows that it exhibits a higher X-ray sensitivity. Figure I-37 (c) illustrates that MOF 1 exhibits a higher RL intensity that the ligand and metallic salt as well as a mixture of both those precursors present in the MOF. W. Wang *et al* claim that the MOF also shows a higher RL intensity than the reference PWO and anthracene scintillators, but failed to give the right scintillation yields for both materials. This result needs to be considered with a pinch of salt in order to extract any relevant information. Lastly, this RL intensity was also compared to other scintillating MOFs in literature, namely the SMOF-1, SMOF-2 and SMOF-3 that we have encountered in the study above by J. Lu *et al.*[122]

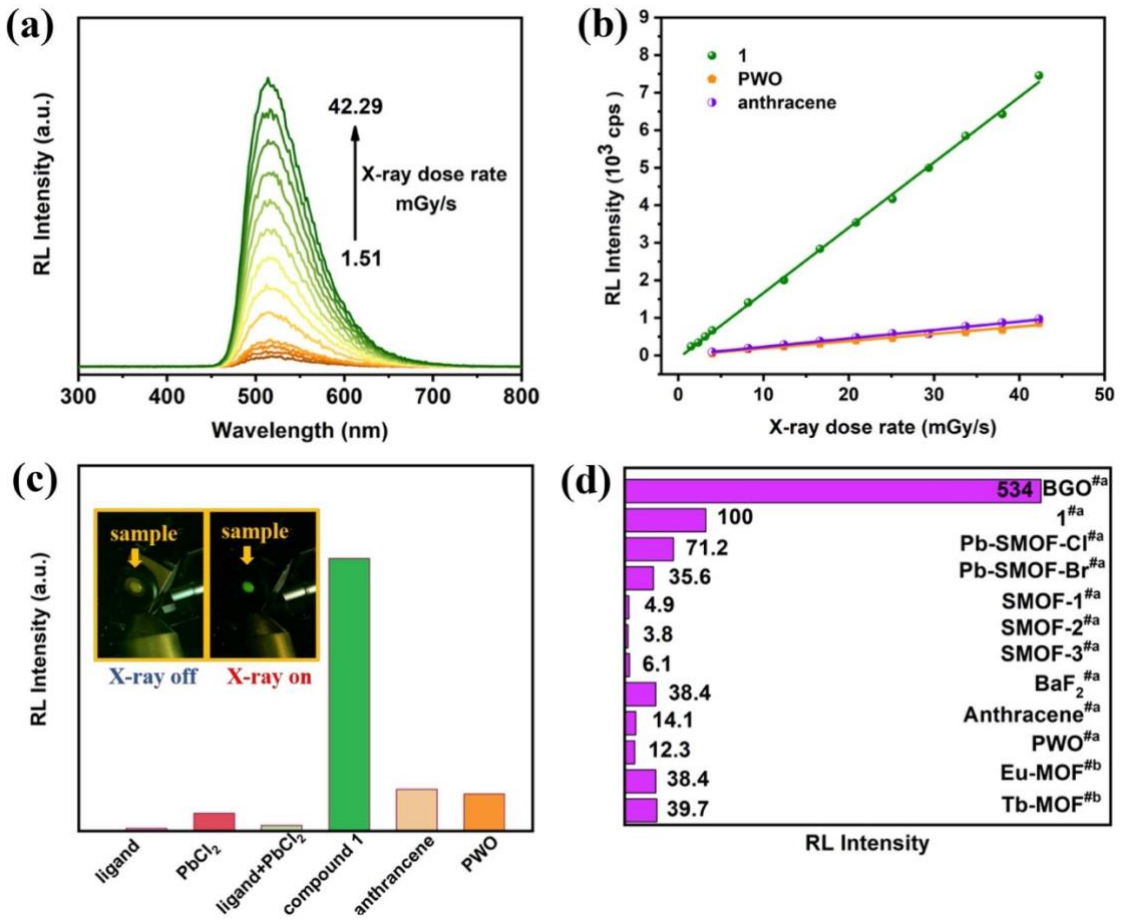

Figure I-37: Illustrating in (a) the X-ray dose rate dependent RL of MOF 1 (b) the linear relationship between the RL intensity and the X-ray dose (c) the RL intensity of the different components of the MOF, the MOF and reference materials, (d) comparison of the RL intensity with reference materials and other scintillating MOFs found in literature[123].

Colleagues from the SPARTE project at the University of Milano-Bicocca have also been working on scintillating nanoMOFs[124] using a metallic node with a high atomic number (Zr) and combing it with a 9,10-diphenylanthracene (DPA) ligand whose photoluminescence quantum yield is positioned around 0.96. They then went on to incorporating this MOF into different polymer matrixes, polydimethylsiloxane (PDMS) and poly(methyl methacrylate), also known as PMMA, to make a nanocomposite scintillator. Figure I-38 shows the Zr:DPA MOF embedded in a PDMS matrix and the fluorescence response under a UV lamp as well as the scintillation under X-rays. They demonstrated under X-ray exposure, an ultra-fast rise time of the order of ps, which is essential in time-of-flight positron emission tomography (TOF-PET), a medical imaging technique used in oncology. However, their technique posed two major disadvantages, the first one being the diffusion of light in their material, which therefore does not allow for the efficient detection of all photons emitted by scintillation. The second problem that would be detrimental to an application like ours for gas detection is the lost in porosity of the MOF by embedding it into a polymer matrix.

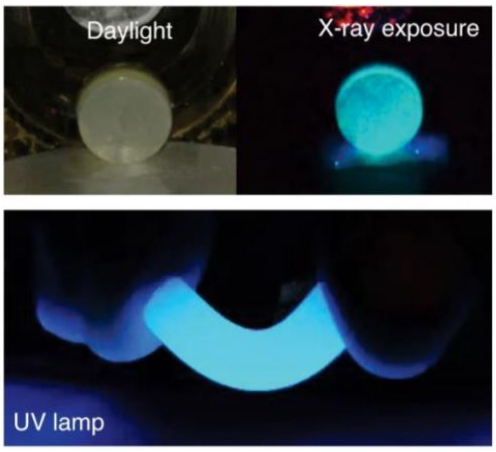

Figure I-38: Photos of the Zr:DPA in a PDMS matrix[124].

The same research group more recently worked on a hetero-ligand MOF with a Zr cluster also embedded in a polymer matrix[125]. The structure and fluorescent mechanism of this MOF is shown in Figure I-39. The DPA ligand gets excited by an external source, transfers its energy and excites, by non-radiative energy transfer, the 5,12-diphenyl-tetracenedicarboxylate (DPT) ligand. The DPA ligand then recombines radiatively and emits a green photon. Authors demonstrated that this fluorescence mechanism provides a larger Stokes shift than the mono-ligand MOF equivalent. By matching the emission frequency of the anthracene with the absorption of the tetracene, they showed an energy transfer of 97% and a photoluminescence quantum yield of 60% even with only 8% of DPT in the structure. They demonstrate the thermal stability, stability to atmospheric moisture and radiation exposure stability (up to 100 Gy) of this MOF composite by radioluminescence experiment with an unfiltered X-ray source. They also once again demonstrated its fast-rising time of 190 ps showing that the non-radiative transfer between the ligands is fast.

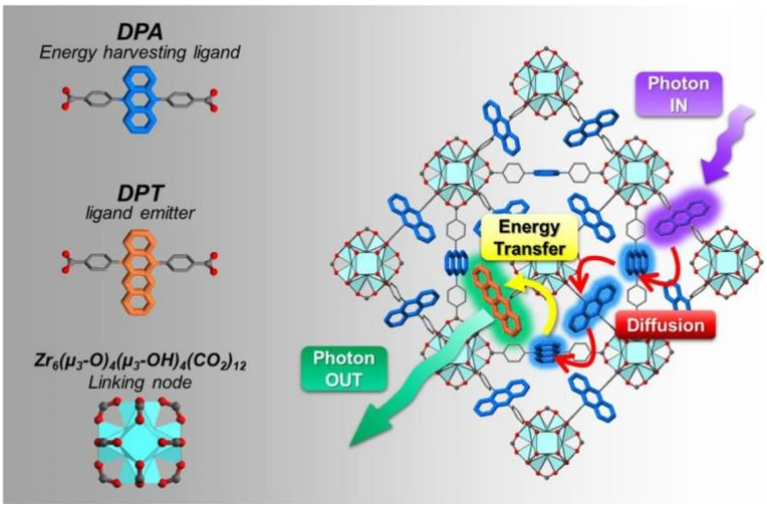

Figure I-39: Illustrating the structure and fluorescent mechanism of the Zr:DPA:DPT MOF[125].

Based on the same principle of using a high Z metal centre that acts on the antenna to the ligand, J. Wang *et al.*[126] created a highly efficient and reabsorption-free X-ray harvesting system using a luminescent MOF-fluorescent chromophore composite film. The MOF was Zr-BADC (Biphenyl Anthracenedicarboxylic acid) nanoparticles in an fcu configuration. They determined a low detection limit 60 times lower for the MOF-chromophore composite film that the MOF alone and 7 times lower than the fluorescent organic chromophore alone. The detection limit determined for the MOF-chromophore composite film was also 22 times lower (256 $nGy \cdot s^{-1}$) than what the standard dosage is for a medical exam (5.5 $\mu Gy \cdot s^{-1}$), which makes this film a novel candidate for X-ray radiography.

Integrating a MOF in a matrix or film has proven to be advantageous for their use as scintillators. However, as we have seen light scattering caused by the incorrect matching of the refractive index of the MOF and the matrix can be detrimental to the scintillating light output. MOF crystals or nanocrystals can be difficult to characterize as scintillators because of the small-size and low density. The characterisation techniques often need to be adapted, for example using high dose rate or nanocrystals suspension in a liquid. The latter entails that the MOF is not being characterised in its possible final form for its application. Therefore, our group decided to explore sintering MOF-only pellets[127] to overcome the issue of low density and size. The densification was performed by sintering 80-90 mg of MOF-205 with a pressure of 1.1 GPa and a temperature of 100°C (heating at $10°C \cdot min^{-1}$). MOF-205 having a cubic structure makes it an ideal candidate for sintering, as theoretically under uniaxial pressure the crystallographic planes should slide and collapse. This process resulted in translucent 400 ± 20 µm pellets with a 300% densification compared to the non-sintered MOF. The MOF pellets are amorphised through this process as proven by the X-ray diffraction experiments. We obviously here lose the porosity of our MOF, which is one of the most attractive attributes of MOFs; however, we wanted to characterise the pellets potential as scintillators with a cathodoluminescence experiment with a $^{90}Sr/^{90}Y$ beta source as well as a radioluminescence experiment with an X-ray excitation. Figure I-40a) shows the emission wavelength of our MOF pellet under the different excitation sources with an inset figure showing the transparency of the pellet as well as its luminescence under a 365 nm excitation source. Figure I-40 shows the RL experiment of the pelleted MOF-205 compared to a BC-404 cylinder of the same thickness and diameter. BC-404 is a reference in the field of plastic scintillation. The area under the curve corresponds to the number of emitted photons and therefore can be used to determine a scintillation efficiency. We estimated here that the MOF pellet emits 55% of the photons emitted by BC-404. When looking at literature, we have found that this value validates the use of MOF pellets as intrinsic scintillators and even puts it at the top of the list as far as MOF-based scintillators are concerned. The unpelletised MOF-205 crystals were also tested under the same RL conditions and the results were two orders of magnitude lower than the pellet which once again validates the need for sintering. In this study, alpha, beta and gamma detection experiments were carried out and validated by comparison to MCNP6.2 simulations. Gamma detection with the MOF-205 pellet allowed for the observation of a full absorption peak at 59 keV with a ^{241}Am source and at 356 keV with a ^{133}Ba source. To the best of our knowledge,

this is the first time this observation was achieved with a MOF and this was possible due to the densification of the MOF. It is important to note that this study also resulted in the first quantitative identification of alpha/beta and alpha/gamma particle discrimination in a MOF scintillator.

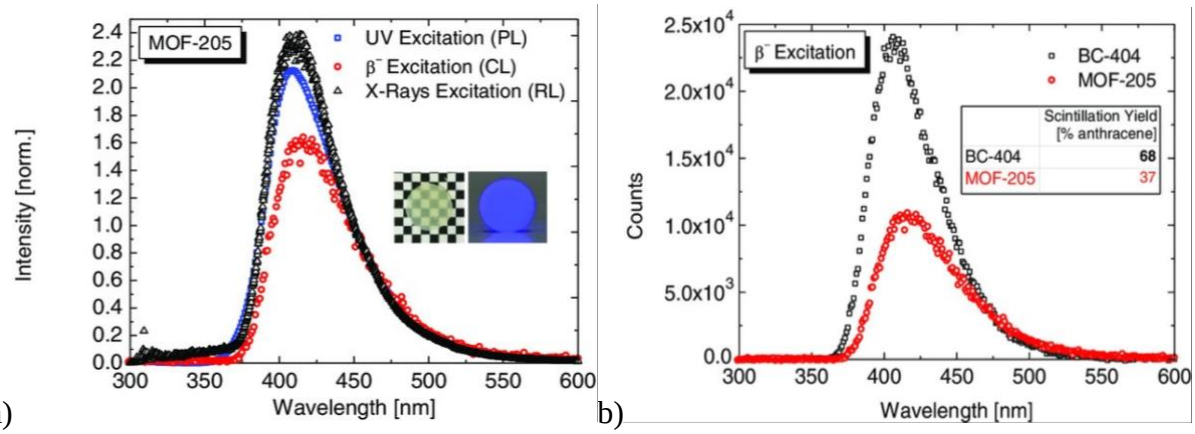

Figure I-40: Illustrating a) the emission of the MOF pellet by PL, CL and RL and b) the RL results of the MOF pellet compared to the BC-404 reference[127].

Another strategy for exploring scintillating MOFs is to study those whose scintillation might be centred on the metal centres rather than the ligand. Wang *et al.*[128] adopted such a strategy and went even further by showing that colour tunability of a scintillating MOF can be achieved by changing the ratio of the mixture of Eu^{3+} to Tb^{3+} in their MOF. Colour tunability is important in achieving the highest photon count measurements using photomultiplier tubes and also in light-emitting diodes.

An out of the ordinary study was carried out by Andrea *et al.*[129] who were able to synthesise and characterise an autoluminescent MOF. This MOF is composed of a radioactive element and a scintillating component. Thorium was chosen as the radioactive metal centre as it emits low penetrating alpha particles that release most of their energy inside the MOF structure and hence maximise photoemission. Th^{4+} is also a closed-shell system, which limits charge transfers that might reduce luminescence. Thorium MOFs have also shown a relatively good stability in air and water. 2,6-Naphthalene dicarboxylic acid ligand was chosen as it has shown to be efficient scintillator and produce rigid 3D networks in MOFs which reduces flexibility and hence reduces quenching probabilities. They managed perform RL experiments with the MOF, the 2,6-NDC ligand, thorium nitrate metallic salt and a mixture of the salt and the ligand. In these experiments, they found that the signal for the ligand was comparable to the background value, that the metallic salt generated 10.9 counts per minute per milligram (which contains 0.42 mg of thorium) and that the MOF produced 173 counts per minutes per milligram (which contains 0.35 mg of thorium). The mixture of metal and ligand revealed a higher count than the ligand and metal separately but a lower scintillating yield than the MOF proving that the MOF structure strongly improves the autoluminescent properties.

The use of scintillating MOFs for radioactive gas detection has been studied by our SPARTE colleagues[130]. They demonstrate the capacity of a hafnium-based MOF with dicarboxy-9,10-diphenylanthracene as the ligand for the detection of ^{85}Kr, ^{222}Rn and ^{3}H using the same gas detection system as us (described in Chapter II). Their Hf MOF, emits at 450 nm and an emission lifetime of 2.4 ns. An emission under 3 ns is ideal for detection in coincidence. Compared to commercially available MOF, their MOF showed better performance for ^{85}Kr detection with a limit of detection calculated at 1 $kBq \cdot m^{-3}$. They are currently working on incorporating their MOF into a porous polymeric host for practical handling. We will be comparing our gas detection results to this work throughout this manuscript.

7. Chapter conclusion and thesis overview

In this chapter, we have introduced the concept of radioactivity and ionising radiation. We discussed the properties, sources and detection methods available for the three following radioactive gases of interest: ^{85}Kr, ^{222}Rn and ^{3}H. These three gases are representative of most radioactive gases in terms of energy and type of ionising radiation which is essential for testing if this innovative porous scintillator is indeed efficient.

We introduced the fundamentals of photophysics necessary to understand this manuscript including the concept of photoluminescence and scintillation.

The structure, synthesis methods and application for Metal Organic Frameworks were discussed. Their properties were also discussed with an emphasis on two properties essential for gas detection, their interaction with gases and their luminescence/scintillating properties. Applications related to luminescent properties were also discussed and the several scintillating MOF studies were talked over.

The detection of radioactive gases using Metal Organic Frameworks have so far only been theorised. We propose combining the porosity and luminescence properties discussed in this chapter to explore MOFs as a new class of volumic scintillating material for the online detection of radioactive gases.

For this manuscript, we are going to concentrate on Zinc and Zirconium metal clusters since they have a d^0 and d^{10} electronic configuration. This means that electronic transitions from the empty or full d orbitals are not very probabilistic and hence make the interpretation of electronic excitation easier. The electronic transitions will be mainly centred on the ligand of the MOF or due to ligand-to-ligand charge transfers. We will also be exploring only carboxylate ligands as they can easily be used to synthesise crystalline materials as explained in section 4.1 of this chapter and they are also readily available for purchase.

After a description of the materials and methods (Chapter II) we will be starting in Chapter III with zinc-based MOFs as they have been widely studied before. Studies have shown that the synthesis of pure single crystals of MOFs are possible at certain temperature and concentration

conditions. However, as seen in section 4.2, zinc-based MOF are very sensitive to humidity/water and this greatly affects their porosity and luminescence properties.

Therefore, we will be moving to Chapter IV, where more stable zirconium-based MOF will be explored. A comparison between their zinc counterpart, i.e. a MOF with the same ligand but different metal, will be possible. In both chapters, the structural and photophysical characterisation of each MOF will be discussed as well as their results upon exposure to radioactive gases.

In Chapter V, we will be discussing the doping strategy which we have adopted whereby an intrinsically fluorescent ligand is incorporated in small quantities in the structure of a MOF that we can already synthesised to enhance the fluorescence properties of the MOF while maintaining its synthesis protocol and overall structure.

REFERENCES

1. Radvanyi, P. & Villain, J. The discovery of radioactivity. *Comptes Rendus Physique* vol. 18 544–550.
2. Klotz, F., Bergdolt, J., Le Clech, L.,. La Radioactivité. in *Commissariat à l'énergie atomique (CEA) Livret pédagogique* (2018).
3. Orano. All about radioactivity. https://www.orano.group/en/unpacking-nuclear/all-about-radioactivity.
4. Arpansa. Alpha Particles. https://www.arpansa.gov.au/understanding-radiation/what-is-radiation/ionising-radiation/alpha-particles.
5. Arpansa. Beta Particles. https://www.arpansa.gov.au/understanding-radiation/what-is-radiation/ionising-radiation/beta-particles.
6. Arpansa. Gamma Radiation. https://www.arpansa.gov.au/understanding-radiation/what-is-radiation/ionising-radiation/gamma-radiation.
7. Brown, J. G. *X-rays and their applications*. (1975).
8. Beckers, M. *et al.* 2 - Basics of light guidance. in *Polymer Optical Fibres* (eds. Bunge, C.-A., Gries, T. & Beckers, M.) 9–46 (Woodhead Publishing, 2017).
9. Grupen, C. & Rodgers, M. *Radioactivity and radiation*. *An Introduction to Radiation Protection, Fifth edition* (2016).
10. Priyamstudycentre. Radioactive decay. https://www.priyamstudycentre.com/2019/04/radioactive-decay-half-life.html (2019).
11. Borak, T. B. & Johnson, J. A. Estimating the risk of lung cancer from inhalation of radon daughters indoors: review and evaluation. Final report, October 1986-April 1988. (1988).
12. WHO. Radon. https://www.who.int/news-room/fact-sheets/detail/radon-and-health.
13. Le Bourillet, C., Ramain, P., Adam, F., Salomon, J. & Gupta, O. *National action plan 2020-2024 for the management of the radon risk*. http://inis.iaea.org/search/search.aspx?orig_q=RN:52111223 (2020).
14. Mauree, S. *et al.* Detection of Radioactive Gas with Scintillating MOFs. *Adv Funct Mater* (2023).
15. Chisté, V. LNE - LNHB/CEA Table de Radionucléide. http://www.lnhb.fr/nuclides/Rn-222_tables.pdf (2010).
16. Cinelli, G., De Cort, M., Tollefsen, T. *European atlas*. (2019).

17. Bateman, H. Solution of a system of differential equations occurring in the theory of radioactive transformations. *Proc. Cambridge Phil. Soc.* **15**, 423–427 (1910).

18. Kellett, Mark A. & Bersillon, Olivier. The Decay Data Evaluation Project (DDEP) and the JEFF-3.3 radioactive decay data library: Combining international collaborative efforts on evaluated decay data. *EPJ Web Conf.* **146**, 2009 (2017).

19. Pressyanov, D. New generation of highly sensitive radon detectors based on activated carbon with compensated temperature dependence. *Sci Rep* **12**, 1–9 (2022).

20. Schroeder, M. C., Vanags, U. & Hess, C. T. An activated charcoal-based, liquid scintillation-analyzed airborne Rn detector. *Health Phys* **57**, 43–49 (1989).

21. Schönhofer, F., Pock, K. & Friedmann, H. Radon surveys with charcoal and liquid scintillation counting - Field experience and comparison to other techniques. *Journal of Radioanalytical and Nuclear Chemistry Articles* **193**, 337–346 (1995).

22. Maier, A. *et al.* Radon adsorption in Charcoal. *Int J Environ Res Public Health* **18**, (2021).

23. RadonEye. SMART Radon detectors for Home owner. http://radonftlab.com/radon-sensor-product/radon-detector/rd200/.

24. Alphaguard. *Bertin Technologies* https://www.bertin-technologies.fr/produits/surveillance-professionnelle-du-radon/radon-alphaguard/.

25. RSSI. RSSI's Alpha-track Radon Detectors. https://www.rssi.us/radon-alpha-track-radon-detector.htm.

26. Sabot, B. Étalonnage des instruments de mesure de l'activité volumique du thoron (220 Rn) dans l'air, L'université Pairs-Saclay, 2016.

27. Pressyanov, D. *et al.* Testing and calibration of cds as radon detectors at highly variable radon concentrations and temperatures. *Int J Environ Res Public Health* **16**, (2019).

28. Orano group. Orano Cycle Rapport d'information du site de la Hague. 1–90 (2019).

29. Ahlswede, J., Hebel, S., Ross, J. O., Schoetter, R. & Kalinowski, M. B. Update and improvement of the global krypton-85 emission inventory. *J Environ Radioact* **115**, 34–42 (2013).

30. Council Directive 96/29/Euratom of 13 May 1996 laying down basic safety standards for the protection of the health of workers and the general public against the dangers arising from ionizing radiation, Council of the European Union. *Official Journal L* (1996).

31. IRSN. *Fiche Radionucleide 85Kr*. https://www.irsn.fr/sites/default/files/documents/larecherche/publications-documentation/fiches-radionucleides/Kr85SAN.pdf (2011).

32. EPA. Radionuclide Basics : Tritium. https://www.epa.gov/radiation/radionuclide-basics-tritium (2023).

33. ITER. Tritium Breeding. https://www.iter.org/fr/mach/tritiumbreeding.

34. Fichet, P., Bultel, A., Markelj, S. & Moreno, C. Review of the different techniques to analyse tritium. *TRANSAT(Transversal Actions for Tritium).* 1–36 (2020).

35. IBS. Fluorescent Proteins. https://www.ibs.fr/fr/recherche/assemblage-dynamique-et-reactivite/groupe-imagerie-integree-de-la-reponse-au-stress/equipe-pixel/techniques-utilisees/photophysics-of-fluorescent-proteins?lang=fr#4.

36. Foresman, J. B. & Frisch, Æ. *Exploring Chemistry with Electronic Structure Methods*. (2015).

37. What is the Stokes Shift. *Edinburgh Instruments* https://www.edinst.com/blog/what-is-the-stokes-shift/.

38. Marian, C. M. Spin-orbit coupling and intersystem crossing in molecules. *Wiley Interdiscip Rev Comput Mol Sci* **2**, 187–203 (2012).

39. Allendorf, M. D., Bauer, C. A., Bhakta, R. K. & Houk, R. J. T. Luminescent metal-organic frameworks. *Chem Soc Rev* **38**, 1330–1352 (2009).

40. Wikipedia. Scintillation (physics). https://en.wikipedia.org/wiki/Scintillation (physics).

41. Mitev, K. & Cassette, P. *Radioactive Noble Gas Detection and Measurement with Plastic Scintillators*. (2021).

42. Tomic, E. A. Thermal stability of coordination polymers. *J Appl Polym Sci* **9**, 3745–3752 (1965).

43. Yaghi, O. M., Li, G. & Li, H. Selective binding and removal of guests in a microporous metal–organic framework. *Nature* **378**, 703–706 (1995).

44. Li, H.; Eddaoudi, M.; O'Keeffe, M.;Yaghi, O. M. Design and synthesis of an exceptionally stable and highly porous metal-organic framework. *Nature* **402**, 276–279 (1999).

45. Eddaoudi, M. *et al.* Systematic design of pore size and functionality in isoreticular MOFs and their application in methane storage. *Science (1979)* **295**, 469–472 (2002).

46. Koner, S. Chapter 25 - Adsorption and storage of hydrogen into porous metal-organic framework solids. in *Metal-Organic Framework-Based Nanomaterials for Energy Conversion and Storage* (eds. Gupta, R. K., Nguyen, T. A. & Yasin, G.) 565–587 (Elsevier, 2022).

47. François-Xavier Coudert. Isoreticular metal-organic frameworks, illustrated by some members of the IRMOF family. https://fr.wikipedia.org/wiki/Metal–

organic_framework#/media/Fichier:Isoreticular_metal-organic_frameworks_of_the_IRMOF_family.png (2012).

48. Mai, Z. & Liu, D. Synthesis and Applications of Isoreticular Metal-Organic Frameworks IRMOFs-n (n = 1, 3, 6, 8). *Cryst Growth Des* **19**, 7439–7462 (2019).

49. Gong, Y. N., Zhong, D. C. & Lu, T. B. Interpenetrating metal-organic frameworks. *CrystEngComm* **18**, 2596–2606 (2016).

50. Yang, S. *et al.* A partially interpenetrated metal-organic framework for selective hysteretic sorption of carbon dioxide. *Nat Mater* **11**, 710–716 (2012).

51. Sharmin, E. & Zafar, F. Introductory Chapter: Metal Organic Frameworks (MOFs). in *Metal-Organic Frameworks* (eds. Zafar, F. & Sharmin, E.) (IntechOpen, 2016). doi:10.5772/64797.

52. Chen, L., Wang, H. F., Li, C. & Xu, Q. Bimetallic metal-organic frameworks and their derivatives. *Chem Sci* **11**, 5369–5403 (2020).

53. Wu, Z. F. & Huang, X. Y. A Mechanoresponsive Fluorescent Mg-Zn Bimetallic MOF with Luminescent Sensing Properties. *ChemistrySelect* **3**, 4884–4888 (2018).

54. Luo, X. *et al.* Trimetallic metal–organic frameworks and derived materials for environmental remediation and electrochemical energy storage and conversion. *Coord Chem Rev* **461**, 214505 (2022).

55. Li, Z. *et al.* Fe-Co-Ni trimetallic organic framework chrysanthemum-like nanoflowers: Efficient and durable oxygen evolution electrocatalysts. *J Mater Chem A Mater* **10**, 4230–4241 (2022).

56. Rocío-Bautista, P., Taima-Mancera, I., Pasán, J. & Pino, V. Metal-organic frameworks in green analytical chemistry. *Separations* **6**, 1–21 (2019).

57. Furukawa, H., Cordova, K. E., O'Keeffe, M. & Yaghi, O. M. The chemistry and applications of metal-organic frameworks. *Science (1979)* **341**, (2013).

58. Bunzen, H. Chemical Stability of Metal-organic Frameworks for Applications in Drug Delivery. *ChemNanoMat* **7**, 998–10007 (2021).

59. Ming, Y., Kumar, N. & Siegel, D. J. Water Adsorption and Insertion in MOF-5. *ACS Omega* **2**, 4921–4928 (2017).

60. Ding, M., Cai, X. & Jiang, H. L. Improving MOF stability: Approaches and applications. *Chem Sci* **10**, 10209–10230 (2019).

61. Mouchaham, G., Wang, S. & Serre, C. Metal-Organic Frameworks: Applications in Separations and Catalysis. 1–28 (2018).

62. Rubio-Martinez, M. *et al.* New synthetic routes towards MOF production at scale. *Chem Soc Rev* **46**, 3453–3480 (2017).

63. Remya, V. R. & Kurian, M. Synthesis and catalytic applications of metal–organic frameworks: a review on recent literature. *Int Nano Lett* **9**, 17–29 (2019).

64. Lee, Y. R., Kim, J. & Ahn, W. S. Synthesis of metal-organic frameworks: A mini review. *Korean Journal of Chemical Engineering* **30**, 1667–1680 (2013).

65. Sarode, A. L., Wang, P., Obara, S. & Worthen, D. R. Supersaturation, nucleation, and crystal growth during single- and biphasic dissolution of amorphous solid dispersions: Polymer effects and implications for oral bioavailability enhancement of poorly water soluble drugs. *European Journal of Pharmaceutics and Biopharmaceutics* **86**, 351–360 (2014).

66. Feng, L., Wang, K. Y., Powell, J. & Zhou, H. C. Controllable Synthesis of Metal-Organic Frameworks and Their Hierarchical Assemblies. *Matter* **1**, 801–824 (2019).

67. Wißmann, G. *et al.* Modulated synthesis of Zr-fumarate MOF. *Microporous and Mesoporous Materials* **152**, 64–70 (2012).

68. Schaate, A. *et al.* Modulated synthesis of Zr-based metal-organic frameworks: From nano to single crystals. *Chemistry - A European Journal* **17**, 6643–6651 (2011).

69. Schaate, A. *et al.* A Novel Zr-Based Porous Coordination Polymer Containing Azobenzenedicarboxylate as a Linker. *Eur. J. Inorg. Chem* 790–796 (2012).

70. Chen, X. *et al.* An efficient modulated synthesis of zirconium metal-organic framework UiO-66. *RSC Adv* **12**, 6083–6092 (2022).

71. Vermoortele, F. *et al.* Synthesis modulation as a tool to increase the catalytic activity of metal-organic frameworks: The unique case of UiO-66(Zr). *J Am Chem Soc* **135**, 11465–11468 (2013).

72. Rouquerol, J. *et al.* Recommendations for the chracterization of porous solids. *Pure and Applied Chemistry* **66**, 1739–1758 (1994).

73. Henke, S. Metal-organic frameworks with additional flexible substituents – Modulating Responsiveness, Gas Sorption Selectivity & Network Topologies. *Dissertation* 271 (2011).

74. Dapaah, M. F. & Liu, B. Recent Advances of Supercritical CO2 in Green Synthesis and Activation of Metal–Organic Frameworks. *J Inorg Organomet Polym Mater* **30**, 581–595 (2020).

75. Nelson, A. P., Farha, O. K., Mulfort, K. L. & Hupp, J. T. Supercritical processing as a route to high internal surface areas and permanent microporosity in metal#organic framework materials. *J Am Chem Soc* **131**, 458–460 (2009).

76. Mondloch, J. E., Karagiaridi, O., Farha, O. K. & Hupp, J. T. Activation of metal-organic framework materials. *CrystEngComm* **15**, 9258–9264 (2013).

77. Thommes, M. *et al.* Physisorption of gases, with special reference to the evaluation of surface area and pore size distribution (IUPAC Technical Report). *Pure and Applied Chemistry* **87**, 1051–1069 (2015).

78. ChemTube3D. MOF-5 (or IRMOF-1) Metal Organic Framework. https://www.chemtube3d.com/mof-mof5/.

79. Micrometrics. Surface Area. https://www.micromeritics.com/particle-testing/analytical-testing/surface-area/.

80. Kumar, K. V. *et al.* Characterization of the adsorption site energies and heterogeneous surfaces of porous materials. *J Mater Chem A Mater* **7**, 10104–10137 (2019).

81. Alhumaimess, M. S. Metal–organic frameworks and their catalytic applications. *Journal of Saudi Chemical Society* **24**, 461–473 (2020).

82. Devkota, J., Ohodnicki, P. R., Gustafson, J. A., Wilmer, C. E. & Greve, D. W. Designing a SAW Sensor Array with MOF Sensing Layers for Carbon Dioxide and Methane. *IFCS/EFTF 2019 - Joint Conference of the IEEE International Frequency Control Symposium and European Frequency and Time Forum, Proceedings* 1–4 (2019).

83. Kus, F. *et al.* Surface acoustic wave (SAW) sensor for volatile organic compounds (VOCs) detection with calix[4]arene functionalized Gold nanorods (AuNRs) and silver nanocubes (AgNCs). *Sens Actuators B Chem* **330**, (2021).

84. Ding, M., Flaig, R. W., Jiang, H. L. & Yaghi, O. M. Carbon capture and conversion using metal-organic frameworks and MOF-based materials. *Chem Soc Rev* **48**, 2783–2828 (2019).

85. Ghanbari, T., Abnisa, F. & Wan Daud, W. M. A. A review on production of metal organic frameworks (MOF) for CO2 adsorption. *Science of the Total Environment* **707**, 135090 (2020).

86. Chen, Y., Mu, X., Lester, E. & Wu, T. High efficiency synthesis of HKUST-1 under mild conditions with high BET surface area and CO2 uptake capacity. *Progress in Natural Science: Materials International* **28**, 584–589 (2018).

87. Tovar, T. M. *et al.* Diffusion of CO2 in Large Crystals of Cu-BTC MOF. *J Am Chem Soc* **138**, 11449–11452 (2016).

88. Chen, X. *et al.* Direct Observation of Xe and Kr Adsorption in a Xe-Selective Microporous Metal-Organic Framework. *J Am Chem Soc* **137**, 7007–7010 (2015).

89. Liu, J., Thallapally, P. K. & Strachan, D. Metal-organic frameworks for removal of XE and KR from nuclear fuel reprocessing plants. *Langmuir* **28**, 11584–11589 (2012).

90. Banerjee, D. *et al.* Metal-organic framework with optimally selective xenon adsorption and separation. *Nat Commun* **7**, 1–7 (2016).

91. Zhao, D., Wang, X., Yue, L., He, Y. & Chen, B. Porous metal-organic frameworks for hydrogen storage. *Chemical Communications* **58**, 11059–11078 (2022).

92. Shet, S. P., Shanmuga Priya, S., Sudhakar, K. & Tahir, M. A review on current trends in potential use of metal-organic framework for hydrogen storage. *Int J Hydrogen Energy* **46**, 11782–11803 (2021).

93. Lin, K. S., Adhikari, A. K., Ku, C. N., Chiang, C. L. & Kuo, H. Synthesis and characterization of porous HKUST-1 metal organic frameworks for hydrogen storage. *Int J Hydrogen Energy* **37**, 13865–13871 (2012).

94. Al Sharabati, M., Sabouni, R. & Husseini, G. A. Biomedical Applications of Metal-Organic Frameworks for Disease Diagnosis and Drug Delivery: A Review. *Nanomaterials (Basel)* **12**, (2022).

95. Sharabati, M. Al, Sabouni, R. & Husseini, G. A. Biomedical Applications of Metal−Organic Frameworks for Disease Diagnosis and Drug Delivery: A Review. *Nanomaterials* **12**, (2022).

96. Baumann, A. E., Burns, D. A., Liu, B. & Thoi, V. S. Metal-organic framework functionalization and design strategies for advanced electrochemical energy storage devices. *Commun Chem* **2**, 1–14 (2019).

97. Jiang, Q., Zhang, H., Ren, Z., Ma, H. & Xue, M. Recent progresses of metal-organic framework-based materials in electrochemical energy storage. *Materials Today Sustainability* **19**, (2022).

98. Lu, X. F., Fang, Y., Luan, D. & Lou, X. W. D. Metal−organic frameworks derived functional materials for electrochemical energy storage and conversion: A mini review. *Nano Lett* **21**, 1555–1565 (2021).

99. Eslava, S. *et al.* Metal-organic framework ZIF-8 films as low-κ dielectrics in microelectronics. *Chemistry of Materials* **25**, 27–33 (2013).

100. Werts, M. H. V. Making sense of lanthanide luminescence. *Sci Prog* **88**, 101–131 (2005).

101. Aulsebrook, M. L., Graham, B., Grace, M. R. & Tuck, K. L. Lanthanide complexes for luminescence-based sensing of low molecular weight analytes. *Coord Chem Rev* **375**, 191–220 (2018).

102. Serre, C. *et al.* Synthesis, characterisation and luminescent properties of a new three-dimensional lanthanide trimesate: M((C6H3)-(CO 2)3) (M = Y, Ln) or MIL-78. *J Mater Chem* **14**, 1540–1543 (2004).

103. Ruan, B. *et al.* Effect of transition metal ions on luminescence of MOFs. *MATEC Web of Conferences* **238**, 1–6 (2018).

104. De Lill, D. T., De Bettencourt-Dias, A. & Cahill, C. L. Exploring lanthanide luminescence in metal-organic frameworks: synthesis, structure, and guest-sensitized

luminescence of a mixed europium/terbium-adipate framework and a terbium-adipate framework. *Inorg Chem* **46**, 3960–3965 (2007).

105. Wang, X., Bi, Y., Lin, H. & Liu, G. Three Novel Cd (II) Metal - Organic Frameworks Constructed from to a 3-D Architecture 2007. **3**, 2–7 (2007).

106. Allendorf, M., Doty, P., Meek, S. & Houk, R. Luminescent Metal-Organic Frameworks: A Nanolaboratory for Probing Energy Transfer via Interchromophore Interactions. *ECS Meeting Abstracts* **MA2010-01**, 1092–1092 (2010).

107. Cui, Y., Yue, Y., Qian, G. & Chen, B. Luminescent functional metal-organic frameworks. *Chem Rev* **112**, 1126–1162 (2012).

108. Bordiga, S. *et al.* Electronic and vibrational properties of a MOF-5 metal-organic framework: ZnO quantum dot behaviour. *Chemical Communications* **5**, 2300–2301 (2004).

109. Tachikawa, T., Choi, J. R., Fujitsuka, M. & Majima, T. Photoinduced charge-transfer processes on MOF-5 nanoparticles: Elucidating differences between metal-organic frameworks and semiconductor metal oxides. *Journal of Physical Chemistry C* **112**, 14090–14101 (2008).

110. Villemot, V., Hamel, M., Pansu, R. B., Leray, I. & Bertrand, G. H. V. Unravelling the true MOF-5 luminescence. *RSC Adv* **10**, 18418–18422 (2020).

111. Pham, H. Q. *et al.* Engineering of band gap in metal-organic frameworks by functionalizing organic linker: A systematic density functional theory investigation. *Journal of Physical Chemistry C* **118**, 4567–4577 (2014).

112. Gutiérrez, M., Möslein, A. F. & Tan, J. C. Facile and Fast Transformation of Nonluminescent to Highly Luminescent Metal-Organic Frameworks: Acetone Sensing for Diabetes Diagnosis and Lead Capture from Polluted Water. *ACS Appl Mater Interfaces* **13**, 7801–7811 (2021).

113. Pamei, M. & Puzari, A. Luminescent transition metal–organic frameworks: An emerging sensor for detecting biologically essential metal ions. *Nano-Structures and Nano-Objects* **19**, 100364 (2019).

114. Samanta, P., Let, S., Mandal, W., Dutta, S. & Ghosh, S. K. Luminescent metal-organic frameworks (LMOFs) as potential probes for the recognition of cationic water pollutants. *Inorg Chem Front* **7**, 1801–1821 (2020).

115. Wang, H. *et al.* A stable and highly luminescent 3D Eu(III)-organic framework for the detection of colchicine in aqueous environment. *Environ Res* **208**, 112652 (2022).

116. Zhang, R., Zhu, L. & Yue, B. Luminescent properties and recent progress in applications of lanthanide metal-organic frameworks. *Chinese Chemical Letters* **34**, 108009 (2023).

117. Wang, Y., Li, H., He, X. & Xu, Z. Application in Anticounterfeiting for Multistimuli Smart Luminescent Materials Based on MOF-on-MOF. *Inorg Chem* **60**, 15001–15009 (2021).

118. Sun, C. Y. *et al.* Efficient and tunable white-light emission of metal-organic frameworks by iridium-complex encapsulation. *Nat Commun* **4**, 1–8 (2013).

119. Doty, F. P., Bauer, C. A., Skulan, A. J., Grant, P. G. & Allendorf, M. D. Scintillating metal-organic frameworks: A new class of radiation detection materials. *Advanced Materials* **21**, 95–101 (2009).

120. Bauer, C. A. *et al.* Influence of connectivity and porosity on ligand-based luminescence in zinc metal-organic frameworks. *J Am Chem Soc* **129**, 7136–7144 (2007).

121. Wang, C. *et al.* Synergistic assembly of heavy metal clusters and luminescent organic bridging ligands in metal-organic frameworks for highly efficient X-ray scintillation. *J Am Chem Soc* **136**, 6171–6174 (2014).

122. Lu, J. *et al.* Efficient X-ray scintillating lead(ii)-based MOFs derived from rigid luminescent naphthalene motifs. *Dalton Transactions* **48**, 1722–1731 (2019).

123. Wang, W. F. *et al.* Sensitive X-ray detection and imaging by a scintillating Lead(II)-based Metal-Organic framework. *Chemical Engineering Journal* **430**, 133010 (2022).

124. Perego, J. *et al.* Composite fast scintillators based on high-Z fluorescent metal–organic framework nanocrystals. *Nat Photonics* **15**, 393–400 (2021).

125. Perego, J. *et al.* Highly luminescent scintillating hetero-ligand MOF nanocrystals with engineered Stokes shift for photonic applications. *Nat Commun* **13**, 1–10 (2022).

126. Wang, J. X. *et al.* Nearly 100% energy transfer at the interface of metal-organic frameworks for X-ray imaging scintillators. *Matter* **5**, 253–265 (2022).

127. Villemot, V. *et al.* From Sintering to Particle Discrimination: New Opportunities in Metal–Organic Frameworks Scintillators. *Adv Photonics Res* 2100259 (2021).

128. Wang, X. *et al.* Color-tunable X-ray scintillation based on a series of isotypic lanthanide-organic frameworks. *Chemical Communications* **56**, 233–236 (2019).

129. Andreo, J. *et al.* Autoluminescent Metal-Organic Frameworks (MOFs): Self-Photoemission of a Highly Stable Thorium MOF. *J Am Chem Soc* **140**, 14144–14149 (2018).

130. Orfano, M. *et al.* Efficient radioactive gas detection by scintillating porous metal–organic frameworks. *Nat Photonics* **17**, 672–678 (2023)

Chapter II: Materials and methods

II. Materials and methods

In this chapter, we will have a look at the different synthesis and activation protocols developed for each MOFs. The wide range of experimental methods used to characterise those MOFs will be explained in two different sections, namely the structural characterisation and the photophysical characterisation. As we have seen in Chapter I, the scintillating properties of a material can vary slightly from its photoluminescent properties because of the incident energy. The photophysical characterisation section will, therefore, also include a radioluminescence experiment to characterise the scintillating properties of our MOF material. The last section of this chapter will be dedicated to the gas detection experiment. Since the radioactive gas rejection in the atmosphere needs to be monitored, a careful screening of the MOFs is done first before testing them on the gas benches. Only the most promising MOFs in terms of porosity and fluorescent/scintillating properties were selected for the gas detection experiments.

1. Metal Organic Framework synthesis and activation

1.1 Precursors

Since the photoluminescent properties of MOFs are affected by their purity, the aim was to synthesise pure millimetric single crystals of MOFs. This is more readily achieved by solvothermal synthesis. The reagents used during the synthesis are listed in Table II-1together with the abbreviation of each precursor. The molecular weights of the precursors (excluding the solvents) are also listed in Table II-1, as they have been used to calculate the concentration of each precursor for the synthesis solution.

Table II-1: Table summarising the reagents used during MOF synthesis.

Reagent	Abbreviation	Molecular Weight MW	Purity/Supplier
N,*N*-Dimethylformamide	DMF	-	≥99.8% Sigma Aldrich
N,*N*-Diethylformamide	DEF	-	For synthesis Sigma Aldrich
Anhydrous *N*,*N*-Dimethylformamide	Anhyd. DMF	-	99.8% Sigma Aldrich
Extra dry Dichloromethane	DCM	-	99.8% Acros Organics
Zinc nitrate hexahydrate	$Zn(NO_3)_2 \cdot 6H_2O$	297.49	99% Alfa Aesar 98% Sigma Aldrich
Zirconium (IV) chloride	$ZrCl_4$	233.04	99.5% Sigma Aldrich
1,4-Benzenedicarboxylic acid	BDC	166.13	98% Sigma Aldrich
1,4-Naphthalenedicarboxylic acid	1,4-NDC	216.19	Thermoscientific
2,6-Naphthalenedicarboxylic acid	2,6-NDC	216.19	99% Sigma Aldrich
Biphenyl-4,4′-dicarboxylic acid	BPDC	242.23	97% Sigma Aldrich
1,3,5-Tris(4-carboxyphenyl)benzene	BTB	438.43	98% Alfa Aesar ≥98% Sigma Aldrich
1,2,4,5-Tetrakis(4-carboxyphenyl)benzene	TCPB	558.53	Sigma Aldrich
9,10-Anthracenedicarboxylic acid	9,10-ADC	266.25	95% Sigma Aldrich
Benzoic acid	BA	122.12	99.6% Acros Organics

1.2 Synthesis Protocol

The metallic salt, $Zn(NO_3)_2 \cdot 6H_2O$ or $ZrCl_4$, and organic ligand/s precursors were weighed and dissolved in a capped glass vial using a solvent (DMF or DEF). The choice of solvent depends on the solubility of the precursors in the former. The exact concentration of each precursor and synthesis conditions differs from one MOF to the other and are presented in Table II-2. Note that this table represents the conditions for the main MOF structures and that conditions for doped MOFs will be presented in Chapter IV. The solution was sonicated for 15 minutes to help break down any clump of the precursors. Certain ligands (e.g. BPDC) required some heat to dissolve. They formed a cloudy solution which was carefully heated using a heat gun until it turned into a clear solution, i.e. all the precursors dissolved into the solvent. The solution was transferred to smaller 10 mL vials to increase the surface area between the glass and the solution and hence increase potential nucleation sites. The vials were then sealed and immediately placed in a heated oven.

Zinc metal is reactive and only requires reaction temperatures around 75°C to 85°C, as explained in Chapter I. Zirconium metal, however, is less reactive and requires higher temperatures in order to self-assemble with the corresponding ligand and form MOFs. The synthesis temperature was around 120°C. Due to the low reversibility of the Zirconium-carboxylate bond, the modulated synthesis approach discussed in Chapter I was also used for the Zr-based MOF (UIO and CAU) to obtain crystalline products[1]. Benzoic acid was used as the modulator for every Zr-based MOF synthesis.

Table II-2 below describes all the precise precursor quantities used in each synthesis.

Table II-2: Table summarising the concentration of precursors and synthesis conditions for each MOF.

MOF	$c_{Metallic\ Salt}$ ($mol \cdot L^{-1}$)	c_{ligand} ($mol \cdot L^{-1}$)	$c_{modulator}$ ($mol \cdot L^{-1}$)	Solvent	Temperature (°C)	Time (h)
MOF-5	$Zn(NO_3)_2 \cdot 6H_2O$ 0.118	1,4-BDC 0.038	-	DEF	85	192
MOF-1,4-NDC	$Zn(NO_3)_2 \cdot 6H_2O$ 0.091	1,4-NDC 0.030	-	DMF	75	144
MOF-205	$Zn(NO_3)_2 \cdot 6H_2O$ 0.064	2,6-NDC 0.022 1,3,5-BTB 0.013	-	DMF	85	96
IRMOF-9	$Zn(NO_3)_2 \cdot 6H_2O$ 0.124	4,4'-BPDC 0.041	-	DMF	85	96
UIO-66	$ZrCl_4$ 0.017	1,4-BDC 0.017	BA 0.0514	DMF	120	24
UIO-67	$ZrCl_4$ 0.026	4,4'-BPDC 0.026	BA 0.771	DMF	120	24
UIO-1,4-NDC	$ZrCl_4$ 0.043	1,4-NDC 0.043	BA 2.36	DMF	120	24
CAU-24	$ZrCl_4$ 0.013	1,2,4,5-TCPB 0.008	BA 1.38	DMF	120	48

1.3 Activation

Since the MOFs are formed in a solvent, the pores are filled with said solvent. In order to access the pores for gas interaction with the framework, the MOF has to be activated. One possible way to achieve this is the evaporation of the solvent by heating the MOF at the boiling point of that solvent. However, if we were to directly evaporate the DMF from the MOF at its boiling point of 153°C, there would be a consequent capillary force variation resulting in the collapse of the MOF and loss of its surface area. To remedy this, it is necessary to exchange the DMF with a solvent with a much lower boiling point, such as DCM (39°C).

Since zinc-based MOFs are sensitive to moisture, the washing process was performed inside a Jacomex glovebox flooded with N_2 gas and the MOF was washed with anhydrous solvent. The MOF was washed three times with anhydrous DMF in order to get rid of any leftover unreacted

precursors. DMF was then slowly exchanged with DCM by washing with the following solutions of different proportions of anhydrous DMF and DCM.

DMF/DCM 75%: 25%

DMF/DCM 50%: 50%

DMF/DCM 25%: 75%

Extra Dry DCM ×2

The MOF was then decanted from DCM. Since the Zr-based MOFs were in powdered form rather than millimetric single crystals, centrifuge 5702 from Eppendorf was used to help with the washing. The UIO and CAU samples were centrifugated at 3500 rpm for 10 min before decanting each solution. Using a needle in the glass vial, the vial was connected to a ramp vacuum pump for two hours and then placed in a vacuum oven at 60°C overnight.

2. Structural characterisation experiments

2.1 X-Ray Diffraction

The X-Ray diffraction (XRD) experiments were performed in collaboration with Vincent Mertens and Nathalie Herlin at the "*Nanoscience et Innovation pour les Matériaux, Biomédecine et l'Energie"* (NIMBE) at CEA Saclay. The 2nd Generation tabletop D2 Phaser powder X-Ray diffractometer shown in Figure II-1 was used for the measurements. The MOF samples were gently crushed on a silicon sample holder. The X-Ray source is a Cu Kα with the voltage and current set at 40 kV and 40 mA, respectively. The diffractogram was measured between 3° and 50° with a step of 0.03° and an acquisition time of 5 s.

Figure II-1: Showing the benchtop PXRD setup.

2.2 Adsorption measurements

Since our host laboratory was not equipped with the necessary equipment to perform an adsorption measurement, the measurements adsorption measurements were performed at three different external laboratories equipped with different devices. These measurements were performed in collaboration with Charles Rivron also at NIMBE, Jonathan Bachir and Clémence Sicard at the Institut Lavoisier de Versailles (ILV) and Jacopo Perego and Angiolina Comotti at the University Milano-Biccoca (UNIMIB, a SPARTE partner).

The activated MOF samples were degassed for 3 h at 100°C on a VacPrep degassing station from Micromeritics shown in Figure II-2 below.

Figure II-2: Illustrating the VacPrep degassing station from Micromeritics.

N_2 adsorption isotherms were then collected using the following equipment at each location:

NIMBE – 3flex Analyser from Micromeritics shown in Figure II-3.

Figure II-3: Illustrating the 3flex Analyser from Micromeritics.

ILV –BELSORP-Mini porosimeter.

UNIMIB – Micromeritics analyser ASAP2020 HD.

Isotherms of quantity adsorbed against relative pressure as described in Chapter 1 were obtained with these experiments. These adsorption measurements were used to determine the specific surface areas, pore size and pore size distribution.

The BET mathematical model was then used to obtain the specific surface area of the MOF samples. The BET model is governed by the following equation[2]:

$$\frac{{}^{p}/_{p_0}}{v\left[1-\left({}^{p}/_{p_0}\right)\right]} = \frac{c-1}{v_m c}\left(\frac{p}{p_0}\right) + \frac{1}{v_m c}$$

Equation II-1

Where p and p_0 are the equilibrium and saturation pressure of the adsorbates respectively, v is the adsorbed gas quantity and v_m is the monolayer adsorbed gas quantity, and c is the BET constant. This equation can be plotted as a straight line with ${}^{1}/_{v\left[1-\left({}^{p}/_{p_0}\right)\right]}$ on the y axis and ${}^{p}/_{p_0}$ on the x-axis from the experimental results. The value of the slope (A) and intercept (I) are used to calculate v_m and c as follows:

$$v_m = \frac{1}{A+I}$$

Equation II-2

$$c = 1 + \frac{A}{I}$$

Equation II-3

From these the total surface area S_{total} and the specific surface area S_{BET} can be calculated as follows:

$$S_{total} = \frac{v_m N s}{V}$$

Equation II-4

$$S_{BET} = \frac{S_{total}}{a}$$

Equation II-5

Where N is the Avogadro number, s the adsorption cross section of the adsorbate, V the molar volume of the adsorbate gas and a mass of the porous material.

2.3 Thermogravimetric Analysis

Thermogravimetric Analysis (TGA) is a technique used to evaluate the changes in the mass of a sample with respect to temperature. In our case, it allows us to determine if our MOF has been properly activated (no humidity in the sample and no residual solvents after activation). It is also used to determine the temperature at which our MOF disintegrates. The remaining mass is also an indication of the metal/organic ratio present in our MOF. The TGA was recorded using the Perkin Elmer TGA4000 shown in Figure II-4, where approximately 10 mg of MOF sample were heated from 30°C to 600°C with a step of 5°C·min^{-1}.

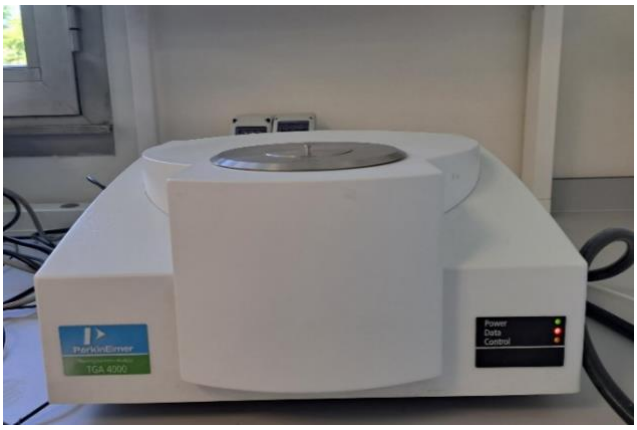

Figure II-4: Showing the TGA setup.

2.4 FT-IR experiments

Fourier Transform Infrared Spectroscopy (FT-IR) was performed using a Thermoscientific Nicolet Summit X FTIR spectrometer shown in Figure II-5. A FT-IR spectrum allows to study the composition of a given material. Infrared radiation is sent through the sample. The sample absorbs part of the radiation and allows some to pass through. The radiation absorbed is converted in the molecules present in the sample to rotational and/or vibrational energy. Since different molecules contain different bonds and functional groups, they absorb different frequencies. Hence this method can be used as a chemical fingerprint to identify materials.

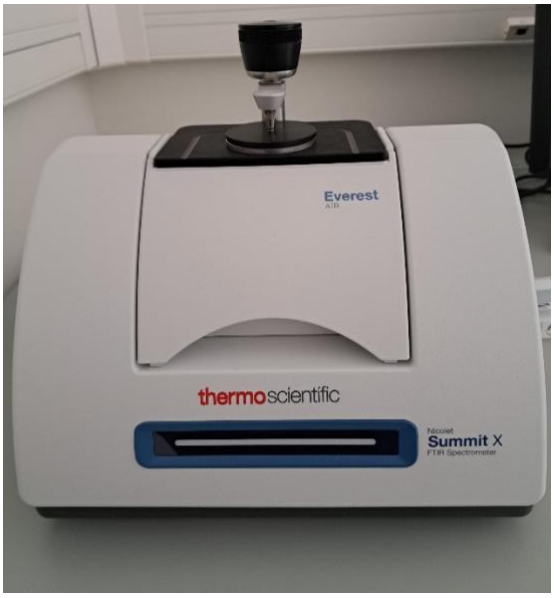

Figure II-5: Showing FT-IT experimental setup.

2.5 Scanning Electron Microscopy

Scanning Electron Microscopy or SEM was used to obtain images of the powdered Zr-based MOFs as well as measure some particle sizes. The MOF powders were dispersed on silicon sheets of 1 cm × 1 cm. The equipment used was the SUPRA 40 SEM-FEG (Field Emission Gun) from Carl Zeiss shown in Figure II-6. The detector was positioned in an “In-Lense” configuration. The work distance (WD), which is the distance between the microscope tip and the sample, was set to 5 mm to minimise the signal-to-noise ratio. The Electron High Tension (EHT), which is the accelerating electron voltage, was set to 3 kV for the best resolution.

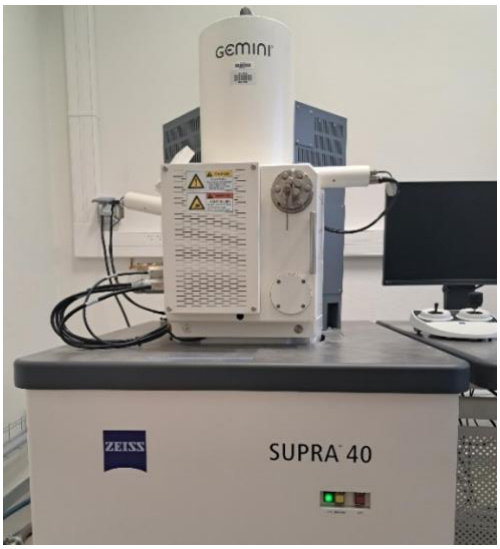

Figure II-6: Showing the SEM experimental setup.

2.6 ^{13}C, ^{1}H and ^{129}Xe NMR

NMR stands for Nuclear Magnetic Resonance. ^{13}C and ^{1}H NMR allow for the identification of carbon and hydrogen atoms respectively. In short, carbon atoms in a molecule each have different neighbors and hence have different spin resonance frequency. As a consequence, they appear at different chemical shifts on a Fourier transform spectrum (relative to a standard reference). Hyperpolarization ^{129}Xe NMR is a powerful tool that has been used to explore the structure of porous materials such as MOFs and Zeolites[3,4]. Xe is an inert gas with a large electron cloud which makes it readily polarizable. ^{129}Xe has a non-zero spin $\left(+\frac{1}{2}\right)$ necessary for magnetic resonance. Compared to free Xe, the pores of a MOF cause a chemical shift resulting from the interaction between Xe and the structure and the confined environment in the MOF.

Silvia Bracco, Jacopo Perego and Angiolina Comotti carried these experiments out at the University of Milano-Bicocca under the following conditions[5,6].

^{13}C and ^{1}H solid-state NMR experiments were carried out with a Bruker Avance 300 instrument operating at a static field of 7.04 T equipped with high-power amplifiers (1 kW) and a 4 mm double resonance MAS (Magic Angle Spinning) probe. The experiments were performed at 75.5 MHz for the ^{13}C NMR and 300.1 MHz for the ^{1}H solid-state NMR. $^{13}C\{^{1}H\}$ ramped-amplitude Cross Polarization (CP) experiments were performed at 293 K at a spinning speed of 12.5 kHz using a recycle delay of 5 s and contact times of 2 ms and 0.05 ms. The 90° pulse for proton was 2.9 µs. Quantitative $^{13}C\{^{1}H\}$ Single-Pulse Excitation (SPE) experiments were run using a 90° pulse of 4.6 ms and a recycle time (between measurements) of 60 s.

Hyperpolarization ^{129}Xe NMR experiments were performed using home-built apparatus with a continuous delivery of hyperpolarized xenon gas with a Bruker Avance 300 spectrometer operating at a Larmor Frequency of 83.02 MHz for ^{129}Xe. A diode array laser continuously delivering 6 W at 795 nm was applied, and circular polarization was achieved using a beam-splitting cube and quarter wave plate. A stream of gas mixture containing 2% xenon, 2% nitrogen and 96% helium at 2 atm was used with a gas flow rate maintained at 20 Lh^{-1}. Prior to NMR analysis, the samples were activated at 130°C under a high vacuum for sixteen hours. A pulse duration of 7 µs was applied, with a recycle delay of 0.5 s. Variable temperature experiments in the range 292 – 192 K were achieved by flowing cooled nitrogen gas to the sample.

These NMR experiments were only carried out on two of our samples as the experiments are quite time consuming and needed to be carried out at an international laboratory. MOF-205 and MOF-5 + 1.38% ADC were chosen as they presented the best results for ^{85}Kr detection, and we hence wanted to characterize them as fully as possible.

3. Photophysical characterisation experiments

3.1 Photoluminescence experiments

The photoluminescence experiments were carried out at our laboratory using a Fluoromax-4P Horiba-Jobin Yvon spectrofluorometer, as shown in Figure II-7.

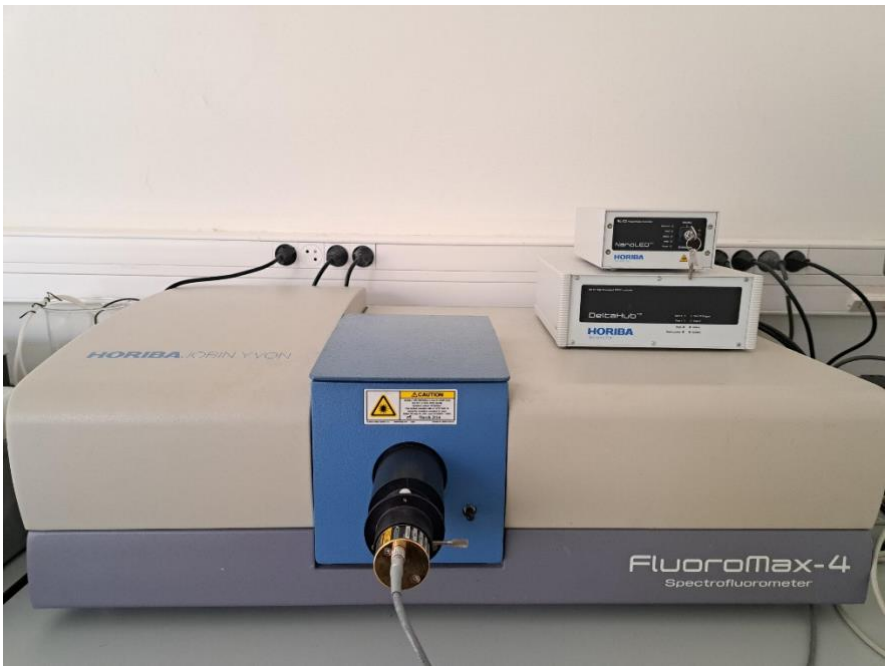

Figure II-7: Showing the spectrofluorometer equipped with a pulsed laser diode (nanoLED) and on the top right the nanoLED synchronous detection devices.

These experiments allowed us to obtain excitation and emission spectra of the solid ligands, ligands in solution (concentration of 10^{-5} mol·L^{-1} in DMF), and the MOFs. A xenon lamp produces white light which is subsequently diffracted by a monochromator to select the required excitation wavelength. The light emitted by the sample is collected perpendicularly to the excitation beam and passed through another monochromator to then be detected by a photomultiplier tube.

To obtain an excitation spectrum, a fixed emission wavelength is selected and the excitation wavelength range is scanned. On the contrary, to obtain an emission spectrum, the excitation wavelength is fixed and the emission wavelength range is scanned.

The spectra are corrected by the variation of the intensity of emission of the Xenon lamp with the wavelength and the quantum efficiency of detection of the photomultiplier tube.

The sample holders were different depending on the type of sample. They are all shown in Figure II-8. Ligands dissolved in DMF were placed in a 10 × 10 × 45 mm quartz cuvette, solid ligands and polycrystalline powdered MOFs were crushed on a quartz plate placed at an angle of 30° to the excitation source (to minimise the diffusion of the excitation source) and lastly millimetric MOF single crystals were placed in a quartz capillary at an angle of 15°.

a) 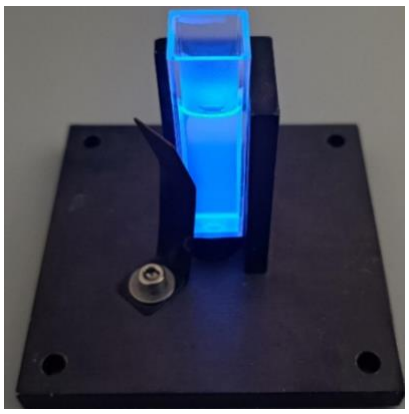 b) 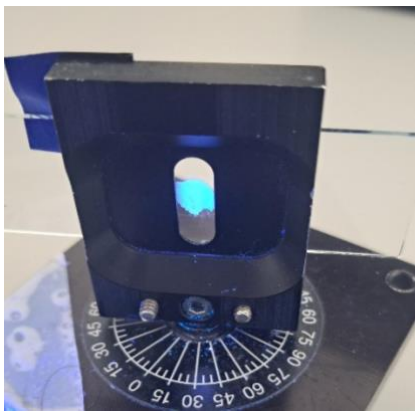

c) 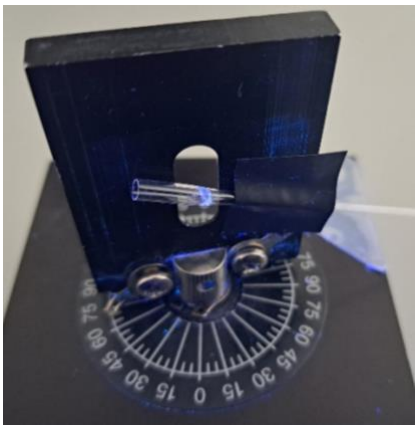

Figure II-8: Showing the different sample holders used for the photoluminescence measurements - a) liquid, b) powder, c) crystal.

3.2 Time-correlated single photon counting (TCSPC)

Time-correlated single photon counting (TCSPC) is a technique used to determine the fluorescence lifetime of the excited state of a molecule. The same spectrofluorometer described in section 3.1 above can be fitted with NanoLED pulsed source from Horiba emitting at 274 nm, 309 nm, 339 nm or 368 nm. One of those nanoLED is shown in Figure II-9.

Figure II-9: Showing a pulsed nanoLED connected to the spectrofluorometer.

The lifetime decay measurements were performed with the nanoLED emitting the closest to the maximum excitation of the fluorescent molecule being studied. The data was then fitted using a mono, biexponential or 3rd order decay function. For experimental ease, the response factor was not removed from the apparent decay. Median decay time were calculated by ponderation of each individual decay constant by their respective weight coefficient.

3.3 Photoluminescent light yield

In order to determine the photoluminescent light yield, the following experiment with an integrating sphere was performed at the University of Milano-Biccoca with the help of Matteo Orfano and Angelo Monguzzi.

A Labsphere integrating sphere is necessary to determine the radiative quantum efficiency of MOF samples, be it crystal or powder, as contrary to solutions, we cannot assume an isotropic angular distribution for the emission. An integrating sphere is a hollow sphere whose inner surface is coated with a diffusely reflecting material and allows for a light source to be redistributed isotropically over the sphere.

The experimental setup is shown in Figure II-10. An Edinburgh Instrument EPL excitation laser at 405 nm with a 90 ps pulse width was directed into the sphere using optical lenses and through an entrance hole. An optical fibre was connected to the sphere's wall at 90° to the entrance hole. The fibre was connected at the other end to a Charged Couple Device, CCD.

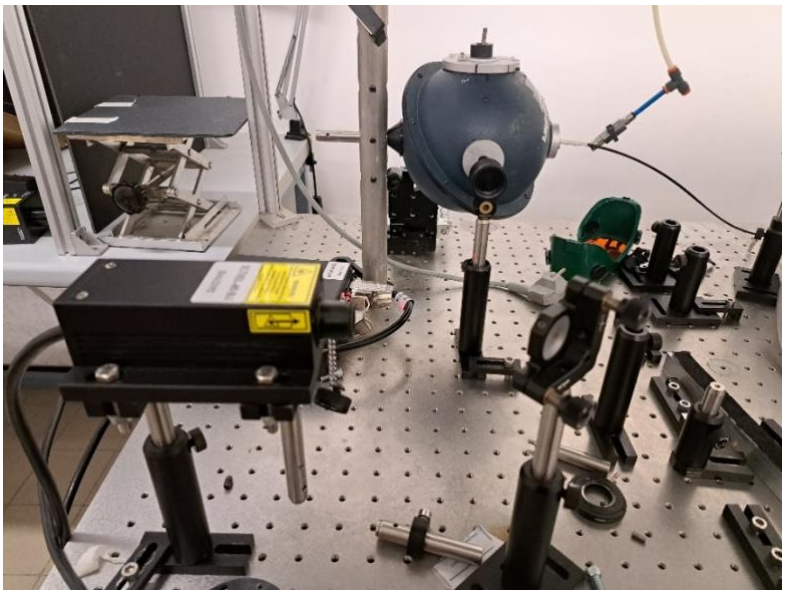

Figure II-10: Showing the experimental setup for the photoluminescence light yield measurements with an integrating sphere.

The experimental procedure is shown in Figure II-11[7]. As it can be seen, three measurements were carried out using the sphere. Experiment (a) was performed with an empty sphere, i.e. no sample present. Only the laser light is detected by the spectrometer. Experiment (b) was performed with the sample in the sphere and the laser beam directed off the sample and onto the walls of the sphere. This allows us to determine how our sample interacts with light that bounces off the walls of the sphere and the proportion that is reabsorbed by our sample. Experiment (c) was performed with the sample inside the sphere and the laser beam positioned directly on the sample. This determines the direct interaction of the sample with the light.

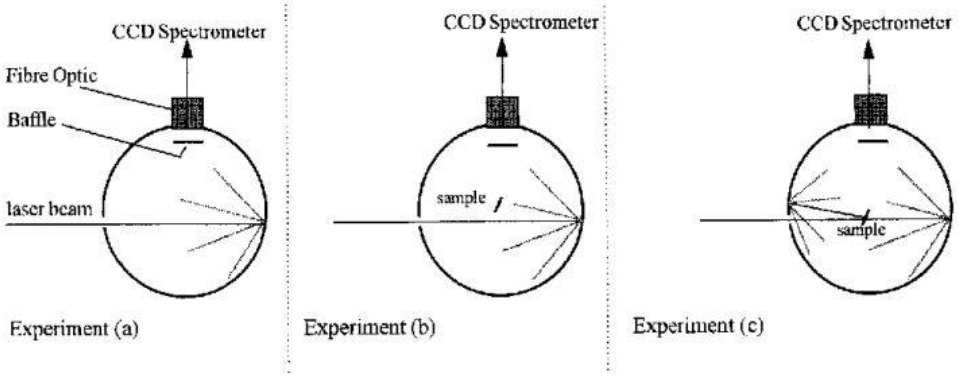

Figure II-11: Illustrating the three experiments performed to obtain a precise PL yield measurement [7].

Since MOF crystals go from transparent before activation to white and opaque after activation, the experiments were performed before and after activation to quantify the loss in photoluminescence yields after the crystals have been activated.

3.4 Radioluminescence experiments

The radioluminescence experiments were performed at the *"Institut Lumière Matière de Lyon"* in collaboration with Christophe Dujardin, the coordinator of the SPARTE project. Their homemade experimental setup is shown in Figure II-12[8].

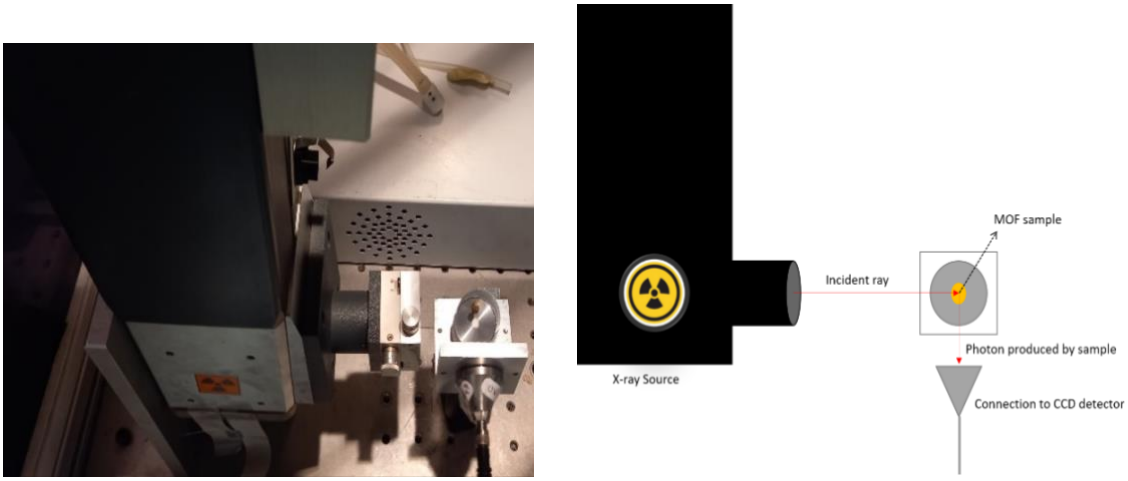

Figure II-12: Showing on the right - Radioluminescence experiment; left - Illustration of the radioluminescence experiment principle.

The setup consists firstly of an excitation source obtained by irradiating a beryllium window using the Philips 2274 X-Ray tube with a Tungsten Target at 20 kV. This produces an electron beam directed to the target sample perpendicularly.

The detection system was composed of a Charged Coupled Device, CCD (Jobin-Yvon Spectrum One 3000) coupled to a spectrograph (Jobin-Yvon Triax 180) operating on a wavelength range from 200 nm to 1100 nm. The results are corrected by the intrinsic response of the system. The sample holder for this experiment contains a hole with a diameter of 4mm and depth of 1mm. Since the same volume of MOF powder can be used in the sample holder for each experiments the radioluminescence light yield can be compared with one another. The experiment was also performed with a single crystal of anthracene whose radioluminescence light yield was attributed to 100%, and the MOF material's relative light yield to the anthracene was calculated.

4. Gas detection experiments

4.1 Gas benches

Two unique in the world homemade gas benches have been developed at the *Laboratoire National Henri Becquerel* (LNHB) over the years: one to produce a radioactive sample of known activity and one to test a materials' ability to detect radioactive gases. These experimental setups were conceived and improved by Benoît Sabot over the years.

Firstly, the experimental setup shown in Figure II-13 allows for the metrological preparation of radioactive gas samples of desired activity[9]. One part of the setup grants the preparation of ^{222}Rn atmosphere from ^{226}Ra sources. Another section equipped with a mass flowmeter controls the flow from pressurised standard concentration bottles (bottle b in Figure II-13) of ^{3}H and ^{85}Kr[9] to produce a desired activity concentration. Those radioactive environments can be produced in chamber c or d (Figure II-13) or in a small 104.4(5) cm^3 container which can then be connected to the second setup shown in Figure II-14. For experimental ease, the small container was always used to produce our radioactive atmospheres.

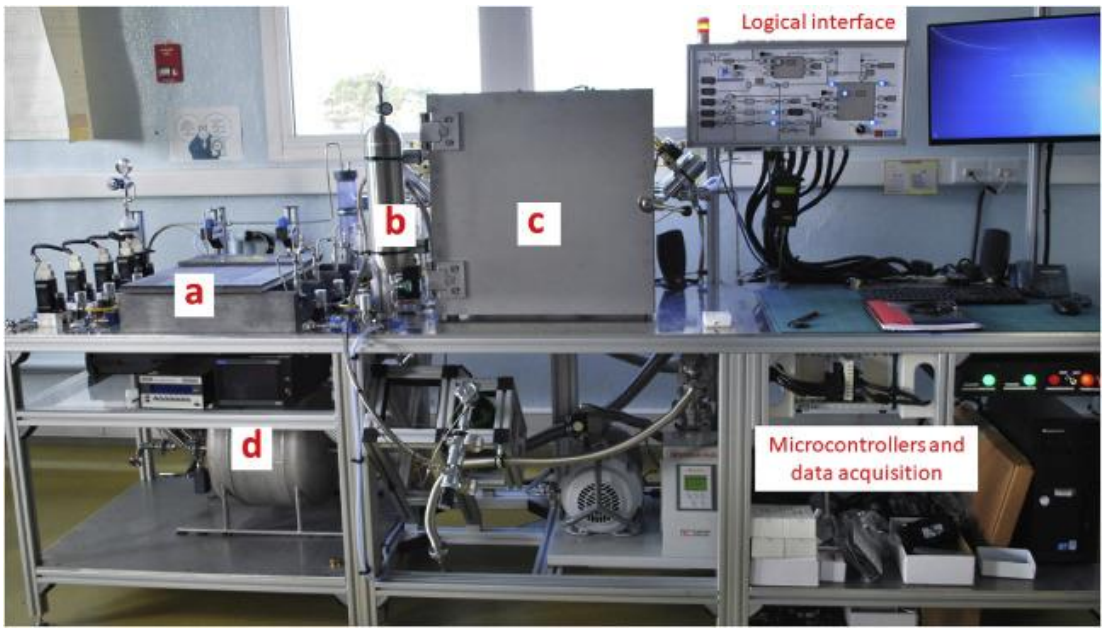

Figure II-13: Showing the gas bench used in the preparation of radioactive gas samples.

Figure II-14 below, was used to test the ability of different MOFs to detect radioactive gases at very high activity concentration - some tens of kBq·m^{-3} to some MBq·m^{-3}. The setup was adapted as shown here to allow for experiments with MOF crystals. It also accommodates for the flow of radioactive gases.

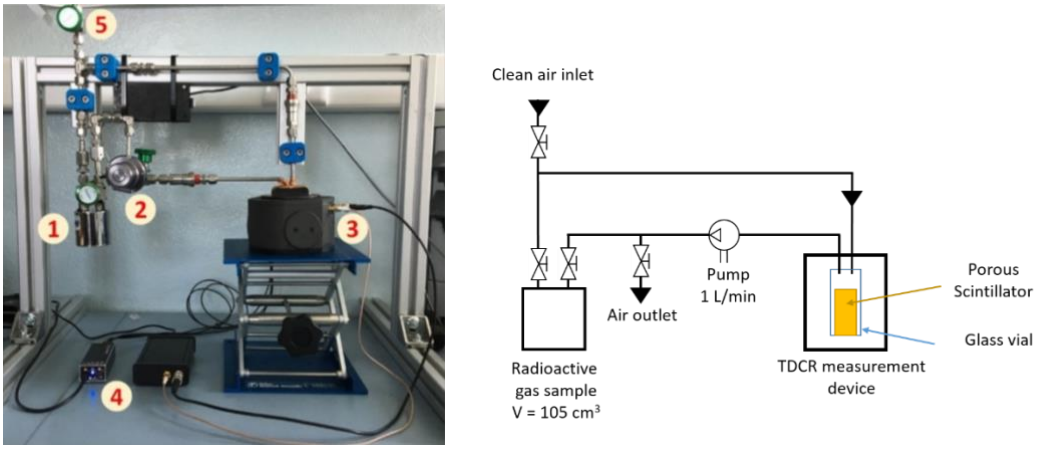

Figure II-14: Showing on the left - the gas detection experimental setup with each components explained below and right - an illustration of the setup.

The different numbered components of the setup are listed below:

1. A 104.4(5) cm^3 container containing a certified activity of radioactive gas.
2. A pump controlling the flow of radioactive gas through the system with a rate set at 0.70(5) $L \cdot min^{-1}$.
3. The µ-TDCR, a portable Triple-to-Double Coincidence Ratio (TDCR) measurement device with an adapted cap containing a glass vial as sample holder and three photomultiplier tubes (PMT), H11234-203-MOD Hamamatsu[10], at 120° to each other to collect emitted photons. The sealed setup is light tight. Figure II-15 shows the setup inside the TDCR device which has been adapted from the setup for liquid scintillation by inserting a smaller tube of 4 mm diameter where MOF samples can be inserted. This adaptation compensates for light diffusion phenomenon that happen within MOF crystals and allows the light to pass through the material.

Figure II-15: Showing from left to right - Inside the TDCR device with sample holder; the sample holder; the head of the TDCR device to which the sample vial is screwed and which itself is screwed into the TDCR device.

4. Associated electronics, based on FPGA and developed by V. Jordanov *et al.*[11], enable the processing of the signals from the 3 PMTs using the MAC3 logic with extendable dead time[12].
5. An outlet to inject dry air into the system of vacuum the circuit. This allows for the removal of radioactive gas from the system.

One such setup, as shown in Figure II-14, was solely used for tritium experiments as tritium may be a contaminant if some water is in the carrier gas. Another identical setup was used to test several other gases.

It is important to note that the total volume of the circuit in Figure II-14, i.e. container, pipes and vial is 139 cm^3. As we know the precise activity inside the container we can deduce the volumetric activity used in every experiment.

A protocol for the gas experiment was setup as follows:

- The empty glass vial was filled with a known mass of activated MOF. The tube can accept a maximum of 200 mg depending on the morphology of the MOF crystals.
- The vial was carefully screwed to the black head with two holes for gas circulation (refer to Figure II-15 right)
- The gas sample was created in container 1 using the gas bench in Figure II-13 and then attached to the small bench in Figure II-14 keeping the valve closed and hence the container isolated from the rest of the circuit.
- The TDCR device was closed and a background was measured, i.e. while keeping container 1 closed. This measurement was performed in order to obtain a stable background count without radioactivity.
- Container 1 was opened and the gas flew through the circuit within seconds. It is important to note that the gas was also homogenously dispersed into the circuit within few seconds.
- Upon reaching the MOF sample, the gas was absorbed by the MOF and so was the ionising radiation emitted by the radioactive gas. The MOF subsequently emits photons which are detected by 3 PMTs in coincidence.
- When a stable photon count is reached, dry and clean air (<3%RH) is injected into the system to rinse the radioactive gas out. The count rate is collected to monitor the release of the radioactive gas from the MOF. The count rate after rinsing should be similar to the one before injection to ensure the MOF is not retaining any of the radioactive gas within its pores.

It is important to note that a measurement, i.e. without any MOF in the sample vial, was also performed for each radioactive gas. This measurement will be referred to as the “blank measurement”.

The same methodology was also applied for microspheres of scintillating polystyrene. This is the material we have chosen for comparison purposes with our MOFs as they are porous and

exhibited scintillation properties similar to our MOFs. However, we do not consider here the difference in light-matter interaction between both materials. These microspheres of polystyrene and their scintillating properties are described in L.M Santiago *et al.*[13]

4.2 Triple-to-Double Coincidence Ratio (TDCR)

A MOF was chosen to perform the gas detection experiment by examining its emission profile from the photoluminescence experiments. An emission centred around 380 to 450 nm is desired since the PMTs in the TDCR device, and in general, have a maximum quantum efficiency of photon detection around these wavelength as seen in Figure II-16 below. The PMT of interest is the -200 type in the red solid line.

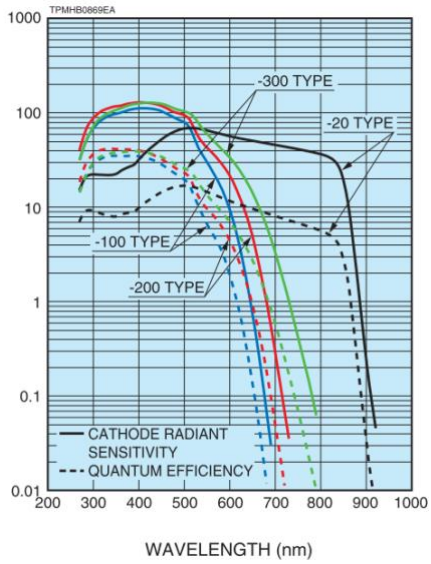

Figure II-16: Showing the quantum efficiency of photon detection for the PMTs. The PMT used are the -200 type in the solid red line[14].

As mentioned in section 4.1 above, the TDCR device has three PMTs at 120° to each other and collects photons in coincidence. Let us consider the three PMTs as A, B and C. The coincidence detection method works as follows for 2 PMTs in coincidence: when a scintillation event is detected by PMT A, a temporal window is opened, this is known as the coincidence window. Form this moment, the photon count will be increased only if another event is detected by another PMT such as PMT B. This coincidence window can be varied from 10 ns to 2 µs and was fixed at 40 ns and 400 ns for our measurements. The 400 ns window should be explored for scintillators with a longer decay time but conducts to a higher probability of accidental coincidences[15]. This coincidence detection method allows for the reduction and hence a more precise signal. Another parameter for these measurements is the extendable dead time, which

can be varied from 80 ns to 500 µs. For the sake of our experiments, it was set at 10 µs and 50 µs, which are the usual value applied in the system in order to count scintillation events properly, especially to remove the thermal noise of the PMTs. This measurement dead time was then measured by the electronic module with a reference clock of 10 MHz.

Figure II-17 shows a simplified schematic representation of the coincidence on three PMTs. For the following explanation, logical operators ∨ and ∧ are going to be used, where ∨ is the logical "or" operator and ∧ is the logical "and" operator. From this we can see that there are three single event channels A, B and C and their logical sum is S = A ∨ B ∨ C. There are also three double coincidence channels (AB = A ∧ B, BC = B ∧ C and AC = A ∧ C) with their logical sum D = AB ∨ BC ∨ AC. Lastly, a triple coincidence channel also exists between the three PMTs simultaneously where T = A ∧ B ∧ C.

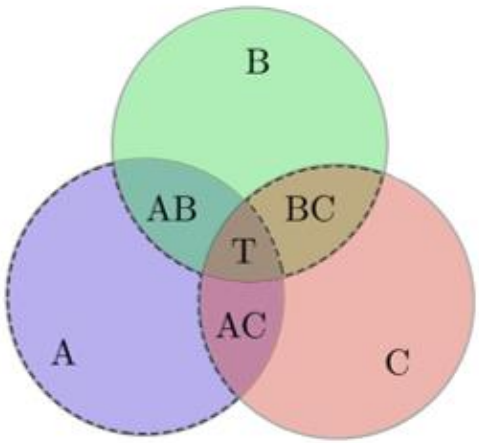

Figure II-17: Schematic simplification of the three PMTs in coincidence[15].

The TDCR detection method allows us to obtain a ratio (refer to Equation II-6) from these values which give us an indicator of the scintillation yield of our material at a fixed spectral energy, i.e. for the same radioactive gas, same emission spectrum. This ratio was derived from Birks Law by colleagues at LNHB[16,17] but won't be discussed in detail in this manuscript. The effect of the geometry on the scintillation yield have been neglected for this approximation, as they cannot be quantified.

$$Scintillation\ yield \equiv \frac{T}{D}$$

Equation II-6

A scintillator will emit photons isotropically after each interaction with an ionising particle. For the same gas, i.e. the same ionising radiation, the energy is fixed therefore the only parameter influencing the amount of photons detected is the scintillation yield of the material. An efficient scintillator will hence emit the most amount of photons which therefore have a higher

probability to be detected by two or three PMTs in coincidence. This ratio will give us an indicator to compare the scintillation yield of different MOFs being exposed to the same radioactive gas (however, we neglect geometrical effect). As the T/D value tends to 1, we are approaching a good scintillator yield.

For this purpose of this manuscript, we will mainly discuss the D photon count rate in s^{-1} and the T/D values.

5. Intermediary Conclusion

To conclude, we have presented here the synthesis and activation protocols used to produce our MOFs. We have shown different methods of characterisation used to determine the potential of a MOF as scintillation porous materials for radioactive gas detection. We have managed to make coexist three types of characterisation, namely structural, photophysical and radiophysical/scintillating. From these characterisation results, we were able to get information out of our MOFs library for radioactive gas detection. The gas bench and TDCR detection method was thoroughly explained. It is important to note that the initial use of the TDCR method was to calculate the activity of a radionuclide in a liquid scintillator. For the first time, we have adapted this detection system to suit our need for the detection of radioactive gases using MOF as the scintillator.

REFERENCES

1. Butova, V. V. *et al.* Modulator effect in UiO-66-NDC (1, 4-naphthalenedicarboxylic acid) synthesis and comparison with UiO-67-NDC isoreticular metal-organic frameworks. *Cryst Growth Des* **17**, (2017).
2. Determining the surface area of solids using the BET equation. Preprint at https://www.bath.ac.uk/publications/mc2-app-notes-on-porosity-surface-area/attachments/mc2note-surface-area-bet.pdf.
3. Fan, B., Xu, S., Wei, Y. & Liu, Z. Progresses of hyperpolarized 129Xe NMR application in porous materials and catalysis. *Magnetic Resonance Letters* **1**, 11–27 (2021).
4. Zeng, Q. *et al.* Hyperpolarized Xe NMR signal advancement by metal-organic framework entrapment in aqueous solution.
5. Mauree, S. *et al.* Detection of Radioactive Gas with Scintillating MOFs. *Adv Funct Mater* (2023).
6. Mauri, M. & Simonutti, R. Hyperpolarized xenon nuclear magnetic resonance (NMR) of building stone materials. *Materials* **5**, 1722–1739 (2012).
7. de Mello, J. C., Wittmann, F. H. & Friend, R. H. An Improved Experimental Determination of External Photoluminescence Quantum Efficiency. *Advanced Materials* **9**, 230–232 (1997).
8. Meng, Z. *et al.* Perspectives for CdSe/CdS spherical quantum wells as rapid-response nano-scintillators. *Nanoscale* **13**, 19578–19586 (2021).
9. Sabot, B., Rodrigues, M. & Pierre, S. Experimental facility for the production of reference atmosphere of radioactive gases (Rn, Xe, Kr, and H isotopes). *Applied Radiation and Isotopes* **155**, 108934 (2020).
10. Sabot B., Cassette P., Dutsov Ch., M. K. Performance of portable TDCR systems developed at LNE-LNHB. in *LSC 2020 International Conference on Advances in Liquid Scintillation Spectrometry* vol. 24 13–14 (2020).
11. Jordanov, V., Cassette, P., Dutsov, C. & Mitev, K. Development and applications of a miniature TDCR acquisition system for in-situ radionuclide metrology. *Nucl Instrum Methods Phys Res A* **954**, 161202 (2020).
12. Bouchard, J. & Cassette, P. MAC3: An electronic module for the processing of pulses delivered by a three photomultiplier liquid scintillation counting system. *Applied Radiation and Isotopes* **52**, 669–672 (2000).
13. Santiago, L. M., Bagán, H., Tarancón, A. & Garcia, J. F. Synthesis of plastic scintillation microspheres: Alpha/beta discrimination. *Applied Radiation and Isotopes* **93**, 18–28 (2014).

14. Hamamatsu. PHOTOMULTIPLIER TUBES AND PHOTOMULTIPLIER TUBE ASSEMBLIES R11265U SERIES / H11934 SERIES G High Energy Physics. (2013).

15. Dutsov, C., Cassette, P., Sabot, B. & Mitev, K. Evaluation of the accidental coincidence counting rates in TDCR counting. *Nucl Instrum Methods Phys Res A* **977**, 164292 (2020).

16. LNHB. MESURE DIRECTE D'ACTIVITÉ PAR SCINTILLATION LIQUIDE, MÉTHODE DU RAPPORT DES COÏNCIDENCES TRIPLES À DOUBLES (RCTD). 3–4 http://www.lnhb.fr/pdf/SL-RCTD_infos_complementaires.pdf.

17. Broda, R., Cassette, P. & Kossert, K. Radionuclide metrology using liquid scintillation counting. *Metrologia* **44**, (2007).

Chapter III: Developing Zn-based MOFs for radioactive gas detection

III. Developing Zn-based MOFs for radioactive gas detection

In this Chapter we will present four Zn-based MOFs that have been synthesised and characterised. Zn-based MOFs were chosen first due to the large array of publications on them and their ease of synthesis. The optimisation of the synthesis protocol for MOF-5, IRMOF-9 and MOF-205 were carried out as part of another thesis[1] and won't be discussed on detail here. The structural characterisation will help us determine if we have indeed synthesised the respective MOF as well as its physical properties. For the photophysical characterisation, we will mainly determine if our MOF emits in the correct wavelength range for the PMTs used in the radioactive gas detection experiments, i.e. between 380 nm and 450 nm. The fluorescence lifetime of our MOF will also be determined. A fast fluorescence lifetime is more adapted to the detection of photons in coincidence in the gas detection experiments especially when using short coincidence windows. We will also analyse the results from the detection of 10 kBq or 76 $Bq \cdot cm^{-3}$ of ^{85}Kr gas individually for every MOF and compare them with one another in the last section of this chapter. Reproducibility experiments as well as the effect of varying of the activity of radioactive gases will also be analysed using MOF-205. The latter will also be tested for ^{222}Rn and ^{3}H detection. The mass of the samples used for each experiment can be found in the Appendix Tables 1-3. Some small variations in the activity of radioactive gas samples exist and the same tables indicates the exact activity used for each experiment. The results for the radioluminescence experiments will also be studied and compared in the last section of this chapter.

1. IRMOF-1/MOF-5

1.1 Structure and Synthesis

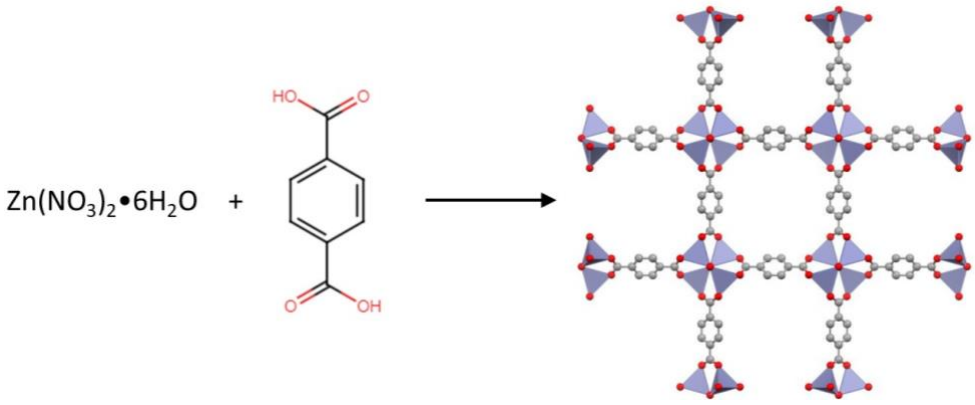

Figure III-1: Precursors and structure of MOF-5.

MOF-5 consist of Zn_4O nodes linked by six linear 1,4-benzenedicarboxylic acid ligands leading to a 3D primitive cubic porous (pcu) network with an Fm(-3)m space group[2] as shown in Figure III-1. The protocol listed below is the optimised synthesis conditions to obtain millimetric single crystals of MOF-5.

$Zn(NO_3)_2$•$6H_2O$ (0.118 mol·L^{-1}, 3.54 g) and 1,4-benzenedicarboxylic acid (0.038 mol·L^{-1}, 658 mg) were dissolved in 100 mL of *N*,*N*-diethylformamide (DEF). The mixture was equally divided into twelve 10 mL scintillation vials, which were then sealed with a screw cap. The vials were placed in an oven at 75°C for 192 h (8 days) yielding millimetric sized MOF-5 single crystals as seen in Figure III-2. The closed vials were removed and placed in an N_2 glovebox. The crystals were washed according to the protocol described in Chapter II.

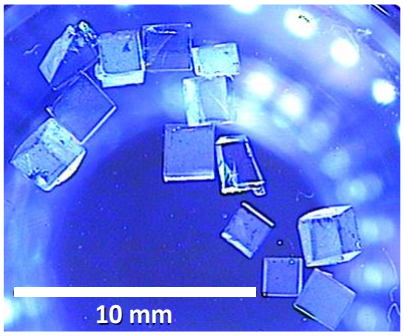

Figure III-2: Photo of millimetric IRMOF-1 single crystals[3].

MOF-5 is the only MOF presented here where DEF is used as the solvent instead of DMF. The synthesis of millimetric single crystals of MOF-5 with DMF as the solvent under the same conditions yields a white opaque and non-crystalline product. Under other conditions and using DMF, polycrystalline powder of MOF-5 could be obtained.

1.2 Structural characterisation

1.2.1 X-Ray Diffraction

Figure III-3 shows the X-ray Diffraction spectrum of our MOF-5 compared to the simulated XRD from the first reported work of Yaghi *et al.*[4] The peak positions are similar in both data sets showing us that we have indeed synthesised MOF-5 single crystals. However, we can see that the peak intensities vary from our experimental data to that of Yaghi *et al.* This is because the XRD we carried out was a powdered XRD done by crushing single crystals of MOF-5 on a sample holder. Compared to a single X-ray diffraction, this method will lead to preferential orientation of the crystals and hence influence the intensity for the different diffraction planes.

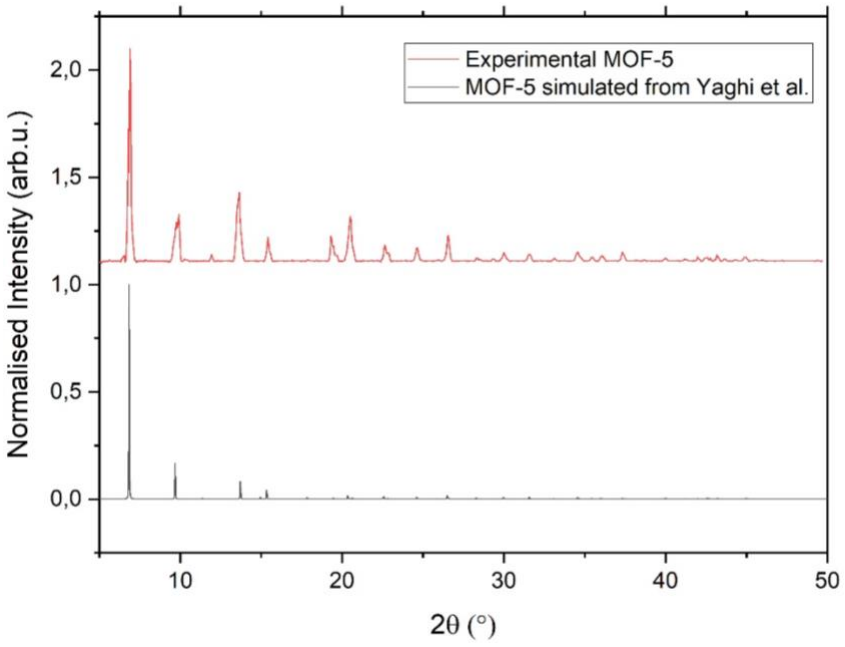

Figure III-3: PXRD spectrum showing experimental results compared to literature.

1.2.2 Adsorption measurements

The N_2 adsorption experiments for MOF-5 were carried out at the University of Milano-Bicocca. The N_2 adsorption isotherm is shown in Figure III-4 and Table III-1 shows the results extracted from these data. The BET surface area of this MOF is consistent with literature values[5].

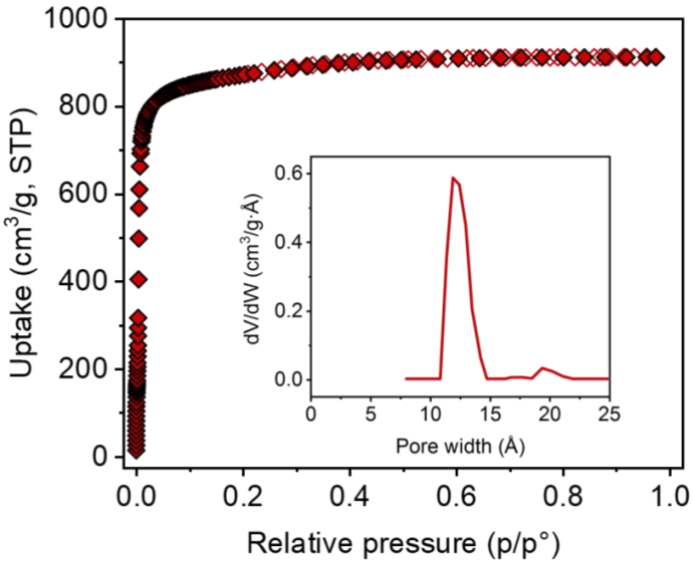

Figure III-4: Illustrating the N_2 adsorption isotherm of MOF-5. Inset of pore width measurement.

Table III-1: Showing the data calculated from N_2 adsorption of MOF-5.

MOF	Langmuir SA (m^2g^{-1})	BET SA (m^2g^{-1})	Pore size (Å)	Pore volume (cm^3g^{-1})
MOF-5	3768	3360	12.5	1.27

1.2.3 Thermogravimetric Analysis

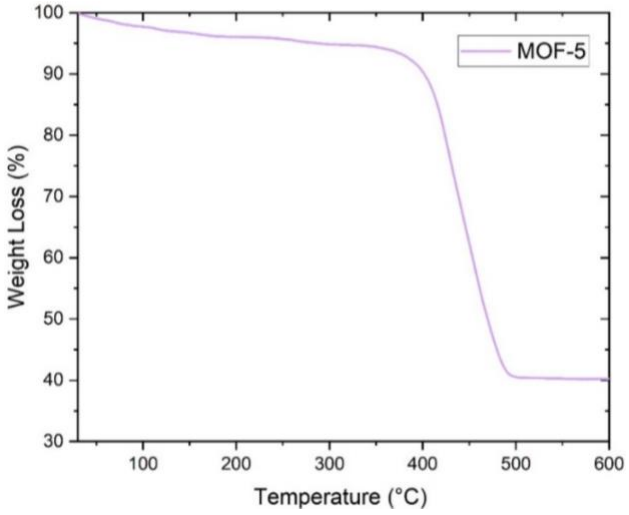

Figure III-5: TGA results of MOF-5.

Figure III-5 shows the TGA results of MOF-5. The small 7% weight loss before 350°C is due to the removal of surface molecules such as water or DMF that might still be present in the

pores of the MOF. We can then observe a large drop of about 50% in the weight of the sample between 350-500°C. This result is consistent with the literature where the decomposition temperature (T_d) is reported between 400°C and 500°C depending on the sample preparation, activation and experimental conditions[6]. The MOF decomposes to ZnO at these temperatures.

1.2.4 FT-IR experiments

Figure III-6 shows the FT-IR spectrum of MOF-5. The sample presents two strong peaks centered at 1564 cm^{-1} and 1394 cm^{-1}, related to the asymmetric and symmetric stretching vibrations of the carboxylate groups respectively coordinated to the Zn^{2+} cations of the inorganic node. This observation is consistent with literature[7]. Wang *et al.* attributed a stronger peak between 3500-3200 cm^{-1} than the one we can observe here. This peak was attributed to O-H bonds of water. The weak peak that we can observe in our FT-IR means that our MOF was very well kept from moisture using our glovebox.

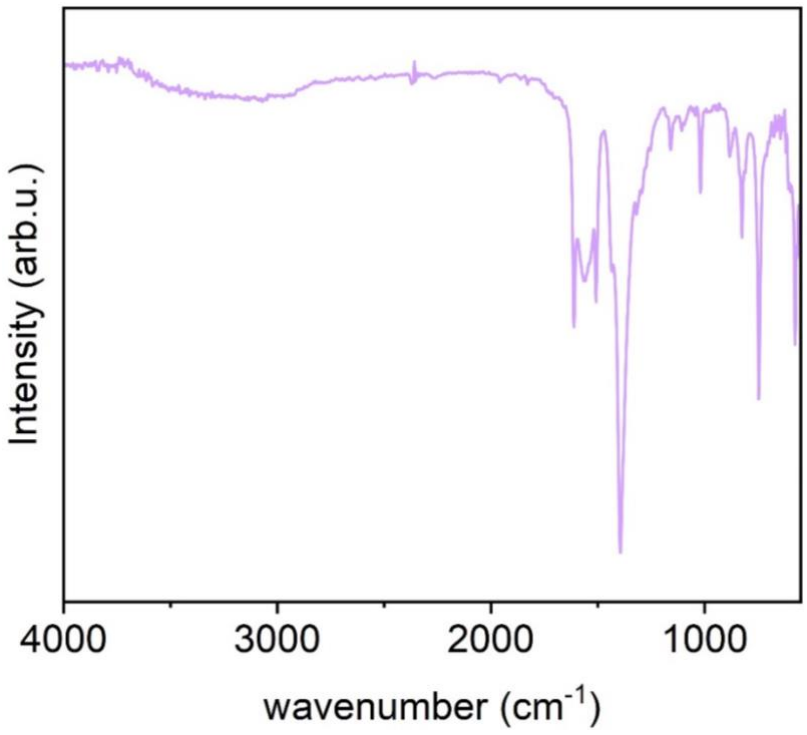

Figure III-6: FT-IR results of MOF-5.

1.3 Photophysical characterisation

1.3.1 Excitation and Emission spectra

Figure III-7 shows the excitation and emission spectra of MOF-5. This experiment was carried out on a single crystal of MOF-5 in a capillary. We can observe a peak excitation at 290 nm. The maximum emission peak is observed at 341 nm. A trident emission is observed with another peak at 325 nm and a shoulder around 357 nm. It is important to note that the emission wavelength of this MOF is not ideal for our gas detection experiment since it does not emit in the range of maximum quantum efficiency of photon detection of the PMTs used.

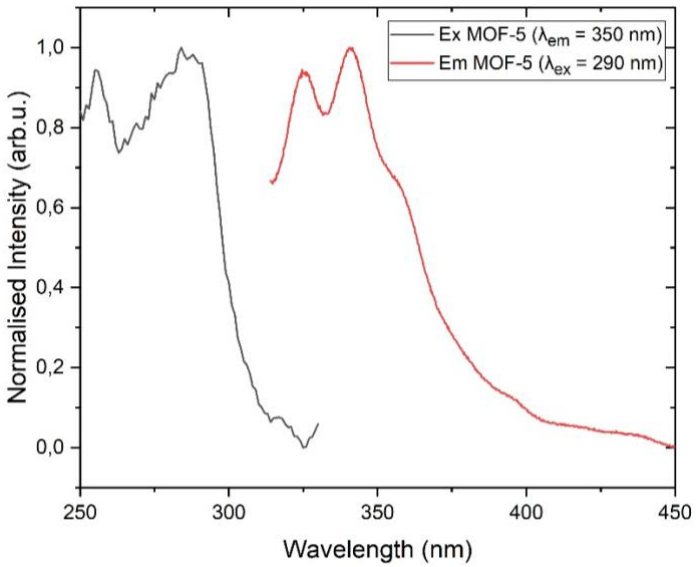

Figure III-7: Illustrating the excitation and emission spectra of MOF-5.

This trident/vibronic emission is typical of ligands in solution. We can see in Figure III-8 below that the emission of MOF-5 is very similar to a 10^{-5} M solution of its ligand (BDC) in DMF. This is because the coordination of the ligand in a MOF holds the ligands far enough apart that they mimic the behaviour of the ligand in a very dilute solution. Because MOF-5 is made from d^0 Zn metal, electronic transition involving the metal is least probable. Therefore, we have proven here the fluorescence of MOF-5 is indeed centred on its ligand. The slight bathochromic shift is due to the rigidification of the ligand in the MOF structure after the coordination with the Zn_4O clusters. As explained in Chapter I, our team showed that upon activation the emission of the MOF is broaden and centred at 358 nm[3].

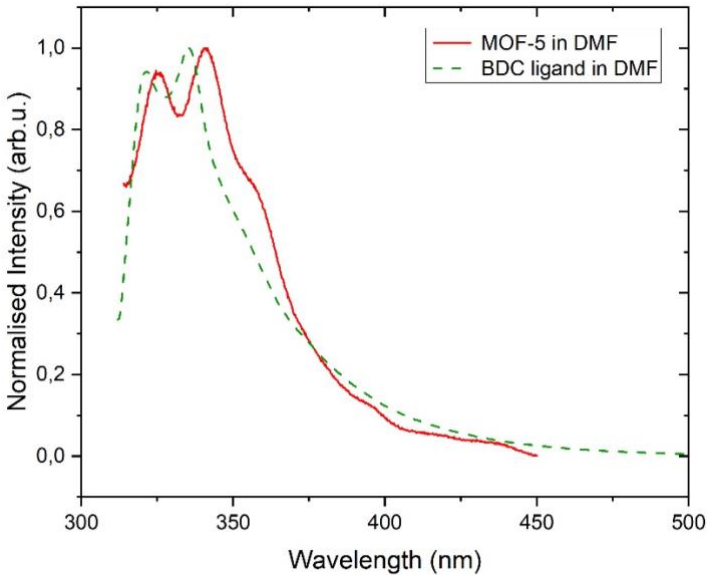

Figure III-8: Illustrating the emission spectrum of MOF-5 and that of a 10^{-5} M solution of BDC ligand in DMF.

1.3.2 TCSPC

The decay of MOF-5 was reported from an in depth photophysical study performed by V.Villemot *et al.*[3] at our laboratory where a monoexponential decay was observed. The fluorescence lifetimes are reported in Table III-2 below. The fluorescence lifetime is faster than 3 ns which is ideal for detection in coincidence.

Table III-2: Showing the calculated fluorescence lifetime of MOF-5.

MOF	**Diode λ_{ex} (nm)**	**λ_{em} (nm)**	**τ_1 (ns)**	**$<\tau>$ (ns)**
MOF-5	274	350	1.5 (100%)	1.5

1.4 Radioactive gas bench test

1.4.1 ^{85}Kr

Figure III-9 shows the results from the detection of ^{85}Kr gas. The D value on the y-axis is the photon count rate calculated by logical sum of double coincidence between every pair of PMT in the detection system. The graph on the left shows the photon count rate with a coincidence window of 40 ns while the one on the right with 400 ns. Presenting both coincidence windows allow us to see the difference in the photon count for a MOF which may have a slow

contribution to its fluorescence lifetime or delayed fluorescence. The photon count rate is higher for all the tests with the 400 ns coincidence window compared to the 40 ns coincidence window. This is because more time is allocated for the photons to be detected hence increasing the probability of there being a coincidence event. A common problem of systems of multiple detectors working in coincidence is the possibility of two or more unrelated events to occur within the same coincidence resolving time, thus resulting in an accidental coincidence[8]. Those accidental coincidences are not corrected here but are estimated to be around 0.17% and 1.5% for a measurement with a 40 ns and 400 ns coincidence window respectively at dead time of 10 µs using our detection system. We can observe in Figure III-9(left) that the count rate of MOF-5 is higher than the blank experiment. This means that our MOF does indeed produce photons in the presence of ^{85}Kr and is hence a scintillator. However, we can also observe that the count rate of MOF-5 is lower than that of the microspheres of polystyrene. As for Figure III-9(right), the MOF-5 count rate is comparable to that of the microsphere of polystyrene, which means that MOF-5 have some longer-lived excited state. Therefore, these experiments show that MOF-5 is considered as a scintillator for the detection of ^{85}Kr but not a very efficient one compared to the microspheres of polystyrene in the same geometry. This was expected due to the MOF's linkers containing only one conjugated ring and therefore not many delocalised electrons are involved in the excitation/emission mechanism. This implies a low fluorescence quantum yields (reported as only 0.05[9]), and a very energetic transition (< 300 nm). The emission wavelength discussed above is also not in the convenient range for this experiment. We will see in Chapter V how we were able to improve the scintillation of MOF-5 via a doping strategy.

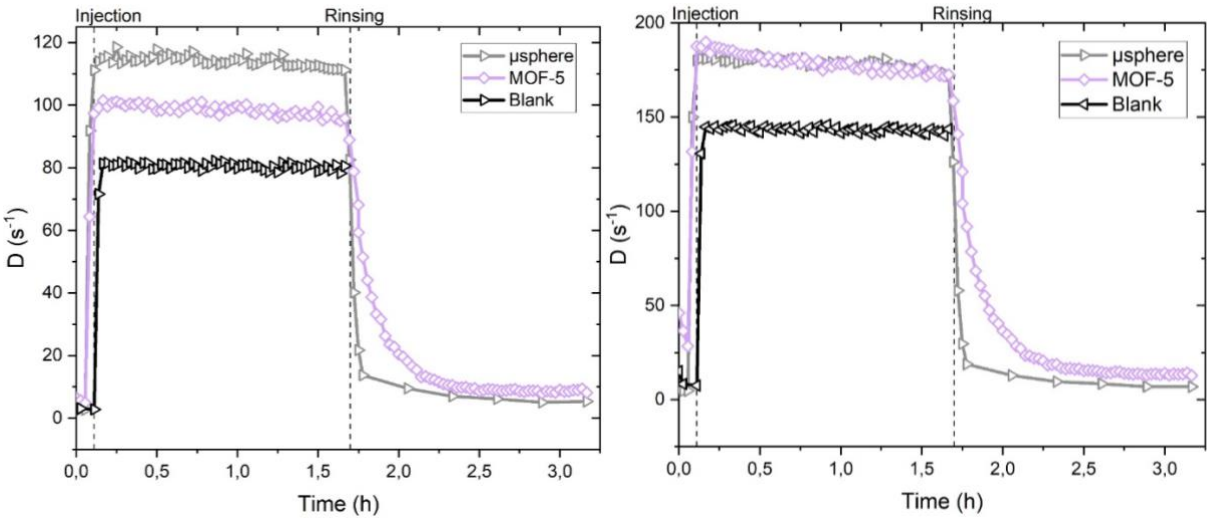

Figure III-9: Showing the results from ^{85}Kr detection with MOF-5. Left – with a coincidence window 40 ns. Right – with a coincidence window of 400 ns.

The photon counts of MOF-5 shown in these graphs is not the absolute photon count due to the MOF-5 alone. This would be the photon count of MOF-5 showed here minus that of the blank.

In the case of the 40 ns coincidence window, this would be around 18 s^{-1}. The blank measurement here hence makes up 80% of the photon count of MOF-5. One of the recurrent questions we have come across is why we have such a high photon count for the blank experiment, i.e. an experiment with no MOF/scintillator in the detection system while injecting the same activity of the targeted radioactive gas. This is due to Cherenkov phenomenon. Cherenkov radiation is the electromagnetic radiation emitted in an anisotropic manner between 250-300 nm, when a charged particle passes through a dielectric medium at a speed greater than the speed of light in that medium[10]. As seen in Chapter I, ^{85}Kr emits beta particles with a maximum energy of 687.1 keV and an average energy of 251.4 keV. This relatively high energy implies the generation of Cherenkov light in the glass walls and the air medium of our scintillating vials. This is why even without a MOF in the detection system the Cherenkov light accounts for the photon count rate of the blank experiment. This Cherenkov phenomenon is important to keep in mind, as it will be valuable for every interpretation of ^{85}Kr detection later on as well. We will analyse a control experiment in Chapter V (section 1.4.1) to evaluate whether our MOF is a simple Cherenkov wavelength shifter.

2. MOF-7

2.1 Structure and Synthesis

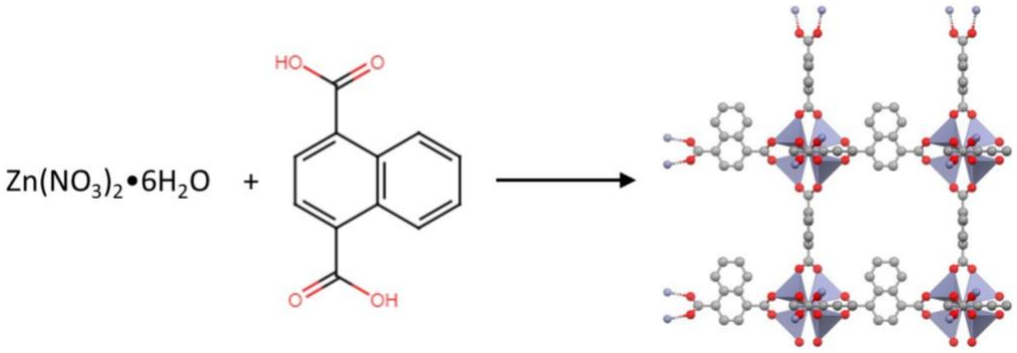

Figure III-10: Precursors and structure of IRMOF-7.

IRMOF-7 consist of Zn_4O nodes linked by six linear 1,4-naphthalenedicarboxylic acid ligands leading to a 3D cubic porous network with an Pm(-3)m space group as shown in Figure III-10. This MOF was chosen as its ligand has more conjugated benzene rings and a higher fluorescence yield reported as 0.23 compared to than that of MOF-5 and is hence known to have a better scintillation yield than the one ring BDC ligand (with a fluorescence yield of 0.05[9]). The fluorescence yield of the NDC ligand is reported at 0.23 compared to the previous BDC ligand reported at 0.05[9]. Naphthalene derivatives such as DIN (di-isopropyl-naphthalene) are also known as good scintillating molecules in liquid or plastic scintillator[11].

Several synthesis protocols are reported in literature for this MOF. They were all tried out but obtaining crystalline single crystals were unsuccessful. It is important to note that they used Teflon-lined stainless-steel vessel to perform their synthesis which was not available to us. With Teflon autoclaves, the pressure can be adjusted by adjusting the temperature of the autoclave. A protocol to establish attempt to obtain single crystals was devised as summarised in Table III-3. The attempts 1-5 were all unsuccessful. Attempts 6 produced transparent crystals which were then used throughout this experiment.

Table III-3: Summarising the attempts to crystalline synthesis single crystals.

Attempt Number	Metal concentration ($mol \cdot L^{-1}$)	Ligand concentration ($mol \cdot L^{-1}$)	Temperature	Solvent	Synthesis Outcome
1	0.091	0.010	85	DMF	Opaque granules
2	0.091	0.010	75	DMF	White precipitate – XRD no diffraction
3	0.091	0.020	85	DEF	Opaque yellow granules
4	0.091	0.020	85	DMF	Opaque white granules
5	0.091	0.030	85	DMF	White precipitate – XRD no diffraction
6	0.091	0.030	75	DMF	Transparent crystals – XRD Diffraction

The protocol listed below is the synthesis conditions used to obtain millimetric single crystals of IRMOF-7 (Attempt 6). $Zn(NO_3)_2 \cdot 6H_2O$ (0.091 $mol \cdot L^{-1}$, 2.716 g), 1,4-naphthalene dicarboxylic acid (0.030 $mol \cdot L^{-1}$, 0.658 g) were dissolved in 100 mL of *N*,*N*-dimethylformamide (DMF). The mixture was equally divided into twelve 10 mL glass vials, which were then sealed with a screw cap. The vials were placed in an oven at 75°C for 144 h (6 days) yielding millimetre-sized single crystals as shown in Figure III-11. The closed vials were removed and placed in a N_2 glovebox. The crystals were washed according to the protocol described in Chapter II.

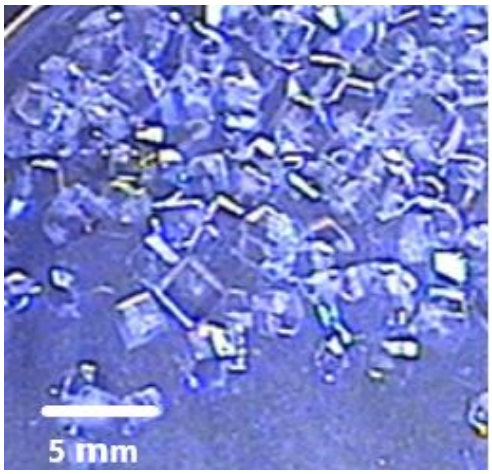

Figure III-11: Photo of millimetric IRMOF-7 single crystals.

2.2 Structural Characterisation

2.2.1 X-Ray Diffraction

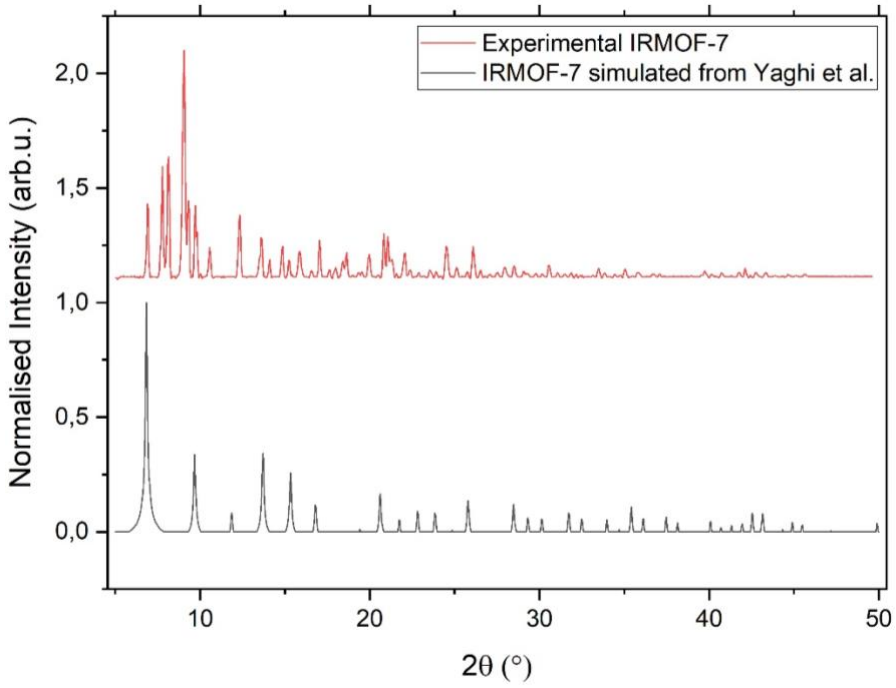

Figure III-12: PXRD spectrum showing experimental results compared to literature.

The PXRD in Figure III-12 is not in complete agreement with the reported XRD data for IRMOF-7[4]. Diffraction peaks at such low angles are however not typical of the precursors used in the synthesis of IRMOF-7 showing that those precursors did not simply recrystallize during the synthesis. Diffraction peaks at such low angles are typical however of MOFs and some

peaks do correspond to the data from literature. This shows that some of the planes are similar to the structure of IRMOF-7 but unfortunately, we cannot conclude here that we have successfully synthesised IRMOF-7. We will see more evidence of this in the rest of the structural characterisation. Even though a MOF was not obtained via this synthesis, we thought it relevant to show our array of characterisation and tests on this material for scientific rigour and comparison purposes. Future attempts to synthesise this MOF should include varying the metal to ligand ratio, the metal concentration and attempting a synthesis at high temperature not to obtain single crystals but a crystalline powder.

2.2.2 Adsorption measurements

Figure III-13 shows the N_2 adsorption experiment performed on our sample. We can see that no gas uptake was observed hence confirming that our synthesised material is not porous and is probably not a MOF.

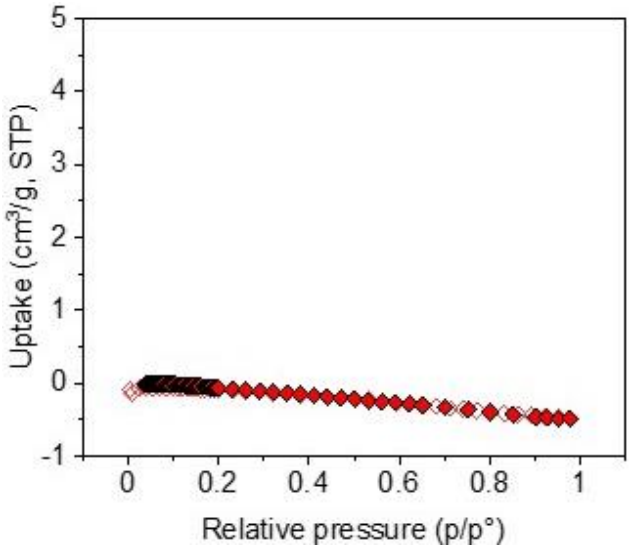

Figure III-13: Illustrating the N_2 adsorption isotherm of IRMOF-7.

2.2.3 Thermogravimetric Analysis

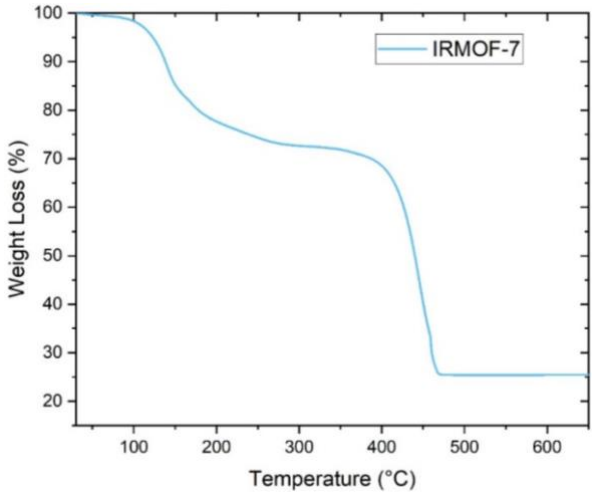

Figure III-14: TGA results of IRMOF-7.

Figure III-14 above shows a drastic weight loss before 400°C, which is not typical for a MOF material. The weight loss starts around 100°C and can be due to the loss of surface water and can also be combined with remaining DMF whose boiling point is at 153°C. However, since this product was washed and activated using the same protocol as all the other MOFs and in a glove box, and that this drop before 400°C is not observed in the other MOFs, the most probable explanation would be the degradation of the structure of this material before 400°C. This further instils doubts on whether the material synthesised here is indeed IRMOF-7.

2.2.4 FT-IR experiments

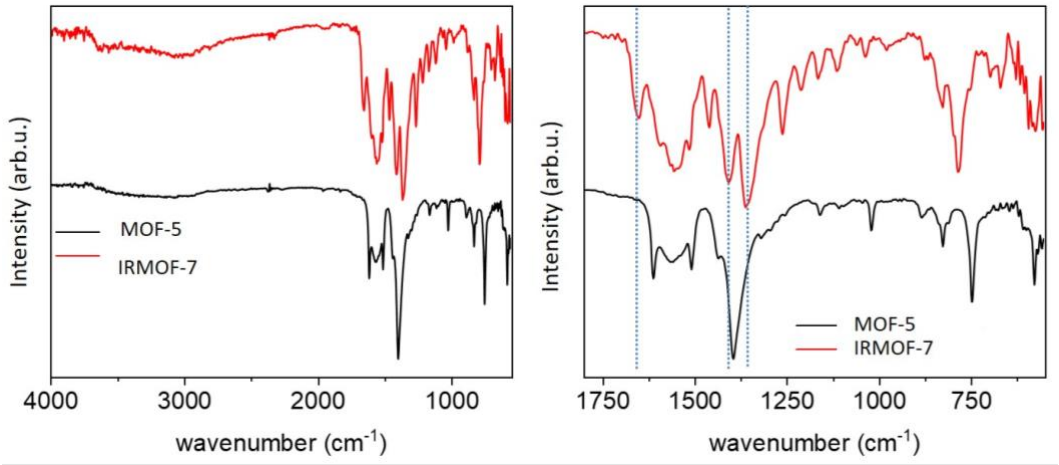

Figure III-15: FT-IR results of IRMOF-7.

Figure III-15 compares the FT-IR experiments of MOF-5 with IRMOF-7. Since their ligands have the same carboxylate coordination, we would expect the coordination to the Zn tetrahedra in the MOF to be similar and hence both MOFs to have similar FT-IR spectra. However, the infrared spectrum of IRMOF-7 after activation displays different peaks in the region between 1200 and 1700 cm^{-1} (as indicated by the dotted lines). This is possibly associated to a different coordination of the 1,4-NDC ligand to the Zn^{2+} cations. This again poses the question of whether this product is indeed IRMOF-7.

2.3 Photophysical characterisation

2.3.1 Excitation and Emission spectra

Figure III-16 shows the excitation and emission spectra of IRMOF-7. This experiment was carried out on a single crystal of IRMOF-7 in a capillary. We can observe a peak excitation at 350 nm. The maximum emission peak is observed at 390 nm. The emission wavelength of this MOF is in the range of maximum quantum efficiency of photon detection of the PMTs used in the gas detection experiment.

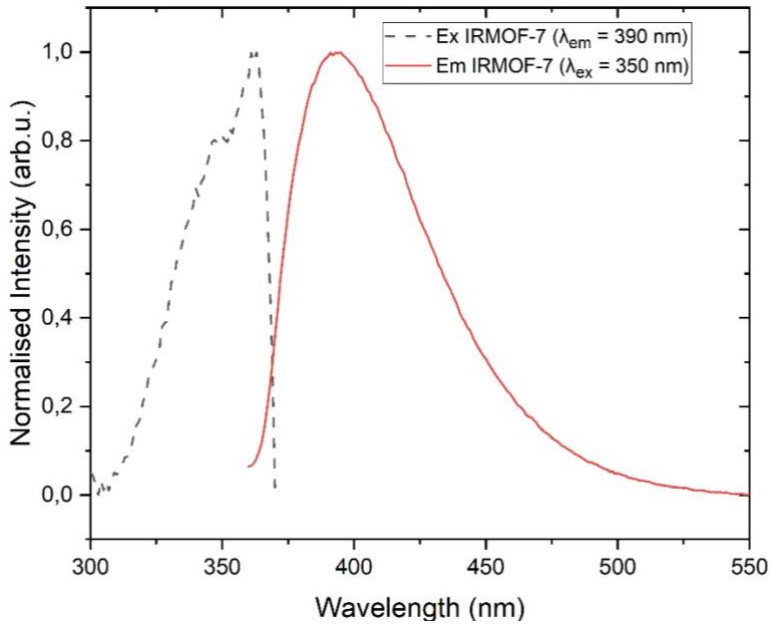

Figure III-16: Illustrating the excitation and emission spectrum of IRMOF-7.

We can see in Figure III-17 below that the emission of IRMOF-7 is very similar to a 10^{-5} M solution of its ligand (1,4-NDC) in DMF. Electronic transition and hence fluorescence contribution from the d^0 Zn metal is least probable. Therefore, the fluorescence is indeed centred on the ligand. The slight bathochromic shift is not observed here as seen with MOF-5 and as we will see with IRMOF-9 maybe revealing that the rigidification of the ligand within

the MOF structure did not occur. As seen in Appendix Figure 1 upon activation, there is a shift of the emission maxima to a higher wavelength, 412 nm.

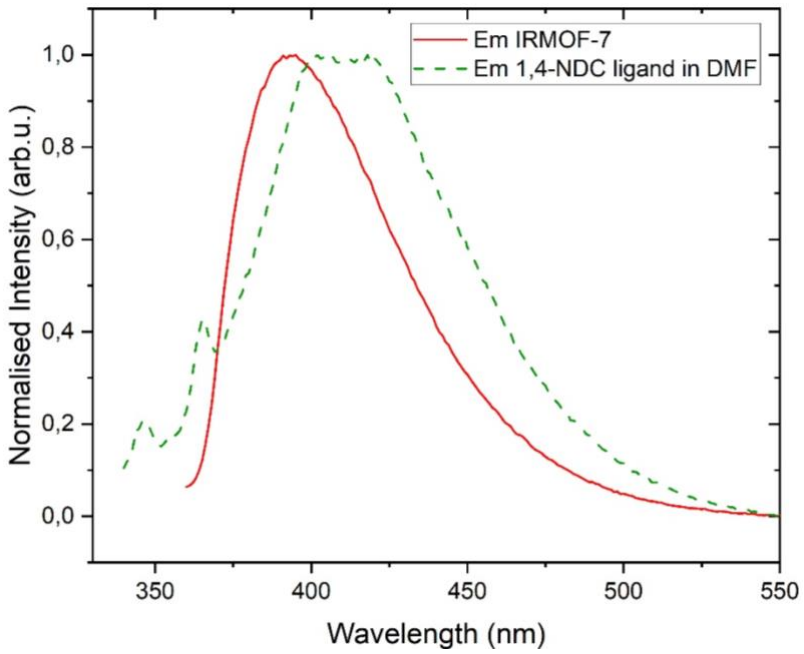

Figure III-17: Illustrating the emission spectrum of IRMOF-7 and that of a 10^{-5} M solution of 1,4-NDC ligand in DMF.

2.3.2 TCSPC

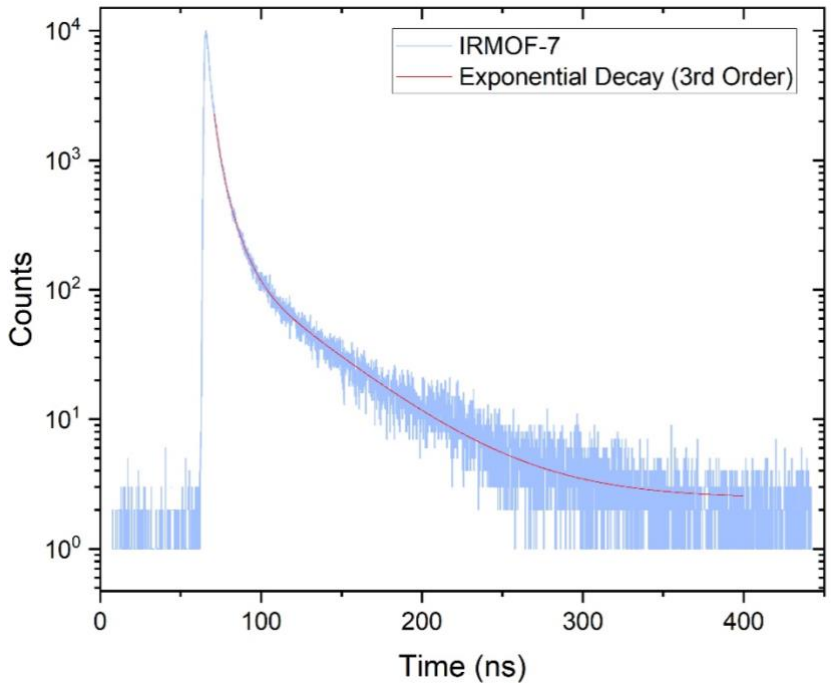

Figure III-18: Showing the TCSPC results for IRMOF-7.

Figure III-18 shows the fluorescence decay of IRMOF-7 with an excitation diode at 368 nm. By fitting this decay curve with a third order exponential fit, we are able to calculate the two fluorescence lifetime components and their respective weight as well as an average fluorescence lifetime. The results are shown in Table III-4 together with the coefficient of determination (R-Square / COD) of the fit. The fluorescence lifetime is higher than our ideal value of 3 ns for coincidence measurements, but since it is below 10 ns it still falls in an acceptable range. It is important to note however, that IRMOF-7 has a much slower fluorescence lifetime compared to the other undoped MOFs studied this Chapter as well as Chapter IV, most of which are around 3 ns.

Table III-4: Showing the calculated fluorescence lifetime of IRMOF-7.

MOF	Diode λ_{ex} (nm)	λ_{em} (nm)	τ_1 (ns)	τ_2 (ns)	τ_3 (ns)	$<\tau>$ (ns)	R-Square (COD)
IRMOF-7	368	390	2.8 (57.1%)	8.2 (37.9%)	45.1 (5.0%)	7.0	0.9983

2.4 Radioactive gas bench test

2.4.1 ^{85}Kr

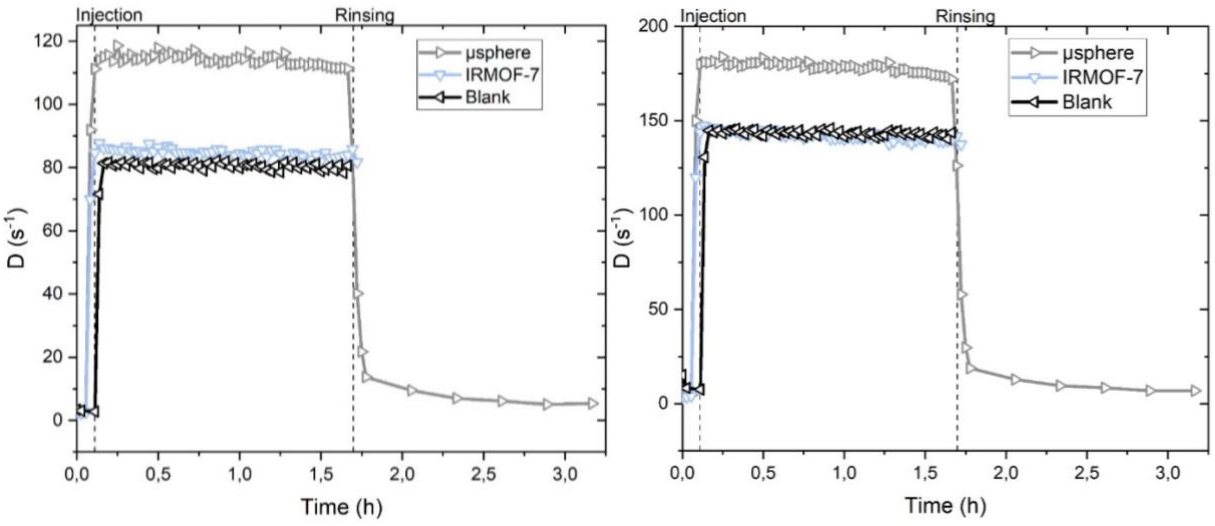

Figure III-19: Showing the results from ^{85}Kr detection with IRMOF-7. Left – with a coincidence window 40 ns. Right – with a coincidence window of 400 ns.

Figure III-19 shows the results from the detection of ^{85}Kr gas. For both coincidence windows (left and right graphs), we can observe that the photon count rate for IRMOF-7 is equal to the blank measurement meaning that this material is not able to detect ^{85}Kr. Even though we have seen that this material is fluorescent in section 2.3, the lack of porosity in the material might

account for its poor results as a scintillator for gas detection. Since we have argued that this material does not have the characteristics of a MOF, the ability of MOFs as scintillators for radioactive gas detection is not questioned by these poor results.

3. IRMOF-9

3.1 Structure and Synthesis

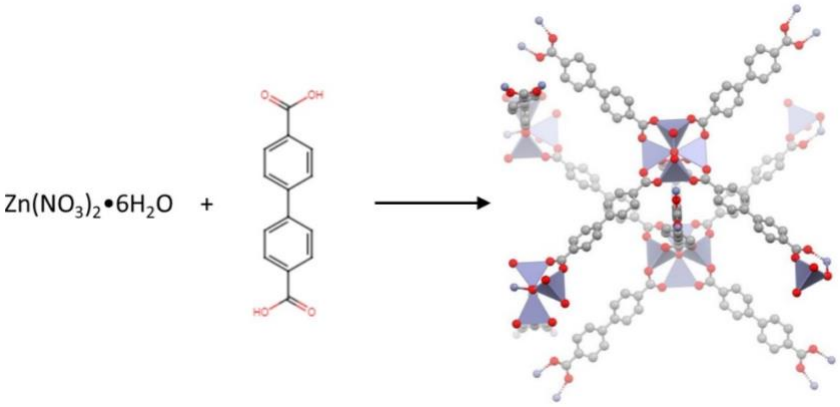

Figure III-20: Precursors and structure of IRMOF-9.

IRMOF-9 consist of Zn_4O nodes linked by linear biphenyl-4,4′-dicarboxylic acid ligands leading to a 3D orthorhombic porous network with aa Pnnm space group as shown in Figure III-20. The protocol listed below is the optimised synthesis conditions to obtain centimetric single crystals of IRMOF-9. This MOF was chosen as a potentially efficient scintillator since the photoluminescence light yield of its ligand is reported as 0.18 compared to 0.05 for the BDC ligand[9].

$Zn(NO_3)_2$•$6H_2O$ (0.124 mol·L^{-1}, 3.68 g) and biphenyl-4,4′-dicarboxylic acid (0.041 mol·L^{-1}, 1.0 g) were dissolved in 100 mL of *N*,*N*-dimethylformamide (DMF). Unlike the other ligands used in this manuscript biphenyl-4,4′-dicarboxylic acid is not easily dissolved in DMF. The mixture has hence been heated with a heat gun to dissolve the ligand before it was equally divided into twelve 10 mL vials, which were then sealed with a screw cap. The vials were placed in an oven at 85°C for 96 h (4 days) before the solution has the time to cool down. The synthesis yielded centimeter-sized IRMOF-9 polycrystals as shown in Figure III-21. The closed vials were removed and placed in a N_2 glovebox. The crystals were washed according to the protocol described in Chapter II.

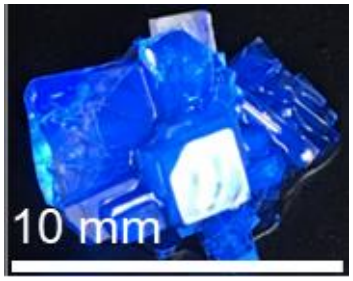

Figure III-21: Photo of a centimetric IRMOF-9 polycrystal[1].

3.2 Structural Characterisation

3.2.1 X-Ray Diffraction

Figure III-22 shows the X-ray Diffraction spectrum of our IRMOF-9 compared to the simulated XRD from the first reported work of Yaghi *et al.*[4] The peak positions are comparable between both data sets showing that we have indeed synthesised IRMOF-9 single crystals. However, we can see that the peak intensity varies from our experimental data to that of Yaghi *et al.* This is because the XRD we carried out was a powdered XRD done by crushing single crystals of IRMOF-9 on a sample holder. Compared to a single X-ray diffraction, this method will lead to preferential orientation of the crystals and hence influence the intensity for the different diffraction planes.

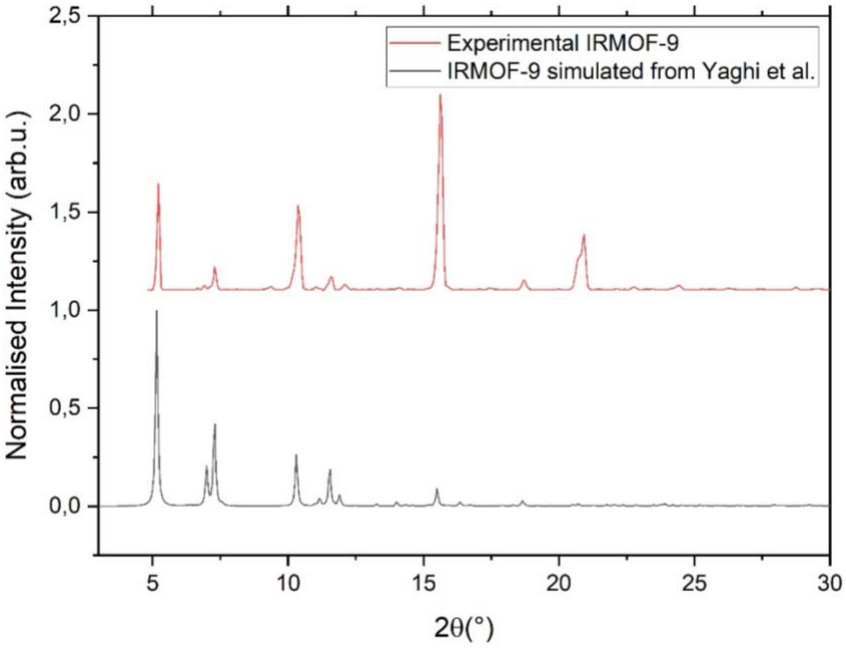

Figure III-22: PXRD spectrum showing experimental results compared to literature.

3.2.2 Adsorption measurements

The N_2 adsorption experiments for IRMOF-9 were carried out at the University of Milano-Bicocca. The measurements were particularly tricky for this MOF because of its easy collapse with humidity. A previous set of measurement at NIMBE revealed a BET surface area of only 9 m^2g^{-1}. The results for the 2nd experiment at UNIMIB are displayed in Figure III-23 and Table III-5. Literature values for the BET measurement of this MOF are quite divergent. A study by A.B. Crom *et al.*[12] demonstrates a drastic decrease from 1168 m^2g^{-1} for a non-interpenetrated IRMOF-9 structure to 412 m^2g^{-1} for an interpenetrated IRMOF-9 structure. Another study by R. Babarao *et al.*[13] shows higher surface areas, 1918 and 1730 m^2g^{-1} for a non-interpenetrated and interpenetrated structure, respectively. Our BET surface area of 902 m^2g^{-1} is comparable to the non-interpenetrated one from A.B. Crom *et al.*

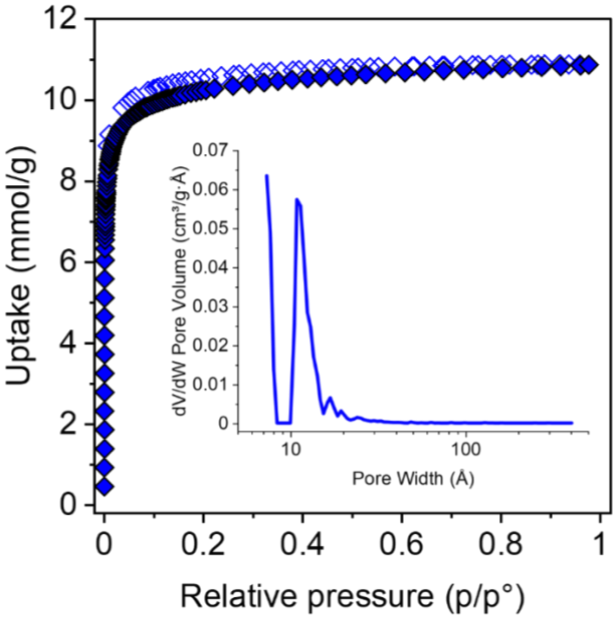

Figure III-23: Illustrating the N_2 adsorption isotherm of IRMOF-9. Inset of pore width measurement.

Table III-5: Showing the data calculated from N_2 adsorption of MOF-5.

MOF	Langmuir SA (m^2g^{-1})	BET SA (m^2g^{-1})	Pore size (Å)
IRMOF-9	970	902	11

3.2.3 Thermogravimetric Analysis

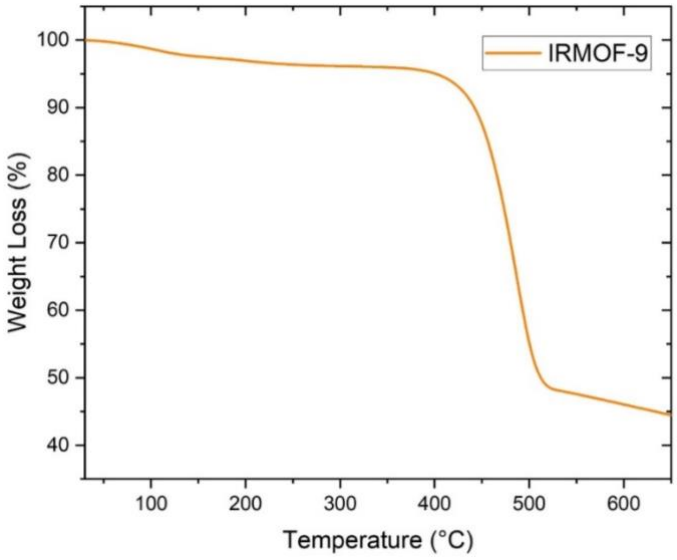

Figure III-24: TGA results of IRMOF-9.

Figure III-24 shows the TGA results of IRMOF-9. Just like for MOF-5, we can then observe a large drop of about 50% in the weight of the sample between 350°C and 500°C. This result is consistent with the literature where the decomposition temperature (T_d) is reported to be between 400°C and 500°C depending in the sample preparation, activation and experimental conditions[6]. The MOF decomposes to ZnO at these temperatures.

3.3 Photophysical characterisation

3.3.1 Excitation and Emission spectra

Figure III-25 shows the excitation and emission spectra of IRMOF-9. This experiment was carried out on a single crystal of IRMOF-9 in a capillary. We can observe a peak excitation at 360 nm. The maximum emission peak is observed at 430 nm. The emission wavelength of this MOF is in the range of maximum quantum efficiency of photon detection of the PMTs used in the gas detection experiment.

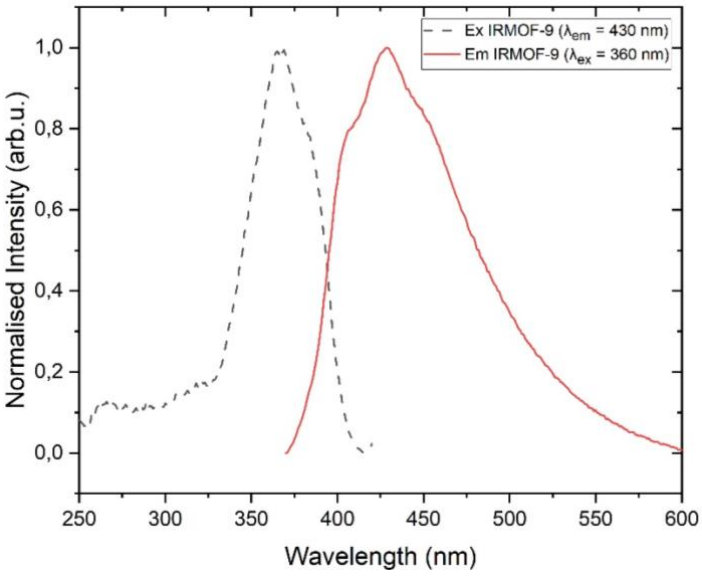

Figure III-25: Illustrating the excitation and emission spectrum of IRMOF-9.

We can see in Figure III-26 below that the emission of IRMOF-9 is very similar to a 10^{-5} M solution of its ligand (BPDC) in DMF. Because IRMOF-9 is made from d^0 Zn metal, electronic transition involving the metal is least probable. Therefore, as we have proven here that the fluorescence of IRMOF-9 is indeed centred on its ligand. The slight bathochromic shift is due to the rigidification of the ligand in the MOF structure after the coordination with the Zn_4O clusters.

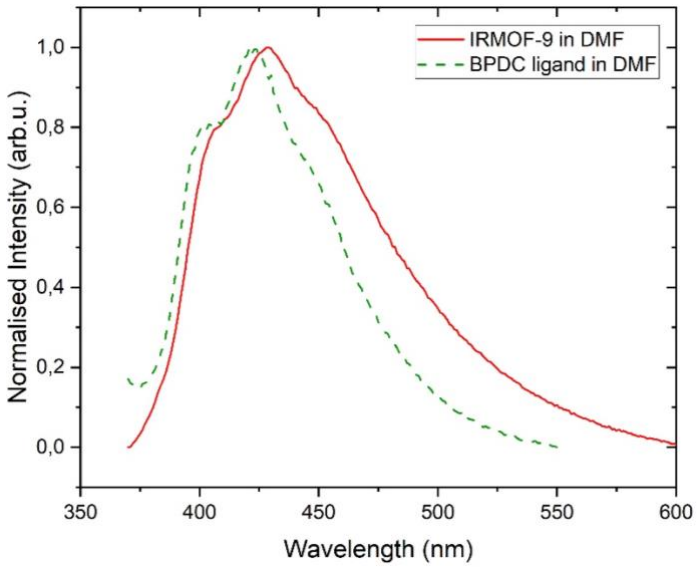

Figure III-26: Illustrating the emission spectrum of IRMOF-9 and that of a 10^{-5} M solution of BPDC ligand in DMF.

3.3.2 TCSPC

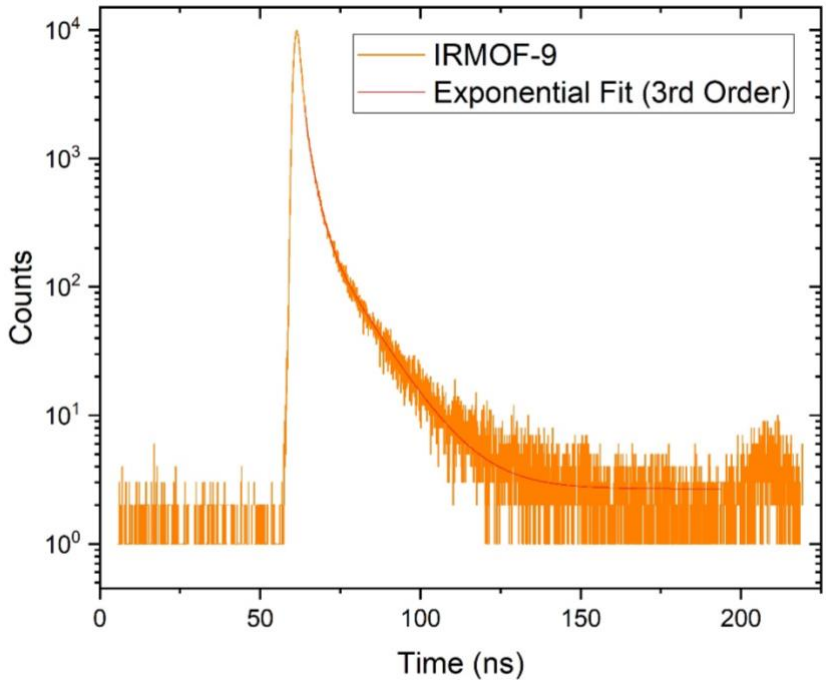

Figure III-27: Showing the TCSPC results for IRMOF-9.

Figure III-27 shows the fluorescence decay of IRMOF-9 with an excitation diode at 368 nm. By fitting this decay curve with a second order exponential fit, we are able to calculate the two fluorescence lifetime components and their respective weight as well as an average fluorescence lifetime. The results are shown in Table III-6 together with the coefficient of determination (R-Square / COD) of the fit. With a 3 ns lifetime, this MOF has an ideal fluorescence lifetime for coincidence measurements.

Table III-6: Showing the calculated fluorescence lifetime of IRMOF-9.

MOF	**Diode λ_{ex} (nm)**	**λ_{em} (nm)**	**τ_1 (ns)**	**τ_2 (ns)**	**τ_3 (ns)**	**<τ> (ns)**	**R-Square (COD)**
IRMOF-9	368	430	2.8 (58.0%)	0.5 (31.0%)	10.9 (11.0%)	3.0	0.9990

3.4 Radioactive gas bench test

3.4.1 ^{85}Kr

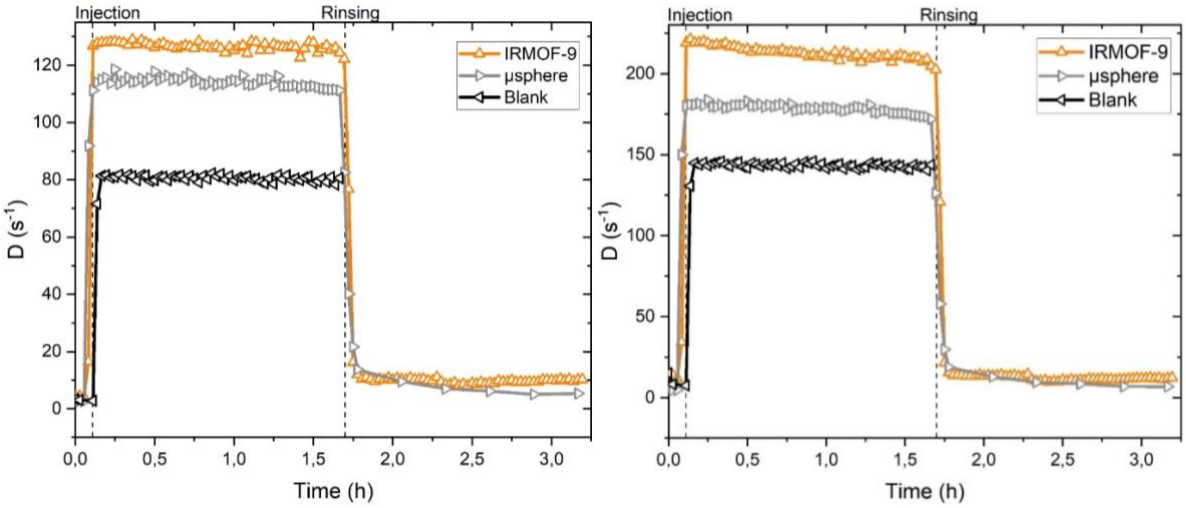

Figure III-28: Showing the results from ^{85}Kr detection with IRMOF-9. Left – with a coincidence window 40 ns. Right – with a coincidence window of 400 ns.

Figure III-28 shows the results from the detection of ^{85}Kr gas. We can observe in both graphs of Figure III-28 that the count rate of IRMOF-9 is higher than the blank experiment. This means that our MOF does indeed produce photons in the presence of ^{85}Kr and is hence a scintillator. We can also observe that the count rate of IRMOF-9 is slightly higher than that of the microspheres of polystyrene (10.1% higher for the 40 ns coincidence window and 17.9% for the 400 ns coincidence window). Therefore, these experiment show that IRMOF-9 is an efficient scintillator for the detection of ^{85}Kr. The relatively high surface area combined with the emission on this MOF in the right wavelength range have probably been key properties to obtaining such results.

4. MOF-205

4.1 Structure and Synthesis

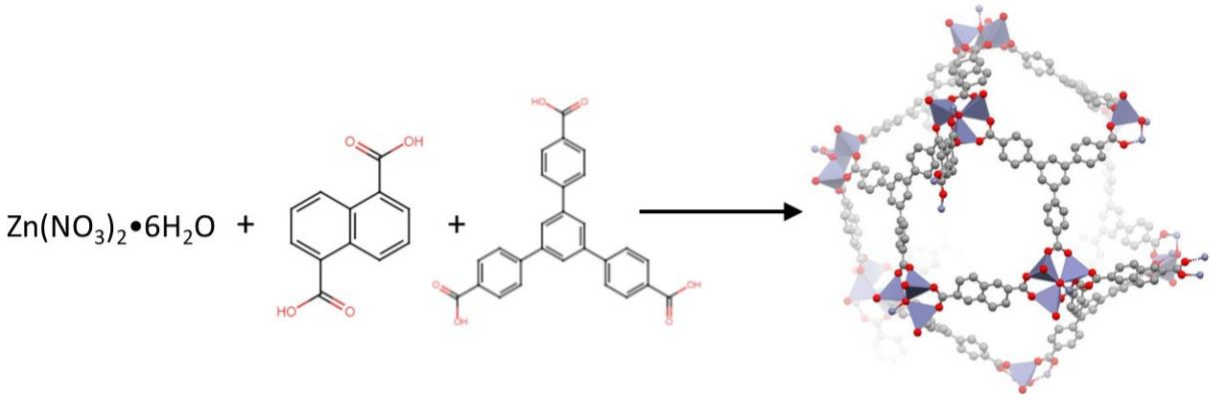

Figure III-29: Precursors and structure of MOF-205.

MOF-205 consist of Zn_4O nodes linked by tritopic H_3BTB ligands and ditopic 2,6-NDC ligands leading to a 3D cubic porous network with an Pm3n space group as shown in Figure III-29. The driving force for studying this MOF was to investigate the effect of a mixed-ligand MOF on its scintillating properties. The protocol listed below is the optimised synthesis conditions to obtain millimetric single crystals of MOF-205.

$Zn(NO_3)_2$•$6H_2O$ (0.064 mol·L^{-1}, 1.9128 g), 2,6-naphthalene dicarboxylic acid (0.022 mol·L^{-1}, 473 mg) and H_3BTB (0.013 mol·L^{-1}, 575.5 mg) were dissolved in 100 mL of *N*,*N*-dimethylformamide (DMF). The mixture was equally divided into twelve 10 mL glass vials which were then sealed with a screw cap. The vials were placed in an oven at 85°C for 96 h (4 days) yielding millimetre sized MOF-205 single crystals as seen in Figure III-30. The closed vials were removed and placed in a N_2 glovebox. The crystals were washed according to the protocol described in Chapter II.

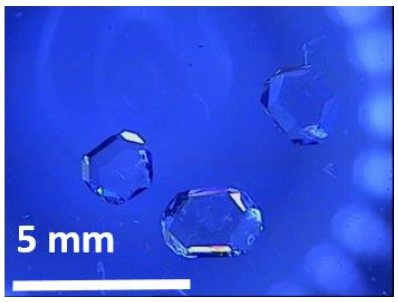

Figure III-30: Photo of millimetric MOF-205 single crystals.

4.2 Structural Characterisation

4.2.1 X-Ray Diffraction

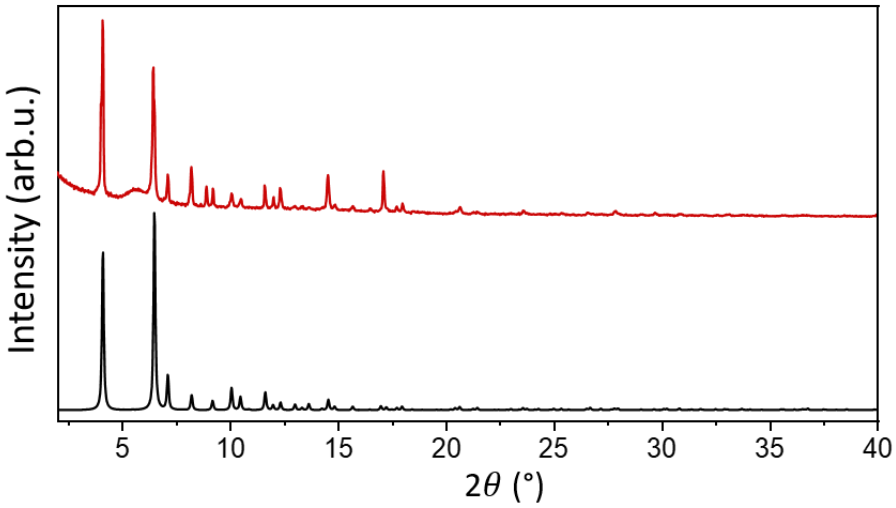

Figure III-31: PXRD spectrum showing experimental results compared to literature.

Figure III-31 shows the X-ray Diffraction spectrum of our MOF-205 compared to the simulated XRD from Furukawa *et al.*[14]. The peak positions are comparable between both data sets showing us that we have indeed synthesised MOF-205 single crystals. We can see that the peak intensity from our experimental data corresponds better to that of Furukawa *et al.* compared to the previous MOFs in this Chapter. This is because a single crystal XRD was carried on MOF-205 at the University of Milano-Bicocca instead of a powder XRD.

4.2.1 Adsorption measurements

The N_2 adsorption experiments for MOF-205 were carried out at the University of Milano-Bicocca. The N_2 adsorption isotherm is shown in Figure III-32 and the results extracted from these data are reported in Table III-7. We can observe here that MOF-205 has two pore sizes of 13.5 and 17.3 Å, which is consistent with the structure and further supported by what has been observed in literature[14,15].

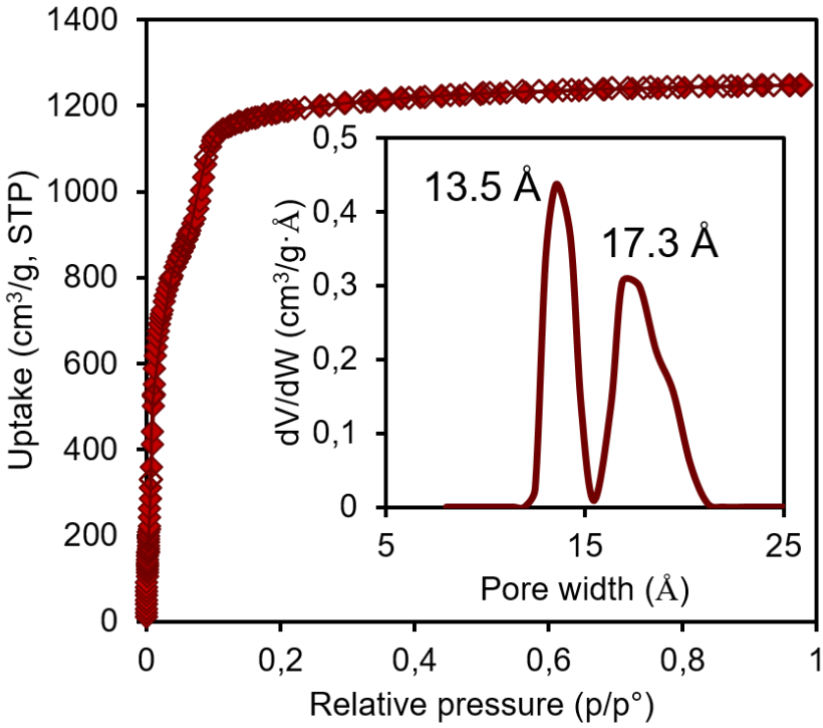

Figure III-32: Illustrating the N_2 adsorption isotherm of MOF-205. Inset of pore width measurement.

Table III-7: Showing the data calculated from N_2 adsorption of MOF-205.

MOF	Langmuir SA (m^2g^{-1})	BET SA (m^2g^{-1})	Pore size (Å)	Pore volume (cm^3g^{-1})
MOF-205	5390	4450	13.5 & 17.3	1.75

4.2.2 Thermogravimetric Analysis

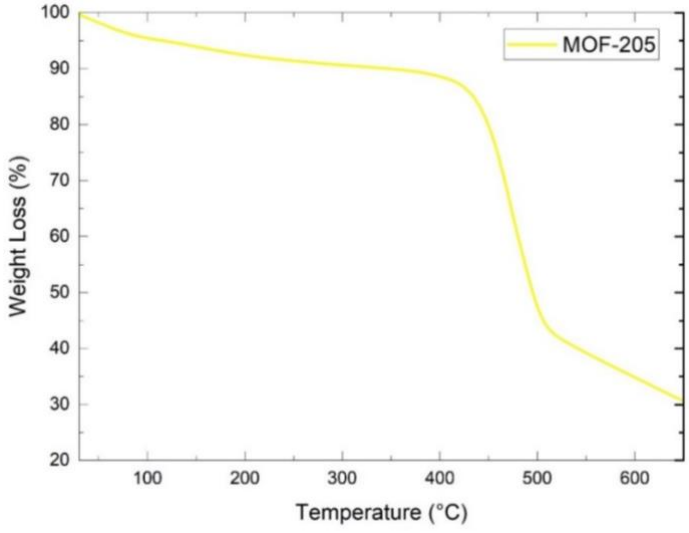

Figure III-33: TGA results of MOF-205.

Figure III-33 shows the TGA results of MOF-205. We can then observe a large drop of about 45% in the weight of the sample between 350-500°C. This result is consistent with the literature where the decomposition temperature (T_d) between 400-500°C depending in the sample preparation, activation and experimental conditions[6]. The MOF decomposes to ZnO at these temperatures.

4.2.3 FT-IR experiments

Figure III-34 shows the FT-IR spectrum of MOF-205. The sample present 2 strong peaks centered at 1584 cm^{-1} and 1409 cm^{-1}, related to the asymmetric and symmetric stretching vibrations of the carboxylate groups respectively coordinated to the Zn^{2+} cations of the inorganic node. This overall spectrum is consistent with literature[15]. Wang *et al.* attributed a stronger peak between 3500-3200 cm^{-1} than the one we can observe here[7]. This peak was attributed to O-H bonds of water. The weak peak that we can observed in our FT-IR means that our MOF was very well kept from moisture using our glovebox.

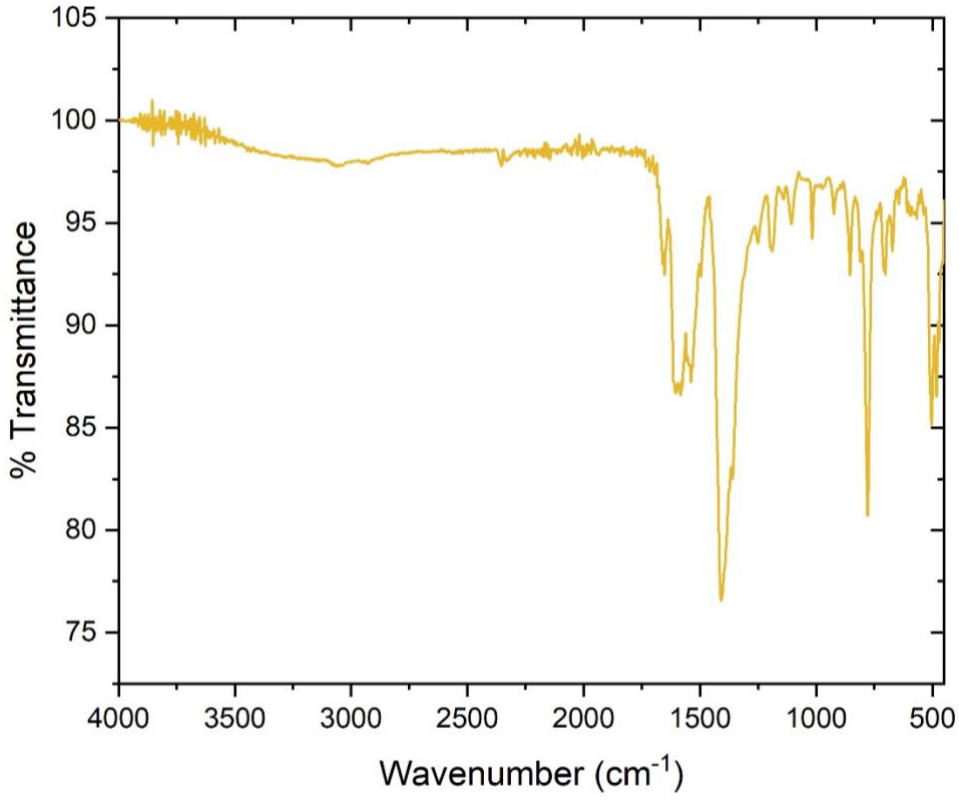

Figure III-34: Illustrating MOF-205 FT-IR spectra.

4.2.4 ^{13}C, ^{1}H and ^{129}Xe NMR results

The ^{13}C magic spin angle spinning (MAS) experiment shown in Figure III-35 below show two resonance signal around 175-176 ppm which account for the presence of the carboxylate groups of the two different ligands present in MOF-205. The coloured labelling of the carboxylate groups in Figure III-35 can be assigned to each ligand (Figure III-36). We can also observe the absence of any signal related to residual solvent such as DMF or DCM confirming once again that our MOF has been well activated.

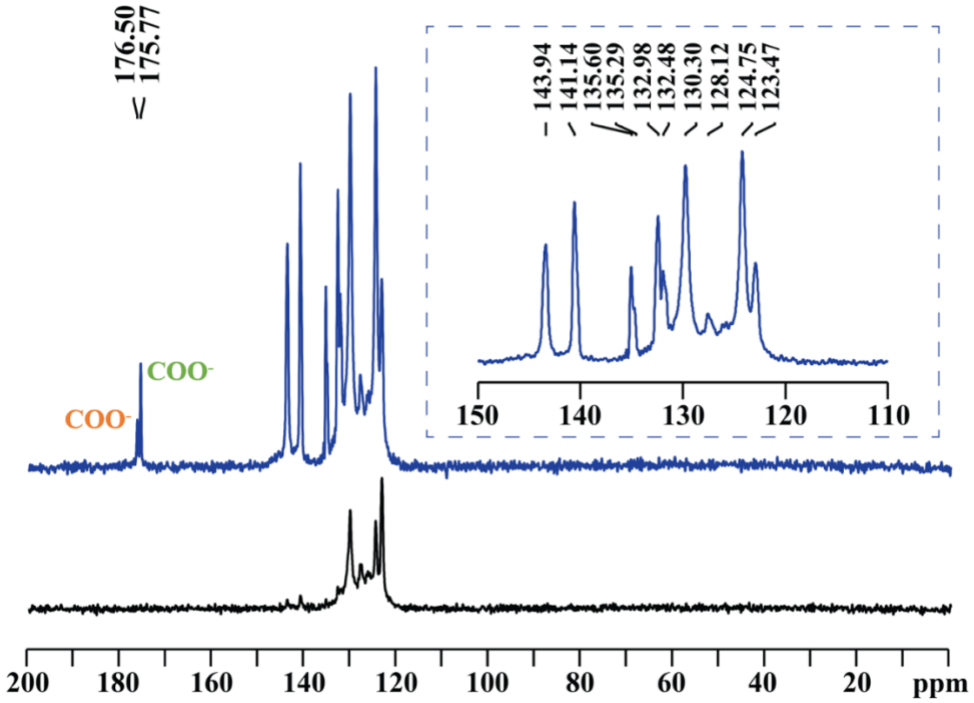

Figure III-35: Illustrating the ^{13}C {^{1}H} solid-state NMR of MOF-205. Black line represents a polarised NMR sequence that gives only quaternary carbon signals.

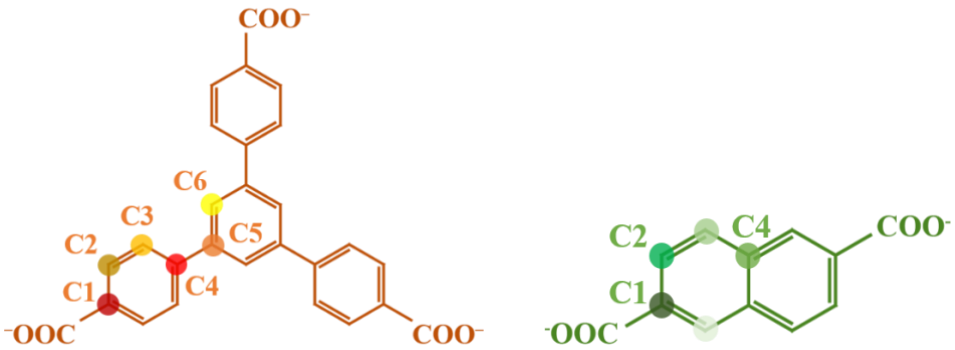

Figure III-36: Illustrating the carbon atoms in both ligands present in MOF-205.

The ^{1}H MAS-NMR in Figure III-37 below also confirms the presence of the two CH signals, one for each ligands present in MOF-205. We have therefore confirmed here using NMR techniques that the MOF we have synthesised is indeed MOF-205.

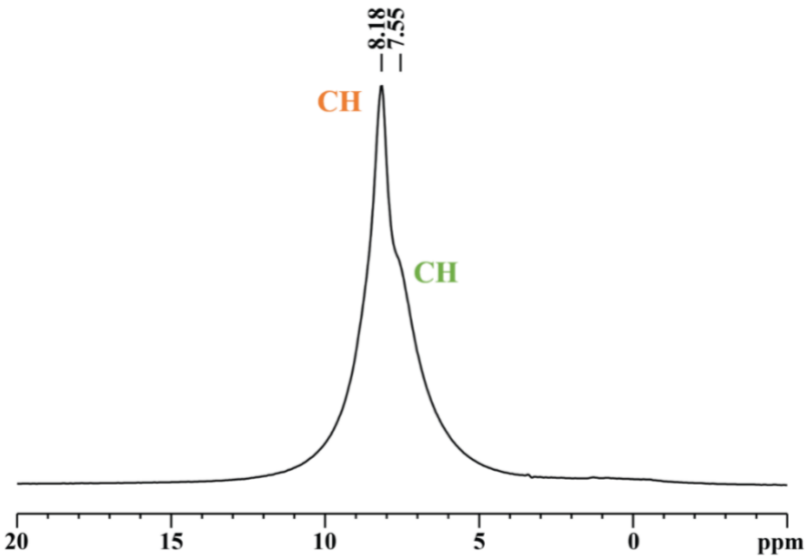

Figure III-37: Illustrating the ^{1}H solid-state NMR of MOF-205.

Figure III-38 below shows the Continuous Flow Hyperpolarised (CW-HP) ^{129}Xe NMR results on MOF-205, which can help us determine the accessibility of the pores to a noble gas such a Xe. The experiments performed at low partial pressure ensure that intermolecular interactions of Xenon with the framework prevail, while Xe-Xe interactions are negligible. Thus, the Xenon chemical shifts depend only on the environment of Xenon confined in restricted spaces. The ^{129}Xe NMR spectra of MOF-205 at room temperature show two predominant signals in the regions at ≈ 60 ppm that are different from the free gas (at 0 ppm), indicate a fast diffusion of Xenon atoms in the confining cavities. At low temperatures, we can distinguish two peaks which have merged into one forming a broader peak. This phenomenon is due to MOF-205 having two different pores as we have seen in the N_2 adsorption experiment in section 4.2.1. What we are observing in the CW-HP ^{129}Xe NMR experiment is the variation of interaction from a xenon atom. At low temperature, the Xe move slowly and are able to interact in a specific way in each type of pores. When temperature increases, this interaction become more and more similar due to molecular agitation. Usually, the signals gradually change from one to two peaks as the temperature increases but here the signals partially overlap because of the small difference between the two pore volumes of MOF-205 (13.5 & 17.3 Å as seen in section 4.2.1). The signal in the ^{129}Xe experiment can be observed only a few ms (< 200 ms) after the contact of the gas with the porous materials. The experiments were performed at only 2% concentration of Xe diluted in 4% N_2 and 94% He, meaning that Xe is efficiently adsorbed even at low partial pressure. We performed experiments with 1% Xe concentration and the result does not change,

confirming the above considerations. Xenon is an intermediate element in the column of the periodic table with respect to the radioactive targeted noble gases ^{85}Kr and ^{222}Rn. Thus, this experiment performed under a continuous flow of Xenon and at room temperature directly demonstrates the absorption of noble gas within MOF-205 and gives us a good demonstration of its interaction with such a gas.

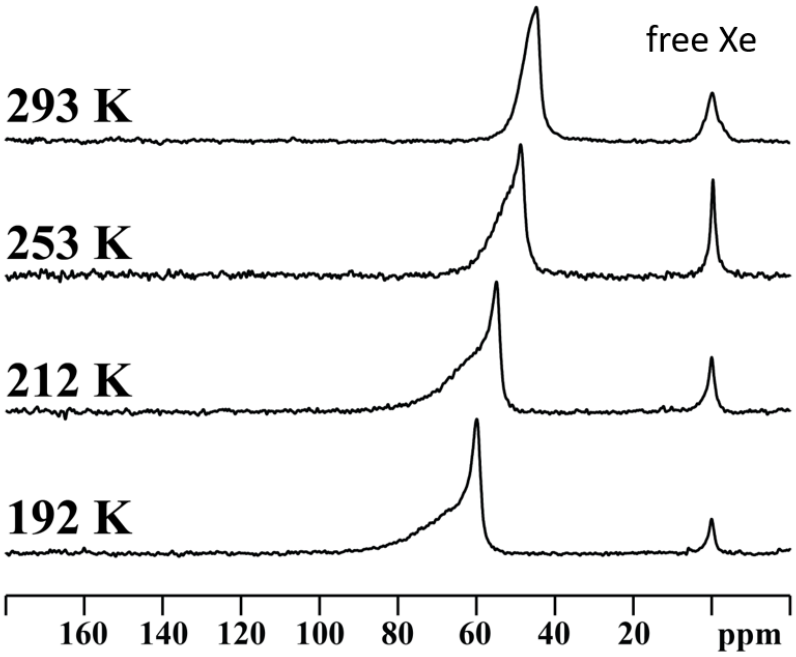

Figure III-38: Illustrating hyperpolarised ^{129}Xe NMR of MOF-205.

4.3 Photophysical characterisation

4.3.1 Excitation and Emission spectra

Figure III-39 shows the excitation and emission spectra of MOF-205. This experiment was carried out on a single crystal of MOF-205 in a capillary. We can observe a peak excitation at 330 nm. The maximum emission peak is observed at 380 nm. The emission wavelength of this MOF is in the range of maximum quantum efficiency of photon detection of the PMTs used in the gas detection experiment.

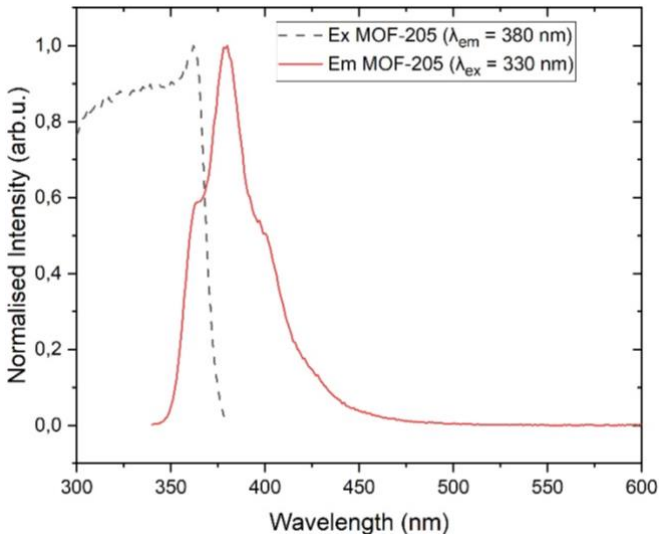

Figure III-39: Illustrating the excitation and emission spectrum of MOF-205.

Since MOF-205 is made from d^0 Zn metal, electronic transition involving the metal is least probable and should hence be centred on the ligand/s present in the structure. This trident/vibronic emission is typical of ligands in solution and might give us an indication that the emission is centred on one of the ligands present in this MOF. MOF-205 being a mixed-ligand MOF, the interpretation of the fluorescence mechanism is a bit more complex than the other MOFs we have seen so far. We can see in Figure III-40 below that the emission of MOF-205 has a very similar vibronic structure to a 10^{-5} M solution of the 2,6-NDC ligand in DMF. However, we can see that is if not fully centred on the latter but rather lies between the two ligands present in the structure. Therefore, we cannot fully disregard the effect of the BTB ligand on the photoluminescence of this MOF.

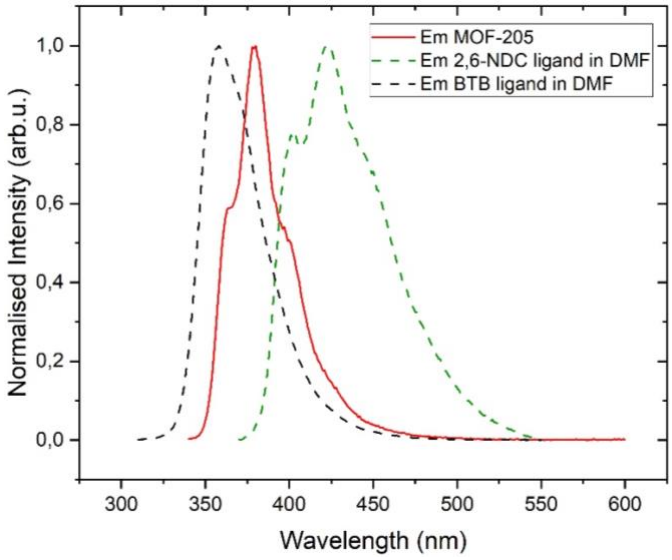

Figure III-40: Illustrating the emission spectrum of MOF-205 crystal and that of a 10^{-5} M solution of 2,6-NDC and BTB ligand in DMF.

To fully understand the fluorescence mechanism of MOF-205 one must consider the possibility of interaction between both ligands present in the structure. In Figure III-41 (Right), we can observe an overlap between the excitation spectra of the 2,6-NDC ligand with the emission of the BTB ligand (both ligands in 10^{-5} M DMF solution). Figure III-41 (Left) shows us that the opposite overlap does not occur. Therefore, we can imagine that in our MOF, the BTB ligand gets excited first and emits photons or transfers its energy to the 2,6-NDC ligand. The MOF-205 therefore undergoes the antenna effect as discussed in Chapter I. Due to the spatial arrangements of MOFs, the energy transfer is most likely non-radiative Forster resonance energy transfer (FRET). This will be investigated as part of a future endeavour by in-depth TCSPC measurements on the ligands and the MOF.

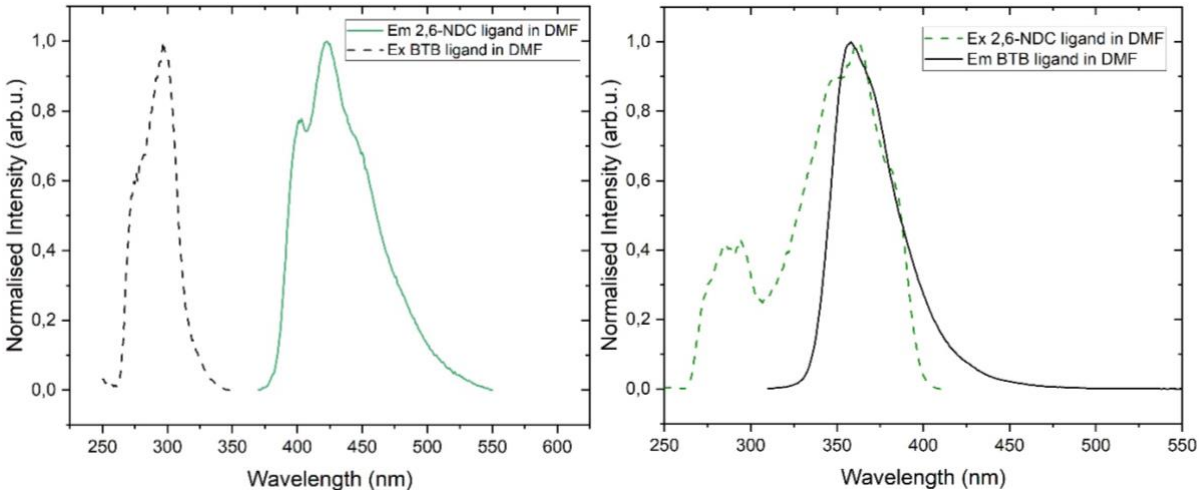

Figure III-41: Left - Ex of BTB ligand and Em of 2,6-NDC.Right - Ex of 2,6-NDC ligand and Em of BTB.

4.3.2 TCSPC

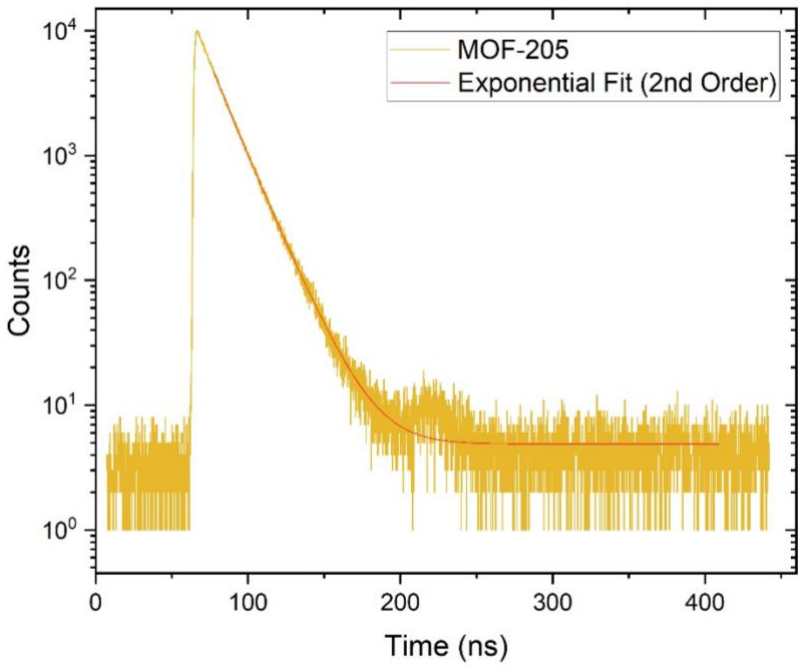

Figure III-42: Showing the TCSPC results for MOF-205.

Figure III-42 shows the fluorescence decay of MOF-205 with an excitation diode at 368 nm. By fitting this decay curve with a first order exponential fit, we are able to calculate the fluorescence lifetime of the MOF. The results are shown in Table III-8 together with the coefficient of determination (R-Square / COD) of the fit. The fluorescence lifetime of the two ligands present in this MOF were also carried out by diluting them in a 10^{-5} M DMF solution. The fluorescence lifetime of solid naphthalene is reported in literature around 80 ns[16]. As we can see in the table, incorporating the ligand in the MOF drastically reduced the fluorescence lifetime of the MOF to 14.8 ns. This faster lifetime is convenient for the detection in coincidence but still not fast enough since our low limit target was defined at 10 ns. MOF-205 also has a much slower fluorescence lifetime compared to the other undoped MOFs studied this Chapter as well as Chapter IV, most of which are around 3 ns. However, we will see that this slower fluorescence lifetime does not affect the performance of this MOF in the gas detection experiment. We can see that the fluorescence of the MOF is between that of both ligands present in it. It is important to note that the solution of ligands have not been degassed and hence the fluorescence lifetime of the 2,6-NDC ligand much be taken with a pinch of salt since its slow contribution can be difficult to evaluate without degassing.

Table III-8: Showing the calculated fluorescence lifetime of MOF-205 and its respective ligands.

MOF	Diode λ_{ex} (nm)	λ_{em}	τ_1 (ns)	τ_2 (ns)	$<\tau>$ (ns)	R-Square (COD)
MOF-205	368	380	16.9 (56.3%)	12.1 (43.7%)	14.8	0.9992
2,6-NDC	303	423	12.8 (62.4%)	8.9 (37.6%)	11.3	0.9995
BTB	274	358	20.8 (83.6%)	9.7 (16.4%)	20	0.9989

4.4 Radioactive gas bench test

4.4.1 ^{85}Kr

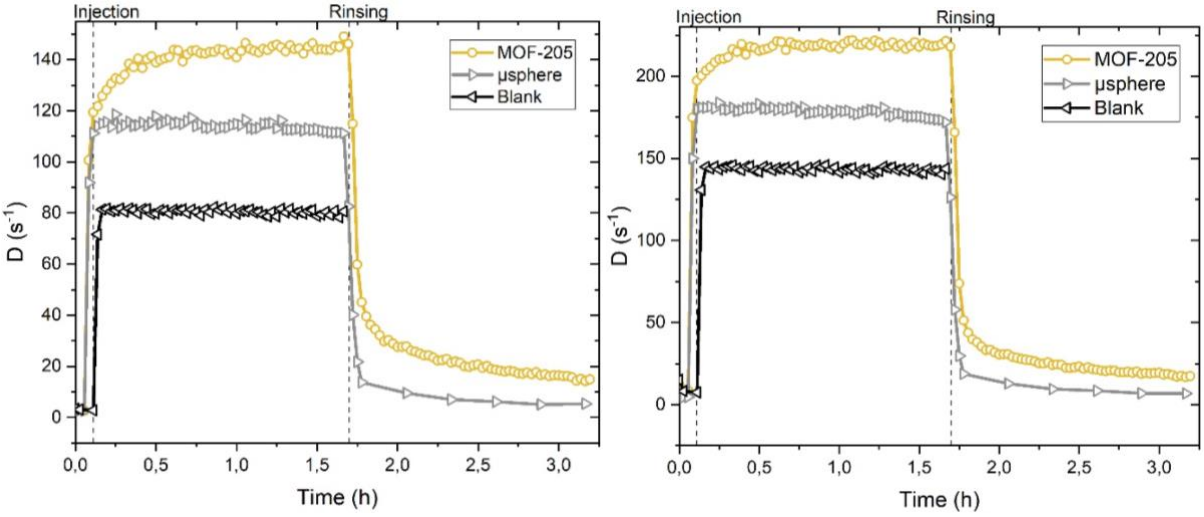

Figure III-43: Showing the results from ^{85}Kr detection with MOF-205. Left – with a coincidence window 40 ns. Right – with a coincidence window of 400 ns.

Figure III-43 shows the results from the detection of ^{85}Kr gas. We can observe in both graphs of Figure III-43 that the count rate of MOF-205 is higher than the blank experiment. This means that our MOF does indeed produce photons in the presence of ^{85}Kr and is hence a scintillator. We can also observe that the count rate of MOF-205 is higher than that of the microspheres of polystyrene (23.2% higher for the 40 ns coincidence window and 20.5% for the 400 ns coincidence window). Therefore, these experiment show that MOF-205 is an efficient scintillator for the detection of ^{85}Kr. The high porosity (the highest registered in this manuscript) and the emission on this MOF in the right wavelength range have probably been key properties to obtaining such results.

With this MOF, we can notice a slow rise in the photon count rate upon injection, i.e. the plateau is achieved after a longer time than with the other MOFs tested in this chapter. We must

therefore acknowledge the possibility that the higher photon count rate can be related to an adsorption kinetic phenomenon which boosts the number of events. This is not a disadvantage in itself. However, the time it takes to reach a stable plateau, i.e. the response time of our system, is considerably lengthened due to this adsorption kinetics phenomenon.

Since very promising results were obtained with MOF-205, we have decided to perform reproducibility tests on the same MOF-205 sample following three consecutive cycles of 10 kBq or 76 Bq·cm^{-3} of ^{85}Kr gas. The photon count rate results together with the errors are shown in Figure III-44. We can see that the photon count rate is very similar for the three cycles with the 40 ns and 400 ns coincidence window. The small fluctuations are due to small changes in the activity of the ^{85}Kr gas produced by our system as well statistical variations. The exact activities are as follows: Experiment 1 – 10380, Experiment 2 – 10220, Experiment 3 – 10620. We can also observe that at each purging stage the photon count rate returns to the same number of photons meaning that all the gas is able to leave the MOFs pores.

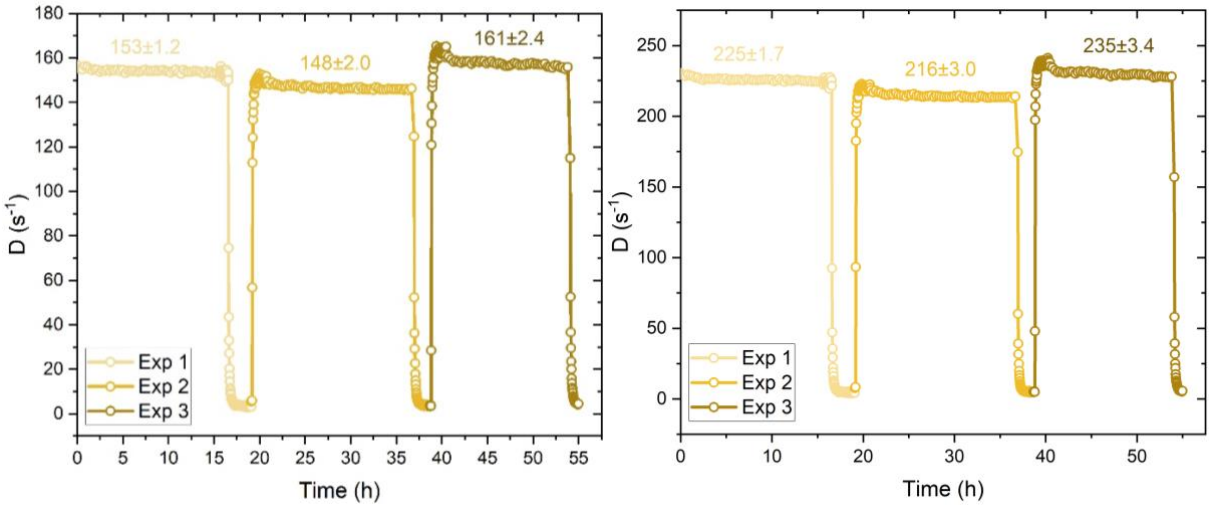

Figure III-44: Illustrating three consecutive 10 kBq ^{85}Kr detection experiments with MOF-205. Left – with a coincidence window 40 ns. Right – with a coincidence window of 400 ns.

The next step was to test the ability of the MOF-205 to detect different activities of ^{85}Kr and determine the detection limit of our configuration. We can observe in Figure III-45 (left) that increasing the activity of ^{85}Kr increases the photon count rate. By plotting the average of the plateau at each activity, we have obtained the response function of our system as plotted in Figure III-45 (Right). With this experimented range, our system gives a remarkable linearity. This experiment also shows that the MOF-205 response is not saturated at the highest tested activity. Nonlinearity is expected at higher injected activity, but 238 Bq·cm^{-3} is the upper limit of our ^{85}Kr source generation capacity. Our linear fit combined with statistical analysis[17] of our control count rate shows that our system has a decision threshold at 3.03 Bq·cm^{-3} and a limit of detection at 6.07 Bq·cm^{-3}. This will be a particular focus in the future, as it will reach a level compatible with the hardest industrial regulation (limit of detection at 1 Bq·cm^{-3}).[18]

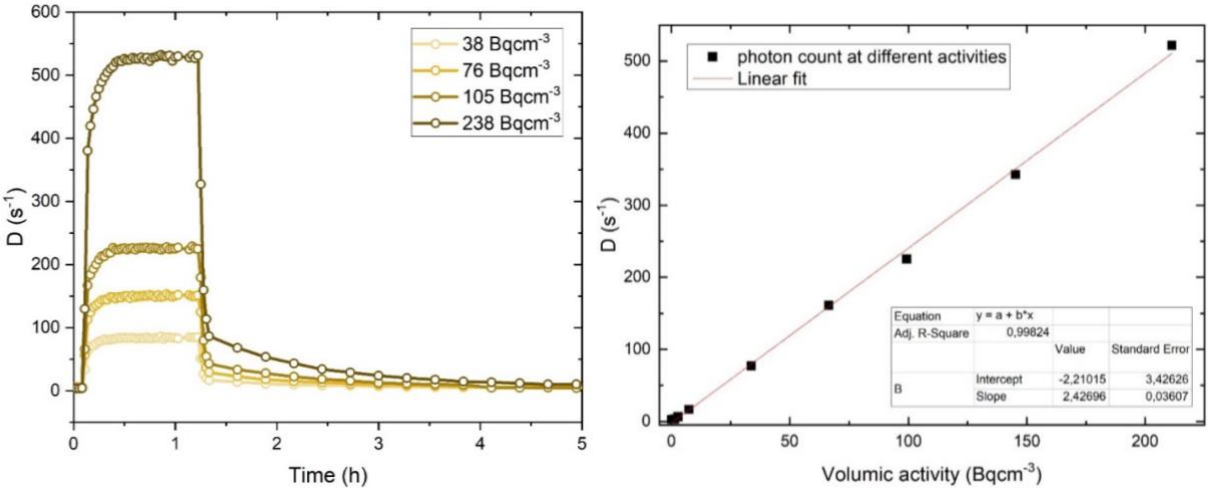

Figure III-45: Illustrating Left - the photon count rate from ^{85}Kr detection experiments with MOF-205 at different activities. Right – the photon count rate at the plateau against the volumic activity.

From Figure III-45 (left), we can also observe a decrease in the photon count rate in two steps: a steep decrease and a slow decay. One possible explanation is that MOF-205 having two distinct pore sizes, as we have seen in the N_2 adsorption experiment and ^{129}Xe NMR, will release the ^{85}Kr at two different rates. ^{85}Kr most probably leaves the bigger pores of the MOF first followed by the smaller one. The interaction at room temperature is stronger with the smaller pore than the larger one. We were not able to show this by ^{129}Xe NMR for MOF-205 since the pore sizes were too similar but we will see that this is the case for doped MOF-5 in Chapter V. This stronger interaction makes it harder for the ^{85}Kr to exit, hence the slower desorption rate.

We can also observe from the plot on the left, that the y-intercept is at -2.21. This is not something we expected and have not been able to this day to formulate a coherent hypothesis for this.

4.4.2 ^{222}Rn

MOF-205 was also used to test for the detection of ^{222}Rn. Figure III-46 shows the results of this experiment where the photon count was normalised with respect to the activity injected to account for some slight variation in the ^{85}Kr activity injected. Even though similar activities of radioactive gas were injected, the blank measurement here, i.e. without any MOF in the system, is higher than the blank for the ^{85}Kr. This is because the number of photons produced are due to two parasitic phenomena, one of them still being the Cherenkov contribution from the beta disintegration of ^{214}Pb and ^{214}Bi, two isotopes of the ^{222}Rn decay chain. The other more important contribution is from the excitation of N_2 in air by the alpha particles emitted by ^{222}Rn. As we can see the photon count rate of MOF-205 is higher than that of the blank and the microsphere showing that the MOF-205 is an efficient porous scintillator for the detection of ^{222}Rn. We can observe here a decay after the injection of the radioactive gas rather than a plateau

as observed with ^{85}Kr. This is because of the relatively short half-life of ^{222}Rn of 3.8232 days meaning the ^{222}Rn is decaying while we are performing the experiment in the closed loop.

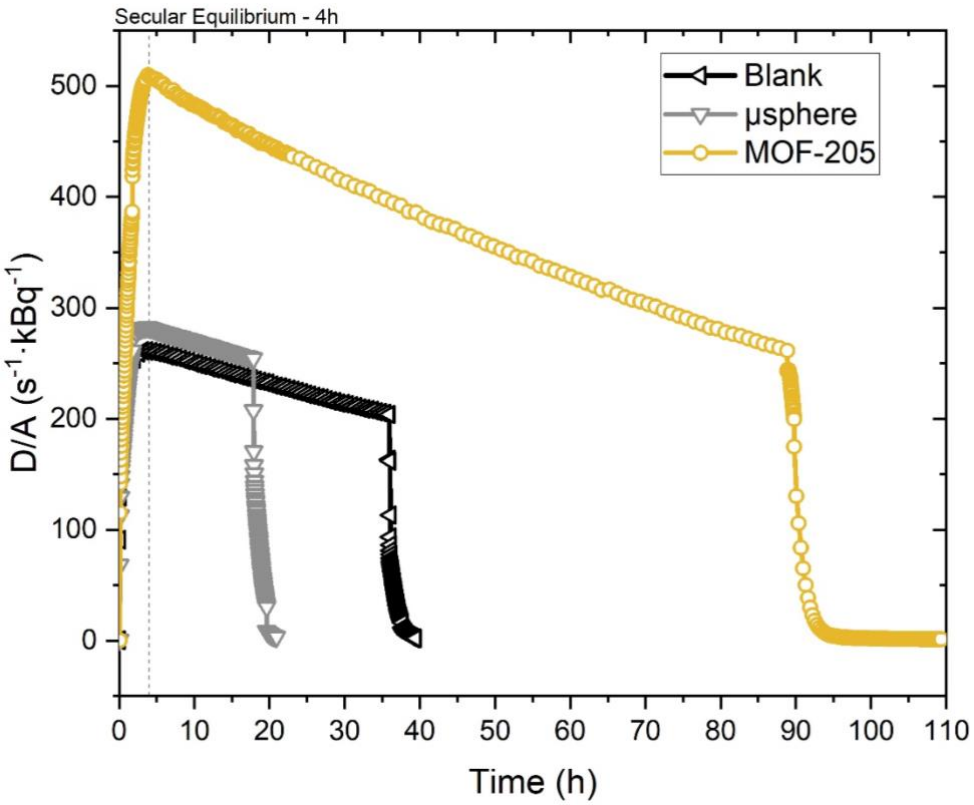

Figure III-46: Illustrating ^{222}Rn detection experiment results with MOF-205.

Performing an exponential fit of this decay will allow us to calculate the experimental half-life of ^{222}Rn as shown in Figure III-47. The fit has to be performed after the secular equilibrium of ^{222}Rn which is calculated to be 4 h as discussed in Chapter I. The half-life is calculated from the t1 value obtained from the fit (Levenberg Marquardt iteration algorithm) as presented in Figure III-47 as well as Equation III-1 followed by Equation III-2. From these calculations, we obtain an experimental half-life for ^{222}Rn of 3.7997 days which is only 0.61% difference from the theoretical half-life of ^{222}Rn. The uncertainty of the fit is calculated at 1.91% which leads to an uncertainty for the half-life of 1.44%. Even though the same equipment has been used to measure half-lives with an uncertainty of only 0.1%, for the uncertainty for a first measurement with a MOF relatively satisfactory.

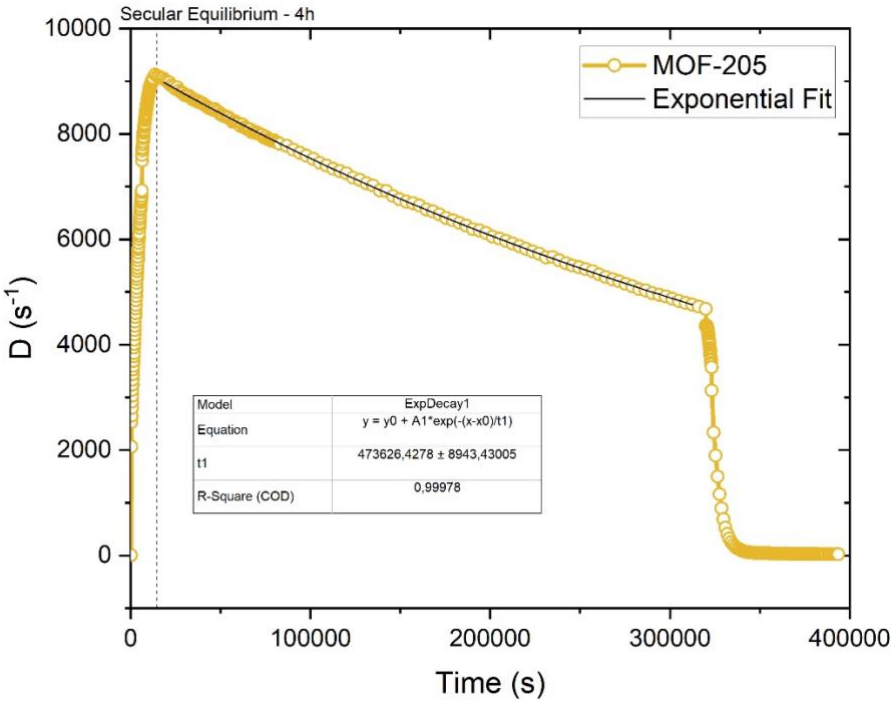

Figure III-47: Illustrating the exponential fit of ^{222}Rn detection experiment with MOF-205.

$$\lambda = \frac{1}{t1}$$

Equation III-1

$$t_{1/2} = \frac{ln\,(2)}{\lambda}$$

Equation III-2

4.4.3 ^{3}H

Since MOF-205 is the Zn-based MOF that has the highest photon count rate with ^{85}Kr detection experiment, it was also used to test for the detection of 9 kBq of ^{3}H. As mentioned in chapter II, a separate gas bench is used for Tritium detection as it is a contaminant. The MOFs used for Tritium detection are also properly discarded and not reused due to the contamination. Figure III-48 shows the results of this experiment. As seen in Chapter I, ^{3}H produced beta particles with very low energy, a maximum energy of 18.59 keV and an average of 5.7 keV, hence generating very few photons with each interaction. Its detection is therefore very challenging. However, even for low energy, the detection efficiency is not negligible as we are set to unique photon detection with the TDCR device. This is where the choice of TDCR measurements shines: we can reliably say that slight variations in the count rate are significant and not

statistical errors. As tritium is a pure, low-energy beta emitter, neither Cherenkov nor air contribution are expected. As predicted, the blank counting rate did not change upon injection of 70 $Bq \cdot cm^{-3}$ of the radioactive gas. Figure III-48 shows the experiment data for MOF-205 where the red and blue line are the averages at the stage of injection and at the stage of rinsing respectively. We can see for MOF-205 that an increase of 2.02 s^{-1} (difference between the two averages) was observed upon injection of ^{3}H. Upon purging, the count rate comes back to its initial value, showing no observable adsorption of the tritium inside the MOFs. If we compare those count rates with the activity present inside the sample cavity (0.5 cm^3) we can deduce a detection efficiency for MOF-205 of 5.8%. This value seems to be low in comparison with liquid scintillation in the same device (40 – 50% efficiency[19]) but the latter does not allow for an online measurement. However, our efficiency is relatively on par with diffusion chambers (5 – 14% efficiency).

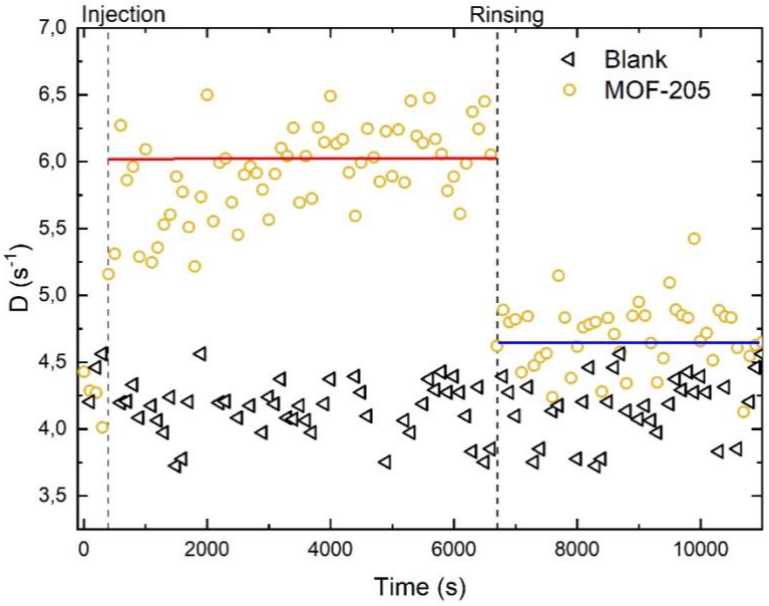

Figure III-48: Illustrating ^{3}H detection results with MOF-205.

5. Comparison and discussion

5.1 Radioluminescence experiments

The results from the radioluminescence experiments are illustrated in Figure III-49. They show the intensity of photons collected against the wavelength. Figure III-49 (Right) shows the radioluminescence result for a single crystal of anthracene.

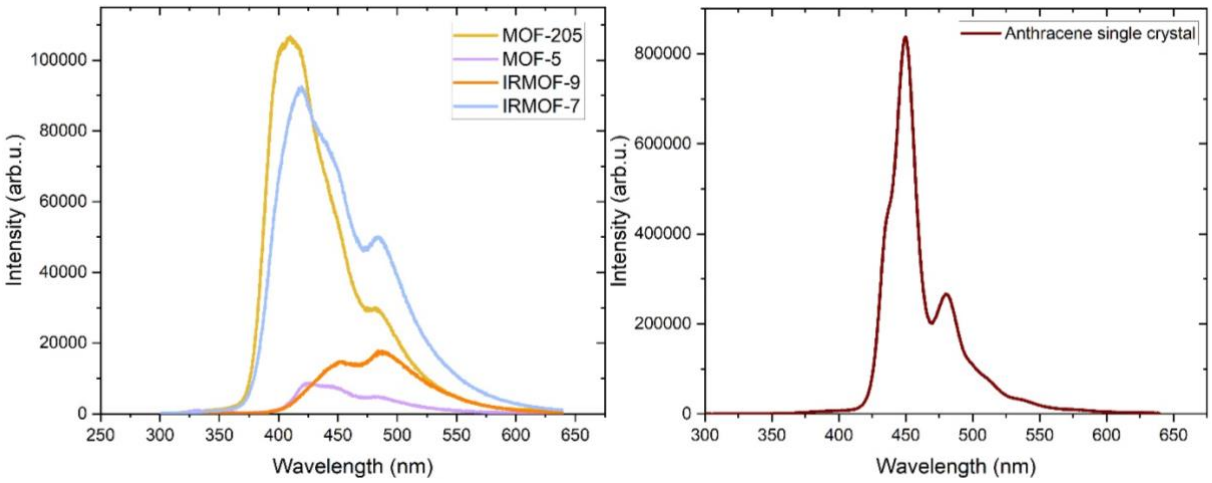

Figure III-49: Illustrating the radioluminescence experiments on Left – the four Zn-MOFs and Right - an anthracene crystal.

As explained in Chapter II, since the same volume of MOFs or anthracene was used for each experiment, the results are comparable with one another. Anthracene is a reference material in the field of scintillation and this is why we have chosen to calculate the scintillation yield of the MOFs with respect to it. Its scintillation yield is found around 15,000 Photons/MeV. It is possible to calculate the total number of photons collected for each MOF by evaluating the area under each curve. The results are shown in Figure III-50. We can firstly see that the scintillation yield of the MOFs is greater than that of their respective ligands which shows that the rigidification of the ligand in the MOF structure is of utmost importance to improve the scintillation yield. These scintillation yield results are mostly in agreement with our gas detection experiment, MOF-205 having the highest yield followed by IRMOF-9 and then MOF-5. We can also observe that IRMOF-7 has a higher radioluminescence scintillation yield that MOF-205 meaning that IRMOF-7 is a better scintillator than MOF-205. This is however surprising since IRMOF-7 was not able to detect any radioactive gas. This might be because the material we thought was IRMOF-7 was a non-porous structure as we have seen in the N_2 adsorption experiments in section 2.2.2. Even though we think the synthesis does not produce a MOF as we have explained in section 2.2, we can however see that this material has a better scintillation yield than its corresponding ligand confirming as we have seen in the FT-IR results of IRMOF-7 some coordination between the ligand and the metal.

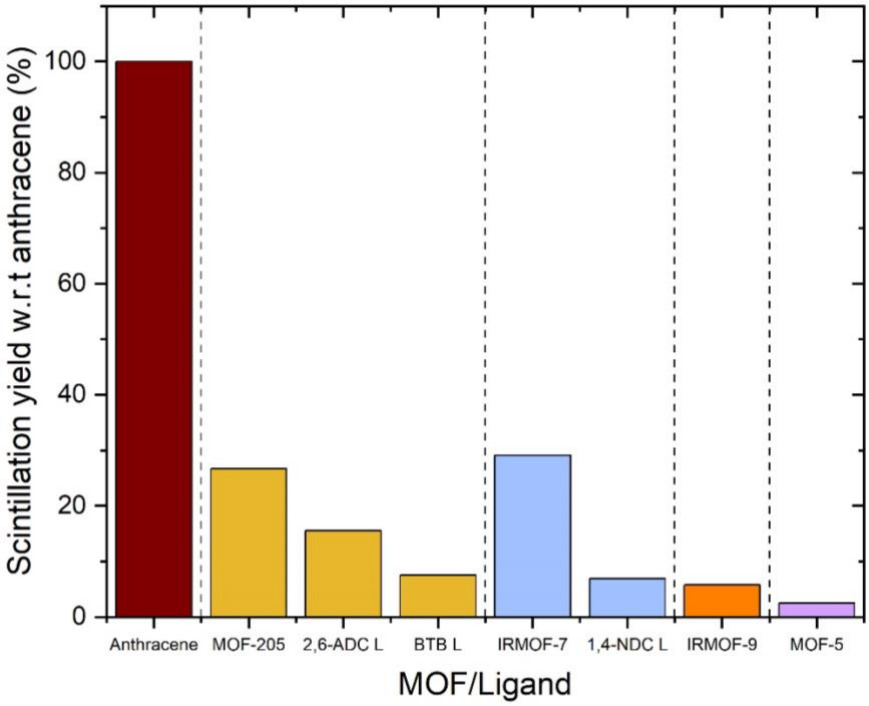

Figure III-50: Illustrating the percentage scintillation yield of each MOF and their associated ligand with respect to an anthracene crystal.

We now have the opportunity to compare the emission profiles of our MOFs with respect to a UV excitation from the photoluminescence (PL) experiments and X-ray excitation from the radioluminescence (RL) experiments. RL is essentially different from PL as it can bring about changes in the electronic and molecular structure of the material being studied. Table III-9 summarised the maximum emission wavelength observed in these two experiments. The table is arranged in order of the MOF with the highest scintillation yield to the lowest. The PL and RL wavelengths are quite similar for IRMOF-7 and MOF-205 and a bigger difference is noticeable for IRMOF-9 and MOF-5.

Table III-9: Comparing the maximum wavelength of emission of the PL experiments with the RL experiments of activated MOFs and showing the scintillation yields of each MOF calculated via radioluminescence experiments.

	PL λ_{em} (nm)	RL λ_{em} (nm)	Scintillation yield w.r.t Anthracene (%)	Scintillation Yield ($ph \cdot MeV^{-1}$)
Anthracene Single Crystal	-	450	100	15000
IRMOF-7	412	418	29	4369
MOF-205	390	408	27	4001
IRMOF-9	430	480	6	867
MOF-5	341	420	2	367

If we compare those scintillation yields (in photons per MeV) reported in Table III-9 with those found in the literature discussed in Chapter I, we would see that our IRMOF-7 and MOF-205 have a higher scintillation yield than the MOF-S1 (1350 ph·MeV^{-1}) and MOF-S2 (3300 ph·MeV^{-1}) studied by F.P. Doty *et al.*[20]. J. Perego *et al.*[21] first estimates the scintillation yield of their Zr:DPA MOF embedded in a PDMS matrix to be around 930 ph·MeV^{-1}. In a more recent study[22] they improved their scintillation yield to 5000 ph·MeV^{-1} using a mixed ligand Zr:DPA:DPT MOF as we have seen in Chapter I. A study that which reports a table of scintillation yield of several MOFs with respect to anthracene crystals is J.J. Perry IV *et al.*[23]. The best yield is shown is at 79% for DUT-6 which is considerably higher than our results and PCN-14-Zn is reported with a 39% intensity, which remains comparable to our results.

5.2 ^{85}Kr radioactive gas bench test

5.2.1 Photon count rate

Figure III-51 shows the photon count rate of all the MOFs discussed in this chapter when detecting a 10 kBq or 76 Bq·cm^{-3} of ^{85}Kr gas. The average of each plateau was calculated and subtracted from the average plateau of the blank measurement to obtain the true photon count rate produced by the MOF only. These results are summarised in Table III-10 with the best results reported in bold.

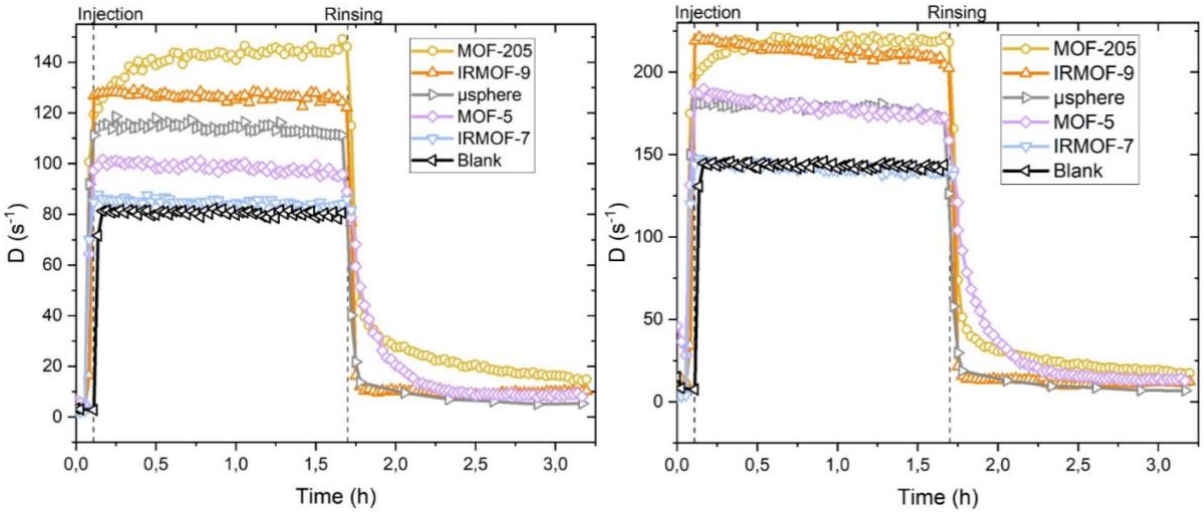

Figure III-51: Comparing the photon count rate of each MOF for the detection of 10 kBq of ^{85}Kr.

Table III-10: Showing the plateau average for each MOF and the microsphere for the 40 ns and 400 ns coincidence windows subtracted from the blank plateau.

	Effective D in cps (CW-40 ns)	**Effective D in cps (CW-400 ns)**
µspheres	34	37
MOF-5	18	35
IRMOF-7	4	0
IRMOF-9	**46**	**69**
MOF-205	**63**	**74**

Table III-10 shows that the MOF that produced the higher net photon count rate in the presence of ^{85}Kr is MOF-205. We have seen that MOF-205 was reported with the highest BET surface area and had an emission wavelength compatible with the PMTs in the experimental setup which might account for the good results evaluated here. The mixed-ligand nature of that MOF and antenna effect discussed in section 4.3.1 might also account for its relatively good performance as a scintillator for gas detection compared to the other MOFs discussed in this chapter.

We can calculate from the net photon count rate of MOF-205 the primary detection efficiency ε_D using Equation III-3 below.

$$\varepsilon_D = \frac{D}{A_V \times V}$$

Equation III-3

where D is the net photon count (MOF count – blank), A_V is the injected volumic activity and V is the volume cavity of the sample holder (values available in Table III-11). This calculation yields to an $\varepsilon_D$value of 170% for MOF-205 which is above 100% thereby providing evidence of a concentration effect of the radioactive gas within the pores of the MOF. ^{85}Kr therefore interacts with the pores of our MOF and this creates a local radioactive gas concentration higher than the injected one.

This ε_D needs to be corrected by estimating the true volume available to the gas since the MOF occupied a specific volume in the sample holder cavity. With the knowledge of the MOFs' mass, we put inside the cavity (181 mg) and the theoretical density of our MOFs being 0.3[24] we can evaluate the percentage of the occupied volume by MOF-205 at 47.6%. As MOFs are porous architectures, this volume must be further corrected by the percentage of the void present in these architectures. This correction was calculated using lattice parameters and experimental pore size, obtained by BET, to obtain a percentage of the MOF actually occupied by matter. The value is 21% for MOF-205 giving us a final volume occupied by the MOF of 9.52%. This percentage can be used to deduce the corrected volume, V_c.

The true activity of radioactive gas that interacts directly with the MOF should also be calculated. By performing MCNP-6 simulation[25] we estimated the percentage of beta that

interacts with our system. Our MOF is not very dense, therefore, there is a possibility that beta escapes and does not interact with our scintillating MOF. The simulation provides us with a 99.7% proportion of beta that interacts and deposits at least 1 keV inside the MOF. Therefore, only 0.3% of the beta from ^{85}Kr decay are not seen by our system, so the corrected volumetric activity, A_{V_c}, is comparable to the uncorrected one. Using Equation III-4 and the corrected values, we calculated a corrected detection efficiency, of 186%. This further validates our assumption of the local concentration of radioactive gases within the pores of our MOF.

$$\varepsilon_c = \frac{D}{A_{V_c} \times V_c}$$

Equation III-4

These calculations are summarised in Table III-11 below.

Table III-11: Summarising the calculations for the corrected detection efficient of 10 kBq of ^{85}Kr detection with MOF-205.

MOF	Net D (s^{-1})	A_V ($Bq \cdot cm^{-3}$)	V (cm^3)	ε_D (%)	ε_c (%)
MOF-205	63	74.6	0.5	170	186

The ε_c efficiency calculated here are not yet true efficiency measurements as several parameters such as scintillation yield, transparency of the media, or nonlinearity of the scintillator are not considered. These effects are however negligible in the case of ^{85}Kr because of its relatively high beta spectrum, hence are not explored here.

5.2.2 T/D indicator

Another indicator of the performance of a MOF as a scintillator is the T/D value that can be obtained from the gas detection experiment. As discussed in Chapter II, the T/D value is an indication of the scintillation yield and its value approaches 1 for a perfect scintillator. However, the interpretation of the T/D value for our system is complexified by the parasite Cherenkov phenomena. Let us look at the first graph exposed in Figure III-52. The T/D value before injection is about 0.32. When we inject the radioactive gas in the system, the gas fills the scintillation vial and is also absorbed by the MOF. At this point we have a scintillation contribution from both the Cherenkov and the MOF. This plateau at about 0.22 therefore does not give us the true scintillation yield of our MOF. Cherenkov phenomenon being anisotropic will contribute towards more double coincidences (D) than triple coincidences (T) leaving a relatively T/D ratio. If we now consider the T/D value just at the point of rinsing out the radioactive gas from the system (encircled in the figure), we get an indicator of the true

scintillation yield of the MOF (without the Cherenkov contribution). This is because at the moment of rinsing the system using dry air, the radioactive gas is first instantly extracted from the scintillating vial alone. This only leaves us with the radioactive gas absorbed in the pores of the MOF, to contribute to the photon count rate. Since our MOFs emit photons isotropically, the T value increases and D decreases which leaves us with a true T/D value of 0.62.

Figure III-52 shows the T/D value of both coincidence windows of IRMOF-9, MOF-205 and the microspheres (top to bottom graphs). We can observe the highest T/D value encircled is that of MOF-205 followed by IRMOF-9, proving that MOF-205 is our best performing scintillator once again. The T/D values of the MOFs are much closer to 1 than the microspheres of polystyrene thereby concluding that our MOF are better scintillators for ^{85}Kr detection that them, especially MOF-205 with a T/D value of 0.71 for the 40 ns coincidence window. These comparisons are however to be taken with a pinch of salt since the geometrical effect of the crystals are not taken in account.

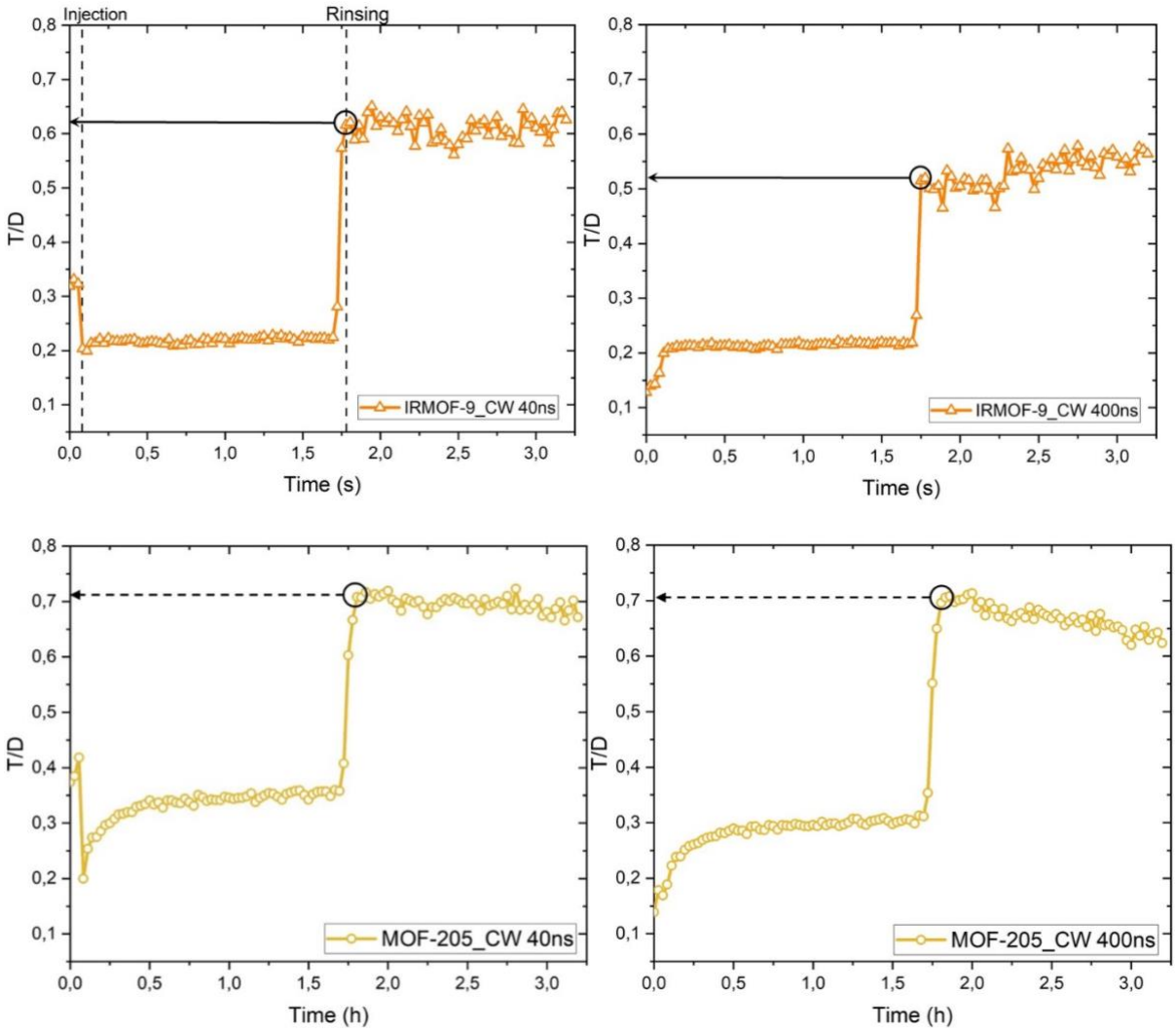

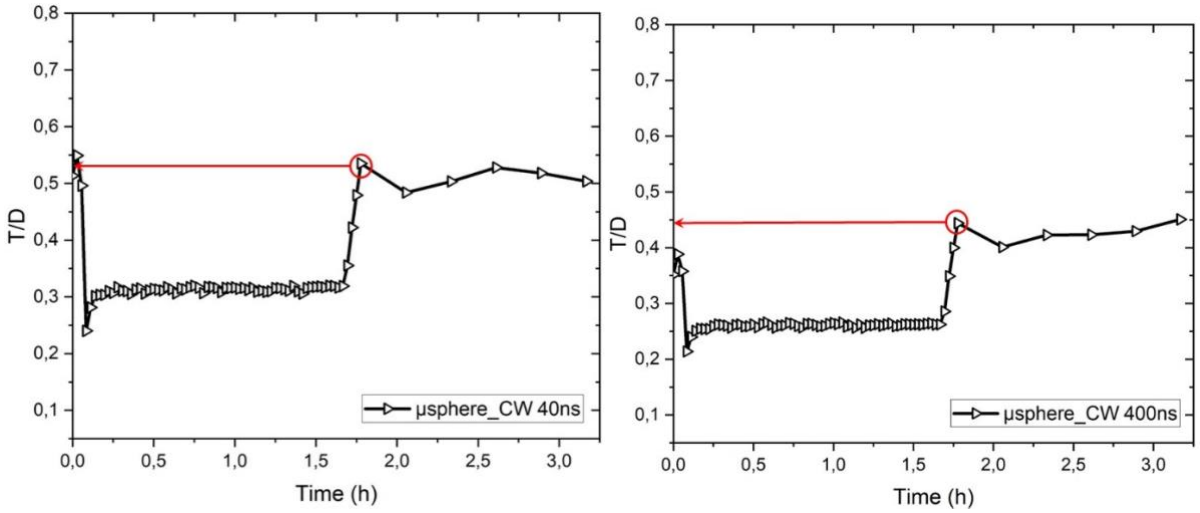

Figure III-52: Illustrating the T/D evolution of ^{85}Kr detection for IRMOF-9, MOF-205 and microspheres.

6. Chapter Conclusion

In this chapter we demonstrated the synthesis of MOF-5, IRMOF-9 and MOF-205 millimetric single crystals. We have proven by structural characterisation that they were indeed the targeted MOFs. Unfortunately, the same was not concluded for IRMOF-7 which showed very poor similarities in the structural characterisation compared to literature. We fully characterise MOF-205 using ^{13}C and ^{1}H NMR as well as scrutinise its interaction with Xe using ^{129}Xe NMR. We have validated that the emission of MOF-5 and IRMOF-9 were centred on their respective ligands and provided evidence of an antenna effect in our mixed ligand MOF-205. We managed to indicate that IRMOF-9 and MOF-205 were efficient scintillators for the detection of ^{85}Kr, MOF-205 showing the most promising results.

We demonstrated via mathematical calculations and simulation a preconcentration effect in MOF-205 for ^{85}Kr detection as hypothesised. We have shown that the detection of 10 kBq of ^{85}Kr with MOF-205 was reproducible with three consecutive cycles. We have also obtained the linear response function of our system by varying the injected activity of ^{85}Kr using the same sample of MOF-205. From these results, we determined that our system has a decision threshold at 3.03 Bq·cm^{-3} and a limit of detection at 6.07 Bq cm^{-3}.

We were also able to show that the detection of ^{222}Rn and ^{3}H were possible with MOF-205. MOF-205 was also used to calculate for the first time the experimental half-life of ^{222}Rn with a good respect to the theoretical value.

These results validate our approach towards the detection of radioactive gas with porous scintillators. Since we must still try to lower our limit of detection, as we are just an order of magnitude away to be compliant with industrial and European policy[18], MOF which can have a better scintillation yield also need to be further explored. The photon count rate obtained by

the detection of ^{3}H is also quite low and needs to be improved for a better efficiency of detection. We will see in Chapter V how we are able to increase the scintillation yield of existing MOFs using a doping strategy.

The Zn-based MOF discussed here are sensitive to humidity as discussed in Chapter I. They can therefore not be used in the long run in a device as their structure and hence scintillating properties will be degraded by the atmospheric moisture. Therefore, we will explore in the next chapter (Chapter IV) Zr-based MOFs which have shown to be much more resilient towards moisture.

REFERENCES

1. Villemot, V. Détection de tritium en ligne par cristaux nanoporeux, L'université Paris-Saclay, (2021).
2. Eddaoudi, M. *et al.* Systematic design of pore size and functionality in isoreticular MOFs and their application in methane storage. *Science (1979)* **295**, 469–472 (2002).
3. Villemot, V., Hamel, M., Pansu, R. B., Leray, I. & Bertrand, G. H. V. Unravelling the true MOF-5 luminescence. *RSC Adv* **10**, 18418–18422 (2020).
4. Yaghi, O. M., Li, G. & Li, H. Selective binding and removal of guests in a microporous metal–organic framework. *Nature* **378**, 703–706 (1995).
5. Gangu, K. K., Maddila, S. & Jonnalagadda, S. B. The pioneering role of metal-organic framework-5 in ever-growing contemporary applications - a review. *RSC Adv* **12**, 14282–14298 (2022).
6. Healy, C. *et al.* The thermal stability of metal-organic frameworks. *Coord Chem Rev* **419**, 213388 (2020).
7. Wang, S. *et al.* Study on the structure activity relationship of the crystal MOF-5 synthesis, thermal stability and N2adsorption property. *High Temperature Materials and Processes* **39**, 171–177 (2020).
8. Dutsov, C., Cassette, P., Sabot, B. & Mitev, K. Evaluation of the accidental coincidence counting rates in TDCR counting. *Nucl Instrum Methods Phys Res A* **977**, 164292 (2020).
9. Taniguchi, M. & Lindsey, J. S. Database of Absorption and Fluorescence Spectra of >300 Common Compounds for use in PhotochemCAD. *Photochem Photobiol* **94**, 290–327 (2018).
10. Liu, Z. What is Cherenkov Radiation? *International Atomic Energy Agency* https://www.iaea.org/newscenter/news/what-is-cherenkov-radiation (2022).
11. Hamel, M., Soumaré, M., Burešová, H. & Bertrand, G. H. V. Tuning the decay time of plastic scintillators. *Dyes and Pigments* **165**, 112–116 (2019).
12. Crom, A. B. *et al.* Deinterpenetration of IRMOF-9. *Chemistry – A European Journal* (2023) doi:10.1002/chem.202302856.
13. Babarao, R. *et al.* Does functionalisation enhance CO2 uptake in interpenetrated MOFs? An examination of the IRMOF-9 series. *Chemical Communications* **50**, 3238–3241 (2014).
14. Furukawa, H. *et al.* Ultrahigh porosity in metal-organic frameworks. *Science (1979)* **329**, 424–428 (2010).

15. Babu, R., Roshan, R., Kathalikkattil, A. C., Kim, D. W. & Park, D. W. Rapid, Microwave-Assisted Synthesis of Cubic, Three-Dimensional, Highly Porous MOF-205 for Room Temperature CO2 Fixation via Cyclic Carbonate Synthesis. *ACS Appl Mater Interfaces* **8**, 33723–33731 (2016).

16. Yamamoto, K., Nakao, T., Yonemochi, E. & Oguchi, T. Time resolved fluorescent analysis for sealed heating of Dimethyl-β-Cyclodextron and Naphthalene System. *Journal of inclusion phenomena and molecular recognition in chemistry* **25**, 121–124 (1996).

17. Vivier, A., Fottorino, R. & Rousse, B. Seuil de décision et limite de détection: estimation, interprétation et optimisation. 1re partie: les principes de base. *Radioprotection* **45**, 321–343 (2010).

18. European Commision. Commission Recommendation of 18 December 2003 on standardised information on radioactive airborne and liquid discharges into the environment from nuclear power reactors and reprocessing plants in normal operation (2004/2/Euratom). *Official Journal of the European Union* 1–36 (2004).

19. Chapon, A., Pigrée, G., Putmans, V. & Rogel, G. Optimization of liquid scintillation measurements applied to smears and aqueous samples collected in industrial environments. *Results Phys* **6**, 50–58 (2016).

20. Doty, F. P., Bauer, C. A., Skulan, A. J., Grant, P. G. & Allendorf, M. D. Scintillating metal-organic frameworks: A new class of radiation detection materials. *Advanced Materials* **21**, 95–101 (2009).

21. Perego, J. *et al.* Composite fast scintillators based on high-Z fluorescent metal–organic framework nanocrystals. *Nat Photonics* **15**, 393–400 (2021).

22. Perego, J. *et al.* Highly luminescent scintillating hetero-ligand MOF nanocrystals with engineered Stokes shift for photonic applications. *Nat Commun* **13**, 1–10 (2022).

23. Perry Iv, J. J. *et al.* Connecting structure with function in metal-organic frameworks to design novel photo- and radioluminescent materials. *J Mater Chem* **22**, 10235–10248 (2012).

24. Sim, J. *et al.* Gas adsorption properties of highly porous metal–organic frameworks containing functionalized naphthalene dicarboxylate linkers. *Journal of the Chemical Society. Dalton Transactions* **43**, 18017–18024 (2014).

25. Mauree, S. *et al.* Detection of Radioactive Gas with Scintillating MOFs. *Adv Funct Mater* (2023).

Chapter IV: Developing Zr-based MOFs for radioactive gas detection

IV. Developing Zr-based MOFs for radioactive gas detection

In this Chapter, we will present four Zr-based MOFs, which are more resistant to moisture. This feature is essential for a potential application in conventional atmospheres, hence, Zr-based MOFs can be better suited to our application than the Zn-based MOFs studied in the previous chapter. Similar ligands to those used in Zn-based MOFs will be explored here. This will allow us to compare the fluorescence and scintillating properties of a MOF with the same ligand but different metal centres with empty (Zn^{2+}) and full (Zr^{2+}) d-orbitals. As discussed in Chapter I, the MOFs explored in this chapter have two different names, namely UIO (University of Oslo) and CAU (Christian-Albrechts-Universität), from the universities where they were discovered. We have also seen in Chapter I (section 4.3) that the synthesis of Zr-based MOFs is somewhat complex, and precipitation tends to occur over crystallisation. In the past, colleagues at our laboratory tried synthesising Zr-based MOFs using the modulated synthesis approach. However, the concentration of modulator used in those synthesis protocols (0.5 molar equivalent of modulator with respect to the zirconium salt [1]) was not enough to drive forward the competing reaction between the modulator molecule and the ligand in the MOF. They, therefore, did not manage to successfully synthesise Zr-based MOFs, as was shown by the lack of crystallinity in their XRD results. These results were in completely agreement with what we discussed in Chapter I on the broad peak XRD results obtained by Schaate *et al.* [2,3]. We derived from these articles new modulated synthesis protocols for each MOF in this chapter. Except for UIO-67, crystalline powders were obtained for these MOFs. Even though we managed to go from nanometric to micrometric MOFs crystals size by adjusting the concentration of modulator used during the synthesis, our attempts to obtain millimetric single crystals for Zr-based MOFs remain unsuccessful.

The structural characterisation will help us determine if we have indeed synthesised the respective MOF and its physical properties. For the photophysical characterisation, we will mainly determine if our MOF emits in the correct wavelength range for the PMTs used in the gas detection experiments. The fluorescence lifetime of our MOF will also be determined. The faster the fluorescence lifetime of our MOF, the fastest the coincidence window in the TDCR gas detection experiment, hence a cleaner signal to noise ratio. We will also analyse the results from the gas detection experiments individually for every MOF and compare them with one another in the last section of this chapter. ^{85}Kr detection experiments have been performed on each MOF in this chapter, and the one with the best results was also used to carry out ^{3}H and ^{222}Rn detection experiments as done with MOF-205 in Chapter III. The results for the radioluminescence experiments will also be studied and compared in the last section of this chapter.

1. UiO-66

1.1 Structure, synthesis and SEM image

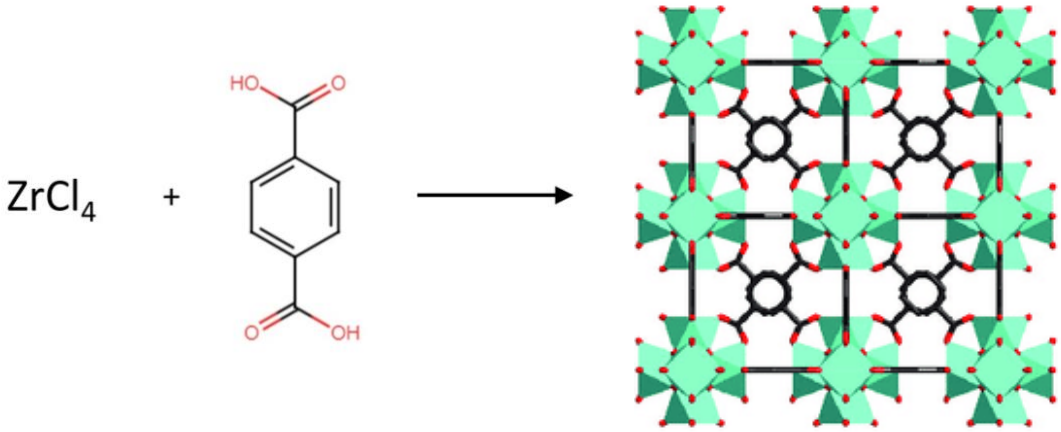

Figure IV-1: Precursors and structure of UIO-66.

UIO-66 consists of cuboctahedral zirconium oxide nodes, allowing a connection with up to twelve linear 1,4-benzene dicarboxylic acid ligands leading to a 3D fcu porous network with an Fm(-3)m space group[4] as shown in Figure IV-1. The protocol listed below is the optimised synthesis conditions derived from Schaate *et al.*[2] to obtain a crystalline powder of UIO-66. By adding a modulator, as explained in Chapter I, we tried to synthesise a crystalline product with the biggest possible crystal size. The aim was to achieve millimetric-size crystals, which proved more complex than Zn-based MOFs. We started with 1 and 2 molar equivalent of benzoic acid with respect to the $ZrCl_4$ which both yielded non crystalline powders since we did not observe any diffraction peaks in the XRD experiments. Upon the synthesis with 3 molar equivalents of BA with respect to the Zr (which is the protocol listed below), we managed to synthesise a crystalline powder of UIO-66. We were unable to reproduce the production of bigger crystals from Schaate *et al.*[2] since we lost the crystallinity of the MOF when increasing the molar equivalent to 5 and 10. The loss of crystallinity with too much modulator has been demonstrated by Butova et al.[5] and will be discussed for UIO-1,4-NDC below since the latter was MOF in this study.

$ZrCl_4$ (0.017 mol·L^{-1}, 0.396 g), 1,4-benzenedicarboxylic acid (0.017 mol·L^{-1}, 0.282 g) and benzoic acid modulator (0.0514 mol·L^{-1}, 0.628 g) were dissolved in 100 mL of *N*,*N*-dimethylformamide (DMF). The mixture was equally divided into twelve 10 mL scintillation vials, which were then sealed with a screw cap. The vials were placed in an oven at 120°C for 24 h, yielding a crystalline powder of UIO-66. The closed vials were removed and left to cool. The powder was washed using the centrifuge according to the protocol described in Chapter II.

Figure IV-2 below shows the SEM image of UIO-66 crystalline powder. Compared to the SEM images of the other MOFs in this chapter, a clear crystalline shape cannot be distinguished here.

We can also notice the aggregation of the particles. The particle sizes observed are of the order of 100 nm, which are the smallest observed in this chapter. The measurements of two particle sizes are also shown in Figure IV-2.

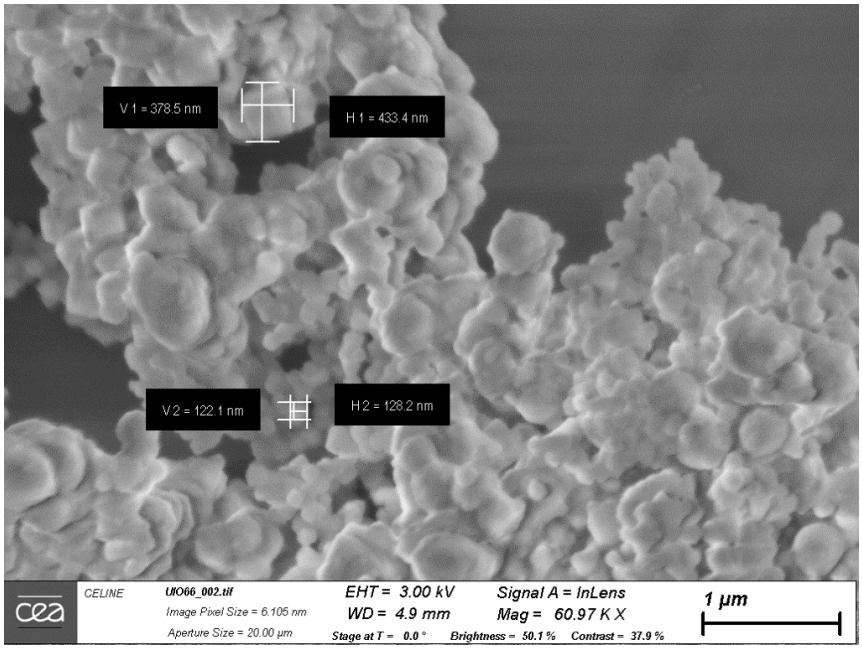

Figure IV-2: Shows the SEM image of UIO-66 crystalline powder.

1.2 Structural characterisation

1.2.1 X-Ray Diffraction

Figure IV-3 shows the X-ray Diffraction spectrum of our UIO-66 compared to the simulated XRD from the literature[2]. The peak positions are similar in both data sets, showing that we have indeed synthesised UIO-66 crystalline powder. With these new proportions of modulator compared our previous concentration (0.5 molar equivalent of modulator with respect to Zr), we managed to go from a non-crystalline product to a crystalline powder of UIO-66.

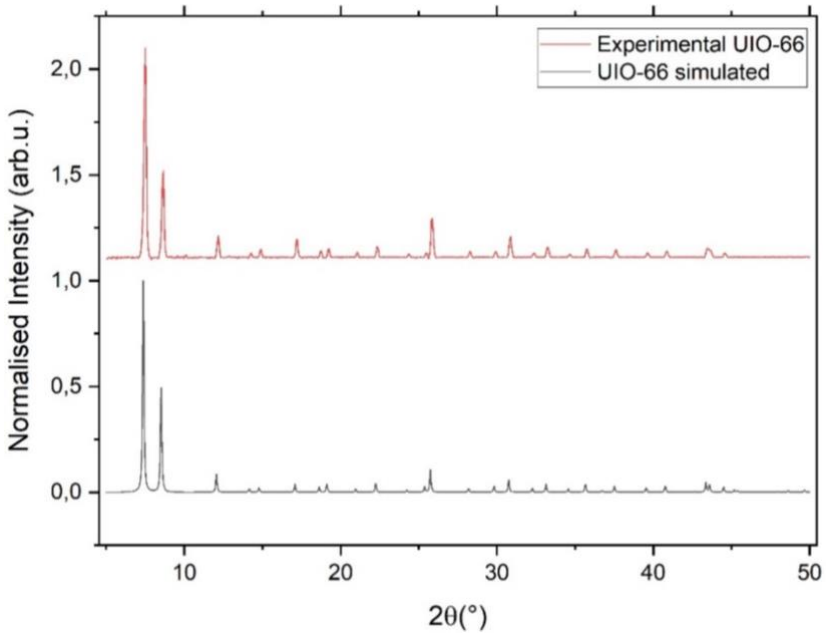

Figure IV-3: PXRD spectrum of UIO-66 showing experimental results compared to literature.

1.2.2 Adsorption measurements

The N_2 adsorption experiments for UIO-66 were carried out at the NIMBE laboratory in CEA. The Type II N_2 adsorption isotherm is shown in Figure IV-4 and hence indicates that UIO-66 exhibits microporosity. By plotting the graph in Figure IV-5 and using the equations developed in Chapter II, section 2.2, we can extract the BET surface area, the pore sizes and pore volume of our MOF are summarised in Table IV-1. The BET surface area for this MOF is lower than that of the MOFs we studied in Chapter I. However, we must keep in mind that the experiments were not all done with the same setup, and the comparison must be done with a pinch of salt. Even though values close to the one we have for our UIO-66 (860 $m^2 \cdot g^{-1}$) have been mainly reported before[6,7], higher surface areas around 1000-1200 $m^2 \cdot g^{-1}$ have also been reported in literature[8,9].

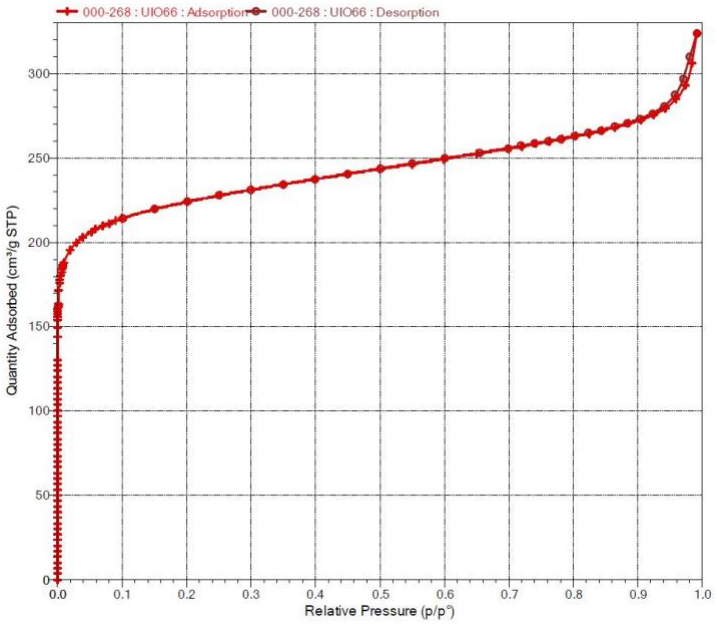

Figure IV-4: Illustrating the N_2 adsorption isotherm of UIO-66.

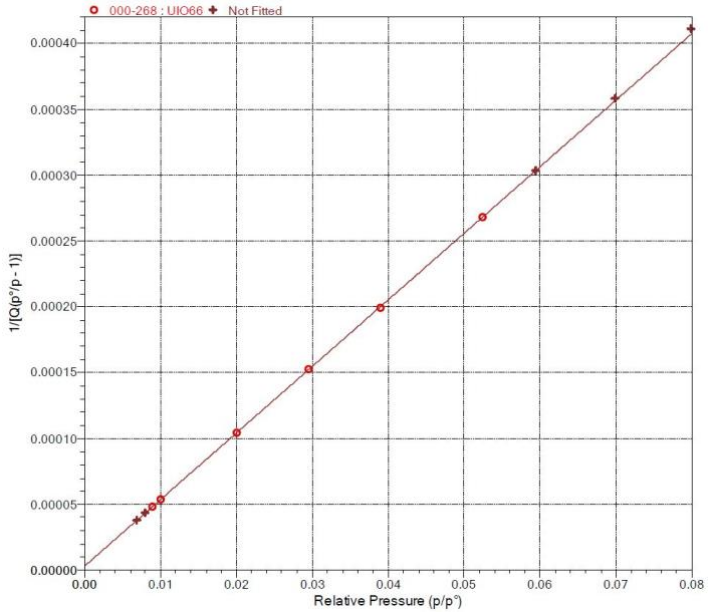

Figure IV-5: BET surface area plot of UIO-66.

Table IV-1: Showing the data calculated from N_2 adsorption of UIO-66.

MOF	BET SA ($m^2 \cdot g^{-1}$)	Pore size (Å)	Pore volume ($cm^3 \cdot g^{-1}$)
UIO-66	860	7.3 & 6	0.5

1.2.3 Thermogravimetric Analysis

Figure IV-6 shows the TGA results of UIO-66. Similar to the MOFs in Chapter III, we can observe a drop before 100°C accounting for surface water and residual DCM loss. A significant drop in the weight of the sample between 350-500°C is also observed, similar to the Zn-based MOFs. This result is consistent with the literature where the decomposition temperature (T_d) is reported to be between 400-500°C depending on the sample preparation, activation and experimental conditions[10]. The MOF decomposes to zirconia at these temperatures.

However, compared to the Zn-based MOFs we have studied in Chapter III, we don't only observe this drop but can see different steps in weight loss for UIO-66 from Figure IV-6.

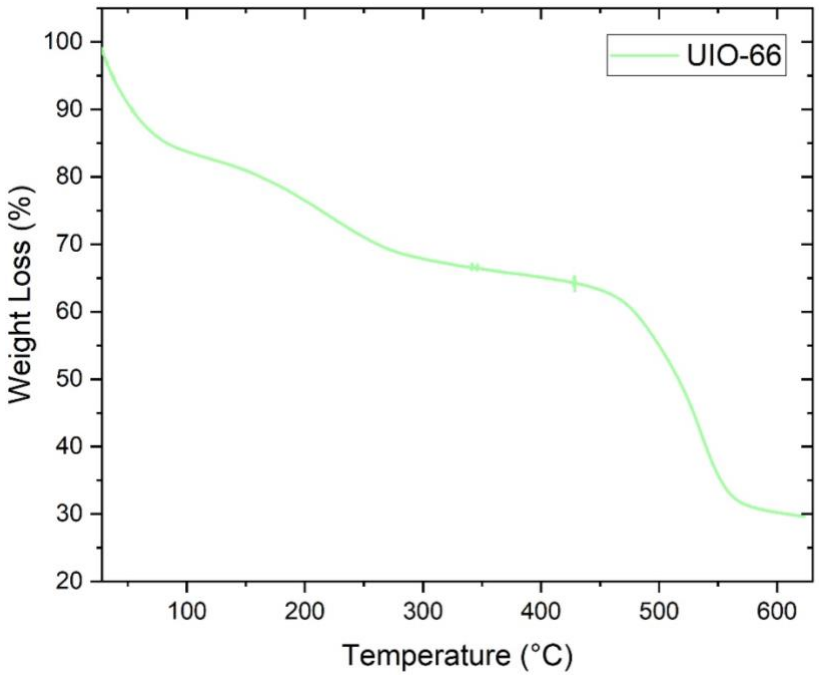

Figure IV-6: TGA results of UIO-66.

The important loss in weight between 100°C and 300°C has been reported in literature for Zr-MOFs, and the weight loss was explained as follows[7,11]. An interesting chemical feature exhibited by Zr-based MOFs is the ability of the $Zr_6O_4(OH)_4$ inorganic cluster to undergo reversible dehydroxylation. The dehydroxylation occurs between 200–300°C, where the cluster loses two equivalents of water, resulting in an inorganic cluster composition of Zr_6O_6. The dehydroxylation reaction explained by Shearer *et al.* is shown schematically in Figure IV-7[12]. Shearer et al. also used FT-IR to explain this dehydroxylation process, as we will see in section 1.2.4 below. It is striking that after the process, the overall structure of the material is almost wholly preserved, despite the fact that the zirconium cations reduce their coordination number

from 8 (square antiprismatic) to 7 during the process, as demonstrated by Extended X-ray Absorption Fine Structure (EXAFS) measurements[13].

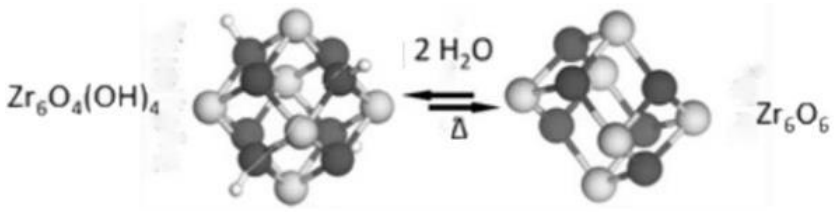

Figure IV-7: Illustration from Shearer et al. explaining dehydroxylation[12].

1.2.4 FT-IR experiments

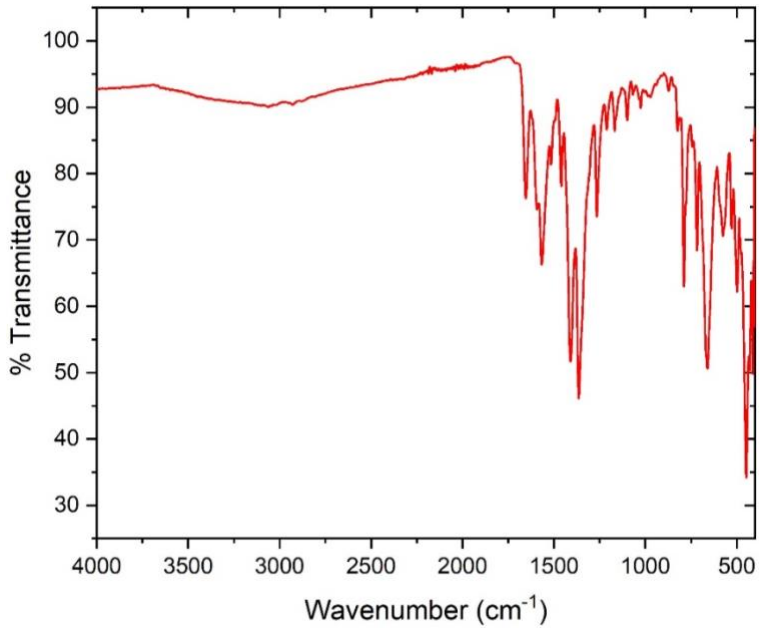

Figure IV-8: FT-IR spectrum of UIO-66.

Figure IV-8 shows the FT-IR spectrum of UIO-66. The sample presents two strong peaks centered at 1572 cm^{-1} and 1386 cm^{-1}, related to the asymmetric and symmetric stretching vibrations of the carboxylate groups, respectively coordinated to the Zr cations of the inorganic node. Furthermore, the peak at 748 cm^{-1} is consistent with the symmetric vibration peak of O-Zr-O and the asymmetric vibration peak of O-Zr-O at 668 cm^{-1}. These observations are consistent with literature[14]. A peak between 3500-3200 cm^{-1} is attributed in literature as the stretching vibration of O-H. This band has a slightly higher intensity than the Zn-based MOFs in Chapter III. The possible explanation is that our Zr-based MOFs were not washed in a glove box as a centrifuge was needed to wash them due to their powdered nature, hence allowing atmospheric moisture to build up on or in the MOF.

1.3 Photophysical characterisation

1.3.1 Excitation and Emission spectra

Figure IV-9 shows the excitation and emission spectra of UIO-66. This experiment was carried out on a powdered UIO-66 sample on a quartz plate. We can observe a peak excitation at 320 nm. The maximum emission peak is observed at 365 nm. It is important to note that the maximum emission wavelength of this MOF is not ideal for our gas detection experiment since it does not emit in the range of maximum quantum efficiency of photon detection of the PMTs used.

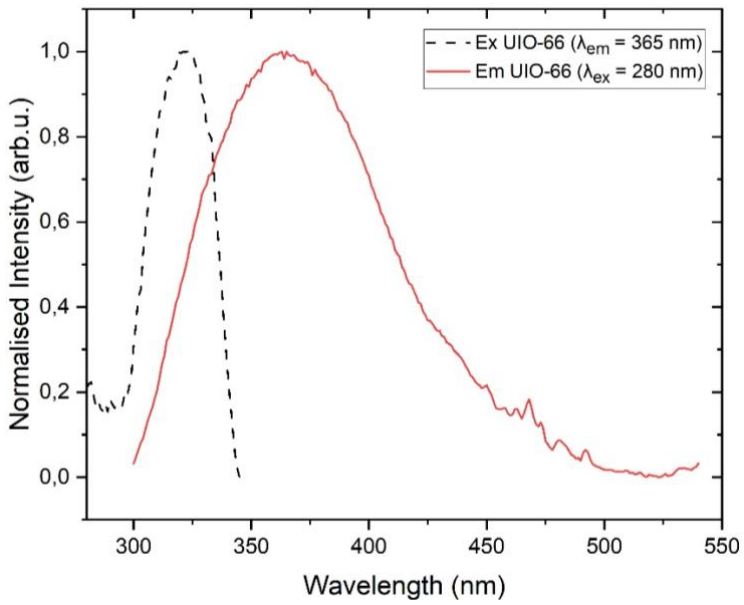

Figure IV-9: Illustrating the excitation and emission spectrum of UIO-66.

1.3.2 TCSPC

Figure IV-10 shows the fluorescence decay of UIO-66 with an excitation diode at 309 nm. By fitting this decay curve with a third-order exponential fit, we can calculate the three fluorescence lifetime components, their respective weights, and an average fluorescence lifetime. The results are shown in Table IV-2 with the coefficient of determination (R-Square / COD) of the fit.

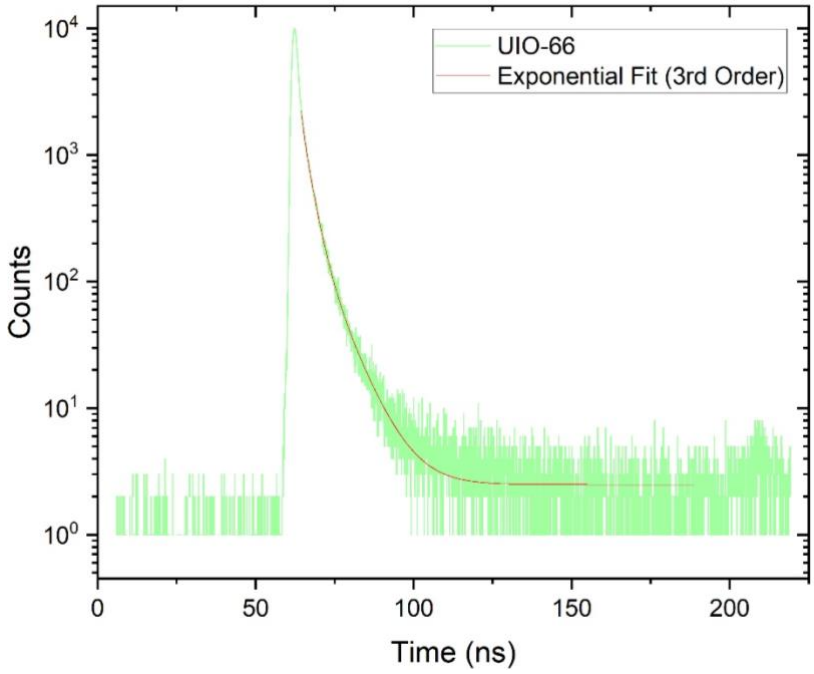

Figure IV-10: Showing the TCSPC results for UIO-66.

Table IV-2: Showing the calculated fluorescence lifetime of UIO-66.

MOF	Diode λ_{ex} (nm)	λ_{em} (nm)	τ_1 (ns)	τ_2 (ns)	T_3 (ns)	$<\tau>$ (ns)	R-Square (COD)
UIO-66	309	365	2.7 (67.8%)	0.7 (19.8%)	7.2 (12.4%)	2.9	0.9988

The fluorescence lifetime is on par with the 3 ns or less that is ideal for detection in coincidence.

1.4 Radioactive gas bench test

1.4.1 ^{85}Kr

Figure IV-11 shows the results from detecting ^{85}Kr gas with UIO-66. For ease of interpretation and comparison with previous experiments, only the results with the 40 ns coincidence window are shown here. We can observe that the count rate of UIO-66 is higher than the blank experiment. This means that our MOF does indeed produce photons in the presence of ^{85}Kr and is, hence, a scintillator. However, we can also observe that the count rate of UIO-66 is lower than that of the microspheres of polystyrene. Therefore, this experiment shows that UIO-66 is considered as a scintillator for the detection of ^{85}Kr but not a very efficient one compared to the microspheres of polystyrene material. This was expected due to the MOF linker containing only one benzene ring; therefore, not many delocalised electrons are involved in the

excitation/emission mechanism. The fluorescence yield of the BDC ligand is also reported to be very low, around 0.05[15]. As for MOF-5, this imply a low fluorescence quantum yields, and a very energetic transition (< 300 nm).Hence the emission wavelength is also not in the convenient range for this experiment.

Let us compare the ^{85}Kr detection of UIO-66 with its Zn-based equivalent (same ligand, different metal centres), i.e. MOF-5. We see from Chapter III, that for the same activity MOF-5 emits slightly more photons (99 s^{-1}) than UIO-66 (91 s^{-1}). Since the scintillation is centred on the ligand for both MOFs, we can attribute the slightly better performance of MOF-5 to its large crystal size, which allows for the diffusion of gas in the medium better than the powdered form of UIO-66. We will see in Chapter V how we can improve the scintillation of UIO-66 via a doping strategy.

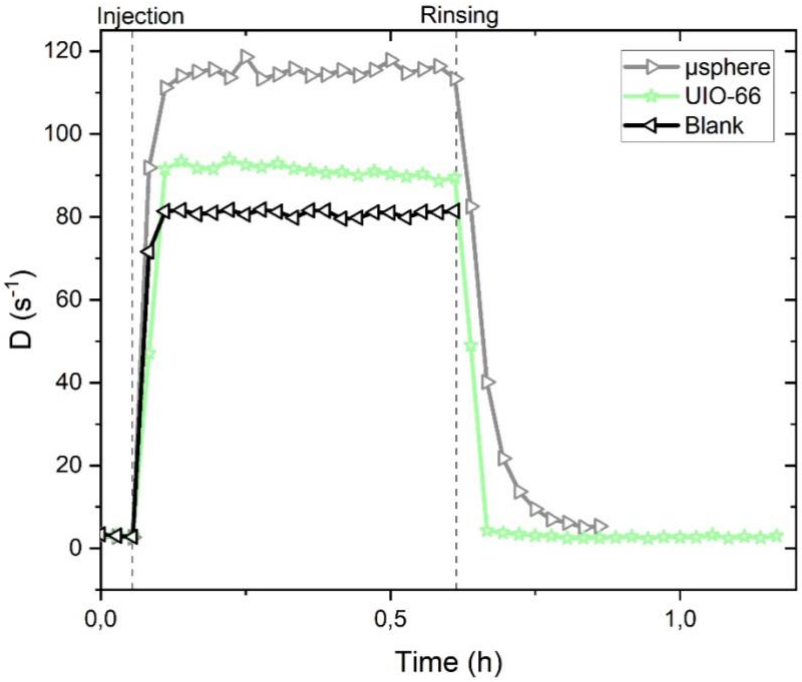

Figure IV-11: Showing the results from ^{85}Kr detection with UIO-66.

2. UIO-67

2.1 Structure, synthesis and SEM image

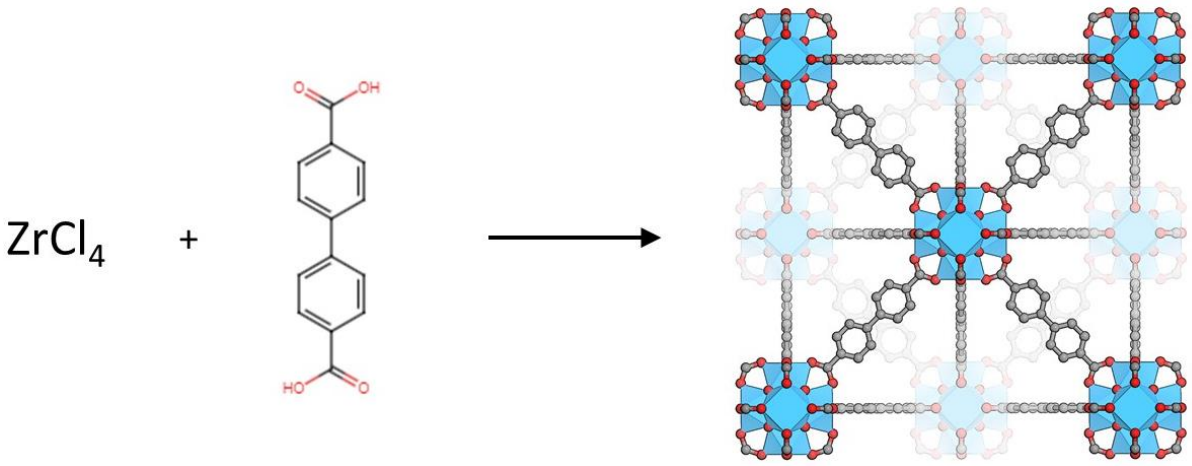

Figure IV-12: Precursors and structure of UIO-67.

UIO-67 consists of cuboctahedral zirconium oxide nodes, allowing a connection with up to twelve linear biphenyl-4,4′-dicarboxylic acid ligands leading to a 3D fcc porous network with an Fm(-3)m space group[16] as shown in Figure IV-12. We decided to move towards a BPDC ligand since its fluorescence yield is higher compared to the BDC ligand in UIO-66, 0.18 compared to 0.05[15].

The protocol listed below is the optimised synthesis conditions derived from Schaate *et al.*[2] to obtain a crystalline powder of UIO-67. By the addition of a modulator, as explained in Chapter I, we tried to synthesise a crystalline product with the biggest possible crystal size. We set out to firstly 1, 3, 5 and 10 molar equivalents of BA with respect to the zirconium salt. Unlike Schaate *et al.*[2], who obtained clear XRD peaks from 5 molar equivalent, we only managed to get a crystalline product from 10 molar equivalents. The protocol below shows the 30 molar equivalent synthesis which produced the biggest crystal sizes. Further increasing the modulator equivalent to 20 takes us back to a non-crystalline product, which showed no diffraction peak by XRD.

$ZrCl_4$ (0.026 mol·L^{-1}, 0.606 g), biphenyl-4,4′-dicarboxylic acid (0.026 mol·L^{-1}, 0.630 g) and benzoic acid modulator (0.771 mol·L^{-1}, 9.415 g) were dissolved in 100 mL of *N*,*N*-dimethylformamide (DMF). The mixture was equally divided into twelve 10 mL scintillation vials, which were then sealed with a screw cap. The vials were placed in an oven at 120°C for 48 h yielding small single crystals of UIO-67. The closed vials were removed and left to cool. The powder was washed using the centrifuge according to the protocol described in Chapter II.

At these synthesis conditions, we were able to synthesise small single crystals closer in appearance to the MOFs discussed in Chapter III. With the help of scanning electron microscopy, we determined their size.

Figure IV-13 below shows the SEM image of UIO-67 crystals. The images show a clear crystalline shape. The particle sizes observed are of the order of 100 µm, which are the biggest observed in this chapter and amongst the biggest observed for Zr-based MOFs in literature. The measurements of two particle sizes are also shown in Figure IV-13.

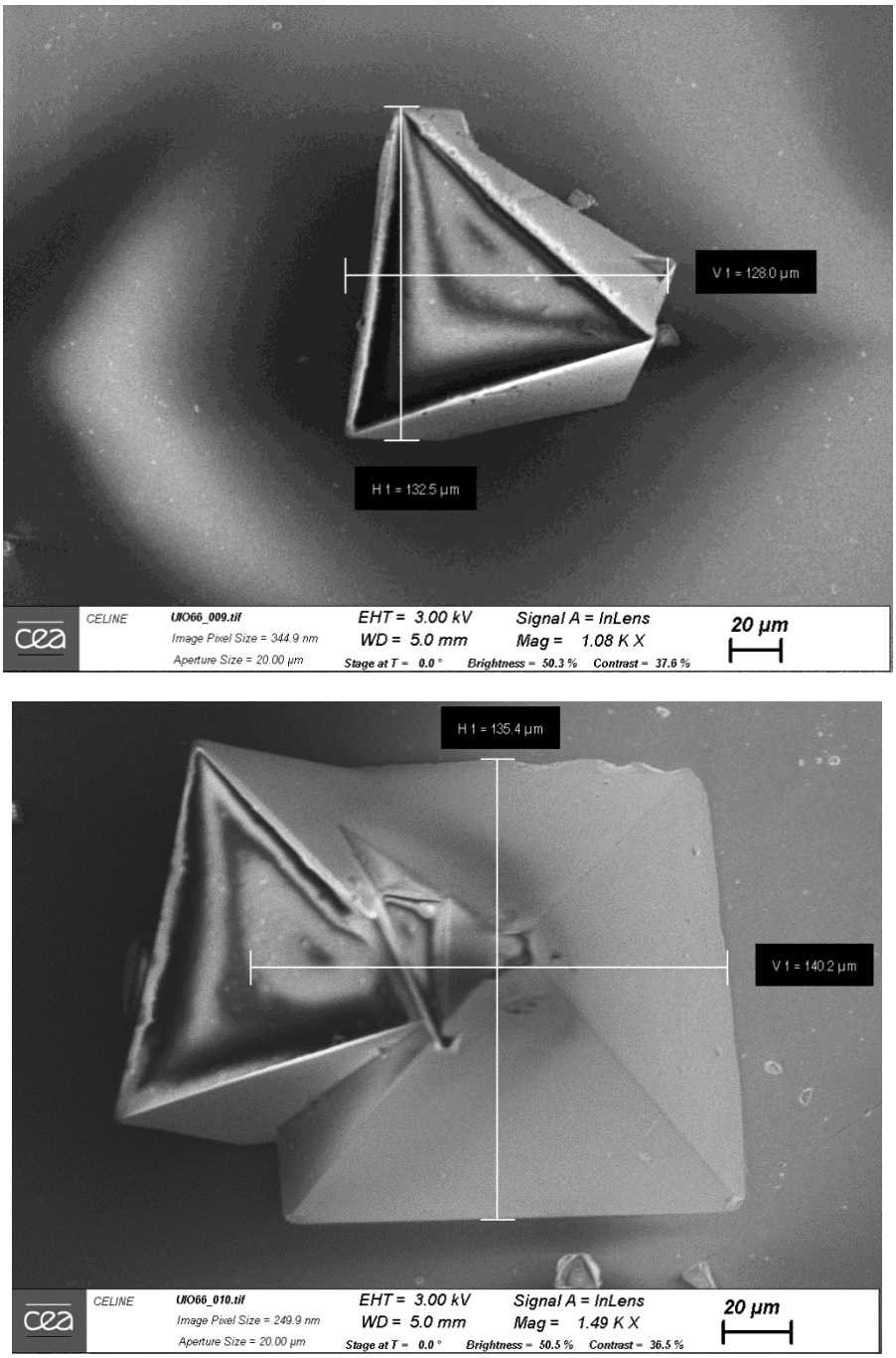

Figure IV-13: Shows the SEM image of UIO-67 single crystals.

2.2 Structural characterisation

2.2.1 X-Ray Diffraction

Figure IV-14 shows the X-ray Diffraction spectrum of our UIO-67 compared to the simulated XRD reported in the literature[2]. The peak positions are similar in both data sets, showing us

that we have indeed synthesised UIO-67 single crystals. However, we can see that the peak intensity varies from our experimental data to the simulated one. This is because the experiment we carried out was a powdered XRD done by crushing single crystals of UIO-67 on a sample holder. Compared to a single X-ray diffraction, this method will lead to preferential orientation of the crystals and hence influence the intensity for the different diffraction planes. By adjusting the concentration of modulator, we managed to go from a non-crystalline product to a small single crystals of UIO-67.

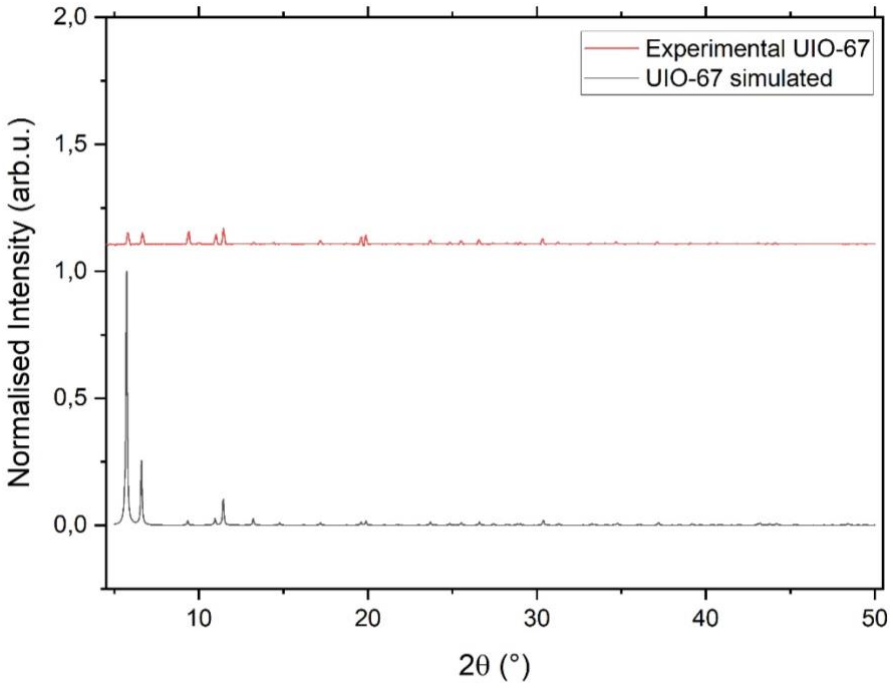

Figure IV-14: PXRD spectrum of UIO-67 showing experimental results compared to literature.

2.2.2 Adsorption measurements

The N_2 adsorption experiments for UIO-67 were carried out at the NIMBE laboratory in CEA. The Type II N_2 adsorption isotherm is shown in Figure IV-15 and hence indicates that UIO-67 exhibits microporosity. By plotting the graph in Figure IV-16 and using the equations developed in Chapter II, section 2.2, we can extract the BET surface area, the pore sizes and pore volume of our MOF are summarised in Table IV-3. The high surface area is comparable to what has been reported in literature[17,18] and much higher than the other UIOs reported in this chapter.

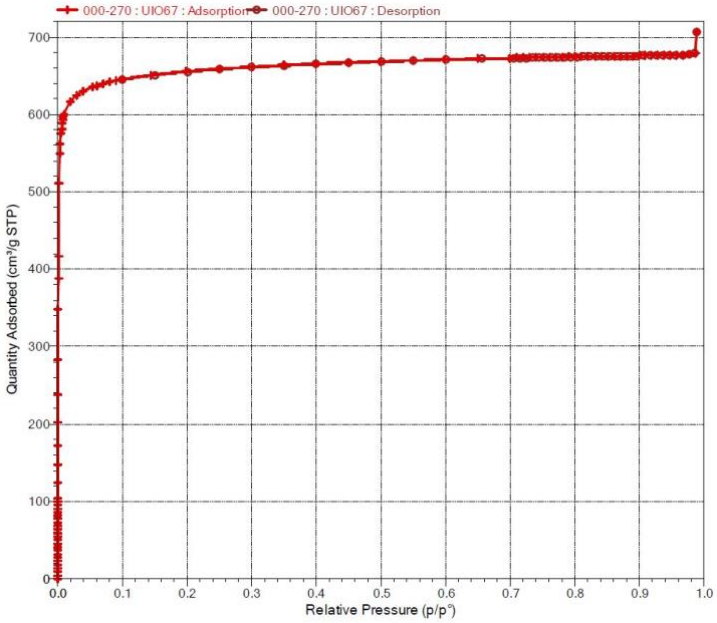

Figure IV-15: Illustrating the N_2 adsorption isotherm of UIO-67.

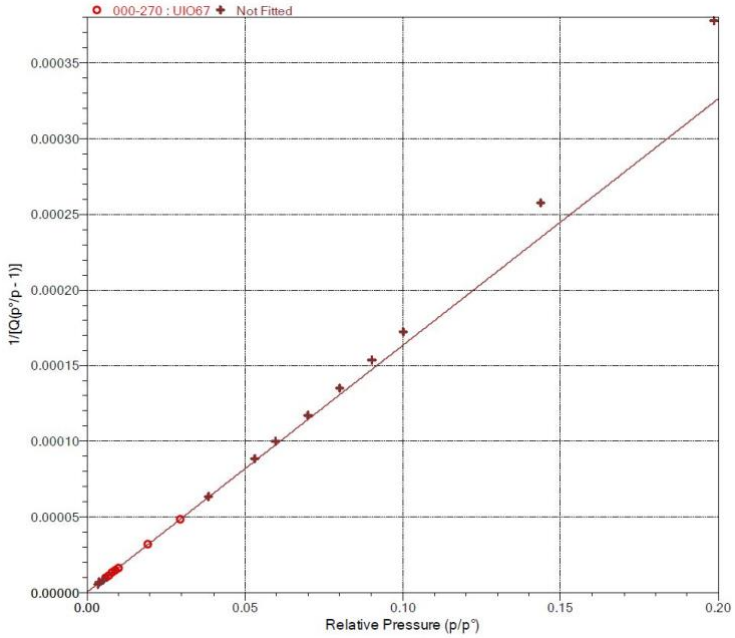

Figure IV-16: BET surface area plot of UIO-67.

Table IV-3: Showing the data calculated from N_2 adsorption of UIO-67.

MOF	BET SA ($m^2 \cdot g^{-1}$)	Pore size (Å)	Pore volume ($cm^3 \cdot g^{-1}$)
UIO-67	2670	6 & 12	1.076

2.2.3 Thermogravimetric Analysis

Figure IV-17 shows the TGA results of UIO-67. Like the MOFs in Chapter III, we can observe a drop before 100°C accounting for the surface water and residual DCM loss. A large drop in the weight of the sample between 350-500°C is also observed, similar to the Zn-based MOFs. This result is consistent with the literature where the decomposition temperature (T_d) is reported between 400-500°C depending on the sample preparation, activation and experimental conditions[10]. The MOF decomposes to zirconia at these temperatures.

We observe weight loss for UIO-67 between 100°C and 300°C, which is attributed to the dehydroxylation of the Zr cluster, as discussed in section 1.2.3. However, this is much smaller than that observed for UIO-66.

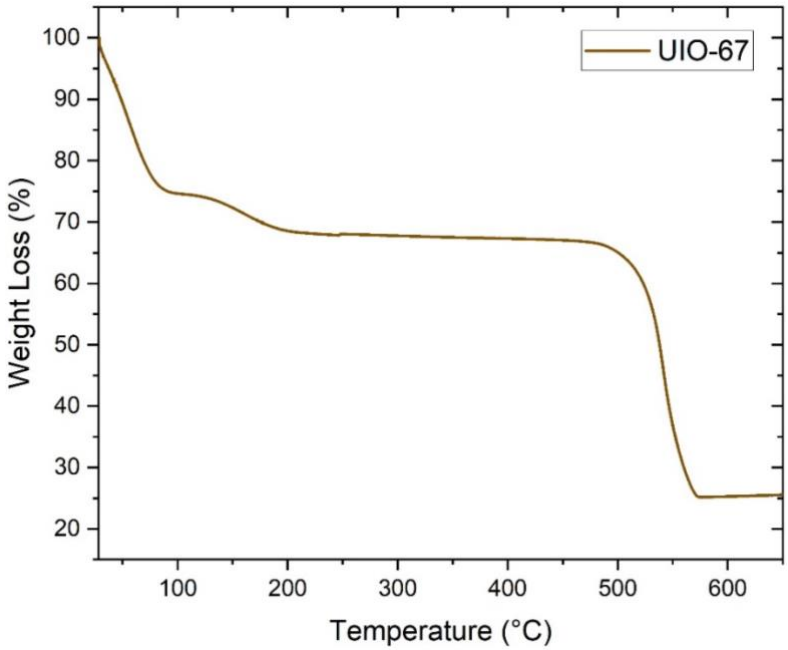

Figure IV-17: TGA results of UIO-67.

2.2.4 FT-IR experiments

Figure IV-18 shows the FT-IR spectrum of UIO-67. The sample presents two strong peaks centered at 1581 cm^{-1} and 1389 cm^{-1}, related to the asymmetric and symmetric stretching vibrations of the carboxylate groups, respectively coordinated to the Zr cations of the inorganic node. Furthermore, the peak at 754 cm^{-1} is consistent with the symmetric vibration peak of O-Zr-O and the asymmetric vibration peak of O-Zr-O at 665 cm^{-1}. These observations are consistent with literature[14]. A broad peak between 3500-3200 cm^{-1} is attributed in literature as the stretching vibration of O-H from surface water.

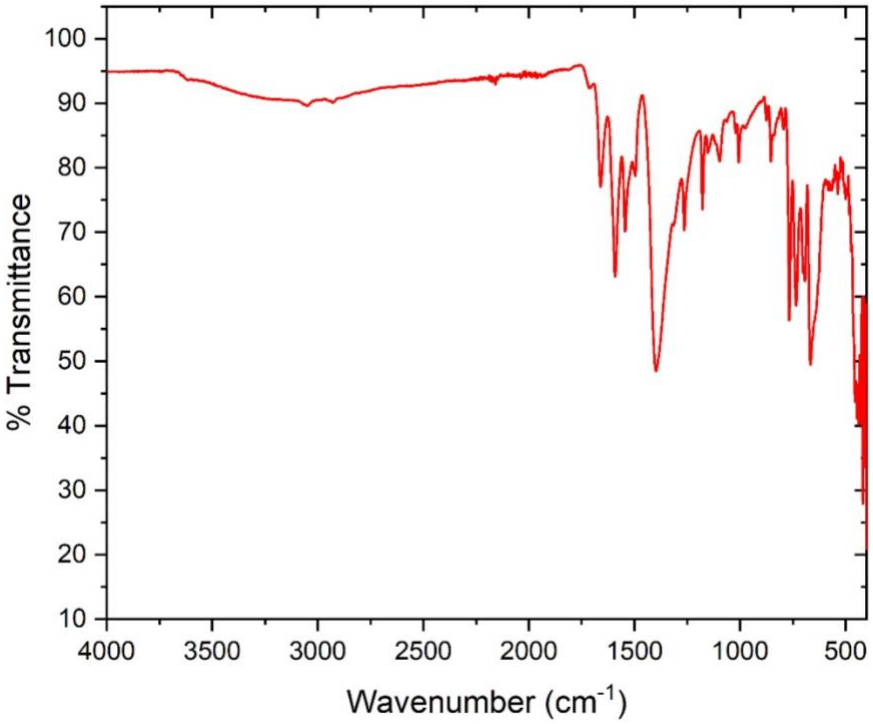

Figure IV-18: FT-IR spectrum of UIO-67.

2.3 Photophysical characterisation

2.3.1 Excitation and Emission spectra

Figure IV-19 shows the excitation and emission spectra of UIO-67. Since the single crystals were too small for the quartz capillary, this experiment could not be performed on one single crystal at a time as for the MOFs discussed in Chapter III. Therefore, this experiment was carried out on crushed UIO-67 single crystal sample on a quartz plate. We can observe a peak excitation at 320 nm. The maximum emission peak is observed at 365 nm. It is important to note that the emission wavelength of this MOF could be better for our gas detection experiment since it does not emit in the range of maximum quantum efficiency of photon detection of the PMTs used.

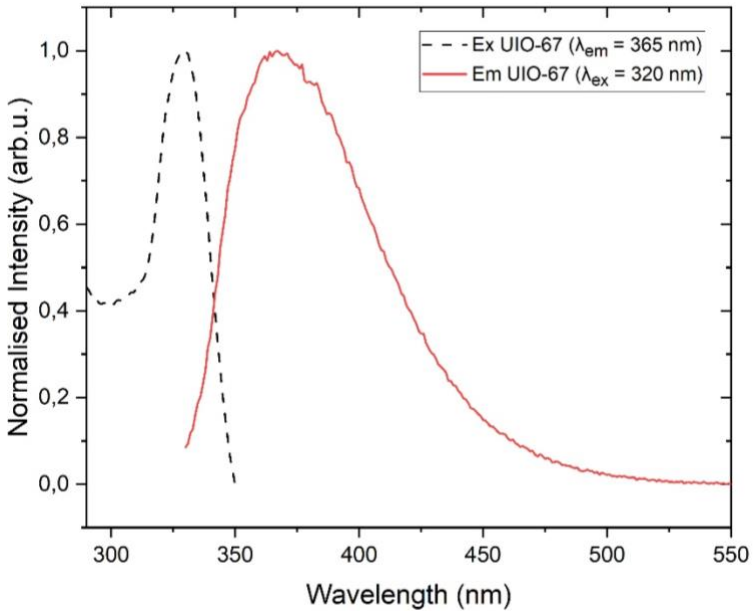

Figure IV-19: Illustrating the excitation and emission spectrum of UIO-67.

2.3.2 TCSPC

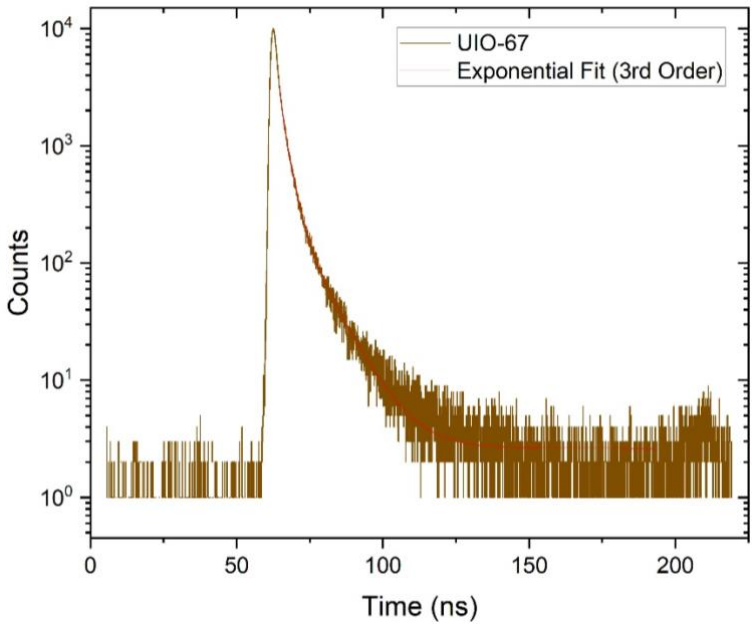

Figure IV-20: Showing the TCSPC results for UIO-67.

Figure IV-20 shows the fluorescence decay of UIO-67 with an excitation diode at 309 nm. By fitting this decay curve with a third-order exponential fit, we can calculate the three fluorescence lifetime components, their respective weights, and an average fluorescence lifetime. The results are shown in Table IV-4, together with the coefficient of determination (R-

Square / COD) of the fit. Since a fluorescence lifetime of around 3 ns is ideal for measurements in coincidence, UIO-67 is an promising candidate on this aspect.

Table IV-4: Showing the calculated fluorescence lifetime of UIO-67.

MOF	Diode λ_{ex} (nm)	λ_{em} (nm)	τ_1 (ns)	τ_2 (ns)	T_3 (ns)	$<\tau>$ (ns)	R-Square (COD)
UIO-67	309	365	2.4 (67.1%)	0.5 (22.9%)	8.9 (10.0%)	2.6	0.9991

2.4 Radioactive gas bench test

2.4.1 ^{85}Kr

Figure IV-21 shows the results from the detection of ^{85}Kr gas. The D value on the y-axis is the photon count rate calculated by a logical sum of double coincidences between every pair of PMT in the detection system. We can observe that the count rate of UIO-67 is higher than the blank experiment. This means that our MOF does indeed produce photons in the presence of ^{85}Kr and is, hence, a scintillator. We can also observe that the count rate of UIO-67 is higher than that of the microspheres of polystyrene. The photon count rate is 38.9% higher than the microspheres. Therefore, this experiment shows that UIO-67 is considered as a very efficient scintillator for the detection of ^{85}Kr. Even though the emission wavelength discussed above was also not in the convenient range for this experiment, the performance of UIO-67 as a scintillator for gas detection is extraordinary. This high performance may be attributed to the high surface area, photoluminescence yield of the ligand present in this MOF, and fast fluorescence lifetime. The particle size might also play a role in this relatively good performance. The single crystal morphology, even if small, allows the gas to diffuse better in the MOF than the powdered samples of the other MOFs discussed in this chapter, as the powder tends to compact in the scintillating vial. Let us now compare the ^{85}Kr detection of UIO-67 with its Zn-based equivalent (same ligand, different metal centres), i.e. IRMOF-9. We derived from Chapter III, that for the same activity IRMOF-9 emits less photons (127 s^{-1}) than UIO-67 (159 s^{-1}). One possible explanation for the slightly better performance of UIO-67 compared to IRMOF-9 is due to its vastly greater surface area, 2970 m^2g^{-1} compared to 902 m^2g^{-1}.Another possible reason is the possibility of a concatenate structure for IRMOF-9 that makes the accessibility to its pores more complex. One more possibility is due to the small size of the UIO-67 crystals compared to the big IRMOF-9 crystals which means that a larger mass of UIO-67 (251 mg) was put in the scintillation vial than IRMOF-9 (200 mg). When you normalise the D photon count rate with respect to the mass of both samples, the result leads to 0.635 $s^{-1}\cdot mg^{-1}$ for both MOFs. The slow adsorption kinetics we can notice for UIO-67 compared to the other MOFs in this chapter and

compared to IRMOF-9 might boost the number of events recorded as explained previously for MOF-205.

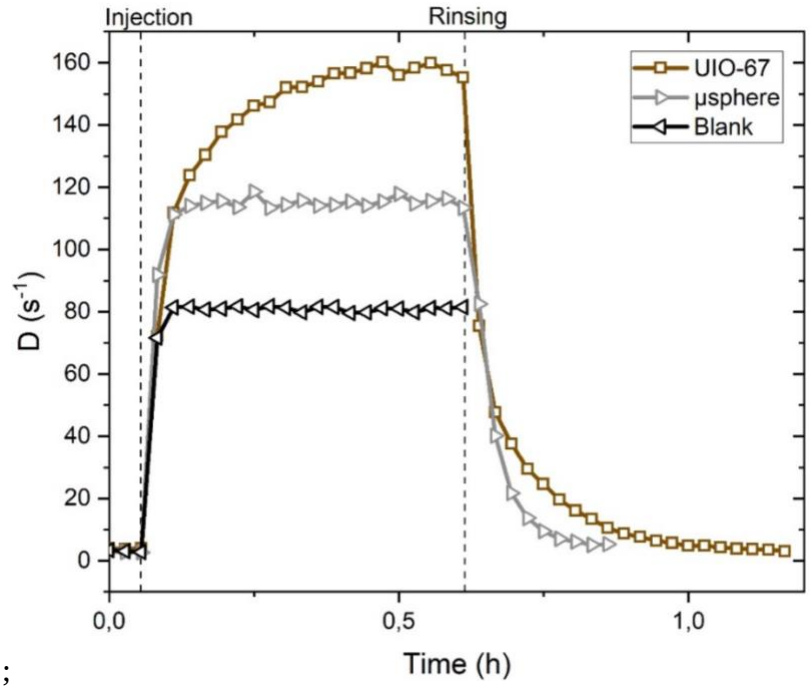

;

Figure IV-21: Showing the results from ^{85}Kr detection with UIO-67.

Since this is our best-performing MOF so far for detecting ^{85}Kr, we also decided to perform ^{222}Rn and ^{3}H detection experiments using this MOF.

2.4.2 ^{222}Rn

UIO-67 was also used to test for the detection of 10 kBq or 76 Bq·cm^{-3} of ^{222}Rn. Figure IV-22 shows the results of this experiment. As we can see, the photon count rate of UIO-67 is higher than that of the blank and the microsphere showing that UIO-67 is an efficient porous scintillator for the detection of ^{222}Rn. UIO-67 has a slightly higher photon count than MOF-205 of Chapter III and considerably higher than MOF-5 + 1.38% ADC which we will see in Chapter V. We could hastily conclude that UIO-67 is the most efficient of the three MOFs tested for ^{222}Rn detection. However, we must take into consideration once again the mass of the sample inside the glass vial. (Appendix Table 2) indicates that more UIO-67 was used than the other two MOFs. A slightly higher activity is also injected for UIO-67 as be seen in the same table. We will see in the conclusion of this manuscript that normalising by the mass of the sample puts UIO-67 at the last place compared to MOF-205 and MOF-5 + 1.38% ADC.

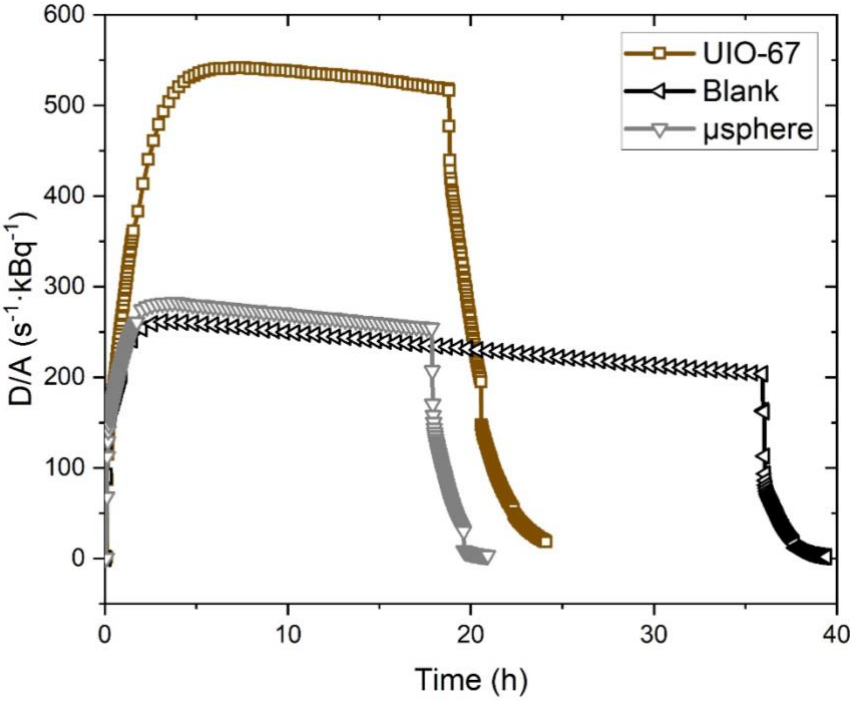

Figure IV-22: Illustrating 222Rn detection experiment results with UIO-67.

2.4.3 ^{3}H

As in this chapter UIO-67 has the highest photon count with ^{85}Kr detection experiment, it was also used to test for the detection of 7 kBq of ^{3}H. Figure IV-23 shows the results of this experiment. As seen in Chapter I, since ^{3}H produces beta particles with very low energy a very few photons with each interaction. Its detection is therefore very challenging. However, even for low energy, the detection efficiency is not negligible as we are able to detect down to two photons event with the TDCR device. This is where the choice of TDCR measurements shines: we can reliably say that slight variations in the count rate are significant and not statistical errors. As tritium is a pure, low-energy beta emitter, neither Cherenkov nor air contribution are expected. An increase of 0.99 s^{-1} was observed in the photon count upon injection of ^{3}H. Upon purging, the count rate comes back to its initial value, showing no observable adsorption of the tritium inside the MOFs. We must also take into account the non-linearity of the scintillation response at low energy. Scintillation from ionisation event with low energy deposition is not well known from both theoretical and experimental point of view. One can also note that the baseline of this measurement is significantly higher than previous tritium measurement's, mainly due to external factors (light leak, external gamma sources…). Unfortunately, we cannot compare here the tritium detection of UIO-67 with the other MOFs in this manuscript because of an experimental mistake where 7 kBq was injected instead of 9 kBq. This experiment will be repeated in the near future to complete our comparison.

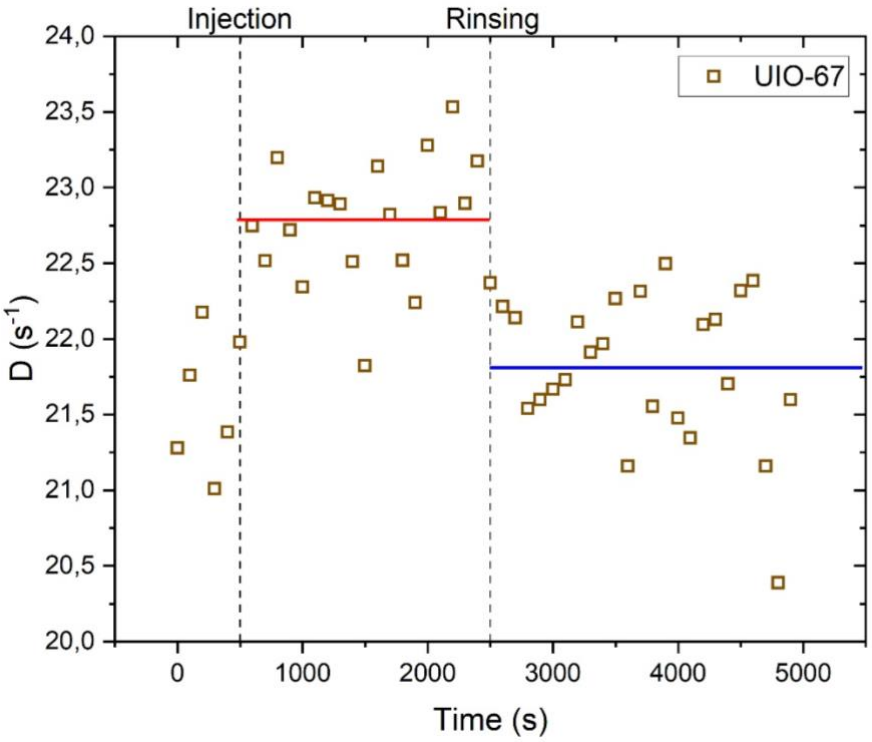

Figure IV-23: Illustrating ^{3}H detection with UIO-67.

3. UIO-1,4-NDC

3.1 Structure, synthesis and SEM image

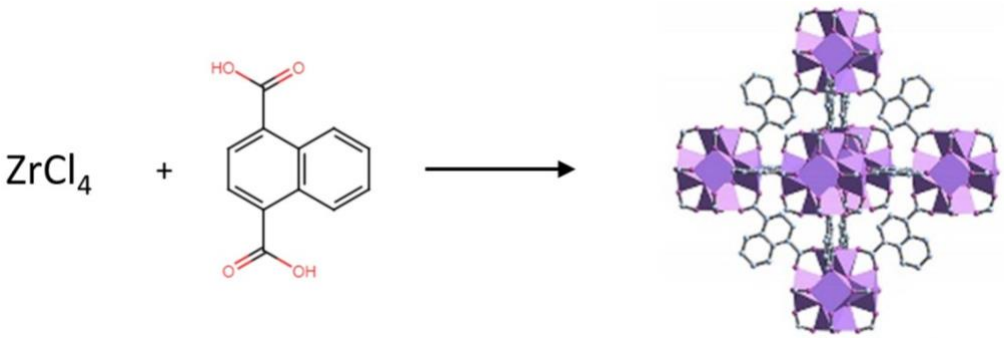

Figure IV-24: Precursors and structure of UIO-1,4-NDC [20].

Since we did not obtain very efficient scintillation properties from UIO-66, we decided to explore a MOF made of a ligand with more conjugated rings than UIO-66. UIO-1,4-NDC consist of linkers with two conjugated rings and, hence, more electrons involved in the excitation/emission mechanisms, which should yield a higher scintillation yield. The photoluminescence light for the NDC ligand is reported at 0.23 compared to the BDC ligand of UIO-66 reported at 0.05[15].

UIO-1,4-NDC consist of cuboctahedral zirconium oxide nodes, allowing a connection with up to twelve linear 1,4-naphthalene dicarboxylic acid ligands leading to a 3D porous network with an Fm(-3)m space group[5] as shown in Figure IV-24. The protocol below is the optimised synthesis conditions derived from Butova *et al.*[5] to obtain crystalline powder of UIO-1,4-NDC. By the addition of a modulator, as explained in Chapter I, we tried to synthesise a crystalline product with the biggest possible crystal size. Since Butova *et al.*[5] already studied the molar equivalents and found out that the 60 molar equivalent produced the biggest crystal size and surface area and then further increasing to a 100 produced non crystalline products, we chose a 55 molar equivalent ratio.

$ZrCl_4$ (0.043 mol·L^{-1}, 1 g), 1,4-naphthalenedicarboxylic acid (0.043 mol·L^{-1}, 0.930 g) and benzoic acid modulator (2.36 mol·L^{-1}, 28.820 g) were dissolved in 100 mL of *N*,*N*-dimethylformamide (DMF). The mixture was equally divided into twelve 10 mL scintillation vials, which were then sealed with a screw cap. The vials were placed in an oven at 120°C for 24 h, yielding a crystalline powder of UIO-1,4-NDC. The closed vials were removed and left to cool. The powder was washed using the centrifuge according to the protocol described in Chapter II.

Figure IV-25 below shows the SEM image of UIO-1,4-NDC crystalline powder. A clear polyhedral crystal shape is observed here. The particle sizes observed are of the order of 2-3 µm. Some particle aggregation can also be observed here, unlike in UIO-67. The measurements of two particle sizes are also mentioned in Figure IV-25.

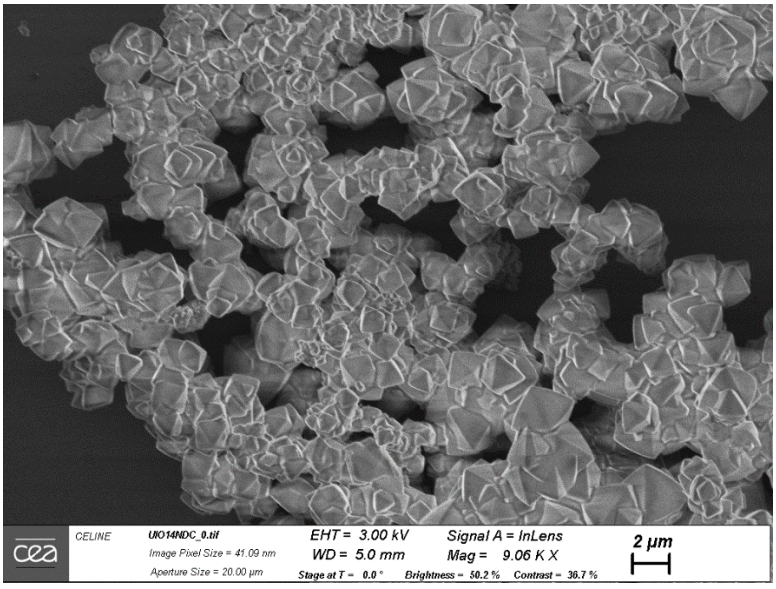

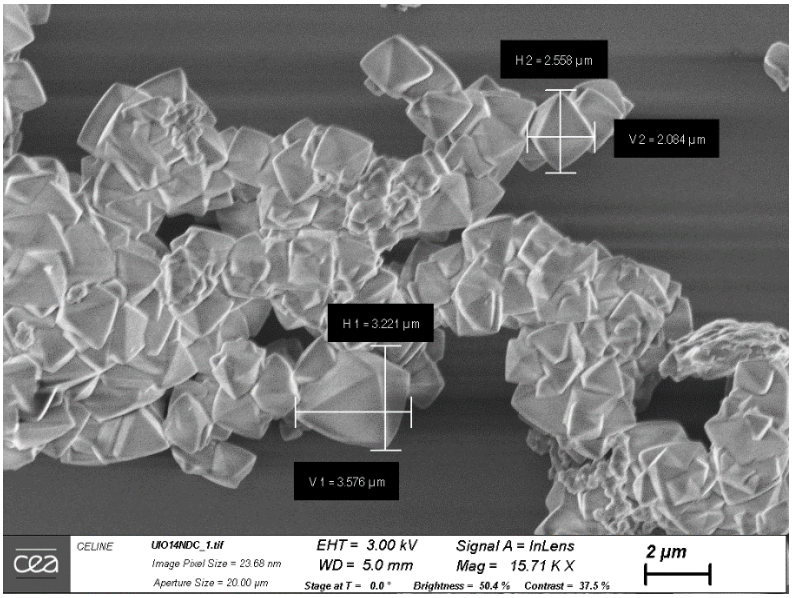

Figure IV-25: Shows the SEM image of UIO-1,4-NDC crystalline powder.

3.2 Structural characterisation

3.2.1 X-Ray Diffraction

Figure IV-26 shows the X-ray Diffraction spectrum of our UIO-1,4-NDC compared to the simulated XRD reported in the literature[5]. The peak positions are similar in both data sets, showing us that we have indeed synthesised UIO-1,4-NDC single crystals. With these new proportions of modulator, we managed to synthesise crystalline powder of UIO-1,4-NDC.

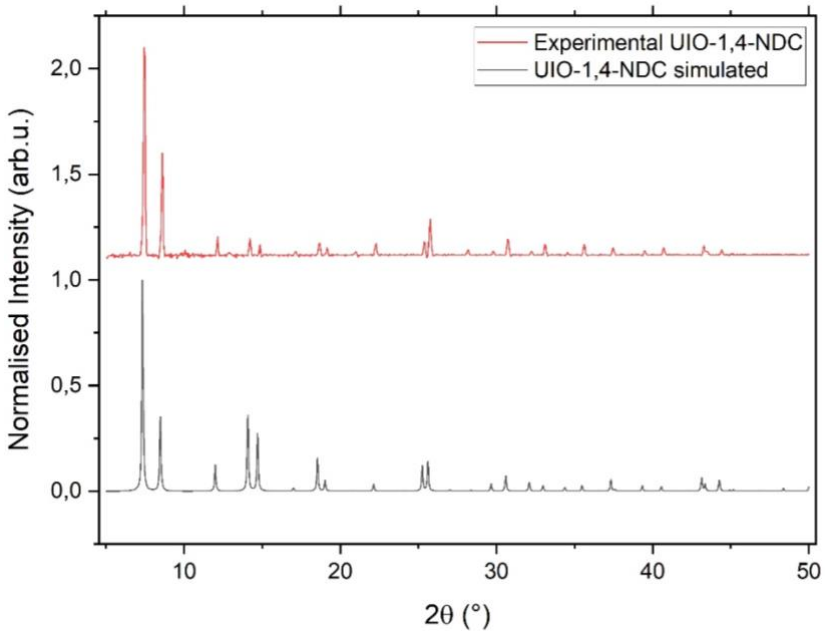

Figure IV-26: PXRD spectrum of UIO-1,4-NDC showing experimental results compared to literature.

3.2.2 Adsorption measurements

The N_2 adsorption experiments for UIO-1,4-NDC were carried out at the ILV laboratory. The Type I N_2 adsorption isotherm is shown in Figure IV-27 and hence shows that UIO-1,4-NDC exhibits microporosity. We can extract the BET surface area, as summarised in Table IV-5. We could not measure our MOF's pore sizes and pore volume since the ILV laboratory did not have the appropriate device to do so. The high surface area reported in Table IV-5 is comparable to what has been reported in the literature[20]. It is smaller than that of UIO-66, which is expected as it consists of a bulkier ligand than UIO-66, which tends to reduce the free space.

Table IV-5: Showing the data calculated from N_2 adsorption of UIO-1,4-NDC.

MOF	BET SA ($m^2 \cdot g^{-1}$)
UIO-1,4-NDC	760

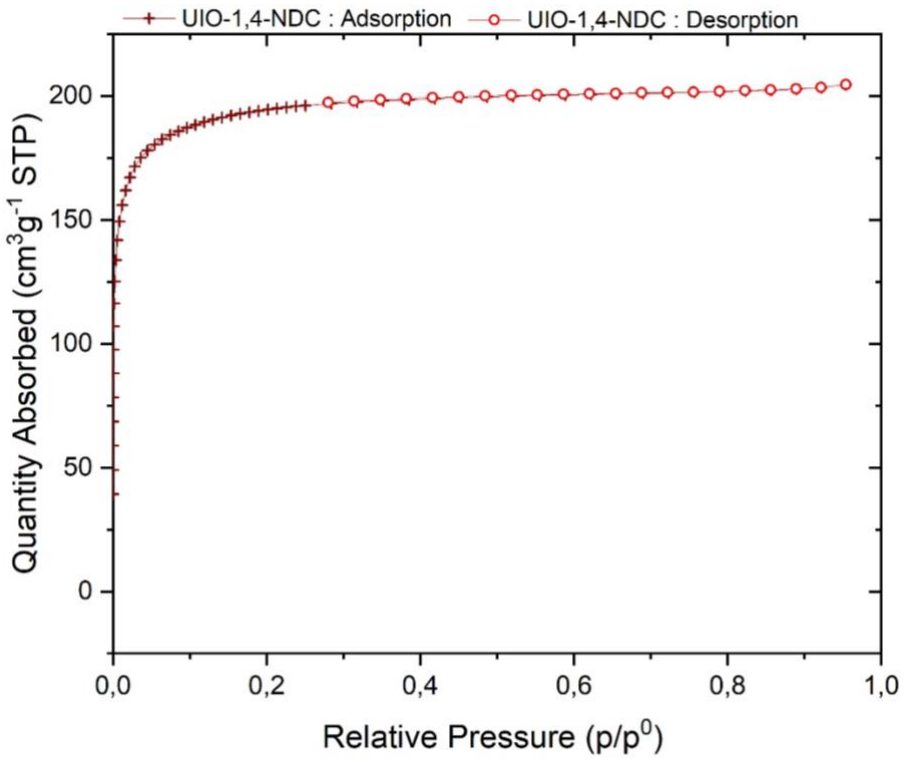

Figure IV-27: Illustrating the N_2 adsorption isotherm of UIO-1,4-NDC.

3.2.3 Thermogravimetric Analysis

Figure IV-28 shows the TGA results of UIO-1,4-NDC. Similar to the MOFs in Chapter III, we can observe a drop before 100°C accounting for the surface water and residual DCM loss. A large drop in the weight of the sample between 350-500°C is also observed, similar to the Zn-based MOFs. This result is consistent with the literature where the decomposition temperature (T_d) is reported between 400-500°C depending on the sample preparation, activation and experimental conditions[10]. The MOF decomposes to zirconia at these temperatures.

The weight loss for UIO-1,4-NDC between 100°C and 300°C is attributed to the dehydroxylation of the Zr cluster, as discussed in section 1.2.3 above.

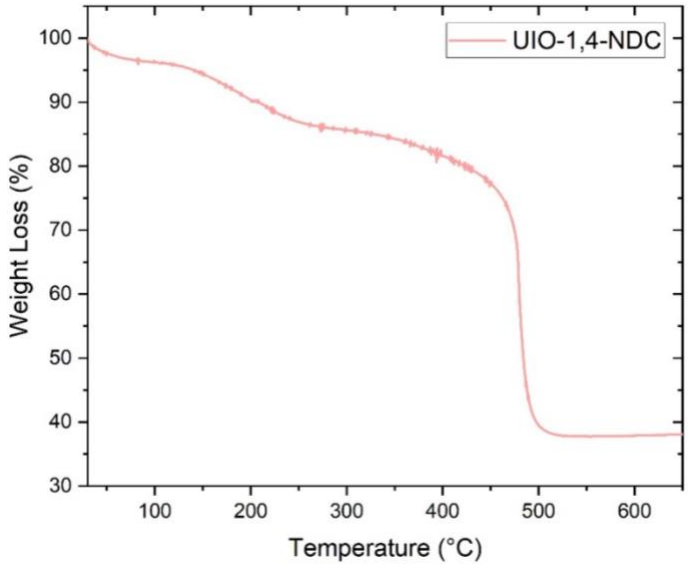

Figure IV-28: TGA results of UIO-1,4-NDC.

3.2.4 FT-IR experiments

Figure IV-29 shows the FT-IR spectrum of UIO-1,4-NDC. The sample presents two strong peaks centered at 1565 cm^{-1} and 1368 cm^{-1}, related to the asymmetric and symmetric stretching vibrations of the carboxylate groups, respectively coordinated to the Zr cations of the inorganic node. Furthermore, the peak at 765 cm^{-1} is consistent with the symmetric vibration peak of O-Zr-O and the asymmetric vibration peak of O-Zr-O at 659 cm^{-1}. These observations are consistent with literature[14]. A broad peak between 3500-3200 cm^{-1} is attributed in literature as the stretching vibration of O-H from surface water.

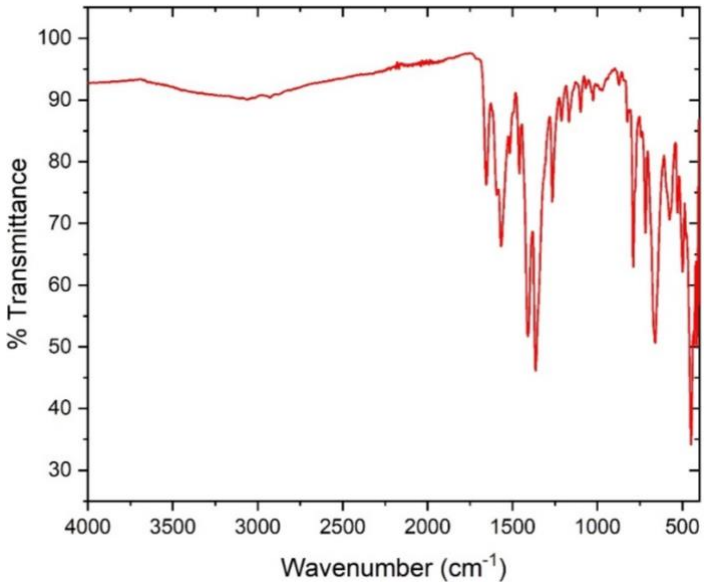

Figure IV-29: FT-IR spectrum of UIO-1,4-NDC.

3.3. Photophysical characterisation

3.3.1 Excitation and Emission spectra

Figure IV-30 shows the excitation and emission spectra of UIO-1,4-NDC. This experiment was carried out on a powder UIO-1,4-NDC sample on a quartz plate. The maximum emission peak is observed at 405 nm. Therefore, the emission wavelength of this MOF lies in the range of maximum quantum efficiency of photon detection of the PMTs used in the gas detection experiments.

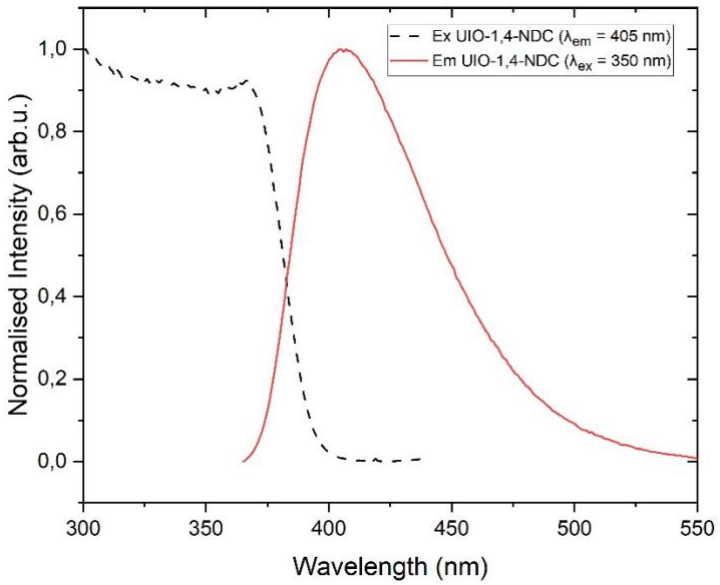

Figure IV-30: Illustrating the excitation and emission spectrum of UIO-1,4-NDC.

3.3.2 TCSPC

Figure IV-31 shows the fluorescence decay of UIO-1,4-NDC with an excitation diode at 339 nm. By fitting this decay curve with a third-order exponential fit, we can calculate the three fluorescence lifetime components, their respective weights, and an average fluorescence lifetime. The results are illustrated in Table IV-6, together with the coefficient of determination (R-Square / COD) of the fit. We can notice that the fluorescence lifetime is slightly higher than 3 ns but still falls in an acceptable range for efficient detection in coincidence.

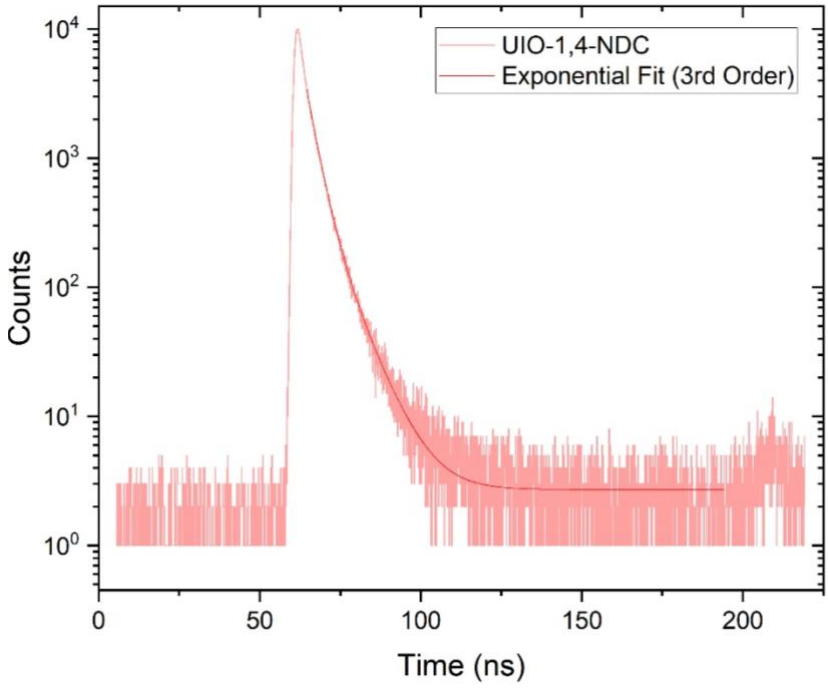

Figure IV-31: Showing the TCSPC results for UIO-1,4-NDC.

Table IV-6: Showing the calculated fluorescence lifetime of UIO-1,4-NDC.

MOF	**Diode λ_{ex} (nm)**	**λ_{ex} (nm)**	**τ_1 (ns)**	**τ_2 (ns)**	**T_3 (ns)**	**<τ> (ns)**	**R-Square (COD)**
UIO-1,4-NDC	339	405	2.9 (79.7%)	7.1 (17.0%)	0.5 (3.3%)	3.5	0.9994

3.4 Radioactive gas bench test

3.4.1 ^{85}Kr

Figure IV-32 shows the results from the detection of ^{85}Kr gas. The D value on the y-axis is the photon count rate calculated by the logical sum of double coincidence between every pair of PMT in the detection system. We can observe that the count rate of UIO-1,4-NDC is higher than the blank experiment. This means that our MOF does indeed produce photons in the presence of ^{85}Kr and is, hence, a scintillator. However, we can also observe that the count rate of UIO-66 is lower than that of the microspheres of polystyrene. Therefore, this experiment shows that UIO-1,4-NDC is considered as a scintillator for the detection of ^{85}Kr but not a very efficient one compared to the microspheres of polystyrene. This was not expected since the 1,4-NDC ligand has two conjugated rings, and hence, more delocalised electrons are involved in the excitation/emission mechanism, and it emits in the correct wavelength range. However, we have seen that UIO-1,4-NDC has a relatively low surface area, which may account for a poor interaction with the radioactive gas. We will see in Chapter V how we were able to slightly improve the scintillation of UIO-1,4-NDC via a doping strategy.

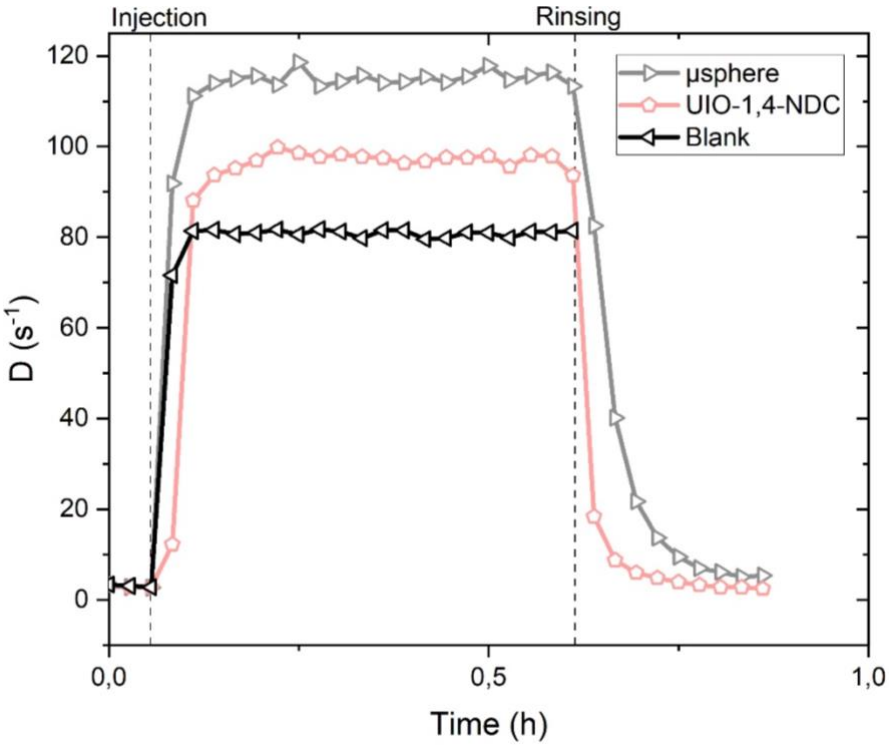

Figure IV-32: Showing the results from ^{85}Kr detection with UIO-1,4-NDC.

4. CAU-24

4.1 Structure, synthesis and SEM image

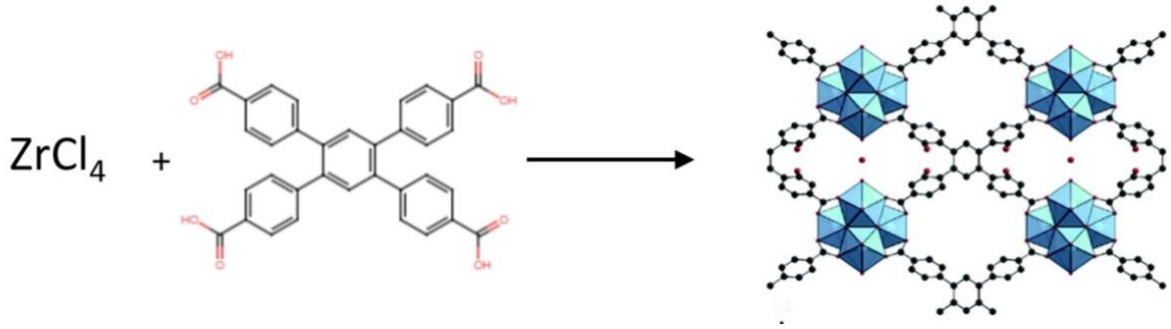

Figure IV-33: Precursors and structure of CAU-24 [21].

In CAU-24, the $[Zr_6(\mu_3\text{-}O)_4(\mu_3\text{-}OH)_4]^{12+}$ clusters are orthorhombically arranged, and each cluster is connected to eight carboxylate groups. The particularity of CAU-24 compared to other MOFs presented in this manuscript is that the inorganic clusters are bridged by all four carboxylate groups of the TCPB linker to give the following unit cell formula: $Zr_6(\mu_3\text{-}O)_4(\mu_3\text{-}OH)_4(OH)_4(H2O)_4(TCPB)_2$. CAU-24 has a 3D scu porous network with a Cmmm space group[21], as shown in Figure IV-33, which is an uncommon and relatively new structure in the field of MOF. The protocol first tried was the optimised synthesis conditions derived from Lammert *et al.*[21] to achieve crystalline powder of CAU-24. Using formic acid as a modulator like Lammert *et al.*[21] did not produce crystalline products at 1,3,5,10,30 molar equivalents. We hence decided to switch to a different synthesis protocol studied by Z. Li *et al.*[22] where they use benzoic acid as a modulator with 100 molar equivalent ratio to zirconium (as described in the protocol below). Attempts to use 60 and 30 molar equivalent of BA produced non-crystalline products. Since the modulator acts like a competing molecule to the ligand to slow down nucleation, one hypothesis for the use of such a large amount of modulator for CAU-24 compared to the UIOs presented in this chapter is the structural difference between the ligand and the BA, which makes the competition less likely.

$ZrCl_4$ (0.013 mol·L^{-1}, 0.303 g), H_4TCPB (0.008 mol·L^{-1}, 0.447 g) and benzoic acid modulator (1.38 mol·L^{-1}, 16.85 g) were dissolved in 100 mL of *N,N*-dimethylformamide (DMF). The mixture was equally divided into twelve 10 mL scintillation vials, which were then sealed with a screw cap. The vials were placed in an oven at 120°C for 48 h, yielding a crystalline powder of CAU-24. The closed vials were removed and left to cool. The powder was washed using the centrifuge according to the protocol described in Chapter II.

Figure IV-34 below shows the SEM image of CAU-24 crystalline powder. A clear but unusual oblong shape is observed here. The particle sizes observed are of the order of 1-2 µm. The measurements of two particle sizes are also shown in Figure IV-34. The size of the particles are consistent with the work of Z. Li *et al.*[22] but they however obtained rod shaped crystals.

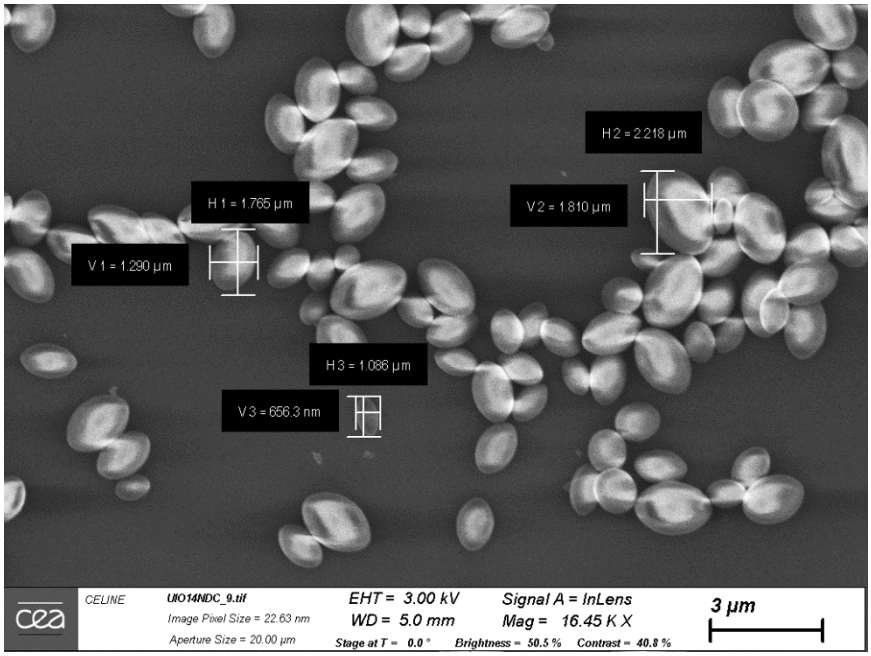

Figure IV-34: Shows the SEM image of CAU-24 crystalline powder.

4.2 Structural characterisation

4.2.1 X-Ray Diffraction

Figure IV-35 shows the X-ray Diffraction spectrum of our CAU-24 compared to the simulated XRD reported in the literature. The peak positions are similar in both data sets, showing that we have indeed synthesised CAU-24 crystalline powder.

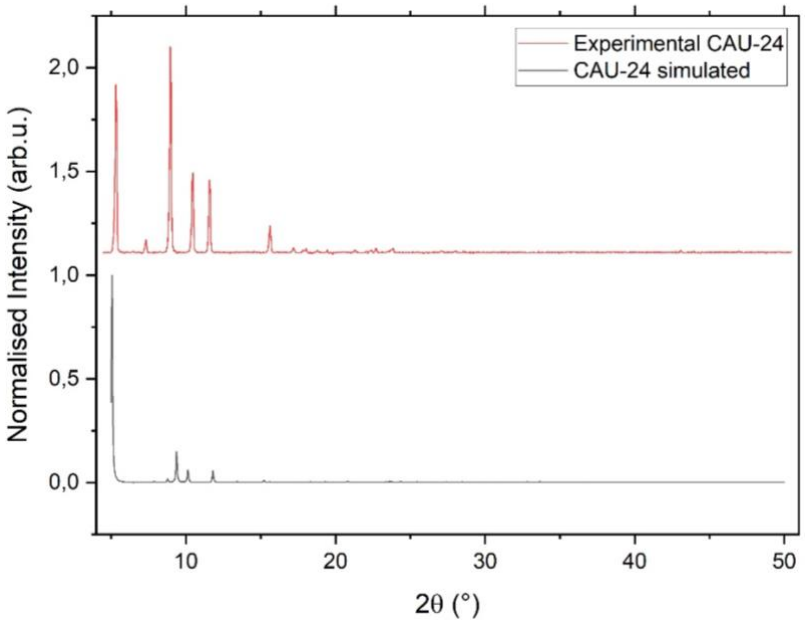

Figure IV-35: PXRD spectrum of CAU-24 showing experimental results compared to literature.

4.2.2 Adsorption measurements

The N_2 adsorption experiments for CAU-24 were carried out at the NIMBE laboratory in CEA. The Type IV N_2 adsorption isotherm is shown in Figure IV-36. This is the only MOF studied in this manuscript that exhibits a small hysteresis loop, meaning that the behaviour of the adsorption and desorption of gases may not be similar. Even though we used the same synthesis protocols as Z. Li *et al.*[22], the N_2 adsorption isotherm is inconsistent with their findings since they recorded a type I isotherm. However, this remains the only characterisation result inconsistent with the literature and might be due to the sample washing and activation protocols being different from the literature. With PXRD, FTIR and TGA data consistent with the literature we remain certain that we obtain the CAU-24 MOF. By plotting the graph in Figure IV-37 and using the equations developed in Chapter II, section 2.2, we extracted the BET surface area, the pore sizes and pore volume of our MOF as summarised in Table IV-7. The surface area is lower than reported in the literature (1610 $m^2 \cdot g^{-1}$) using the same synthesis protocol[21]. Despite that, 1008 $m^2 \cdot g^{-1}$ is still a more than decent surface area for our application.

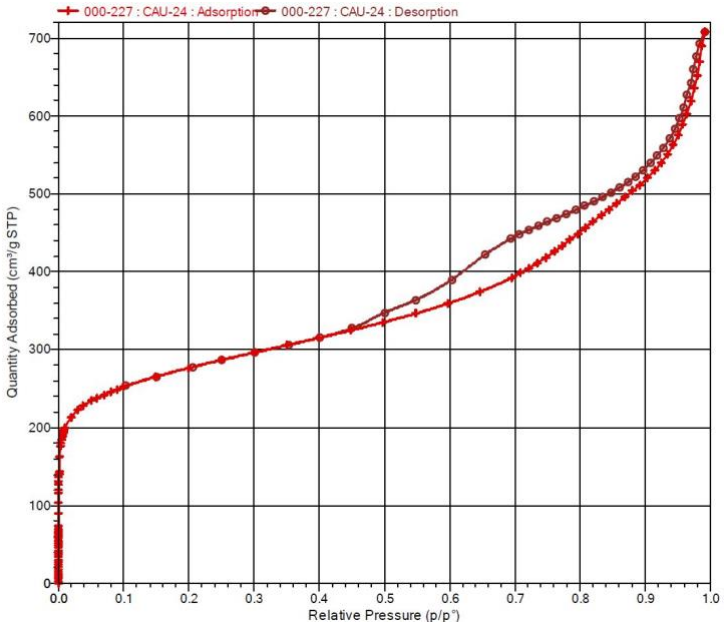

Figure IV-36: Illustrating the N_2 adsorption isotherm of CAU-24.

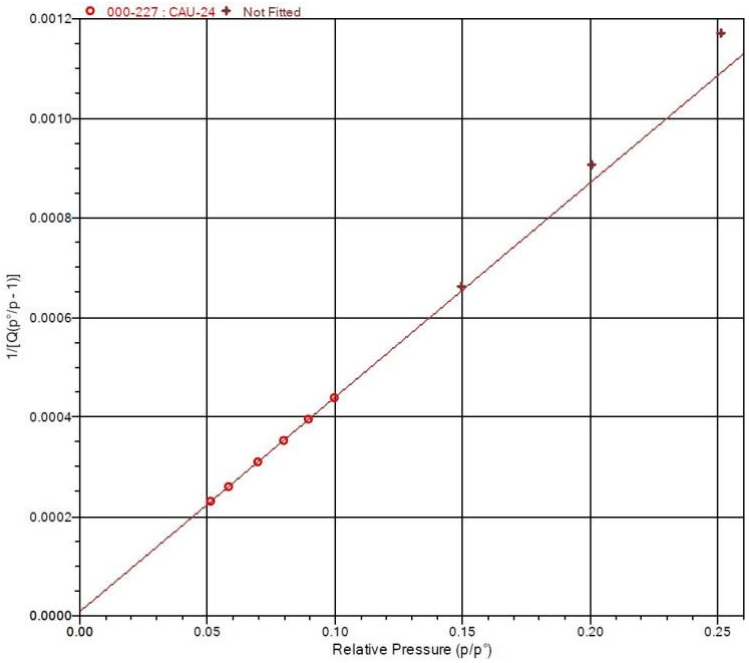

Figure IV-37: BET surface area plot of CAU-24.

Table IV-7: Showing the data calculated from N2 adsorption of CAU-24.

MOF	**BET SA ($m^2 \cdot g^{-1}$)**	**Pore size (Å)**	**Pore volume ($cm^3 \cdot g^{-1}$)**
CAU-24	1008	6 & 10	1.006

4.2.3 Thermogravimetric Analysis

Figure IV-38 shows the TGA results of CAU-24. Similar to the MOFs in Chapter III, we can observe a drop before 100°C accounting for the surface water and residual DCM loss. A large drop in the weight of the sample between 350-500°C is also observed, similar to the Zn-based MOFs. This result is consistent with the literature where the decomposition temperature (T_d) is reported to be between 400-500°C depending on the sample preparation, activation and experimental conditions[10]. The MOF decomposes to zirconia at these temperatures.

We observe weight loss for CAU-24 between 100°C and 300°C, which is attributed to the dehydroxylation of the Zr cluster, as discussed in section 1.2.3 above. The results are consistent with those obtained from Lammert *et al.*[21]

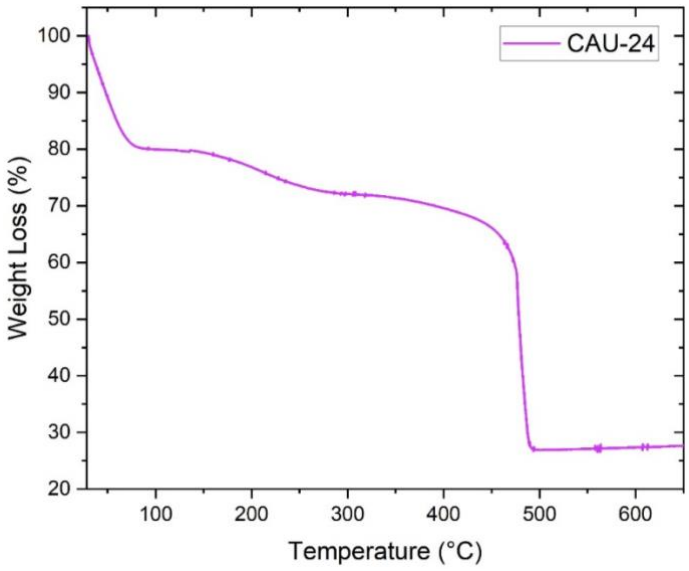

Figure IV-38: TGA results of CAU-24.

4.2.4 FT-IR experiments

Figure IV-39 shows the FT-IR spectrum of CAU-24, which is consistent with the literature[21]. The strongest peak observed is that of the double bond C=C vibration of the TCPB ligand 1408 cm^{-1}. The literature suggests that this peak is stronger for this MOF than the previous ones we have studied since the TCPB ligand possesses a higher number of aromatic rings[23], responsible for this vibration. Furthermore, we observe the asymmetric vibration peak of O-Zr-O at 653 cm^{-1}. A peak between 3500-3200 cm^{-1} is attributed in literature as the stretching vibration of O-H from surface water.

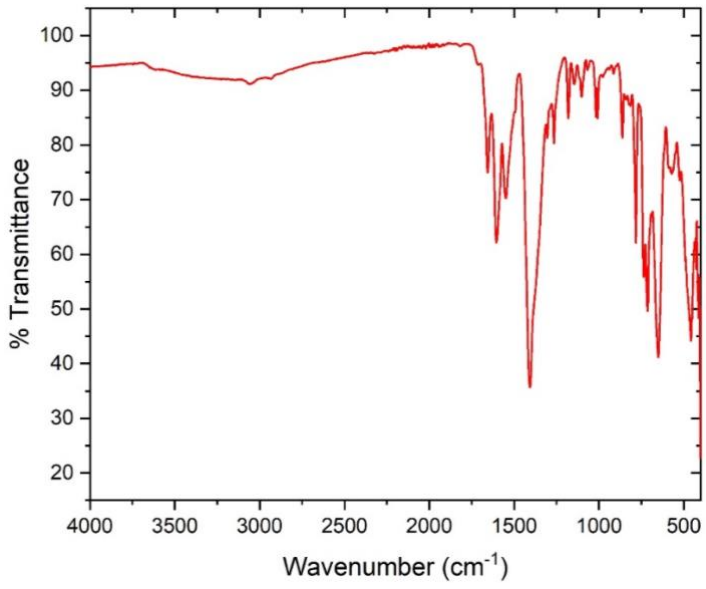

Figure IV-39: FT-IR spectrum of CAU-24.

4.3 Photophysical characterisation

4.3.1 Excitation and Emission spectra

Figure IV-40 shows the excitation and emission spectra of CAU-24. This experiment was carried out on a powder CAU-24 sample on a quartz plate. The maximum emission peak is observed at 390 nm. Therefore, the emission wavelength of this MOF lies in the range of maximum quantum efficiency of photon detection of the PMTs used in the gas detection experiments.

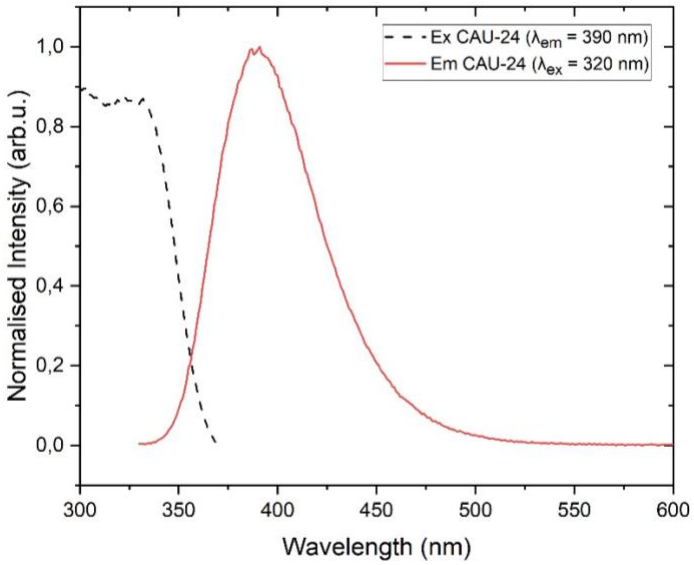

Figure IV-40 Illustrating the excitation and emission spectrum of CAU-24.

4.3.2 TCSPC

Figure IV-41 shows the fluorescence decay of CAU-24 with an excitation diode at 309 nm. By fitting this decay curve with a first-order exponential fit, we can calculate the fluorescence lifetime of CAU-24. The results are shown in Table IV-8, together with the coefficient of determination (R-Square / COD) of the fit. A fluorescence lifetime less than 3 ns is observed here and is ideal for coincidence detection.

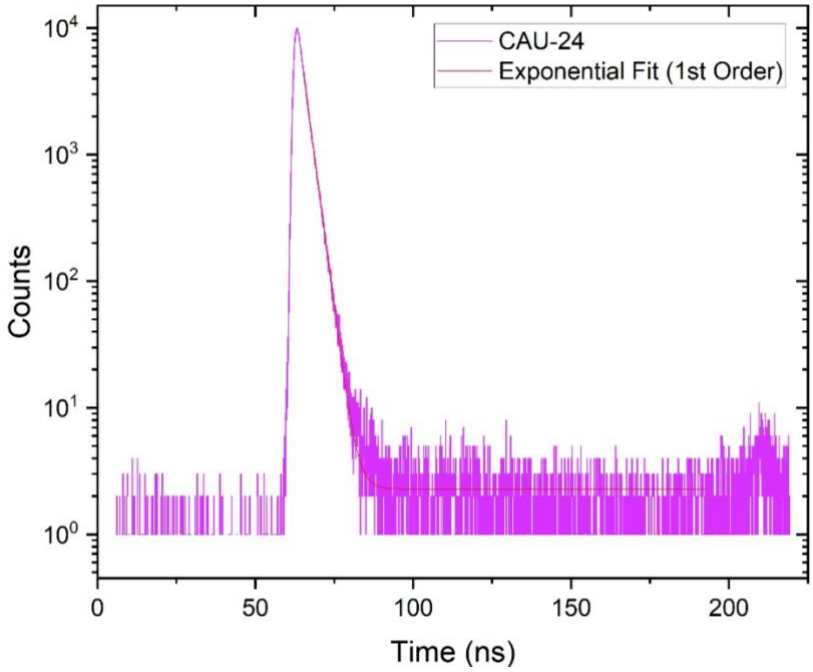

Figure IV-41: Showing the TCSPC results for CAU-24.

Table IV-8: Showing the calculated fluorescence lifetime of CAU-24.

MOF	Diode λ_{ex} (nm)	λ_{em} (nm)	τ_1 (ns)	$<\tau>$ (ns)	R-Square (COD)
CAU-24	309	390	2.3 (100%)	2.3	0.9995

4.4 Radioactive gas bench test

4.4.1 ^{85}Kr

Figure IV-42 shows the results from the detection of ^{85}Kr gas using CAU-24. The D value on the y-axis is the photon count rate calculated by the logical sum of double coincidence between every pair of PMT in the detection system. We can observe that the count rate of CAU-24 is higher than the blank experiment. This means that our MOF does indeed produce photons in the presence of ^{85}Kr and is, hence, a scintillator. We can also observe that the count rate of CAU-24 is slightly higher than that of the microspheres of polystyrene. The photon count rate is 9.4 % higher than the microspheres. Therefore, this experiment shows that CAU-24 is considered as an efficient scintillator for the detection of ^{85}Kr. This slightly higher performance may be attributed to the relatively high surface area and emission in the appropriate wavelength range.

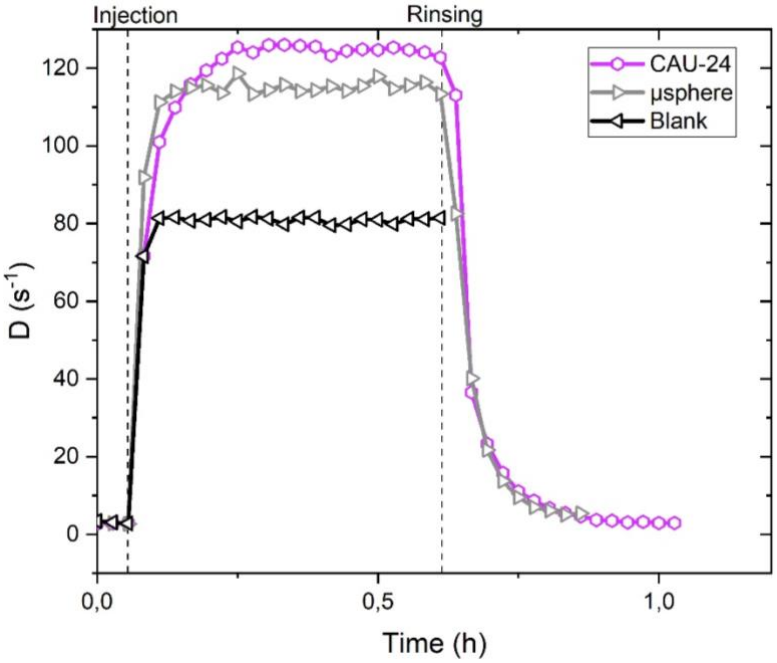

Figure IV-42: Showing the results from ^{85}Kr detection with CAU-24.

5. Comparison and discussion

5.1 Radioluminescence experiments

The results of the RL experiments are shown in Appendix Figure 3. The total number of photons were evaluated by the integral of those curves and compared with respect to an anthracene single crystal. The results are illustrated by the bar chart of Figure IV-43.

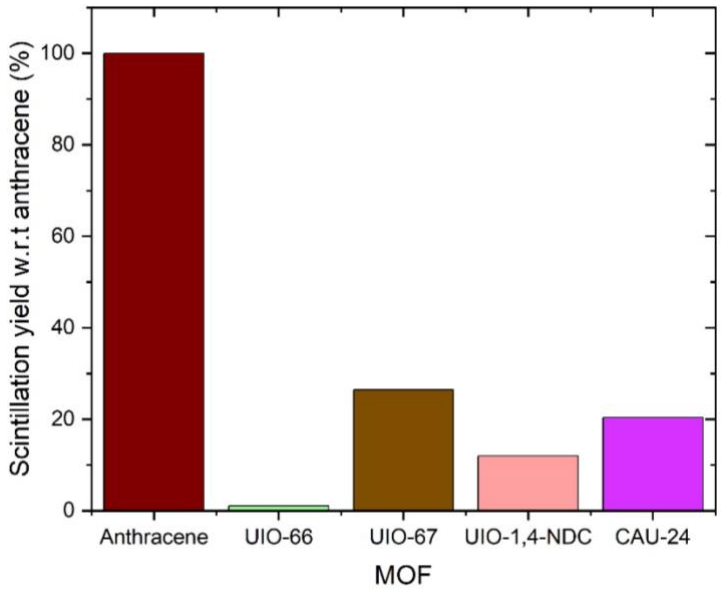

Figure IV-43: Illustrating the percentage scintillation yield of each MOF with respect to an anthracene crystal.

The scintillation yield of the RL experiments are consistent with the gas detection experiments where the least performing to the best performing MOFs are in the following order: UIO-66, UIO-1,4-NDC, CAU-24 and UIO-67.

Using those graphs, we can compare the PL and RL maximum emission wavelength. These results are listed in Table IV-9 together with the scintillation yield in ph.MeV^{-1}.

Table IV-9: Comparing the maximum wavelength of emission of the PL experiments with the RL experiments of activated MOFs and showing the scintillation yields of each MOF calculated via radioluminescence experiments.

	PL λ_{em} (nm)	RL λ_{em} (nm)	Scintillation yield w.r.t Anthracene (%)	Scintillation Yield (ph·MeV^{-1})
Anthracene Single Crystal	-	450	100	15000
UIO-66	365	405	1.1	158
UIO-67	365	420	26	3966
UIO-1,4-NDC	405	433	12	1803
CAU-24	390	418	20	3057

The difference between the PL emission and RL emission is seen to be generally bigger for the Zr-based MOFs studied here than the Zn-based MOFs in Chapter III. One hypothesis that has been put forward is due to the proximity and spatial arrangement of the ligand in Zr-based MOF, which are favourable to π-π interactions[1]. Under X-ray excitation in the RL experiments, this results in the coupling of the excited states and hence a shift in the emission wavelength with respect to the PL emission.

We can notice from the table that the scintillation yield of UIO-66 is extremely low compared to the other MOFs studied here. Even by comparing it to that of its zinc equivalent (MOF-5) we calculate a scintillation yield 2.3 times lower than the latter. Except for UIO-66 all the MOFs studied here have a higher performance than MOF-S1 (1350 ph·MeV^{-1}) and MOF-S2 (3300 ph·MeV^{-1}) studied by F.P. Doty *et al.*[24] and Zr:DPA MOF embedded in a PDMS matric studied by J. Perego *et al.*[25]. J.J. Perry IV *et al.*[26] report the best yield at 79% for DUT-6 which is considerably higher than our results and PCN-14-Zn is reported with a 39% intensity, which remains comparable to our results.

5.2 ^{85}Kr radioactive gas bench test

5.2.1 Photon count rate

Figure IV-44 shows the photon count rate of all the MOFs discussed in this chapter when detecting a 10 kBq or 76 Bq·cm^{-3} of ^{85}Kr gas. For ease of interpretation and comparison, and due to their overall fast decay time, only the results with the 40 ns coincidence window are discussed here. As a reminder from chapter II, the D count represents the logical sum of the double coincidence, which can be viewed as the maximum sum of events seen by the TDCR set-up. The average of each plateau was calculated and subtracted from the average plateau of the blank measurement to obtain the true photon count rate produced by the MOF only. These results are summarised in Table IV-10 with the best results shown in bold.

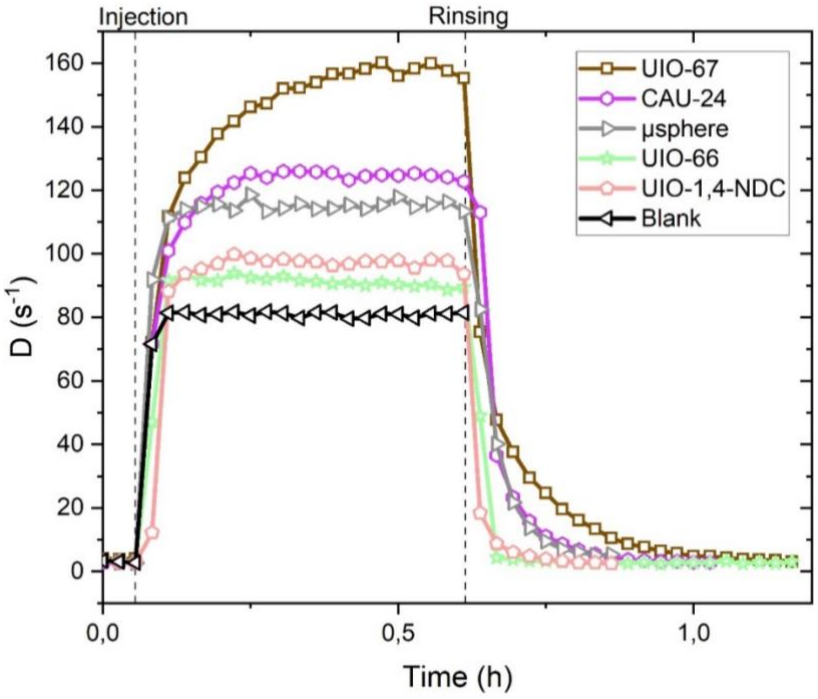

Figure IV-44: Comparing the photon count rate of each UIO/CAU for the detection of 10 kBq of ^{85}Kr.

Table IV-10: Showing the plateau average for each MOF and the µspheres for the 40 ns coincidence window.

	Effective D in cps (CW - 40 ns)
µspheres	34
UIO-66	11
UIO-67	**78**
UIO-1,4-NDC	17
CAU-24	**44**

Table IV-10 shows that UIO-67 and CAU-24 emit more photons than the μspheres of polystyrene and are, therefore, efficient scintillators for the detection of beta radiation from ^{85}Kr. UIO-67 shows a slightly higher effective photon count than the best-performing MOF in Chapter III, MOF-205, with an effective D of 70. This is surprising since MOF-205 exhibited a higher surface area and more appropriate photophysical properties required for our gas detection experiment than UIO-67. However, as we will see in section 5.2.2 below, since they exhibit similar T/D indicator (an indicator of the scintillation efficiency), the slightly higher effective D count for UIO-67 might be attributed to its morphology compared to MOF-205. UIO-67 was synthesised as 0.15 mm single crystals, whereas the single crystals of MOF-205 were synthesised around 3 mm. As it was required in the gas detection experiment to fill the scintillation vial to the same level and UIO-67 being smaller crystals, more crystals were used to fill the scintillation vial. The difference in photon count might be accounted for by a higher quantity of UIO-67 used during the experiment.

5.2.2 T/D indicator

Another indicator of the performance of a MOF as a scintillator is the T/D value that can be obtained from the gas detection experiment. As discussed in Chapter II, the T/D value is an indication of the scintillation yield, and its value approaches 1 for a good scintillator for a specific radionuclei. If we consider the T/D value just at the point of rinsing out the radioactive gas from the system (as encircled in the graphs below), we get the true scintillation yield of the MOF. Figure IV-45 shows the T/D value of UIO-66, UIO-67, UIO-1,4-NDC and CAU-24. We can observe that UIO-66 and UIO-1,4-NDC both have a T/D value less than the μspheres of polystyrene, while UIO-67 and CAU-24 have a higher T/D value than the μspheres of polystyrene (reported in Chapter III as 0.53). The highest T/D value encircled is that of UIO-67, proving that UIO-67 is our best-performing scintillator in this chapter. The T/D values of the MOFs are much closer to 1 than the μspheres thereby concluding that our MOF are better scintillators for ^{85}Kr detection than the μspheres of polystyrene, especially UIO-67 with a T/D value of 0.71. UIO-67 has a T/D value (0.707) also similar to that of our best-performing MOF in Chapter III, MOF-205, with a T/D of 0.713 meaning they exhibit similar performances as scintillators for the detection of ^{85}Kr.

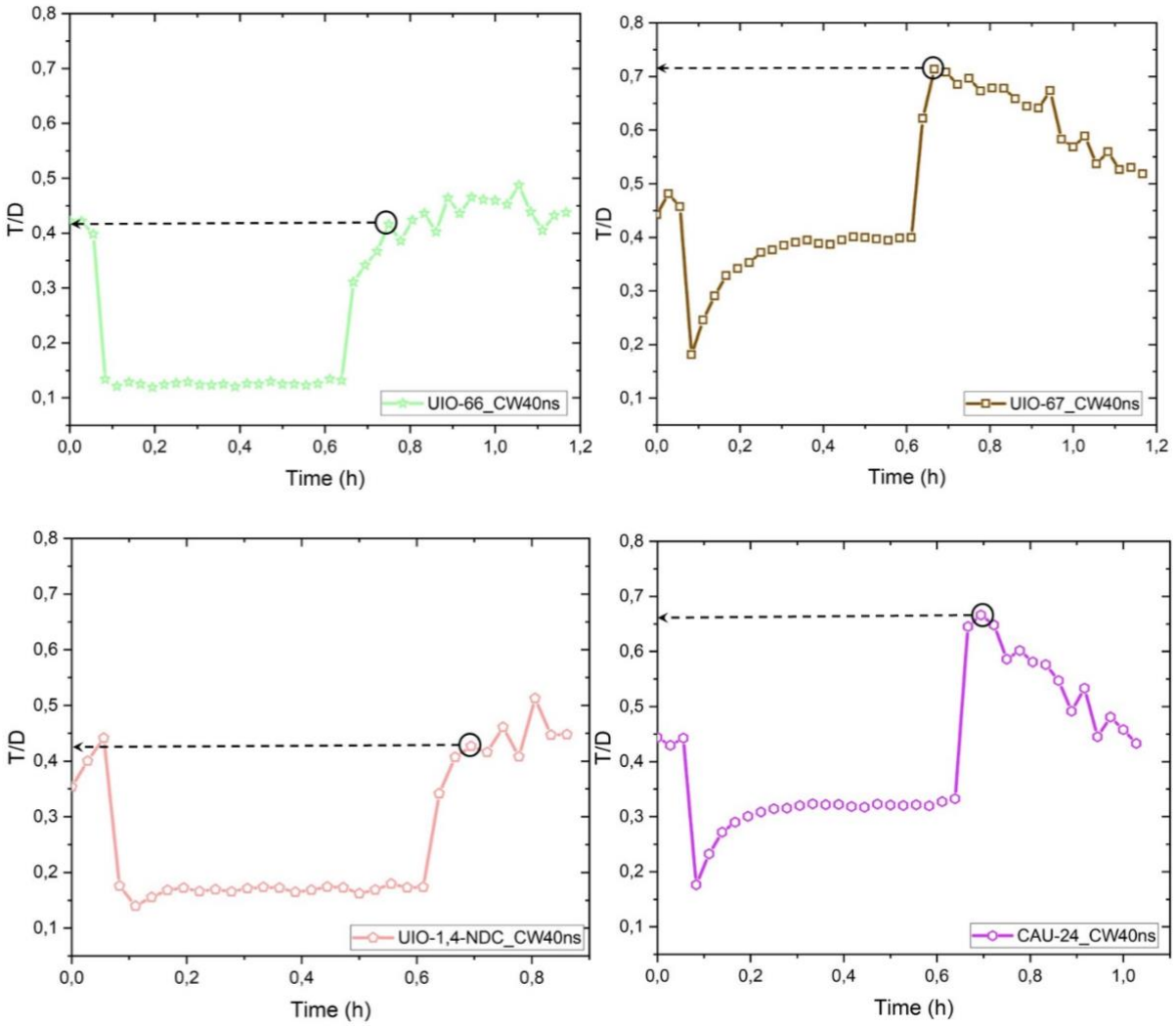

Figure IV-45: Illustrating the T/D evolution of ^{85}Kr detection for UIO-66, UIO-67, UIO-1,4-NDC and CAU-24

6. Chapter Conclusion

In this chapter we demonstrated the synthesis of UIO-66, UIO-67 and UIO-1,4-NDC crystalline powder as well as single crystals of UIO-67. We have demonstrated that by using an excess concentration of modulation we can go from a non-crystalline material to a crystalline MOF. We have proven by structural characterisation that they were indeed the targeted MOFs. We thoroughly investigated their physical and photophysical properties to determine if they were potential candidates for our gas detection experiments.

Through the RL experiment we can say that the MOFs studied in this chapter (except for UIO-66) have higher or comparable scintillation yield to those found in literature, UIO-67 showcasing the highest yield.

We were concluded that UIO-67 and CAU-24 were efficient scintillators for the detection of ^{85}Kr due to their high surface area and emission wavelength. We also compared ^{85}Kr detection

results of MOFs with the same linker but different metal centres showing a better performance for MOF-5 compared to UIO-66 and a better performance of UIO-67 compared to IRMOF-9.

UIO-67 showed the most promising results from the MOFs presented in this chapter and comparable results with MOF-205 in Chapter III per their similar T/D values. This good performance is due to a combination of factors such as its morphology, emission spectrum and surface area.

UIO-67 was found to produce a higher photon count than the two other MOFs tested in this manuscript for ^{222}Rn detection. However, due to non-negligible variations in mass and activity for this sample we cannot conclude that it was indeed the best candidate for ^{222}Rn detection. As for ^{3}H detection, the results are also not comparable to other MOFs due to some unforeseen difference in the activity of the injected gas.

These results validate our approach towards the detection of radioactive gas with Zr-based metal organic frameworks. Since we must still try to lower our limit of detection, as we are just an order of magnitude away to be compliant with industrial and European policy[27], MOF which can have a better scintillation yield also need to be further explored. We will see in Chapter V how we are able to increase the scintillation yield of existing MOFs using an innovative doping strategy.

REFERENCES

1. Villemot, V. Détection de tritium en ligne par cristaux nanoporeux. (2021).
2. Schaate, A. *et al.* A Novel Zr-Based Porous Coordination Polymer Containing Azobenzenedicarboxylate as a Linker. *Eur. J. Inorg. Chem* 790–796 (2012).
3. Schaate, A. *et al.* Modulated synthesis of Zr-based metal-organic frameworks: From nano to single crystals. *Chemistry - A European Journal* **17**, 6643–6651 (2011).
4. Winarta, J. *et al.* A Decade of UiO-66 Research: A Historic Review of Dynamic Structure, Synthesis Mechanisms, and Characterization Techniques of an Archetypal Metal-Organic Framework. *Cryst Growth Des* **20**, 1347–1362 (2020).
5. Butova, V. V. *et al.* Modulator effect in UiO-66-NDC (1, 4-naphthalenedicarboxylic acid) synthesis and comparison with UiO-67-NDC isoreticular metal-organic frameworks. *Cryst Growth Des* **17**, 5422–5431 (2017).
6. Ambroz, F., Macdonald, T. J., Martis, V. & Parkin, I. P. Evaluation of the BET Theory for the Characterization of Meso and Microporous MOFs. *Small Methods* **2**, 1800173 (2018).
7. Ali-Ahmad, A., Hamieh, T., Roques-Carmes, T., Hmadeh, M. & Toufaily, J. Effect of Modulation and Functionalization of UiO-66 Type MOFs on Their Surface Thermodynamic Properties and Lewis Acid–Base Behavior. *Catalysts* **13**, (2023).
8. Su, Z., Miao, Y. R., Zhang, G., Miller, J. T. & Suslick, K. S. Bond breakage under pressure in a metal organic framework. *Chem Sci* **8**, 8004–8011 (2017).
9. Jiao, Y. *et al.* Heat-Treatment of Defective UiO-66 from Modulated Synthesis: Adsorption and Stability Studies. *Journal of Physical Chemistry C* **121**, 23471–23479 (2017).
10. Healy, C. *et al.* The thermal stability of metal-organic frameworks. *Coord Chem Rev* **419**, 213388 (2020).
11. Athar, M., Rzepka, P., Thoeny, D., Ranocchiari, M. & Anton Van Bokhoven, J. Thermal degradation of defective high-surface-area UiO-66 in different gaseous environments. *RSC Adv* **11**, 38849–38855 (2021).
12. Shearer, G. C. *et al.* In situ infrared spectroscopic and gravimetric characterisation of the solvent removal and dehydroxylation of the metal organic frameworks UiO-66 and UiO-67. *Top Catal* **56**, 770–782 (2013).
13. Valenzano, L. *et al.* Disclosing the complex structure of UiO-66 metal organic framework: A synergic combination of experiment and theory. *Chemistry of Materials* **23**, 1700–1718 (2011).

14. Xu, W., Dong, M., Di, L. & Zhang, X. A facile method for preparing uio-66 encapsulated ru catalyst and its application in plasma-assisted CO2 methanation. *Nanomaterials* **9**, 10–13 (2019).

15. Taniguchi, M. & Lindsey, J. S. Database of Absorption and Fluorescence Spectra of >300 Common Compounds for use in PhotochemCAD. *Photochem Photobiol* **94**, 290–327 (2018).

16. Vahabi, A. H., Norouzi, F., Sheibani, E. & Rahimi-Nasrabadi, M. Functionalized Zr-UiO-67 metal-organic frameworks: Structural landscape and application. *Coord Chem Rev* **445**, 214050 (2021).

17. Zhao, W. *et al.* Preparation, characterization, and performance evaluation of UiO-66 analogues as stationary phase in HPLC for the separation of substituted benzenes and polycyclic aromatic hydrocarbons. *PLoS One* **12**, 1–13 (2017).

18. Zhang, Y., Xiao, H., Zhou, X., Wang, X. & Li, Z. Selective Adsorption Performances of UiO-67 for Separation of Light Hydrocarbons C1, C2, and C3. *Ind Eng Chem Res* **56**, 8689–8696 (2017).

19. Chapon, A., Pigrée, G., Putmans, V. & Rogel, G. Optimization of liquid scintillation measurements applied to smears and aqueous samples collected in industrial environments. *Results Phys* **6**, 50–58 (2016).

20. He, Y. *et al.* UiO-66-NDC (1,4-naphthalenedicarboxilic acid) as a novel fluorescent probe for the selective detection of Fe3+. *J Solid State Chem* **285**, 121206 (2020).

21. Lammert, M. *et al.* Synthesis and structure of Zr(IV)- and Ce(IV)-based CAU-24 with 1,2,4,5-tetrakis(4-carboxyphenyl)benzene. *Dalton Transactions* **45**, 18822–18826 (2016).

22. Li, Z. *et al.* A water-stable luminescent metal-organic framework for effective detection of aflatoxin B1 in walnut and almond beverages. *RSC Adv* **9**, 620–625 (2019).

23. Shen, C. H. *et al.* Probing the electronic and ionic transport in topologically distinct redox-active metal-organic frameworks in aqueous electrolytes. *Physical Chemistry Chemical Physics* **24**, 9855–9865 (2022).

24. Doty, F. P., Bauer, C. A., Skulan, A. J., Grant, P. G. & Allendorf, M. D. Scintillating metal-organic frameworks: A new class of radiation detection materials. *Advanced Materials* **21**, 95–101 (2009).

25. Perego, J. *et al.* Composite fast scintillators based on high-Z fluorescent metal–organic framework nanocrystals. *Nat Photonics* **15**, 393–400 (2021).

26. Perry Iv, J. J. *et al.* Connecting structure with function in metal-organic frameworks to design novel photo- and radioluminescent materials. *J Mater Chem* **22**, 10235–10248 (2012).

27. European Commision. Commission Recommendation of 18 December 2003 on standardised information on radioactive airborne and liquid discharges into the environment from nuclear power reactors and reprocessing plants in normal operation (2004/2/Euratom). *Official Journal of the European Union* 1–36 (2004).

Chapter V: Enhancing scintillating properties of MOFs via a doping strategy

V. Enhancing scintillating properties of MOFs via a doping strategy

We have seen so far that the fluorescence properties of the MOFs studied here are governed by the ligand that constitute them. This is because we are using metal centres with d^0 and d^{10} empty and full electronic configuration thereby reducing the probability of d-d orbital transition. It therefore becomes essential for our application to move towards a MOF made up of a highly fluorescent ligand. Anthracene is a popular reference material in the field of organic scintillation, known to exhibit a scintillation yield of nearly 15000 photons per MeV in its monocrystalline state. Figure V-1 derived from Taniguchi *et al.* shows us not only that the emission wavelength of anthracene is in a more appropriate wavelength range for the PMTs used in the gas detection experiment but it also points out that anthracene has a higher quantum yield of fluorescence than the benzene or naphthalene ligands we have explored thus far.

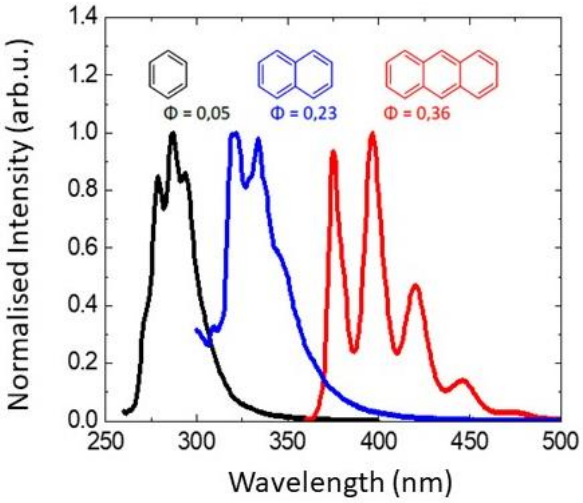

Figure V-1: Emission spectra of benzene, naphthalene and anthracene in cyclohexane together with the quantum yield of fluorescence of each molecule[1].

We therefore saw it fit to synthesise a MOF based on the carboxylate derivative of anthracene: 9-10-anthracene dicarboxylic acid (ADC). The synthesis of powder or millimetric single crystal of Zn-based MOF with solely the ADC ligand, has proven to be quite complex and is to this day unsuccessful. This may be due to the bulkiness of the ADC ligand. However, this misstep made us think of another strategy to incorporate this ligand in our MOF so as to benefit from its high scintillation yield. The doping strategy is certainly innovative for MOFs but has demonstrated to be highly beneficial in the field of plastic scintillators. Since the carboxylate-carboxylate bond length in the 1,4-BDC, 1,4-NDC and 9,10-ADC ligands are similar, we can substitute some BDC or NDC ligands from the MOFs based on 1,4-BDC or 1,4-NDC. For

example, some MOF we have already explored in Chapter III and IV are good candidate for this approach without altering too much their structure, symmetry and porosity. Another advantage of this strategy is the high cost of the ADC ligand compared to the other ligands used for the synthesis of MOFs. As we will see, the doping strategy allows us to use a small quantity of ADC ligand and still reap the benefits of its fluorescence properties thereby limiting the cost. It is important to note that the doping percentages shown in this chapter are those of the ADC precursor. We are not able to evaluate for now whether the percentage of dopant precursor used in the synthesis has been fully incorporated within the structure of the MOF.

We started the doping strategy with Zn-based MOFs rather than directly with Zr-based MOFs since we had already mastered their synthesis when we started exploring this avenue. Synthesising both Zn and Zr-based doped MOFs was also a way to study the effect of doping on both of them and scrutinise any difference in physical and photophysical properties that may or may not occur. Even though we have concluded in Chapter III that IRMOF-7 was not a MOF, we still wanted to study the effect of doping on this material since it presented relatively good scintillation yield during the radioluminescence experiment. Studying the effect of doping on this non-porous crystalline scintillating material for ^{85}Kr detection also allows us to investigate how it compares to the porous scintillating MOFs of this manuscript, thereby giving us an indication of the importance of porosity for this application. The doping strategy with ADC was not possible on our best performing MOF from Chapter IV, UIO-67, because of the different ligand configuration between ADC and BPDC.

Just like in the other chapters, the structural characterisation will help us determine if we have indeed synthesised the respective doped MOF. Their physical properties will be compared to their undoped counterparts. For the photophysical characterisation, we will mainly determine the effect of doping on the emission wavelength and fluorescence lifetime of our MOF. We will analyse if doping shifts the emission of our MOF in the correct wavelength range for the PMTs used in the gas detection experiments. The effect of doping on the scintillation yield of the doped MOF-5 and IRMOF-7 will also be analysed in this chapter where we will also see the limitation of the doping strategy.

We will also analyse the results from the gas detection experiments individually for every MOF and compare them with one another in the last section of this chapter. ^{85}Kr detection experiments have been performed on each MOF in this chapter, and the one with the best results was also used to carry out ^{3}H and ^{222}Rn detection experiments as done with MOF-205 and UIO-67 in Chapter III and Chapter IV respectively. The results for the radioluminescence experiments will also be studied and compared in the last section of this chapter.

1. Doped MOF-5

1.1 Synthesis

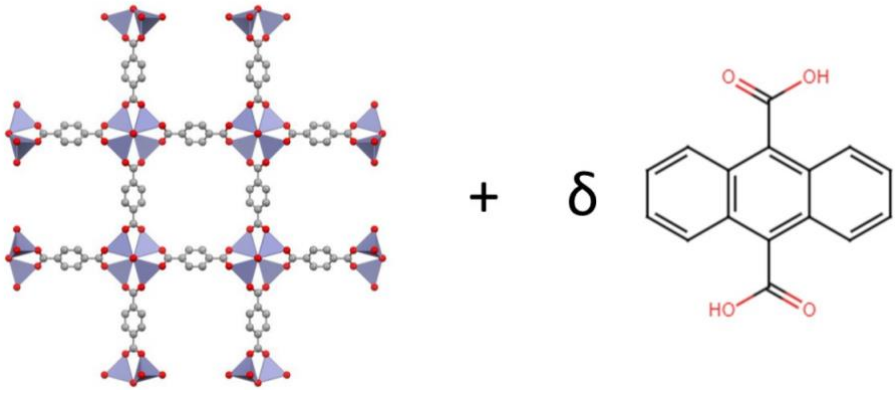

Figure V-2: Illustrating the doping strategy for the MOF-5 lattice.

Table V-1: Showing the doped MOF-5 synthesis protocol.

Doping %	1.38%	2.7%	5.5%	11.1%
ADC:BDC ratio	1:72	1:36	1:18	1:9
ADC:Unit cell	1:24	1:12	1:6	1:3

The doping strategy for MOF-5 consist of substituting the BDC ligand with the ADC ligand as summarised in Figure V-2. We set out to substitute one BDC ligand every 3 unit cell as shown in the far right column. Since MOF-5 has a composition of $Zn_4O(BDC)_3$, meaning 3 BDC ligands are present in every unit cell. Therefore substituting 1 BDC ligand every 3 unit cells is equivalent to substituting 1 BDC every 9 BDC (or adding 1 ADC every 9 BDC). With this 1:9 ratio we can calculate the molar doping % from Equation V-1.

$$\frac{1}{9} \times 100 = 11.1\ \%$$

Equation V-1

We then moved towards lower doping percentages by dividing the $\frac{1}{9}$ ratio by a factor of 2 each time leading to the ratios in the table (right to left) and their associated percentage calculated using Equation V-1.

Since this was the first MOF we doped, five doping percentages were explored. By tuning the synthesis protocol, especially the concentration of the precursors, we were able to synthesis millimetric single crystals of all five doped versions of MOF-5. For ease of interpretation and

comparison with the other MOFs in this chapter, only MOF-5 + 1.38% ADC and MOF-5 + 5.5% ADC have been fully characterised and tested.

Protocol for MOF-5 + 1.38% ADC

For this synthesis the same concentration of metal and combined ligand/s as for MOF-5 synthesis was used to successfully obtain single crystals of MOF-5 + 1.38% ADC. $Zn(NO_3)_2 \cdot 6H_2O$ (0.118 mol·L^{-1}, 3.54 g), 1,4-benzenedicarboxylic acid (0.0375 mol·L^{-1}, 623 mg) and 9,10-anthracenedicarboxylic acid (0.0005 mol·L^{-1}, 14 mg) were dissolved in 100 mL of *N*,*N*-diethylformamide (DEF). The mixture was equally divided into twelve 10 mL scintillation vials, which were then sealed with a screw cap. The vials were placed in an oven at 75°C for 192 hours (8 days) yielding millimetric sized doped MOF-5 + 1.38% ADC single crystals. The closed vials were removed and placed in an N_2 glovebox. The crystals were washed according to the protocol described in Chapter II.

Protocol for MOF-5 + 5.5% ADC

Using the same concentration of metal and combined ligand/s as for undoped MOF-5 or MOF-5 + 1.38% ADC proved unsuccessful for MOF-5 + 5.5% ADC. At these concentrations, non-crystalline powders were obtained. As we were increasing the percentage of ADC dopant, we were increasing the addition of the bulky ADC ligand, which made the crystallisation process more complex. Fast precipitation occurred instead of crystallisation. Dividing the overall concentration of the precursors in the solution by two allowed us to slow down the nucleation rate, successfully obtaining millimetric single crystals of MOF-5 + 5.5% ADC.

$Zn(NO_3)_2 \cdot 6H_2O$ (0.060 mol·L^{-1}, 1.77 g), 1,4-benzenedicarboxylic acid (0.0179 mol·L^{-1}, 297 mg) and 9,10-anthracenedicarboxylic acid (0.00105 mol·L^{-1}, 28 mg) were dissolved in 100 mL of *N*,*N*-diethylformamide (DEF). The mixture was equally divided into twelve 10 mL scintillation vials, which were then sealed with a screw cap. The vials were placed in an oven at 75°C for 192 h (8 days) yielding millimetric sized doped MOF-5 + 5.5% ADC single crystals. The closed vials were removed and placed in an N_2 glovebox. The crystals were washed according to the protocol described in Chapter II.

1.2 Structural characterisation

1.2.1 X-Ray Diffraction

Figure V-3 shows the X-ray Diffraction spectrum of our two doped MOF-5 sample compared to the undoped MOF-5 studied in Chapter III and the simulated XRD from the first reported work of Yaghi *et al.*[2] The peak positions are similar for all the sets indicating that we have indeed synthesised doped versions of MOF-5 single crystals. However, we can see that the peak intensity varies because the XRD we carried out was a powdered XRD done by crushing single crystals of MOF-5 on a sample holder. Compared to a single X-ray diffraction, this method will

lead to preferential orientation of the crystals and hence influence the intensity for the different diffraction planes. Since the do not observe any additional peak between MOF-5 and MOF-5 + 1.38% ADC, we can conclude that the doping is homogenous. It is however difficult to tell if a difference would be observed at such low doping percentages. The MOF-5 + 5.5% ADC however reveal some additional peaks compared to the others which might be due to a non-homogenous doping with the MOF-5 lattice.

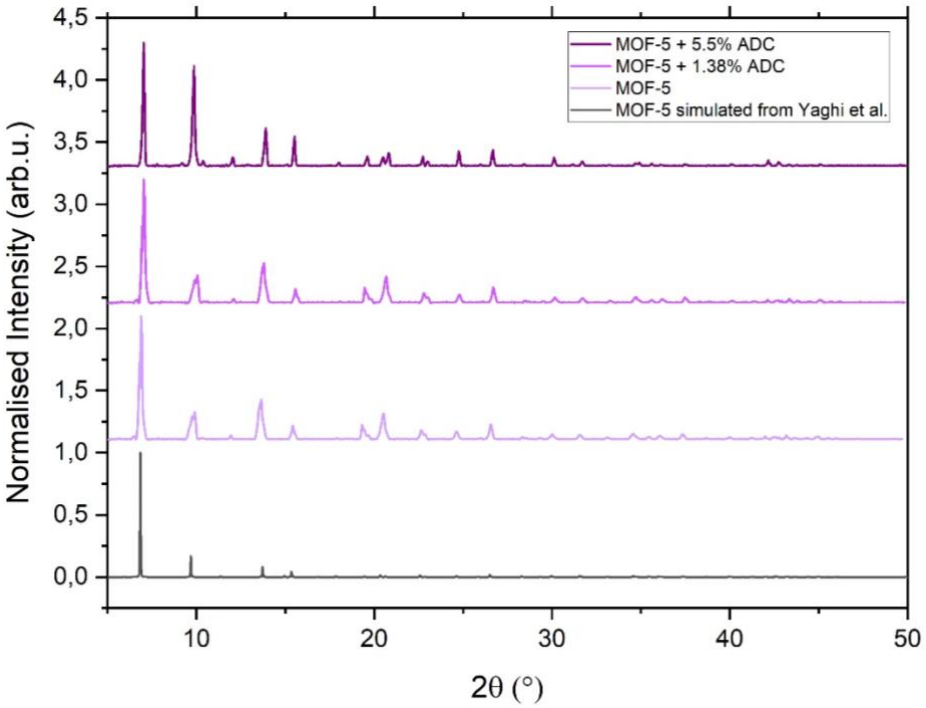

Figure V-3: PXRD spectrum showing experimental results of each doped MOF-5 compared to the undoped MOF-5 and literature.

1.2.2 Adsorption measurements

The N_2 adsorption experiments for MOF-5 and its doped counterparts were all carried out at the University of Milano-Bicocca using the same equipment for comparison purposes. The N_2 adsorption isotherm is illustrated in Figure V-4 and Table V-2 shows the results extracted from these data. The Type I isotherms confirms the microporosity of our MOF with a pore width of 12.5 Å for all three MOFs. The BET surface area of the MOFs are relatively high and consistent with literature values reported for MOF-5[3,4]. No definitive trend is observed between the BET surface area and the doping percentage. One would expect a decrease in the pores while inserting a bulky ligand such as ADC but the doping percentages are still insignificant here to cause such changes.

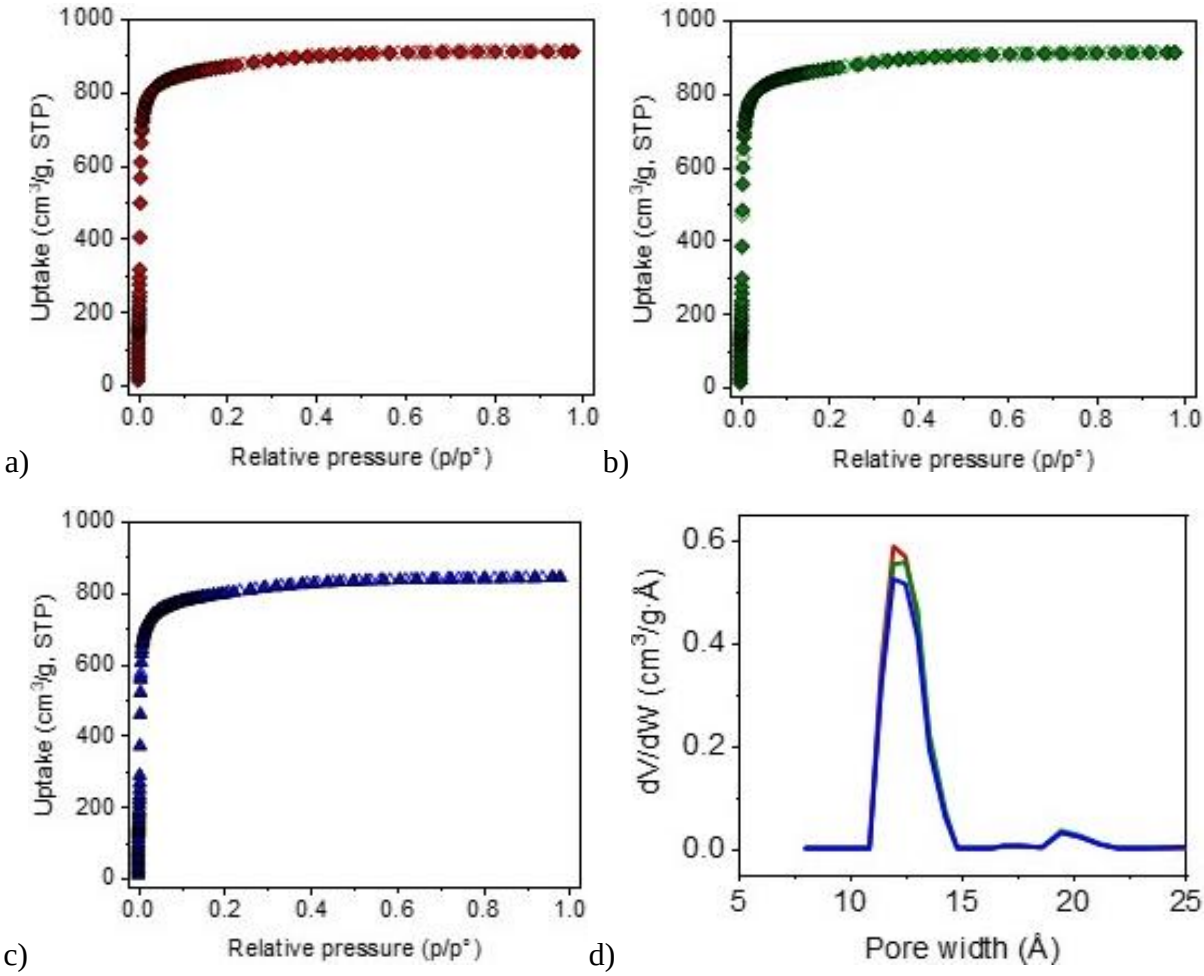

Figure V-4: Illustrating the N_2 adsorption isotherm of a) MOF-5, b) MOF-5 + 1.38% ADC, c) MOF-5 + 5.5% ADC and d) the pore width measurements of the three MOFs, red – MOF-5, green – MOF-5 + 1.38% ADC, blue – MOF-5 + 5.5% ADC.

Table V-2: Summarising the data calculated from N_2 adsorption of undoped MOF-5 and its doped counterparts.

MOF	BET SA ($m^2 \cdot g^{-1}$)	Pore size (Å)	Pore volume ($cm^3 \cdot g^{-1}$)
MOF-5	3360	12.5	1.27
MOF-5+1.38% ADC	3752	12.5	1.27
MOF-5+5.5% ADC	3444	12. 5	1.18

1.2.3 Thermogravimetric Analysis

Figure V-5 shows the TGA results of MOF-5 and its doped counterparts. Similar to the MOFs in Chapter III, we can observe a drop before 100°C accounting for surface water and residual DCM loss. This loss is slightly different for each MOF due to sample preparation. A significant

drop in the weight of the sample between 350-500°C is also observed. This result is consistent with the literature where the decomposition temperature (T_d) is reported to be between 400-500 °C depending on the sample preparation, activation and experimental conditions[5]. The MOF decomposes to ZnO at these temperatures. The beginning and end of decomposition happens at a slightly lower temperature for the undoped MOF-5 than the doped counterparts.

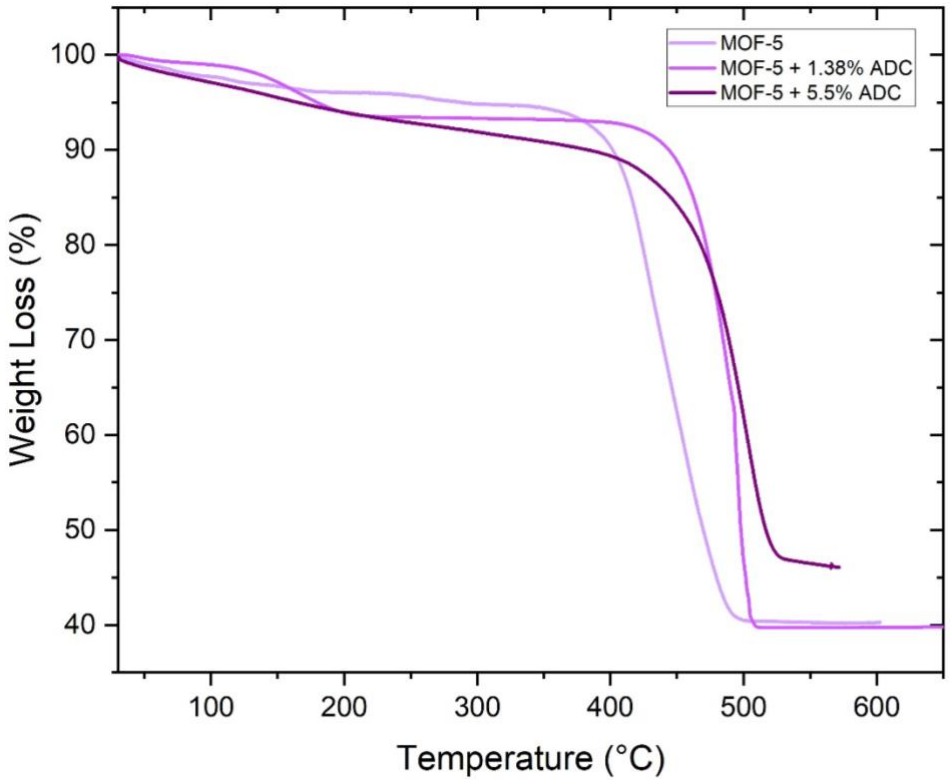

Figure V-5: TGA results of MOF-5 and its doped counterparts.

1.2.4 FT-IR experiments

As seen in Chapter III, the FT-IR spectrum of MOF-5 is consistent with literature. The initial aim of performing FT-IR experiments on the doped MOFs was to try and observe the incorporation of the ADC ligand in the MOF. However, as we can see from Figure V-6, the spectrum of the doped and undoped versions of MOF-5 are identical meaning that at such a low doping percentage the doping is undetectable by our FT-IR experiments. The structure of the BDC and added ADC ligand are so similar that they should exhibit little to no changes in an FT-IR experiment. The same was observed by J. Perego *et al.*[6] when they incorporated 1% DPA

in their Zr-MOF with a main DPT ligand as discussed in Chapter I. Maybe with access to a more precise IR set-up some minor difference could be observed in the 600 to 1600 cm^{-1} region.

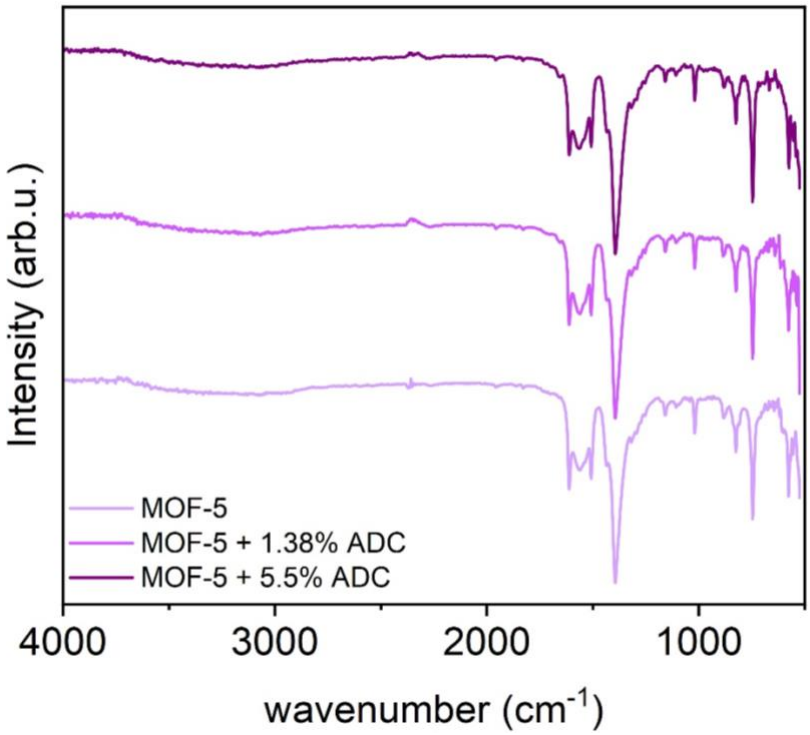

Figure V-6: Showing FT-IR results for MOF-5 and its doped counterparts.

1.2.5 ^{13}C, ^{1}H and ^{129}Xe NMR results

Figure V-7 shows the ^{13}C {^{1}H} solid-state NMR of MOF-5 + 1.38% ADC. We can observe three narrow signals. Unlike for MOF-205 (Chapter III), a single COO^- signal is observed here even though MOF-5 + 1.38% ADC is made up of two ligands as illustrated in Figure V-8. This is because doping percentage of the ADC ligand is very low compared to a 2:3 ligand ratio in MOF-205. We can also observe the absence of any signal related to residual solvent such as DMF or DCM confirming that our MOF has been well activated. The ^{1}H solid state NMR in Figure V-9 only reveals one CH peak signal compared to MOF-205, again because of the low doping percentages for MOF-5.

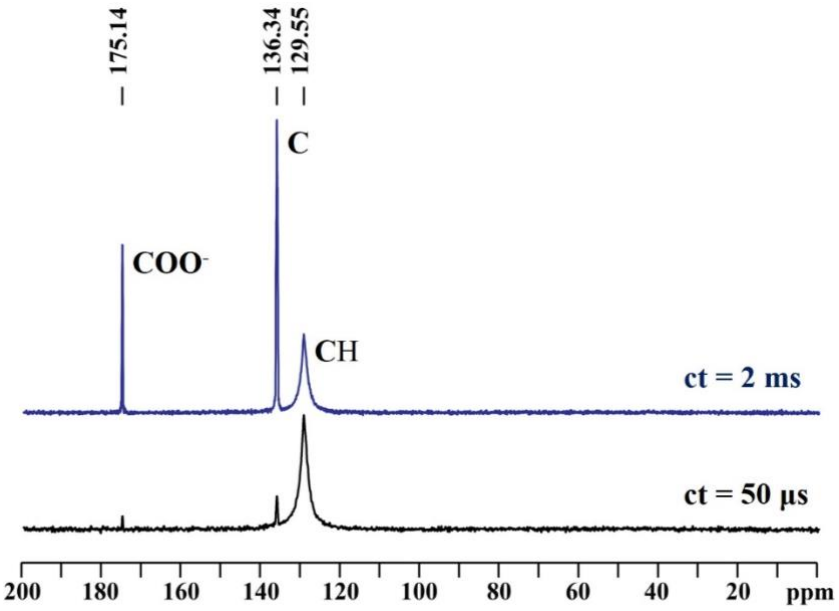

Figure V-7: Illustrating the ^{13}C {^{1}H} solid-state NMR of MOF-5 + 1.38% ADC.

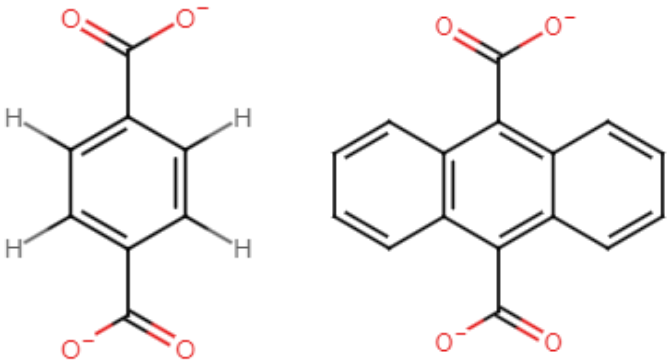

Figure V-8: Illustrating both ligands present in MOF-5 + 1.38% ADC to analyse the solid state NMR.

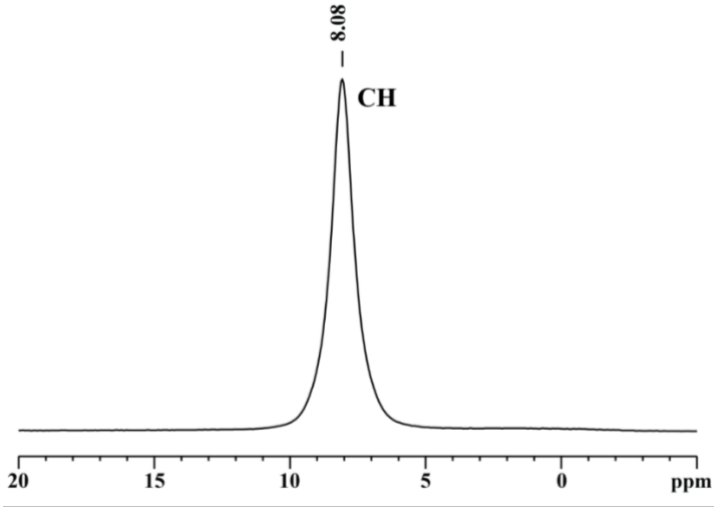

Figure V-9: Illustrating the ^{1}H solid-state NMR of MOF-5 + 1.38% ADC.

Figure V-10 below shows the Continuous Flow Hyperpolarised (CW-HP) ^{129}Xe NMR results on MOF-5 + 1.38% ADC, which can help us determine the accessibility of the pores to a noble gas such a Xe. The experiments performed at low partial pressure ensure that intermolecular interactions of Xenon with the framework prevail, while Xe-Xe interactions are negligible. Thus, the Xenon chemical shifts depend only on the environment of Xenon confined in restricted spaces. The ^{129}Xe NMR spectra of MOF-5 + 1.38% ADC at 192 K reveal a predominant signal in the region at ≈ 50 ppm that are different from the free gas (at 0 ppm), indicating a fast diffusion of Xenon atoms in the confining cavities. What we are observing in the CW-HP ^{129}Xe NMR experiment is the variation of interaction from a xenon atom. At low temperature, the Xe move slowly and are interacts in a specific way in each type of pores. When temperature increases, this interaction becomes more and more similar due to molecular agitation. We can observe that the signals gradually change from one to two peaks as the temperature increases meaning that the gas is interacting with two types of pores. Even though two pore sizes were not observed by our N_2 adsorption experiments above, the two pore sizes of MOF-5 have been calculated by simulation and crystallographic data in literature[7]. On lowering the temperature, the signals shift downfield due to the increase of Xe interactions with the walls and the HP Xe mainly explores the larger cavities leaving one peak. The signal in the ^{129}Xe experiment can be observed only a few ms (< 200 ms) after the contact of the gas with the porous materials. The experiments were performed at only 2% concentration of Xe diluted in 4% N_2 and 94% He, meaning that Xe is efficiently adsorbed even at low partial pressure. We performed experiments with 1% Xe concentration and the result does not change confirming the above considerations. Xenon is an intermediate element in the column of the periodic table with respect to the radioactive targeted noble gases ^{85}Kr and ^{222}Rn. Thus, this experiment performed under a continuous flow of Xenon and at room temperature directly demonstrates the absorption of noble gas within MOF-205 and give us a good demonstration of its interaction with such a gas.

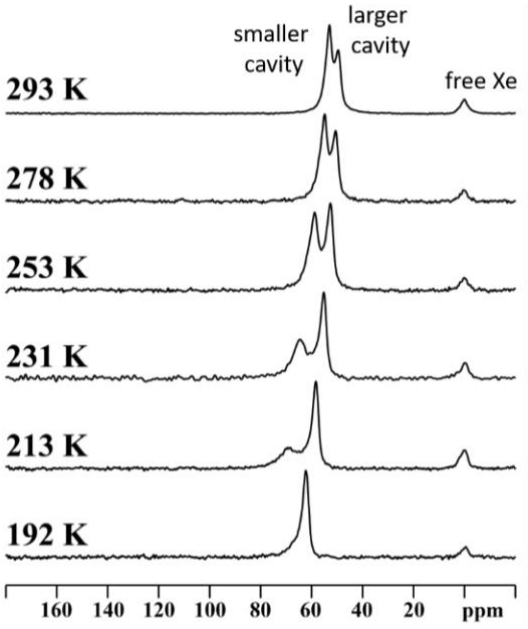

Figure V-10: Illustrating hyperpolarised ^{129}Xe NMR of MOF-5 + 1.38% ADC.

1.3 Photophysical characterisation

1.3.1 Excitation and Emission spectra

As we remember from Chapter III and as we can see in Figure V-11 the emission of MOF-5 is very similar to a 10^{-5} M solution of its ligand (BDC) in DMF. Because MOF-5 is made from d^0 Zn metal, electronic transition involving the metal is least probable. Therefore, the fluorescence of MOF-5 is centred on its ligand. The slight bathochromic shift is due to the rigidification of the ligand in the MOF structure after the coordination with the Zn_4O clusters. As we have seen in Chapter III, the peak emission wavelength of MOF-5 is at 341 nm and hence not ideal for our gas detection experiment since it does not emit in the range of maximum quantum efficiency of photon detection of the PMTs used. We can see in Figure V-11 that by doping our MOF-5 with a small percentage of ADC ligand (1.38% ADC or 5.5% ADC), we have shifted the emission of the MOF-5 from the BDC to being centred on the ADC ligand around 430 nm. MOF-5 + 1.38% ADC and MOF-5 + 5.5% ADC hence both emit in the correct wavelength range for the PMTs. Note that the detailed excitation and emission spectrum of each of each doped MOF in this Chapter can be found in the Appendix Figures 6-9. From Appendix Figure 4, which shows the emission and excitation of both ligands present in this MOF, we can observe an overlap between the excitation spectra of the ADC ligand and the emission of the BDC ligand (both ligands in 10^{-5} M DMF solution). Therefore, we can imagine that in our MOF, the BDC ligand gets excited first and emits photons or transfers its energy to the ADC ligand.

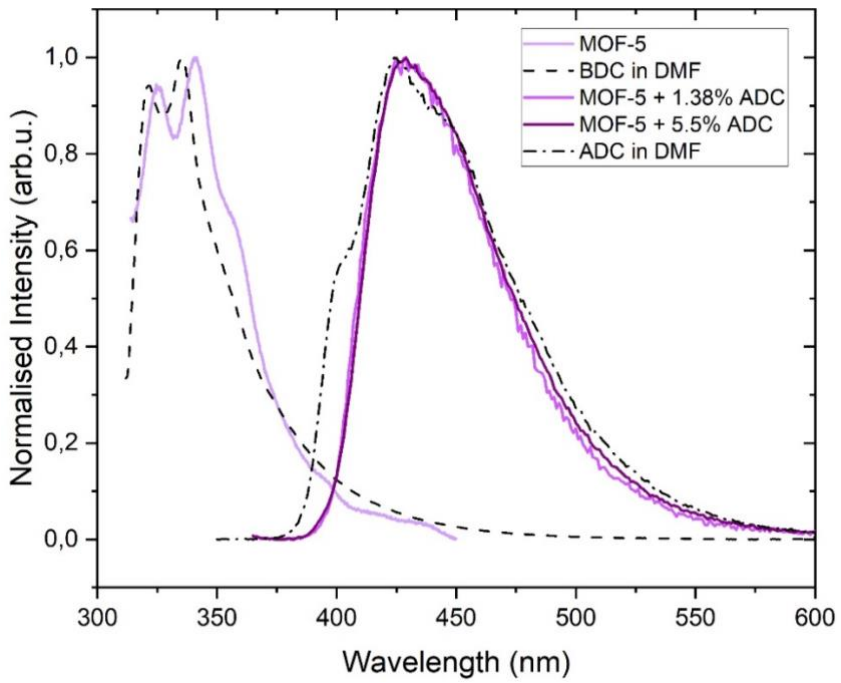

Figure V-11: Emission spectrum of MOF-5 and its doped counterparts (solid lines), BDC ligand in DMF (dashed line) and ADC ligand in DMF (dotted line).

Figure V-12 gives us a simplified qualitative overview of the effect of doping on MOF-5. We can see that even at such a low doping percentage as 1.38% ADC, we are observed a significant increase in the fluorescence yield of the MOF-5 single crystals. We will later observe the effect this has on the photons production in gas detection experiments. We can also see that the light intensity seems to decrease from MOF-5 + 1.38% ADC to MOF-5 + 5.5% ADC even though we have incorporated more ADC ligand. Before explaining this phenomenon, we will investigate the effect of doping on the scintillation yield using a more qualitative method in section 1.3.3 below.

Figure V-12: Showing the fluorescence of a) MOF-5 crystals, b) MOF-5 + 1.38% ADC and c) MOF-5 + 5.5% ADC under an ultraviolet lamp at 365 nm excitation.

1.3.1 TCSPC

Figure V-13 shows the fluorescence decay of MOF-5 with a 274 nm excitation diode and doped MOF-5 with a 368 nm excitation diode since the fluorescence is centred on the ADC ligand. With this excitation wavelength for the doped MOF, we would only be monitoring the decay from the ADC ligand since the BDC is excited at a lower wavelength. Since there are two ligands present in this MOF whose emission and excitation wavelengths overlap, there is a possibility for energy transfer between the ligand (such as in MOF-205). Therefore, assigning the fluorescence lifetime measure here to the MOF assumes that the energy transfer between both ligands is non-radiative. A more in depth study of the fluorescence lifetime contribution of both ligands in the MOFs presented in this chapter should be investigated in the future to

determine if the energy transfer is indeed non-radiative and hence get a more precise fluorescence lifetime for the doped MOFs. The decay of MOF-5 was reported from an in depth photophysical study performed by V.Villemot *et al.*[8] at our laboratory. By fitting this decay curve with a 2nd order exponential fit for the doped MOF-5, we can calculate the fluorescence lifetime components, their respective weights, and an average fluorescence lifetime. The results are summarised in Table V-3, together with the coefficient of determination (R-Square / COD) of the fit. We can see that the average fluorescence lifetimes of the two doped MOF-5 are similar. We can also observe an increase in the fluorescence lifetimes of the doped MOF-5 compared to the undoped MOF-5 (similar to what we will see for ADC-doped UIO-66 and UIO-1,4-NDC) meaning this is slightly more inconvenient for coincidence detection since faster fluorescence lifetimes are desired. However, they remain in at an acceptable value below 10 ns.

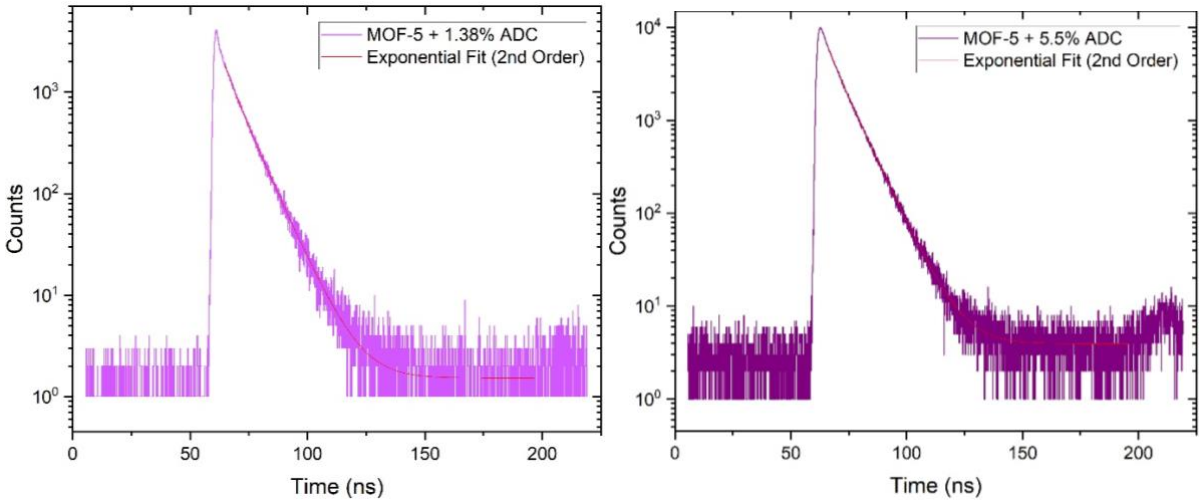

Figure V-13: Showing the TCSPC results of MOF-5 and its doped counterparts.

Table V-3: Showing the calculated fluorescence lifetime of MOF-5 and its doped counterparts.

MOF	**Diode λ_{ex} (nm)**	**λ_{em}**	**τ_1 (ns)**	**τ_2 (ns)**	**τ_3 (ns)**	**<τ> (ns)**	**R-Square (COD)**
MOF-5	274	350	1.5 (100%)	-	-	1.5	-
MOF-5 + 1.38% ADC	368	430	8.6 (73.3%)	4.3 (26.7%)	-	7.5	0.9987
MOF-5 + 5.5% ADC	368	430	8.2 (82.2%)	3.8 (17.8%)	-	7.4	0.9996

1.3.2 Photoluminescence light yield

By performing the photoluminescence light yield experiments using an integrating sphere as explained in section 3.3 of Chapter II, we obtain the photoluminescence intensity vs wavelength results as shown in Figure V-14. This experiment cannot be performed on MOF-5 due to its short emission wavelength. By comparing the different photoluminescence yield of each doped MOF, we can see from Figure V-14 that emission intensity decreases as we increase the doping percentage. One possible explanation is due to a photon reabsorption when doping with too much anthracene.

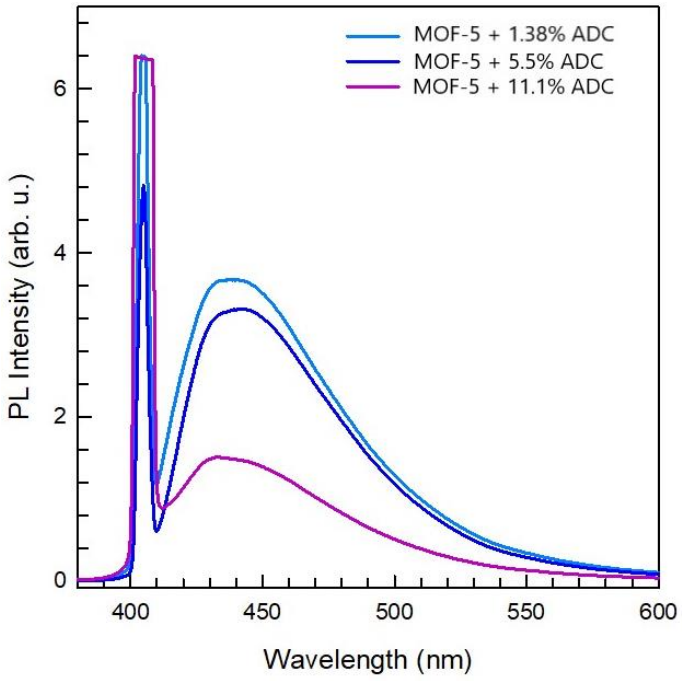

Figure V-14: Photoluminescence light yield of doped MOF-5 single crystals using the integrating sphere method.

We have noticed that while activating our MOF single crystals we have a significant loss in the transparency of our crystals. Since transparency is of utmost importance in the field of scintillators, because diffusion affects the photons pathway and hence the amount of photons emitted by our MOFs. Hence, we wanted to quantify this loss in transparency using the same integrating sphere method. We can see from Figure V-15 that the photoluminescence light yield of the activated MOF samples are significantly less (more than 75% of the intensity) compared to the single crystals in DMF. The experiment was also done with DMF only and the contribution of the solvent emission was concluded to be negligible. This decrease is seen to be more significant for MOF-5 + 5.5% ADC than MOF-5 + 1.38% ADC. We can conclude that we lose a significant amount of photon production and detection by activating of MOFs via the

loss in transparency of the crystals. However, this activation process is necessary to access the pores of the MOF for gas interaction.

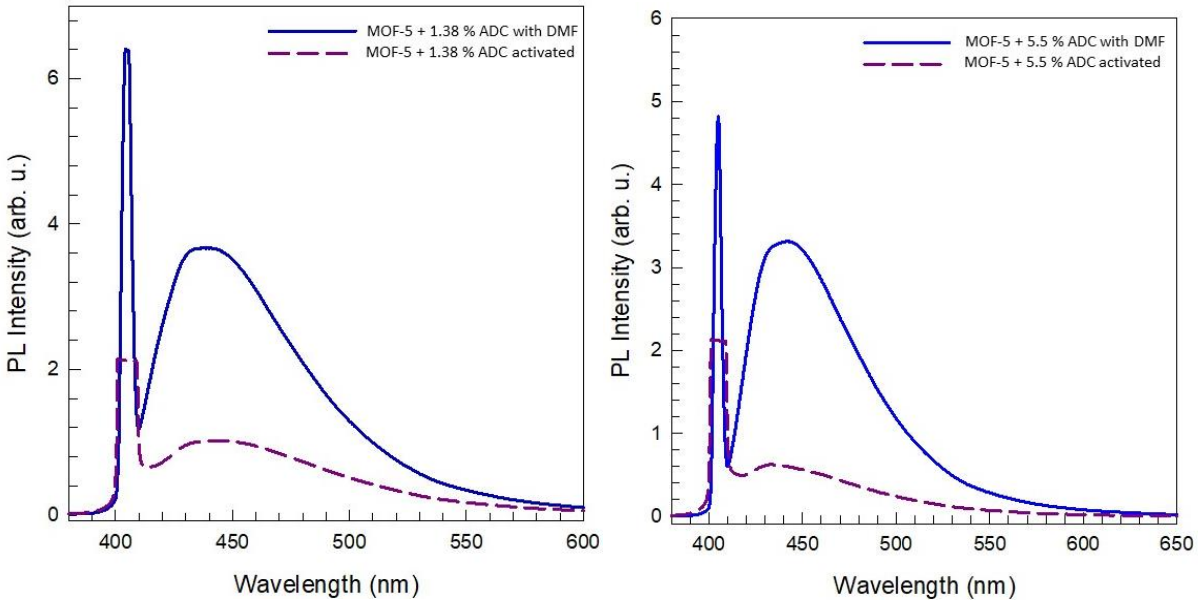

Figure V-15: Comparing the emission intensity of MOF-5 crystals in DMF with activated MOF-5. Right - MOF-5 + 1.38% ADC and Left - MOF-5 + 5.5% ADC.

1.4 Radioactive gas bench test

1.4.1 ^{85}Kr

Figure V-16 shows the results for the detection of ^{85}Kr gas. The D value on the y-axis is the photon count rate calculated by the logical sum of double coincidences between every pair of PMT in the detection system. For ease of interpretation and comparison with previous experiments, only the results with the 40 ns coincidence window are displayed here. We can observe here that the photon count rate increases from 99 s^{-1} for MOF-5 to 150 s^{-1} for MOF-5 + 1.38% ADC. This relays to a 52% increase in the photon count rate with a 1.38% ADC doping. We manage with such a small percentage of ADC to make our MOF-5 + 1.38 % ADC 32% more efficient that than of our microspheres of polystyrene. Since the emission wavelength of this MOF was shifted to the ADC with the doping, which emits in the wavelength range where the quantum efficiency of photon detection of the PMT are the highest and that the ligand also has higher scintillation yield, we manage to obtain a better performance for the detection of ^{85}Kr. The doping also did not affect the pore size nor considerably the surface area of the MOF which also help in maintaining its capacity for radioactive gas detection.

Further increasing the doping percentage to 5.5% ADC decreases the photon count to 97 s^{-1}. This might be due to the photon reabsorption when increasing the percentage of the ADC as we have seen in the photoluminescence light yield experiment in the section above. Another

possible explanation is the relatively low mass of MOF-5 + 5.5% ADC compared to the other undoped/doped MOFs as seen in Table XX in the Annexe.

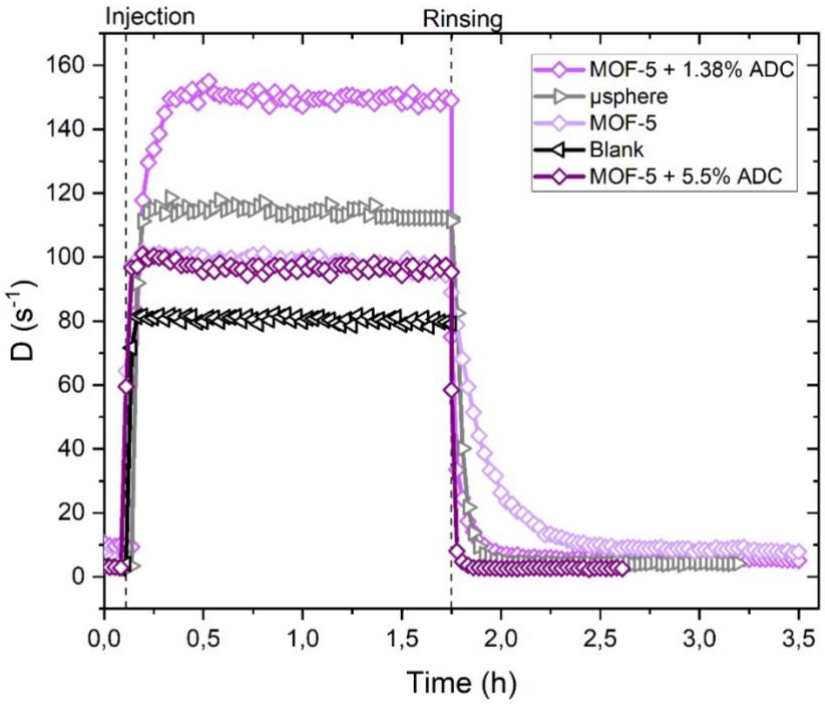

Figure V-16: Showing the results from ^{85}Kr detection with MOF-5 and its doped counterparts.

One of the interrogations that popped up was whether our MOFs were merely acting as a wavelength shifter for the Cherenkov radiation produced by the interaction of the energetic beta from ^{85}Kr with the glass vial medium. Cherenkov radiation is an anisotropic emission between 250-300 nm which accounts for the low but not insignificant number of photons for our blank experiment. A hypothesis was that MOF-5 + 1.38% ADC or any high-performing MOF we have seen so far for ^{85}Kr detection would absorb the Cherenkov radiation and remit photons in an isotropic manner at a wavelength in the correct range for the PMTs. This would result in the amplification of the photon count produce by the Cherenkov radiation rather than the radiation emitted by the radioactive gas. One possible way to check whether our MOF was merely acting as an amplifier for the Cherenkov radiation or actually detecting ^{85}Kr was to perform a control experiment by capping the scintillation vial and thus restricting the access of the MOF to ^{85}Kr while leaving the MOF exposed to Cherenkov radiation. Figure V-17 shows the result of this control experiment. We can see that the results with the capped vial (which gives the MOF access to the Cherenkov radiation but not the radioactive gas) emits a similar number of photons as the blank experiment, i.e. the one without any MOF in the system. This means that the MOF does not act significantly as a wavelength shifter and hence is not a photon count amplifier for the Cherenkov radiation. When the cap is removes and the MOF is in contact with the radioactive gas, the photon count increases meaning the MOF indeed detects the ^{85}Kr.

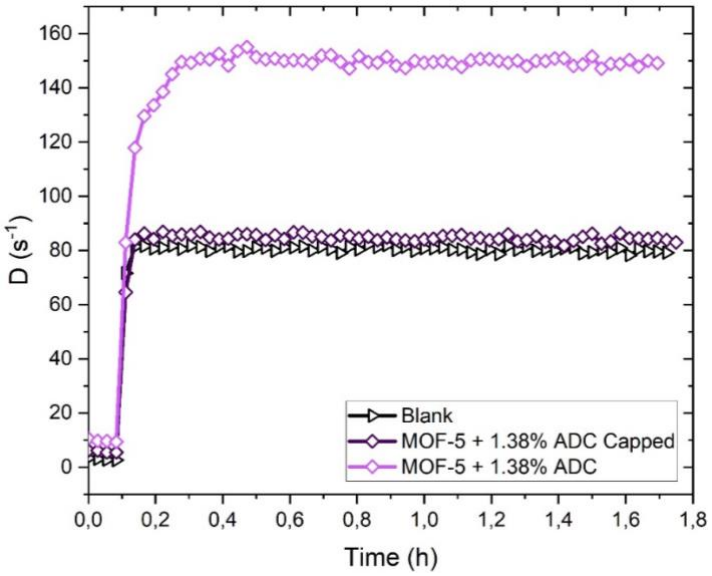

Figure V-17: Showing ^{85}Kr detection control experiment with MOF-5 + 1.38% ADC.

1.4.2 ^{222}Rn

MOF-5 + 1.38% ADC was also used to test for the detection of ^{222}Rn. Figure V-18 shows the results of this experiment. As we can see the photon count rate of MOF-5 + 1.38% ADC is higher than that of the blank and the microspheres indicating that MOF-5 + 1.38% ADC is an efficient porous scintillator for the detection of ^{222}Rn. However, the number of photons produced by MOF-5 + 1.38% ADC for ^{222}Rn detection is less than that produced by MOF-205 in Chapter III and UIO-67 in Chapter IV.

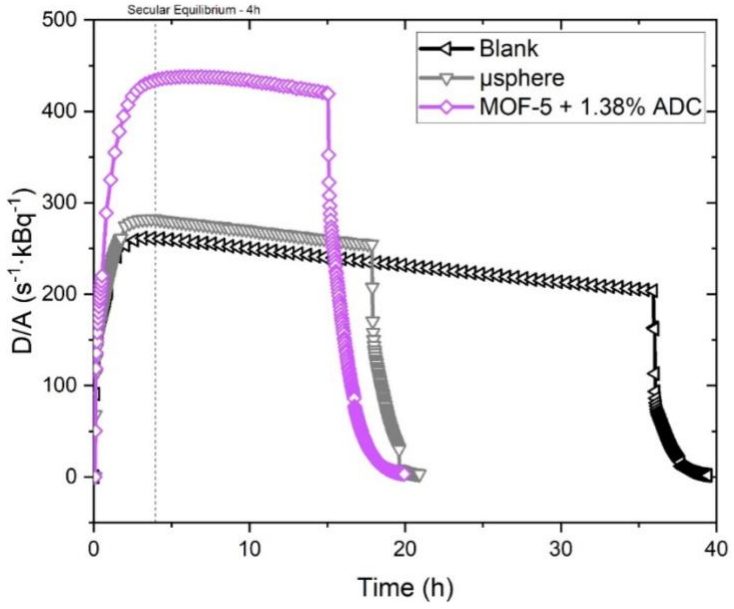

Figure V-18: Illustrating ^{222}Rn detection experiment results with MOF-5 + 1.38% ADC.

1.4.3 ^{3}H

Since MOF-5 + 1.38% ADC is the doped MOF that has the highest photon count with ^{85}Kr detection experiment, it was also used to test for the detection of 9 kBq of ^{3}H. Figure V-19 shows the results of this experiment. The red and blue lines are the average photon counts in within the respective period. As expected, the blank counting rate did not change upon injection of 70 $Bq \cdot cm^{-3}$ of the radioactive gas. But for MOF-5 + 1.38% ADC an increase of 0.99 s^{-1} was observed upon injection of ^{3}H. Upon purging, the count rate comes back to its initial value, revealing no observable adsorption of the tritium inside the MOFs. If we compare those count rates with the activity present inside the sample cavity (0.5 cm^3) we can deduce a detection efficiency for MOF-5 + 1.38% ADC of 2.8%. This value seems to be low in comparison with liquid scintillation in the same device (40 – 76% efficiency)[8]. Even though MOF-5 + 1.38 % ADC produces a slightly higher number of photons that MOF-205 for ^{85}Kr detection, its performance for ^{3}H is less efficient. Its performance is, however, similar to that of UIO-67 seen in Chapter IV.

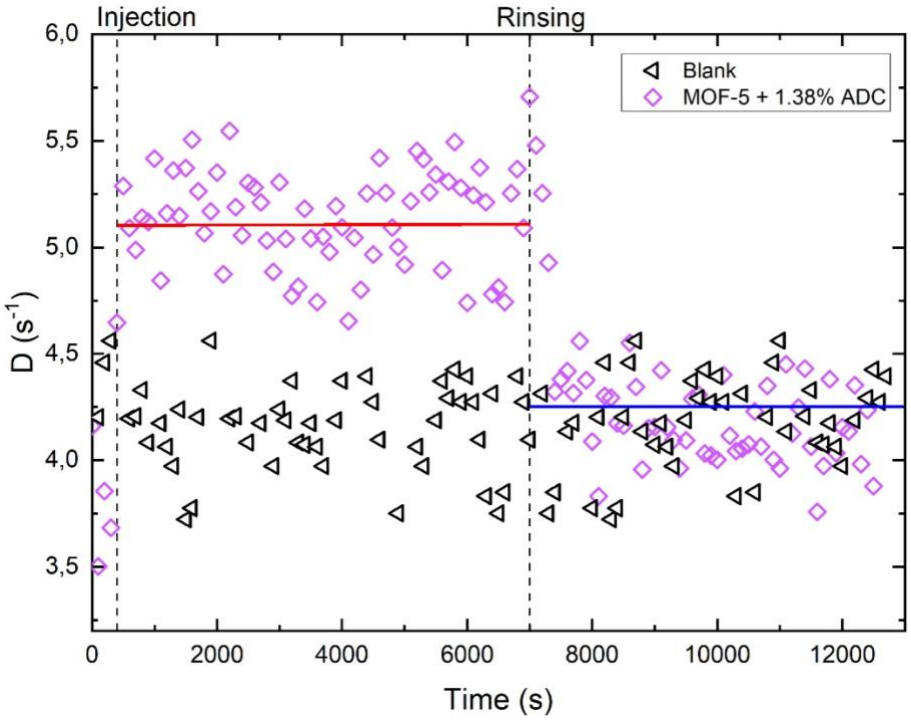

Figure V-19: Illustrating ^{3}H detection with MOF-5 + 1.38% ADC.

2. Doped IRMOF-7

2.1 Synthesis

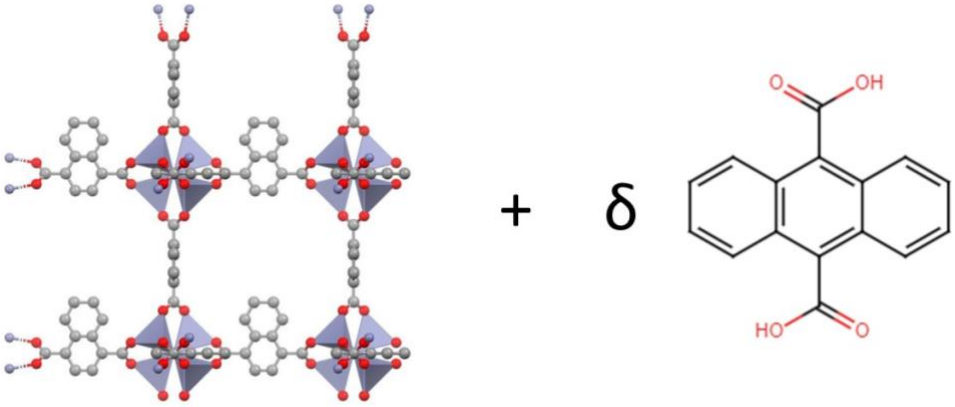

Figure V-20: Illustrating the doping strategy for the IRMOF-7 lattice.

Table V-4: Showing the doped IRMOF-7 synthesis.

Doping %	1.38%	5.5%
ADC:BDC ratio	1:72	1:18
ADC:Unit cell	1:24	1:6

Even though we have shown in Chapter III that IRMOF-7 is possibly not a MOF at all; we have decided to study it here for comparison purposes and to reveal how the doping strategy affects this material compared to our porous material. The doping strategy for IRMOF-7 consist of substituting the NDC ligand with the ADC ligands as illustrated in Figure V-20. Table V-4 shows the two ADC substitution ratio explored here. Since IRMOF-7 has similar unit cell configuration as MOF-5, $Zn_4O(1,4\text{-NDC})_3$, and we keep the ADC:BDC ratio constant throughout this manuscript for comparison purposes, the ADC: unit cell ratio calculations remain the same as detailed for MOF-5.

Protocol for IRMOF-7 + 1.38% ADC

For this synthesis the same concentration of metal and combined ligand/s as for IRMOF-7 synthesis was used to successfully obtain single crystals of IRMOF-7 + 1.38% ADC. $Zn(NO_3)_2 \cdot 6H_2O$ (0.0913 mol·L^{-1}, 2.716 g), 1,4-naphthalene dicarboxylic acid (0.03 mol·L^{-1}, 648 mg) and 9,10-anthracenedicarboxylic acid (0.0004 mol·L^{-1}, 11 mg) were dissolved in 100 mL of *N*,*N*-dimethylformamide (DMF). The mixture was equally divided into twelve 10 mL scintillation vials, which were then sealed with a screw cap. The vials were placed in an oven at 75°C for 144 h (6 days) yielding millimetric-sized doped IRMOF-7 + 1.38% ADC

single crystals. The closed vials were removed and placed in an N_2 glovebox. The crystals were washed according to the protocol described in Chapter II.

Protocol for IRMOF-7 + 5.5% ADC

For this synthesis the same concentration of metal and combined ligand/s as for IRMOF-7 synthesis was used to successfully obtain single crystals of IRMOF-7 + 5.5% ADC. $Zn(NO_3)_2 \cdot 6H_2O$ (0.0913 mol·L^{-1}, 2.716 g), 1,4-naphtalene dicarboxylic acid (0.0287 mol·L^{-1}, 621 mg) and 9,10-anthracenedicarboxylic acid (0.0017 mol·L^{-1}, 45 mg) were dissolved in 100 mL of *N*,*N*-dimethylformamide (DMF). The mixture was equally divided into twelve 10 mL scintillation vials, which were then sealed with a screw cap. The vials were placed in an oven at 75°C for 144 h (6 days) yielding millimetric-sized doped IRMOF-7 + 5.5% ADC single crystals. The closed vials were removed and placed in an N_2 glovebox. The crystals were washed according to the protocol described in Chapter II.

2.2 Structural characterisation

2.2.1 X-Ray Diffraction

Figure V-21 shows the X-ray Diffraction spectrum of our two doped IRMOF-7 sample compared to the undoped IRMOF-7 studied in Chapter III and the simulated XRD from the first reported work of Yaghi *et al.*[2]. As we have seen in Chapter III, the experimental XRD does not agree with literature and we cannot unfortunately conclude that we have successfully synthesised IRMOF-7. The peak positions are however similar for all the experimental data sets indicating that this material has been homogenously doped throughout the lattice.

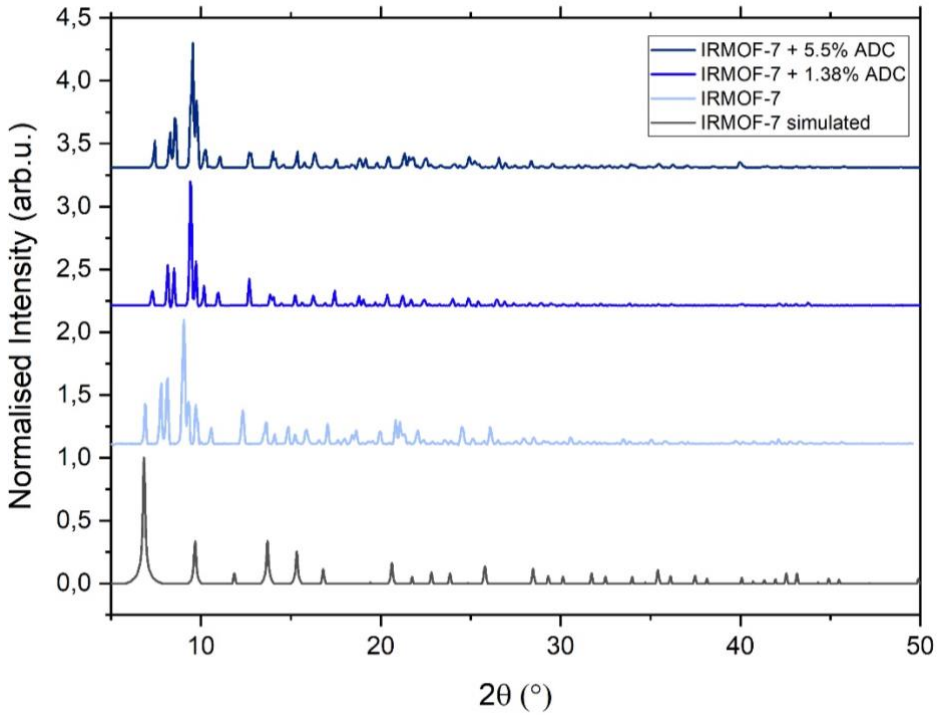

Figure V-21: PXRD spectrum showing experimental results of each doped IRMOF-7 compared to the undoped IRMOF-7 and literature.

2.2.2 Adsorption measurements

Figure V-22 shows the N_2 adsorption isotherms of IRMOF-7 and its doped counterparts. No gas uptake was observed for any of them hence concluding they do not exhibit any porosity. No surface area or pore width can be extracted from these experiments.

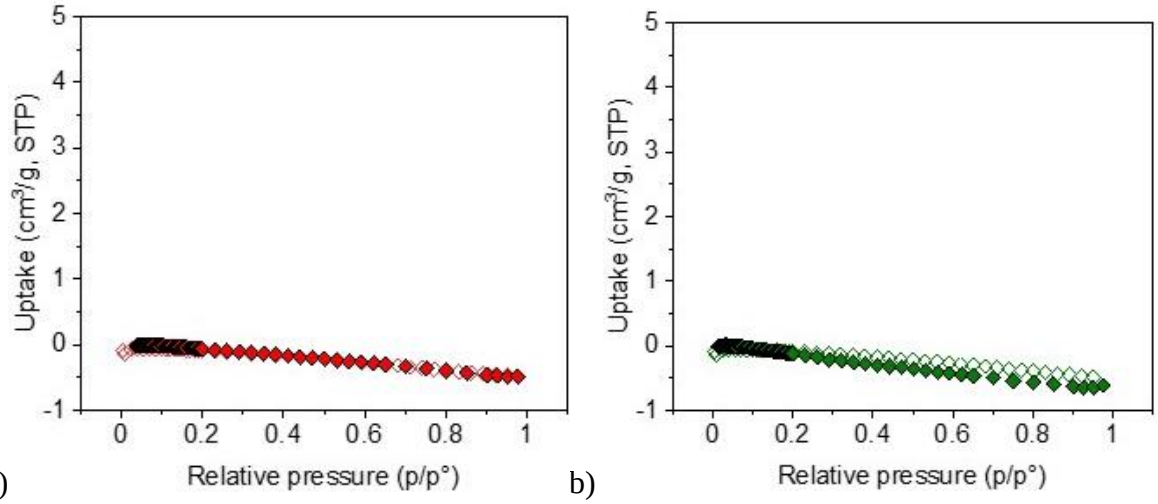

a) b)

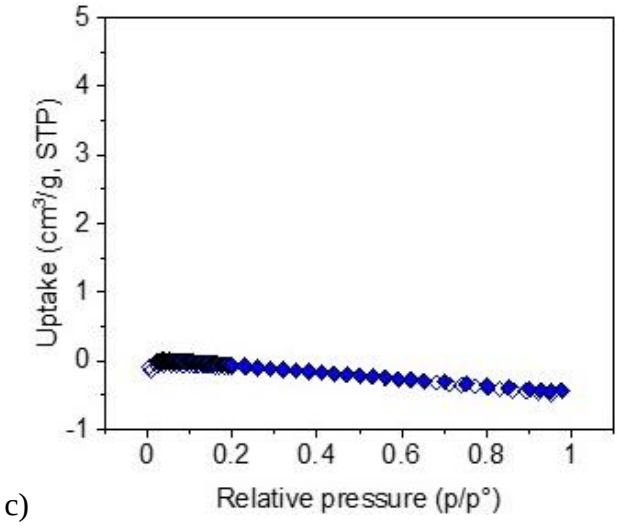

c)

Figure V-22: Illustrating the N_2 adsorption isotherm of a) IRMOF-7, b) IRMOF-7 + 1.38% ADC and c) IRMOF-7 + 5.5% ADC.

2.2.3 Thermogravimetric Analysis

As discussed in Chapter III the TGA of our IRMOF-7 sample does not display the typical behaviour of Zn-based MOFs. We can observe in Figure V-23 that the profiles for the doped MOFs before 400°C is slightly different compared to the undoped IRMOF-7. As we are not sure about the nature of our base MOF-7, there are too many possibility to make here a reasonable hypothesis. The decomposition of all these MOFs however start and end at similar temperatures.

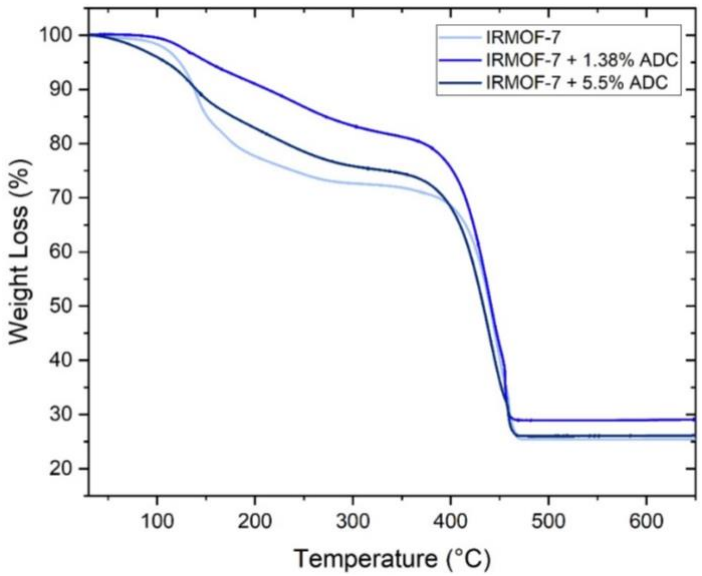

Figure V-23: TGA results of IRMOF-7 and its doped counterparts.

2.2.4 FT-IR experiments

As discussed in Chapter III, the infrared spectrum of IRMOF-7 after activation displays different peaks to literature in the region between 1200 and 1700 cm^{-1}. These peaks can be seen in Figure V-24 for all the doped versions of IRMOF-7 as well. This is possibly associated to a different coordination of the 1,4-NDC ligand to the Zn^{2+} cations. This again poses the question of whether these products are indeed doped and undoped IRMOF-7. We can also see that the spectrum of the doped and undoped versions of IRMOF-7 are identical meaning that at such a low doping percentage the doping is undetectable by FT-IR experiments.

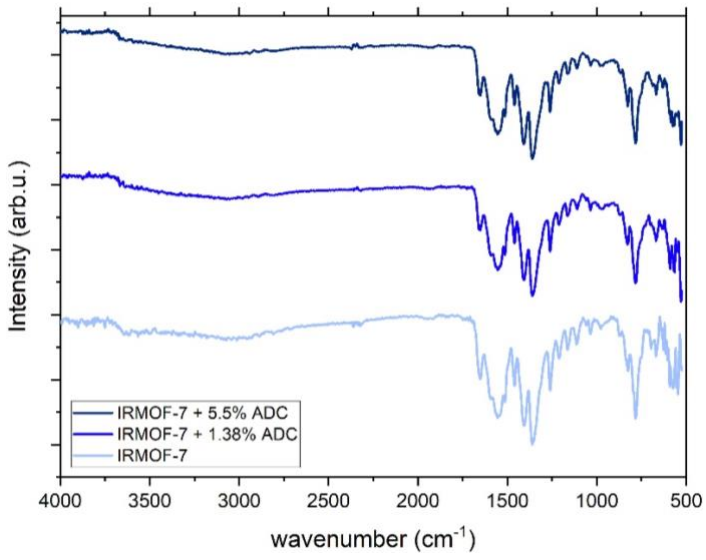

Figure V-24: Showing FT-IR results of IRMOF-7 and its doped counterparts.

2.3 Photophysical characterisation

2.3.1 Excitation and Emission spectra

As we remember from Chapter III and as we can see in Figure V-25 the emission of IRMOF-7 is very similar to a 10^{-5} M solution of its ligand (NDC) in DMF. We can see that by doping our IRMOF-7 with a small percentage of ADC ligand (1.38% ADC or 5.5% ADC), we have shifted the emission of the IRMOF-7 from the NDC to being centred on the ADC ligand around 430 nm. The IRMOF-7 + 5.5% ADC reveals an emission at slightly longer wavelength than the IRMOF-7 + 1.38% ADC as we will also observe in UIO-66 and UIO-1,4-NDC. This might be due to us slowly approaching the emission of solid ADC when doping with more ADC due to more overlap of the ligands like in a solid. We can observe from Appendix Figure 5 an overlap between the excitation spectra of the ADC ligand and the emission of the 1,4-NDC ligand (both ligands in 10^{-5} M DMF solution). Therefore, we can imagine that in our MOF, the NDC ligand gets excited first and emits photons or transfers its energy to the ADC ligand.

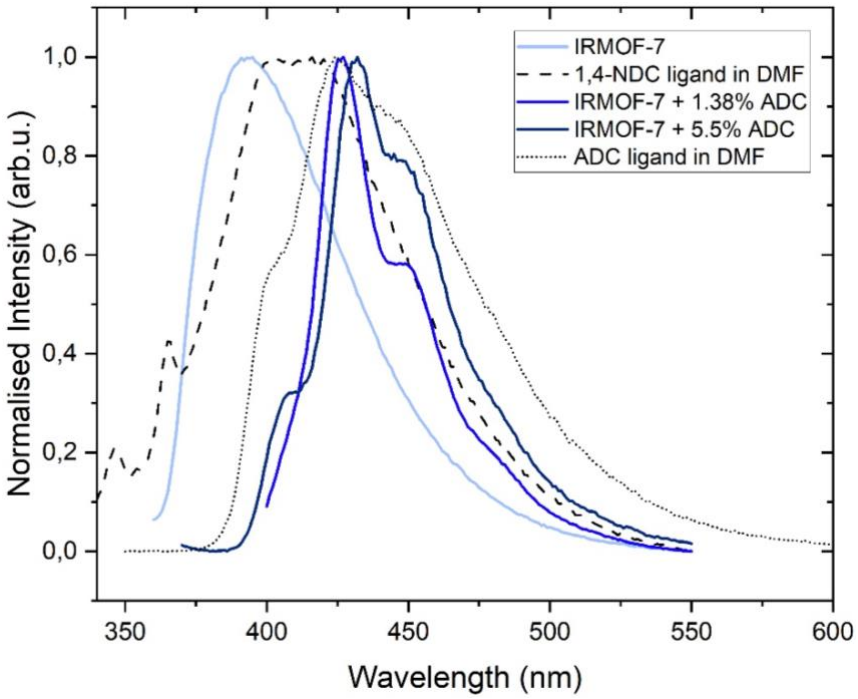

Figure V-25: Emission spectrum of IRMOF-7 and its doped counterparts (solid lines), NDC ligand in DMF (dashed line) and ADC ligand in DMF (dotted line).

2.3.2 TCSPC

Figure V-26 shows the fluorescence decay of IRMOF-7 with a 339 nm excitation diode and doped IRMOF-7 with a 368 nm excitation diode since the fluorescence is centred on the ADC ligand. By fitting these decay curve with a third-order exponential fit, we can calculate the fluorescence lifetime components, their respective weights, and an average fluorescence lifetime. The results are summarised in Table V-5, together with the coefficient of determination (R-Square / COD) of the fit. We can see that the average fluorescence lifetimes of the two doped IRMOF-7 are similar. We can also observe a decrease in the fluorescence lifetimes of the doped IRMOF-7 compared to the undoped IRMOF-7, this is seen only for this MOF in this chapter since the others exhibit a slowing down of the lifetime with doping. This might again give us an indication that IRMOF-7 doped or undoped was not successfully synthesised here.

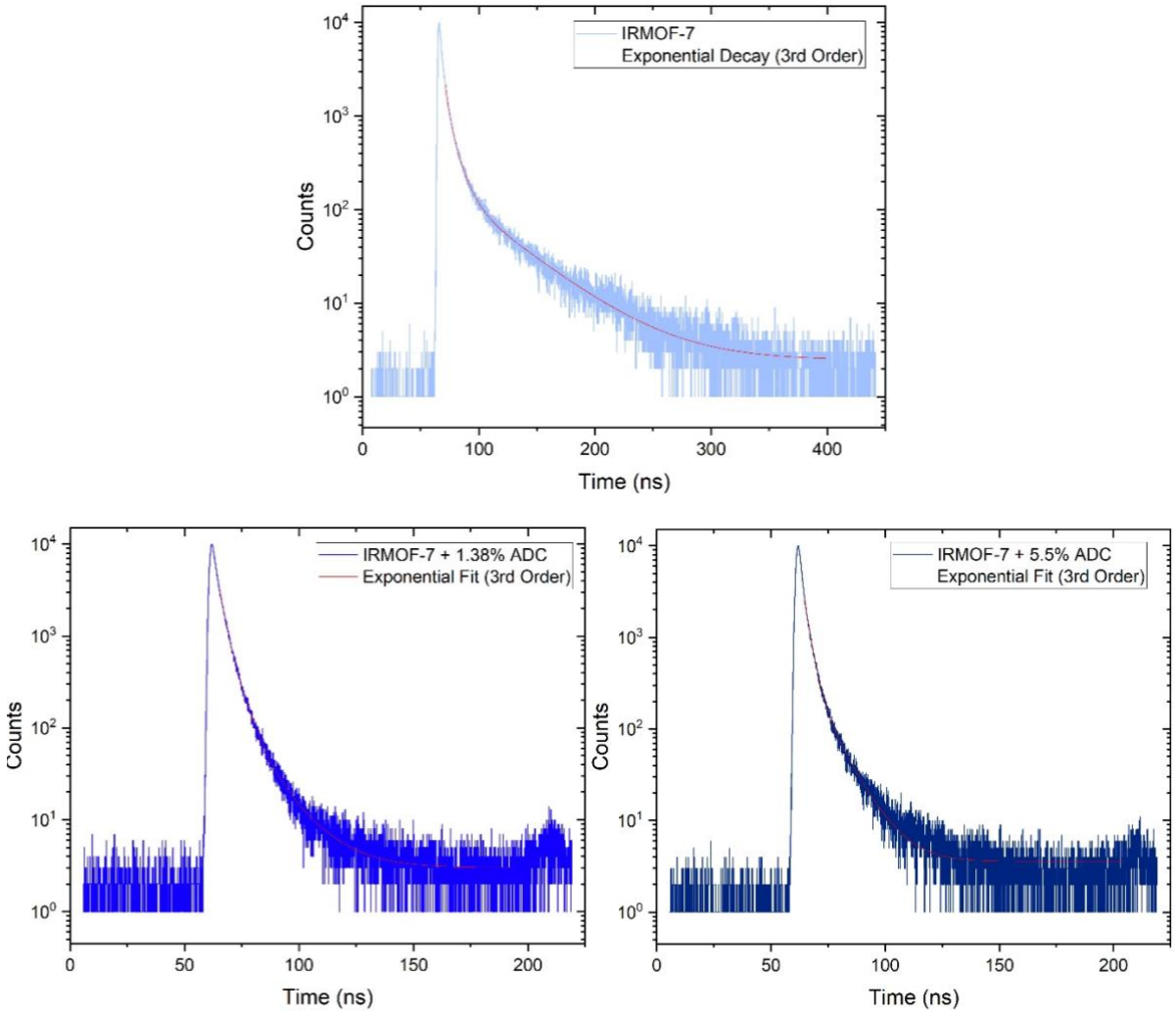

Figure V-26: Showing the TCSPC results of IRMOF-7 and its doped counterparts.

Table V-5: Showing the calculated fluorescence lifetime of IRMOF-7 and its doped counterparts.

MOF	**Diode λ_{ex} (nm)**	**λ_{em}**	**τ_1 (ns)**	**τ_2 (ns)**	**τ_3 (ns)**	**<τ> (ns)**	**R-Square (COD)**
IRMOF-7	339	390	2.8 (57.1%)	8.2 (37.9%)	45.0 (5.0%)	7.0	0.9983
IRMOF-7 + 1.38% ADC	368	430	2.6 (58.6%)	5.0 (37.3%)	13.5 (4.1%)	3.9	0.9992
IRMOF-7 + 5.5% ADC	368	430	2.5 (72.0%)	5.0 (18.1%)	9.4 (9.9%)	3.6	0.9989

2.3.3 Photoluminescence Light Yield

By performing the photoluminescence light yield experiments using an integrating sphere as explained in section 3.3 of Chapter II, we obtain the photoluminescence intensity vs wavelength results as shown in Figure V-27. If we concentrate firstly on the red curves which are experiments performed on the MOFs in DMF, we can see that the emission of IRMOF-7 + 1.38 % ADC (middle curve) is higher than the undoped IRMOF-7 (left curve), meaning that we have increased the luminescence light yield of this MOF by doping. However, by moving to higher doping percentages such as IRMOF-7 + 5.5% ADC (right curve), we can see that the emission decreases compared to IRMOF-7 + 1.38% ADC.

Similar to MOF-5 single crystals, we have noticed that while activating our MOF single crystals we have a significant loss in the transparency of our crystals. Since transparency is of utmost important in the field of scintillators, because it affects the light-matter interaction and hence the amount of photons emitted by our MOF, we wanted to quantify this loss in transparency using the same integrating sphere method. In a porous material the pores filled with DMF will allow more light to diffuse through the solution and the empty pores will cause and interruption in the light path which leads to a decrease in the PL yield as we have seen for MOF-5. However, we can see from Figure V-27(left) that the photoluminescence light yield of the activated undoped IRMOF-7 is similar to the IRMOF-7 in DMF. This is coherent for this non porous material. Nevertheless, for the activated doped samples we can observed a significantly drop compared to the single crystals in DMF which is not coherent with the fact that the doped IRMOF-7 are also non porous. The experiment was also done with DMF only and the contribution of emission was concluded to be negligible.

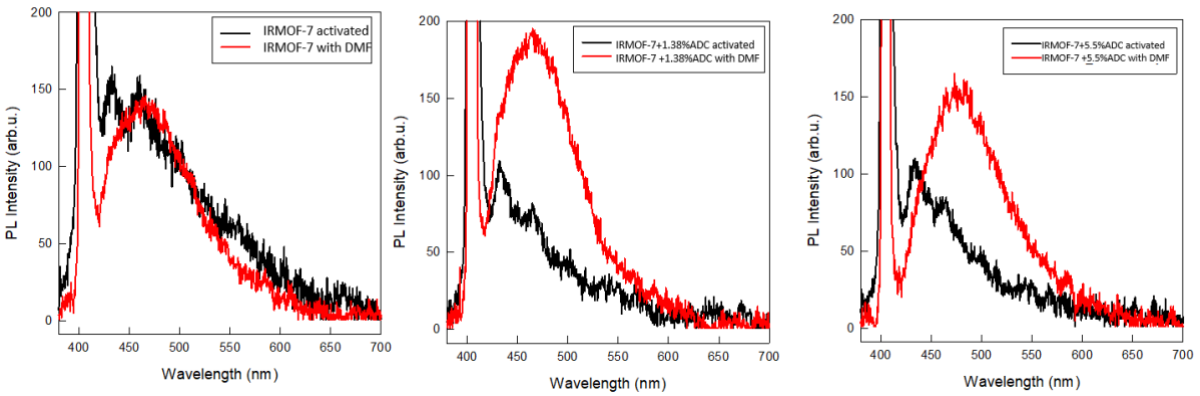

Figure V-27: Photoluminescence light yield of undoped IRMOF-7 (Left), IRMOF-7 + 1.38% ADC (Middle) and IRMOF-7 + 5.5% ADC (Right) single crystals using the integrating sphere method. The red curved are the respective MOFs in DMF while the black are the activated MOFs.

2.4 Radioactive gas bench test

2.4.1 ^{85}Kr

Figure V-28 shows the results from detecting ^{85}Kr gas. We can observe here that the photon count rate increases from 85 s^{-1} for the IRMOF-7 (which has a photon count comparable to the blank meaning it cannot detect ^{85}Kr) to 117 s^{-1} for IRMOF-7 + 1.38% ADC. This relays to a 38% increase in the photon count with a 1.38% ADC doping which is less than what was obtained with MOF-5. We manage with such a small percentage of ADC to make IRMOF-7 detect ^{85}Kr by doping it. Since the emission wavelength of this MOF was shifted to the ADC with the doping and the latter has higher scintillation yield, we demonstrated a better performance for the detection of ^{85}Kr. However, the performance of IRMOF-7 + 1.38% ADC is only comparable to our microsphere of polystyrene.

Further increasing the doping percentage to 5.5% ADC decreases the photon count to 88 s^{-1}. This might be due to the photon reabsorption when increasing the percentage of the ADC as we have seen in the photoluminescence light yield experiment in the section above.

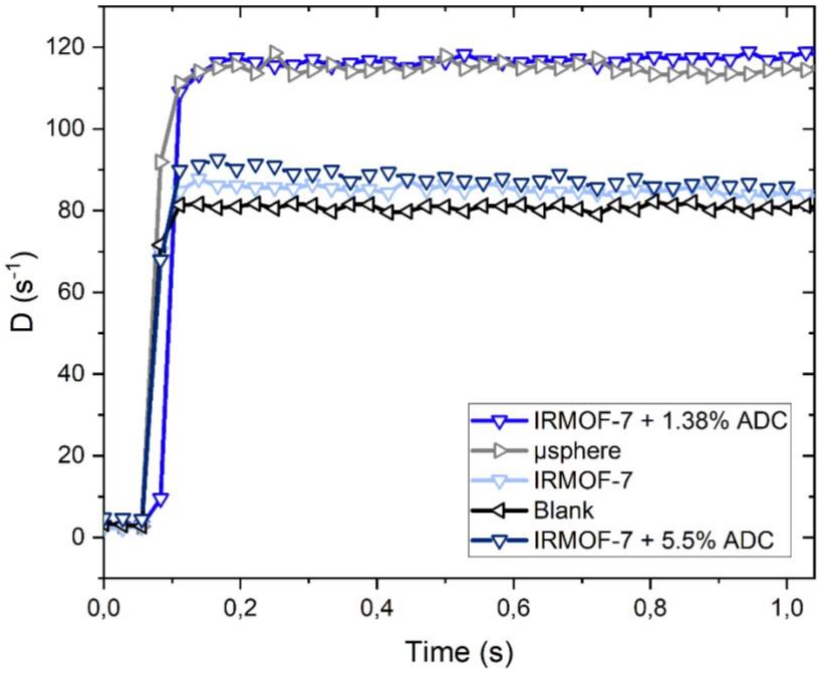

Figure V-28: Showing ^{85}Kr detection results for IRMOF-7 and its doped counterparts.

3. Doped UIO-66

3.1 Synthesis

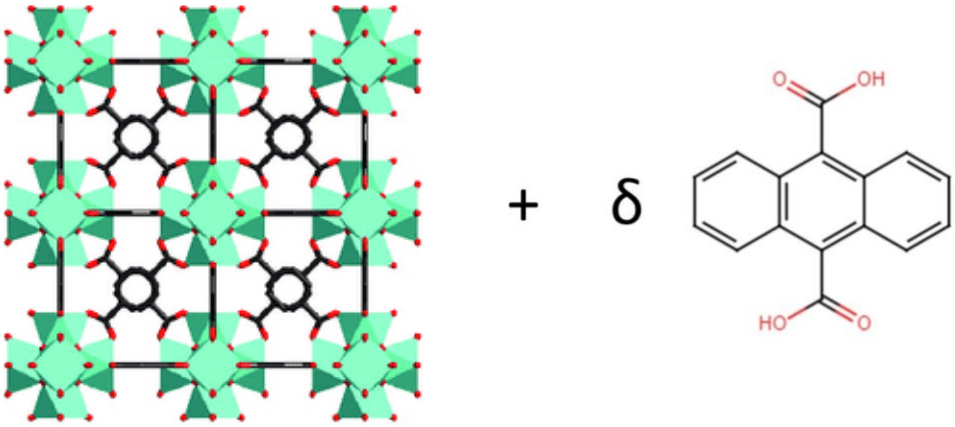

Figure V-29: Illustrating the doping strategy for the UIO-66 lattice.

Table V-6: Showing the doped UIO-66 synthesis.

Doping %	1.38%	5.5%
ADC:BDC ratio	1:72	1:18
ADC:Unit cell	1:6	2:3

Since Zr MOFs have a different coordination to their ligands than Zn MOFs as explained in Chapter IV, the calculations for the ADC:Unit cell ratio are different for UIO-66 compared to MOF-5. We wanted to keep the doping percentage equal across all the MOFs for comparison purposes hence 1.38% and 5.5%. With 12 ligands coordinated to a Zr cluster in every unit cell the 1.38% doping now corresponds to adding 1 ADC every 6 unit cells. The doping strategy for UIO-66 consist of substituting the BDC ligand with the ADC ligands as illustrated in Figure V-29. Table V-6 shows the two ADC substitution ratio explored here. Below is the synthesis protocol for the doped UIO-66. As explained in Chapter IV, the UIO-66 is synthesised in crystalline powder form using the modulated synthesis approach. The same modulator concentration was used here as in Chapter IV.

Protocol for UIO-66 + 1.38% ADC

For this synthesis the same concentration of metal and combined ligand/s as for UIO-66 synthesis was used to successfully obtain doped UIO-66 crystalline powder. $ZrCl_4$ (0.017 mol·L^{-1}, 0.396 g), 1,4-benzenedicarboxylic acid (0.017 mol·L^{-1}, 281 mg), 9,10-

anthracenedicarboxylic acid (0.00024 mol·L^{-1}, 6.35 mg) and benzoic acid (0.05 mol·L^{-1}, 0.6285 g), were dissolved in 100 mL of *N*,*N*-dimethylformamide (DMF). The mixture was equally divided into twelve 10 mL scintillation vials, which were then sealed with a screw cap. The vials were placed in an oven at 120 °C for 24 hours yielding doped crystalline powder of UIO-66 + 1.38% ADC single crystals. The closed vials were removed and left to cool. The powder was washed using the centrifuge according to the protocol described in Chapter II. The SEM image of UIO-66 + 1.38% ADC as well as the measurements of some particle sizes is shown in Figure V-30. A clear crystalline shape cannot be distinguished here. We can also notice the aggregation of the particles. The particle sizes observed are of the order of 150-500 nm, attempts to make bigger particles of UIO-66 + 1.38% ADC were unsuccessful.

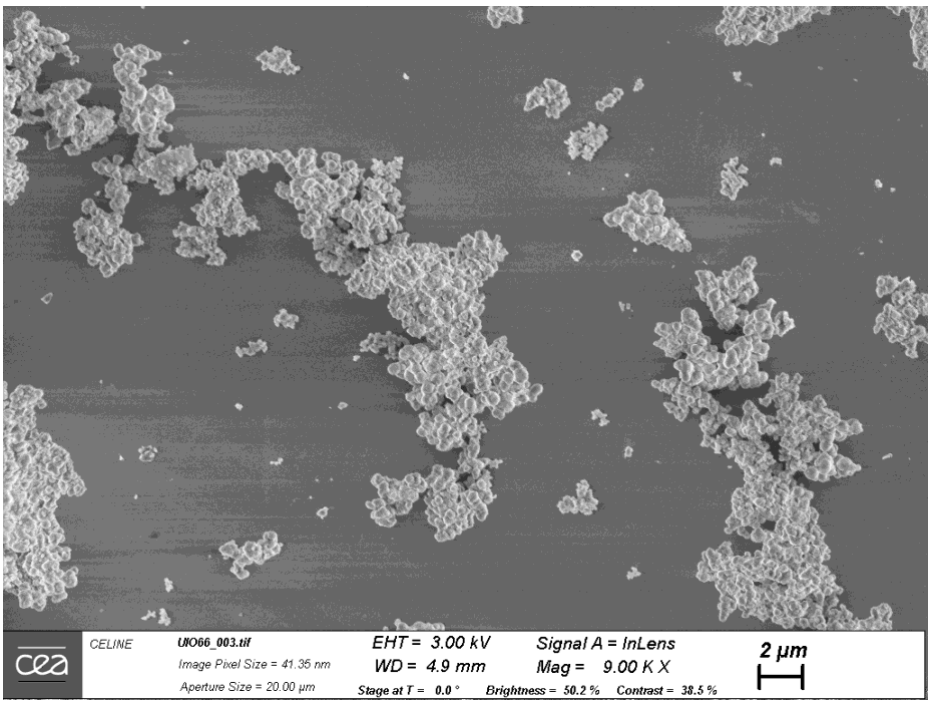

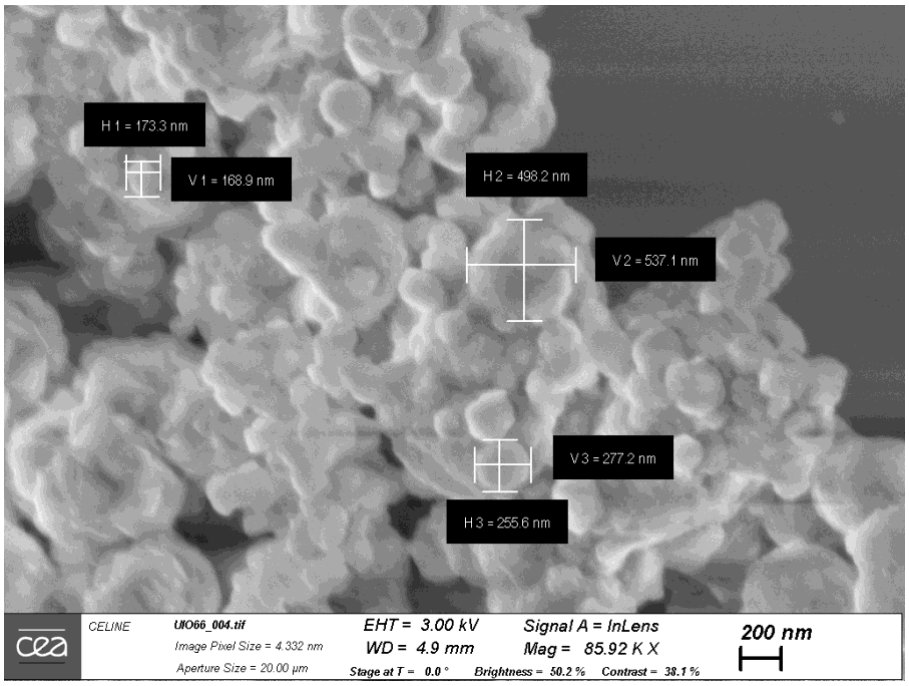

Figure V-30: Shows the SEM image of UIO-66 + 1.38% ADC crystalline powder.

Protocol for UIO-66 + 5.5% ADC

For this synthesis the same concentration of metal and combined ligand/s as for UIO-66 synthesis was used to successfully obtain UIO-66 + 5.5% ADC crystalline powder. $ZrCl_4$ (0.017 mol·L^{-1}, 0.396 g), 1,4-benzenedicarboxylic acid (0.016 mol·L^{-1}, 269 mg), 9,10-anthracenedicarboxylic acid (0.00095 mol·L^{-1}, 25.35 mg) and benzoic acid (0.05 mol·L^{-1}, 0.6285 g), were dissolved in 100 mL of *N*,*N*-dimethylformamide (DMF). The mixture was equally divided into twelve 10 mL scintillation vials, which were then sealed with a screw cap. The vials were placed in an oven at 120°C for 24 h yielding doped crystalline powder of UIO-66 + 5.5% ADC single crystals. The closed vials were removed and left to cool. The powder was washed using the centrifuge according to the protocol described in Chapter II. The SEM image of UIO-66 + 5.5% ADC as well as the measurements of some particle sizes is shown in Figure V-31. A clear crystalline shape cannot be distinguished here and we can also notice the aggregation of the particles. The particle sizes observed are of the order of 150-400 nm, attempts to make bigger particles of UIO-66 + 5.5% ADC were unsuccessful.

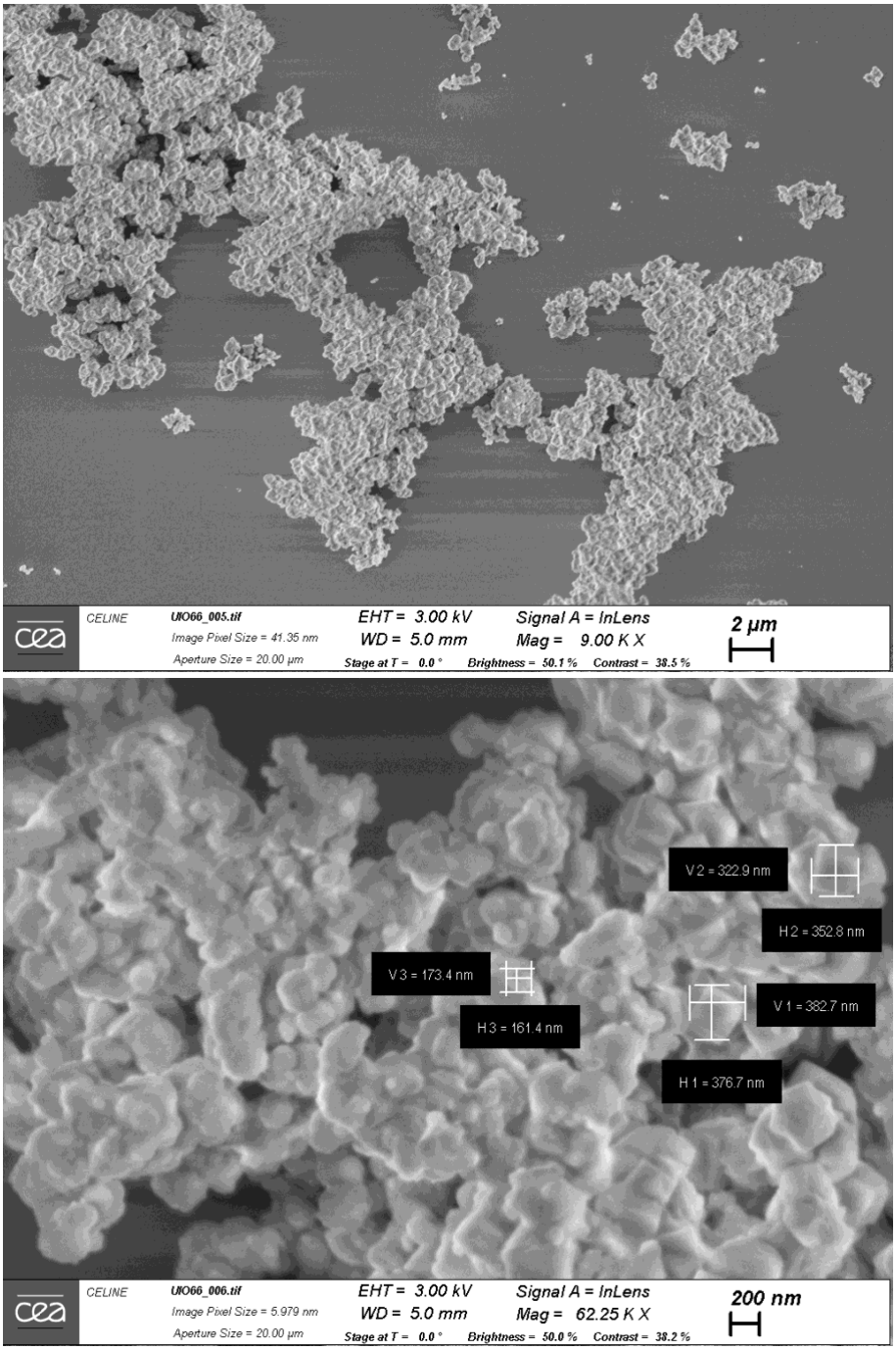

Figure V-31: Shows the SEM image of UIO-66 + 5.5% ADC crystalline powder.

3.2 Structural characterisation

3.2.1 X-Ray Diffraction

Figure V-32 shows the X-ray Diffraction spectrum of our two doped UIO-66 sample compared to the undoped UIO-66 studied in Chapter IV and the simulated XRD reported in literature[9]. The peak positions are similar in all the sets indicating that we have indeed synthesised doped versions of UIO-66 crystalline powder using a modulated synthesis approach. As we can see,

no new peak are seen on the doped UIO-66 spectrum compared to the undoped ones. We can therefore conclude that this MOF have been homogeneous doped.

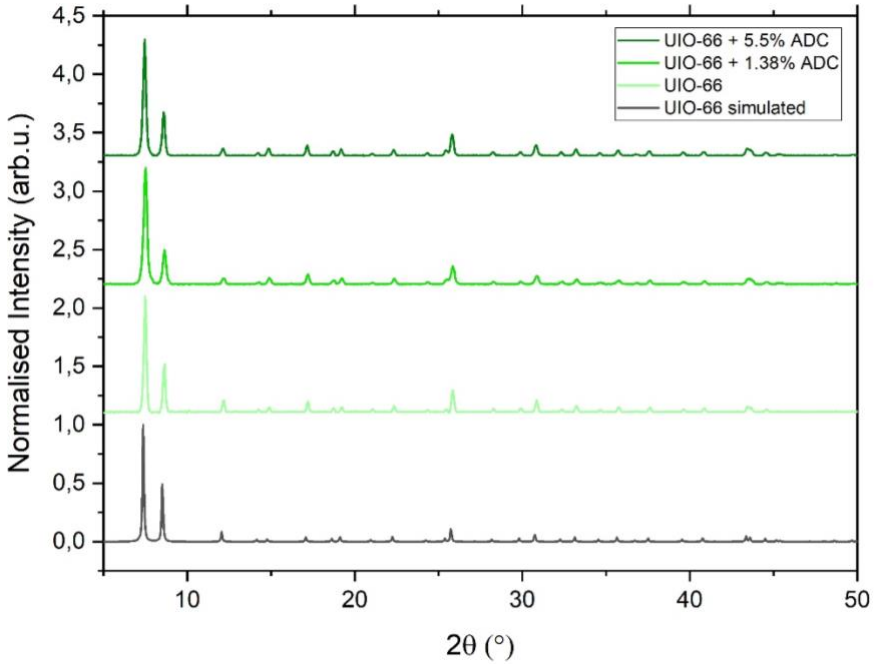

Figure V-32: PXRD spectrum showing experimental results of each doped UIO-66 compared to the undoped UIO-66 and literature.

3.2.2 Adsorption measurements

The N_2 adsorption experiments for UIO-66 and its doped counterparts were all carried out at the NIMBE laboratory using the same equipment for comparison purposes. The N_2 adsorption isotherm is shown in Figure V-33 and Table V-7 summarises the results extracted from these data. The Type II isotherms reveal the microporosity of the doped UIO-66 with a pore widths of 7 and 6 Å for all three MOFs. The BET surface area of UIO-66 doped and undoped are consistent with literature values reported for UIO-66[10,11]. The BET surface area seems to increase slightly with the doping percentage.

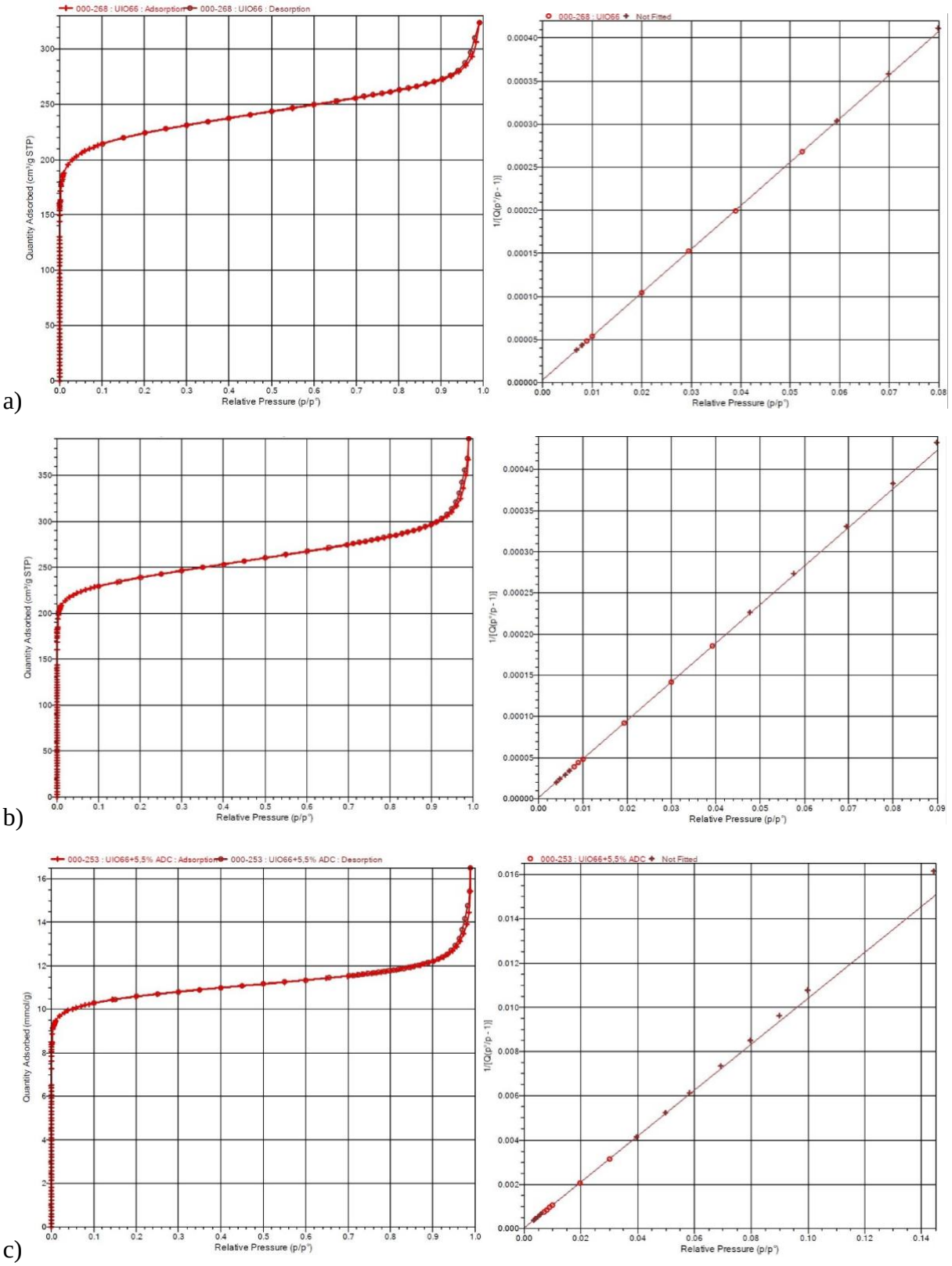

Figure V-33: Illustrating the N_2 adsorption isotherm of a) UIO-66, b) UIO-66 + 1.38% ADC and c) UIO-66 + 5.5% ADC.

Table V-7: Showing the data calculated from N_2 adsorption of undoped UIO-66 and its doped counterparts.

MOF	BET SA ($m^2 \cdot g^{-1}$)	Pore size (Å)	Pore volume ($cm^3 \cdot g^{-1}$)
UIO-66	860	7.3 & 6	0.5
UIO-66 + 1.38% ADC	928	7 & 6	0.57
UIO-66 + 5.5% ADC	940	7 & 6	0.53

3.2.3 Thermogravimetric Analysis

Figure V-34 shows the TGA results of UIO-66 and its doped counterparts. For all the UIO-66 samples we can observe a drop before 100°C accounting for surface water and residual DCM loss. We also observe weight loss between 100°C and 300°C, which is attributed to the dehydroxylation of the Zr cluster, as discussed in section 1.2.3 of Chapter IV. A significant drop in the weight of the sample between 350-500°C is also observed, similar to the Zn-based MOFs. This result is consistent with the literature where the decomposition temperature (T_d) is reported to be between 400-500°C depending on the sample preparation, activation and experimental conditions[5]. The MOF decomposes to zirconia at these temperatures. The discrepancy between UIO-66 or UIO66 + 1.38 % ADC compared to UIO66 + 5.5% ADC was not expected as we did not notice such a difference in the other doped MOFs. The experiment was repeated for peace of mind and the results remain as such. We might advance with caution here an effect of the doping which could stabilize the structure.

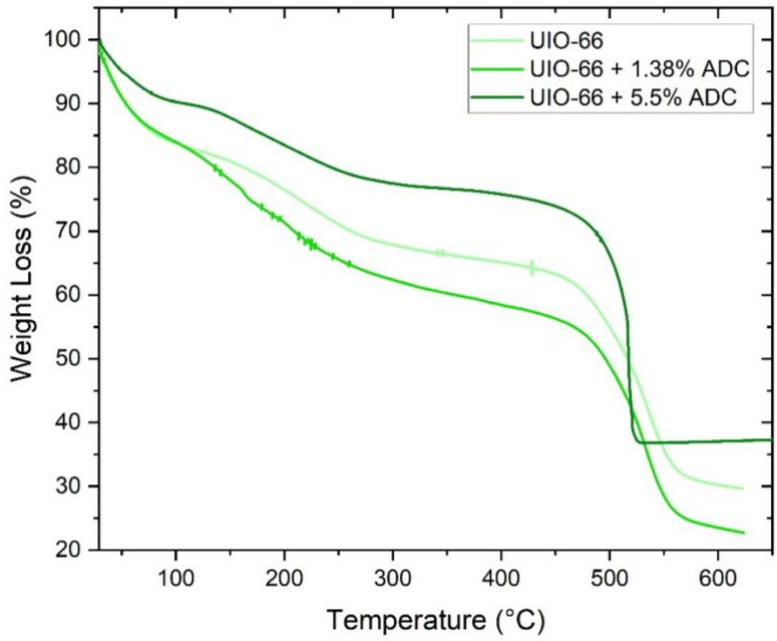

Figure V-34: TGA of UIO-66 and its doped counterparts.

3.2.4 FT-IR experiments

As seen in Chapter IV, the FT-IR spectrum of UIO-66 is consistent with literature[12]. We can see from Figure V-35, the spectra of the doped and undoped versions of UIO-66 are identical meaning that such a low doping percentage is undetectable by FT-IR experiments.

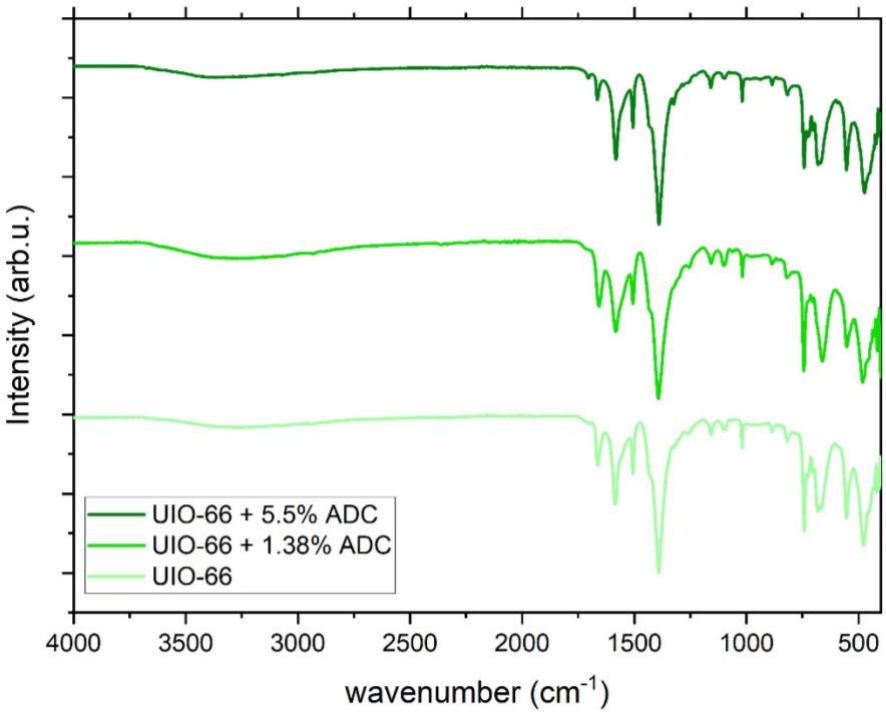

Figure V-35: Showing FT-IR results for UIO-66 and its doped counterparts.

3.3 Photophysical characterisation

3.3.1 Excitation and Emission spectra

We can see in Figure V-36 that the emission of UIO-66 is centered between the emission of a 10^{-5} M solution of its ligand (BDC) in DMF and the emission of solid BDC ligand. This is because for this MOF the emission of UIO-66 was performed on activated powder rather than on crystals. We can also observe in Figure V-36 that by doping our UIO-66 with a small percentage of ADC ligand (1.38% ADC or 5.5% ADC), we have shifted the emission of UIO-66 from the BDC to being centred on the ADC ligand around 430 nm. The UIO-66 + 5.5% ADC emits at a slightly higher wavelength than the UIO-66 + 1.38% ADC as will be seen with UIO-1,4-NDC. Note that a similar energy transfer between both ligands as explained for MOF-

5 is expected for this MOF due to the overlap of the emission and excitation spectra of the ligands (see Appendix Figure 4).

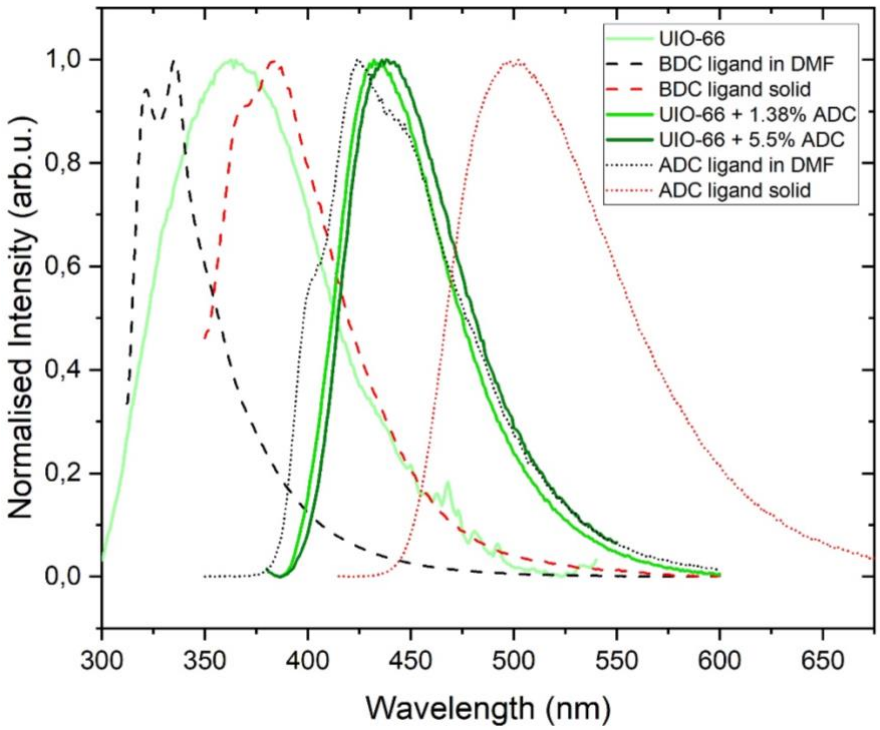

Figure V-36: Emission spectrum of UIO-66 and its doped counterparts (solid lines), BDC ligand in DMF (dashed black line), BDC ligand solid (dashed red line), ADC ligand in DMF (dotted black line) and ADC ligand solid (dotted red line).

3.3.2 TCSPC

Figure V-37 shows the fluorescence decay of UIO-66 with a 309 nm excitation diode and doped UIO-66 with a 368 nm excitation since the fluorescence is centred on the ADC ligand. By fitting this decay curve with a third-order exponential fit, we can calculate the fluorescence lifetime components, their respective weights, and an average fluorescence lifetime. The results are summarised in Table V-8 together with the coefficient of determination (R-Square / COD) of the fit. We can see that the average fluorescence lifetimes of the two doped UIO-66 are similar. We can also observe an increase in the fluorescence lifetimes of the doped UIO-66 compared to the undoped UIO-66 (similar to MOF-5 and UIO-1,4-NDC) meaning this is slightly more inconvenient for coincidence detection since faster fluorescence lifetimes are desired. Even though the lifetime is higher than our desired 3 ns, a value under 10 ns is acceptable for coincidence detection.

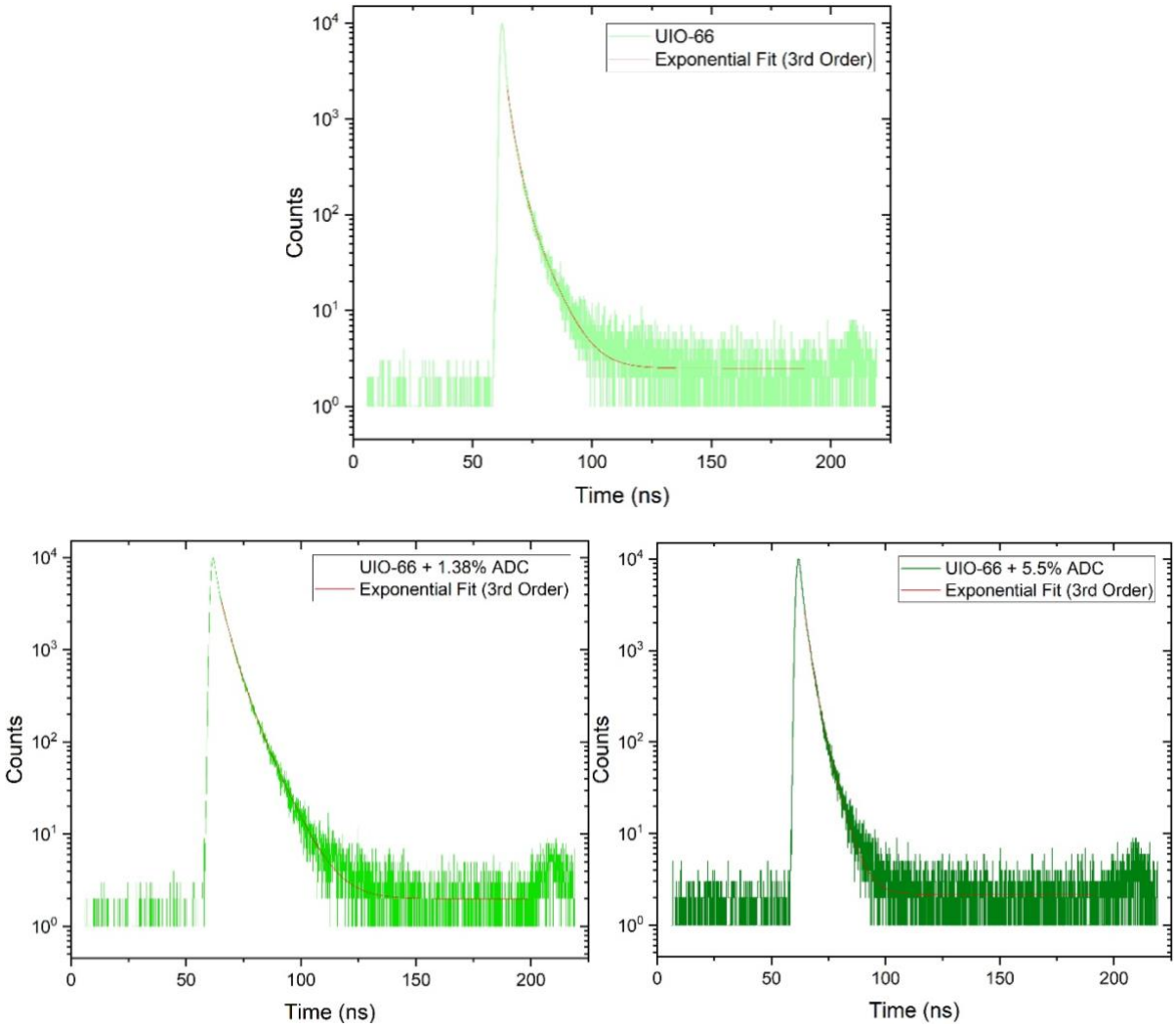

Figure V-37: Showing the TCSPC results of UIO-66 and its doped counterparts.

Table V-8: Showing the calculated fluorescence lifetime of UIO-66 and its doped counterparts.

MOF	**Diode λ_{ex} (nm)**	**λ_{em}**	**τ_1 (ns)**	**τ_2 (ns)**	**τ_3 (ns)**	**<τ> (ns)**	**R-Square (COD)**
UIO-66	309	365	2.7 (67.8%)	0.7 (19.8%)	7.2 (12.4%)	2.9	0.9988
UIO-66 + 1.38% ADC	368	430	3.7 (68.8%)	8.0 (30.3%)	0.2 (0.9%)	5.0	0.9993
UIO-66 + 5.5% ADC	368	430	5.9 (83.9%)	2.3 (13.0%)	0.3 (3.1%)	5.3	0.9992

3.4 Radioactive gas bench test

3.4.1 ^{85}Kr

Figure V-38 shows the results from ^{85}Kr detection . We can observe here that the photon count rate for UIO-66 increased from 91 s^{-1} to 99 s^{-1} for UIO-66 + 1.38% ADC. This relays to only a 9% increase in the photon count with a 1.38% ADC doping which is far less than what was obtained with the doping of MOF-5 with 1.38% ADC (52% increase). Further increasing the doping percentage to 5.5% ADC decreases the photon count to 93 s^{-1}. We can also observe that all the MOFs presents in Figure V-38 have a mediocre performance compared to our microspheres of polystyrene. We can conclude here that the doping strategy has not worked as well in boosting the performance of UIO-66 as it has done for MOF-5. This might be due to the powdered UIO-66 geometry compared to MOF-5 where too much of the photons produced were trapped due to the opacity of the powder.

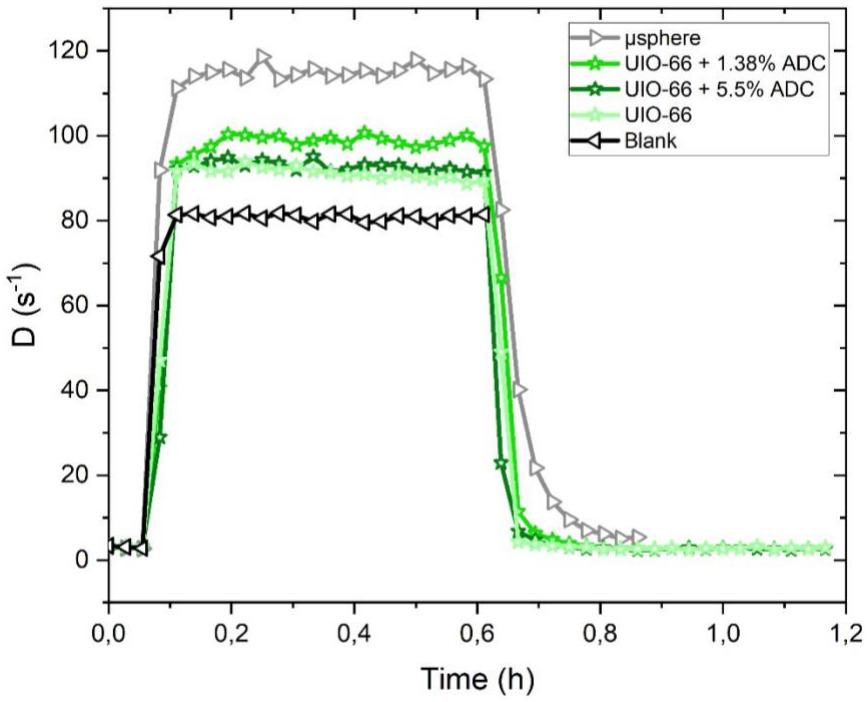

Figure V-38: Showing ^{85}Kr detection results for UIO-66 and its doped counterparts.

4. Doped UIO-1,4,-NDC

4.1 Synthesis

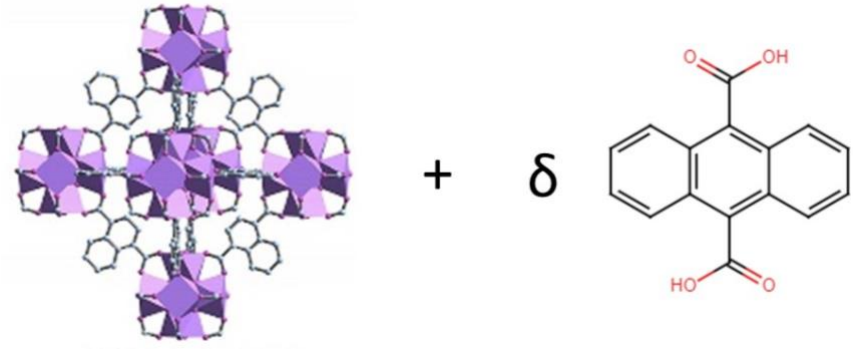

Figure V-39: Illustrating the doping strategy for the UIO-1,4-NDC lattice.

Table V-9: Showing the doped UIO-1,4-NDC synthesis.

Doping %	1.38%	5.5%
ADC:BDC ratio	1:24	1:6
ADC:Unit cell	1:6	2:3

The doping strategy for UIO-1,4-NDC consist of substituting the NDC ligand with the ADC ligands as shown in Figure V-39. The calculations for the ADC:Unit cell is unchanged with respect to UIO-66. Table V-9 summarises the two ADC substitution ratio explored here. Below is the synthesis protocol for the doped UIO-1,4-NDC. As explained in Chapter IV, the UIO-1,4-NDC is synthesised in crystalline powder form using the modulated synthesis approach. The same modulator concentration was used here as in Chapter IV.

Protocol for UIO-1,4-NDC + 1.38% ADC

For this synthesis the same concentration of metal and combined ligand/s as for UIO-1,4-NDC synthesis was used to successfully obtain doped UIO-1,4-NDC crystalline powder. $ZrCl_4$ (0.043 mol·L^{-1}, 1 g), 1,4-naphthalenedicarboxylic acid (0.042 mol·L^{-1}, 0.915 g), 9,10-anthracenedicarboxylic acid (0.0006 mol·L^{-1}, 15.8 mg) and benzoic acid (2.4 mol·L^{-1}, 29 g), were dissolved in 100 mL of *N*,*N*-dimethylformamide (DMF). The mixture was equally divided into twelve 10 mL scintillation vials, which were then sealed with a screw cap. The vials were placed in an oven at 120 °C for 24 hours yielding doped crystalline powder of UIO-1,4-NDC + 1.38% ADC single crystals. The closed vials were removed and left to cool. The powder was washed using the centrifuge according to the protocol described in Chapter II. The SEM image of UIO-1,4-NDC + 1.38% ADC as well as the measurements of some particle sizes is displayed

in Figure V-40. A clear polyhedral crystal shape is observed here. The particle sizes observed are of the order of 2-5 µm.

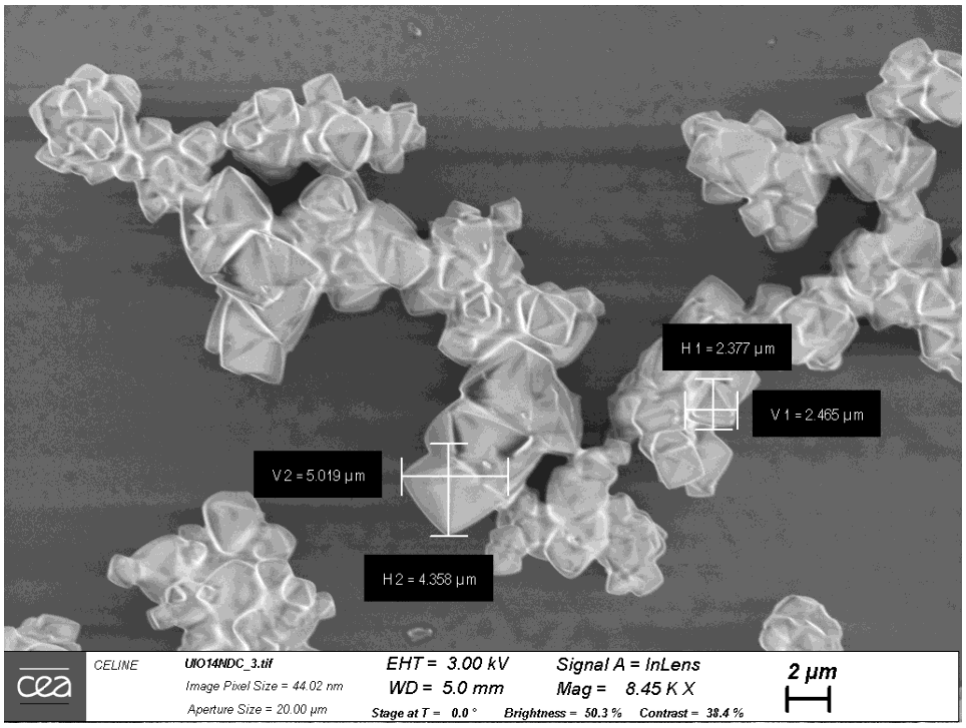

Figure V-40: Shows the SEM image of UIO-1,4-NDC + 1.38% ADC crystalline powder.

Protocol for UIO-1,4-NDC + 5.5% ADC

For this synthesis the same concentration of metal and combined ligand/s as for UIO-1,4-NDC synthesis was used to successfully obtain doped UIO-1,4-NDC crystalline powder. $ZrCl_4$ (0.043 mol·L^{-1}, 1 g), 1,4-naphthalenedicarboxylic acid (0.040 mol·L^{-1}, 0.875 g), 9,10-anthracenedicarboxylic acid (0.0024 mol·L^{-1}, 63.5 mg) and benzoic acid (2.4 mol·L^{-1}, 29 g), were dissolved in 100 mL of *N*,*N*-dimethylformamide (DMF). The mixture was equally divided into twelve 10 mL scintillation vials, which were then sealed with a screw cap. The vials were placed in an oven at 120 °C for 24 hours yielding doped crystalline powder of UIO-1,4-NDC + 5.5% ADC single crystals. The closed vials were removed and left to cool. The powder was washed using the centrifuge according to the protocol described in Chapter II. The SEM image of UIO-1,4-NDC + 5.5% ADC as well as the measurements of some particle sizes is shown in Figure V-41. A clear polyhedral crystal shape is observed here. The particle sizes observed are of the order of 2-5 µm.

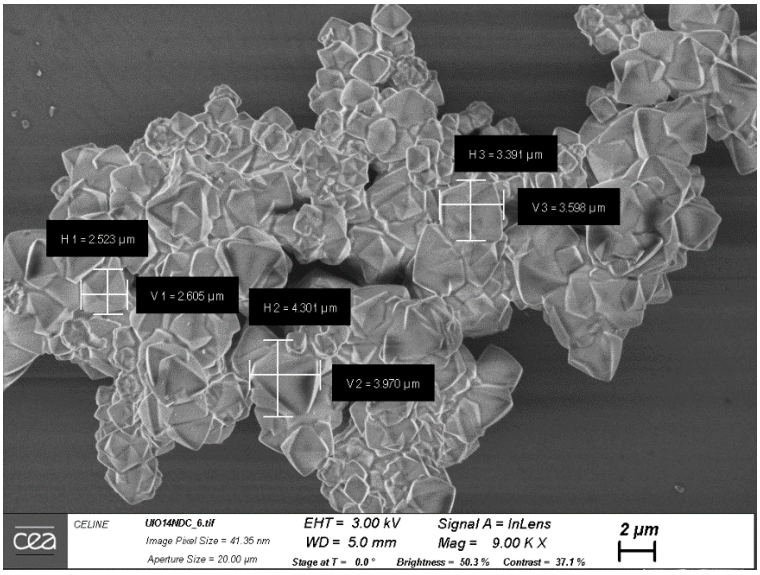

Figure V-41: Shows the SEM image of UIO-1,4-NDC + 5.5% ADC crystalline powder.

4.2 Structural characterisation

4.2.1 X-Ray Diffraction

Figure V-42 shows the X-ray Diffraction spectrum of our two doped UIO-1,4-NDC sample compared to the undoped UIO-1,4-NDC studied in Chapter IV and the simulated XRD reported in literature[13]. The peak positions are similar in all the sets indicate that we have indeed synthesised doped versions of UIO-1,4-NDC crystalline powder. This MOF appears to be homogenously doped since no new peak have appeared in the doped XRD spectrum.

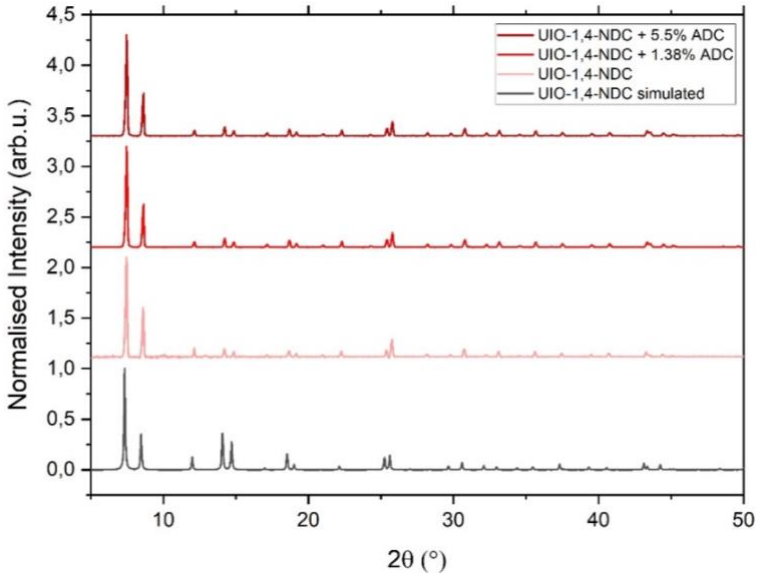

Figure V-42: PXRD spectrum showing experimental results of each doped UIO-1,4-NDC compared to the undoped UIO-1,4-NDC and literature.

4.2.2 Adsorption measurements

The N_2 adsorption experiments for UIO-1,4-NDC and its doped counterparts were all carried out at the ILV laboratory using the same equipment for comparison purposes. The N_2 adsorption isotherm is shown in Figure V-43 and Table V-10 summarises the results extracted from these data. We could not measure our MOF's pore sizes and pore volume since the ILV laboratory did not have the appropriate device to do so. The Type I isotherms show the microporosity of all three MOFs. The BET surface area of UIO-1,4-NDC doped and undoped are consistent with literature[14] values reported for UIO-1,4-NDC. UIO-1,4-NDC + 1.38% ADC has a higher surface area than the undoped UIO-1,4-NDC as well as UIO-1,4-NDC + 5.5% ADC. We can see here and for the other MOFs in this chapter that it is relatively difficult to evaluate a relationship between doping and the specific surface area.

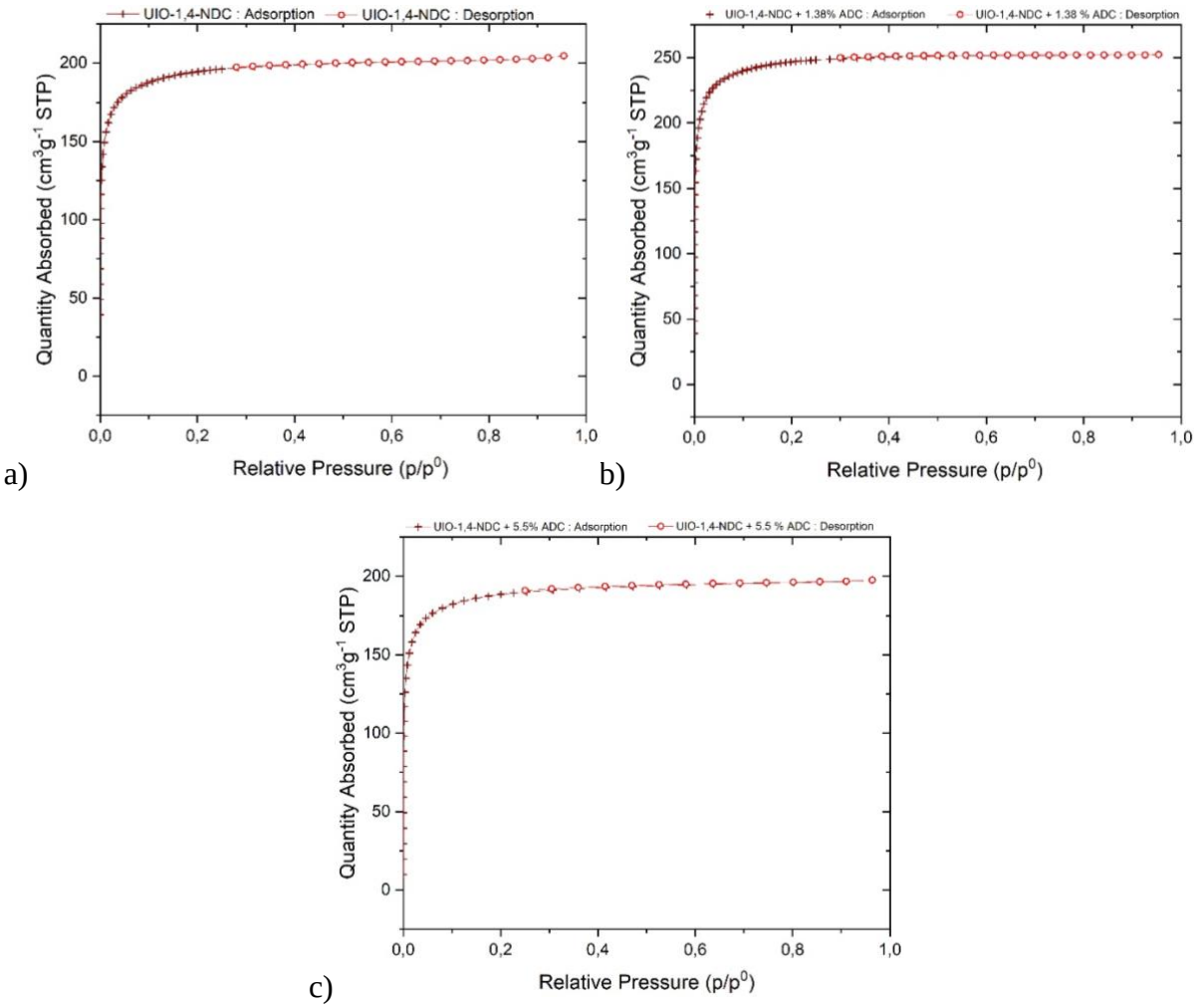

Figure V-43: Illustrating the N_2 adsorption isotherm of a) UIO-1,4-NDC, b) UIO-1,4-NDC + 1.38% ADC and c) UIO-1,4-NDC + 5.5% ADC.

Table V-10: Showing the data calculated from N_2 adsorption of undoped UIO-1,4-NDC and its doped counterparts.

MOF	BET SA ($m^2 \cdot g^{-1}$)
UIO-1,4-NDC	760
UIO-1,4-NDC + 1.38% ADC	976
UIO-1,4-NDC + 5.5% ADC	739

4.2.3 Thermogravimetric Analysis

Figure V-44 shows the TGA results of UIO-1,4-NDC and its doped counterparts. For all the UIO-1,4-NDC samples we can observe a drop before 100°C accounting for surface water and residual DCM loss. We also observe weight loss between 100°C and 300°C, which is attributed to the dehydroxylation of the Zr cluster, as discussed in section 1.2.3 of Chapter IV. A significant drop in the weight of the sample between 350-500°C is also observed, similar to the Zn-based MOFs. This result is consistent with the literature where the decomposition temperature (T_d) is reported to be between 400-500°C depending on the sample preparation, activation and experimental conditions[5]. The MOF decomposes to zirconia at these temperatures. All the UIO-1,4-NDC TGAs have a similar profile.

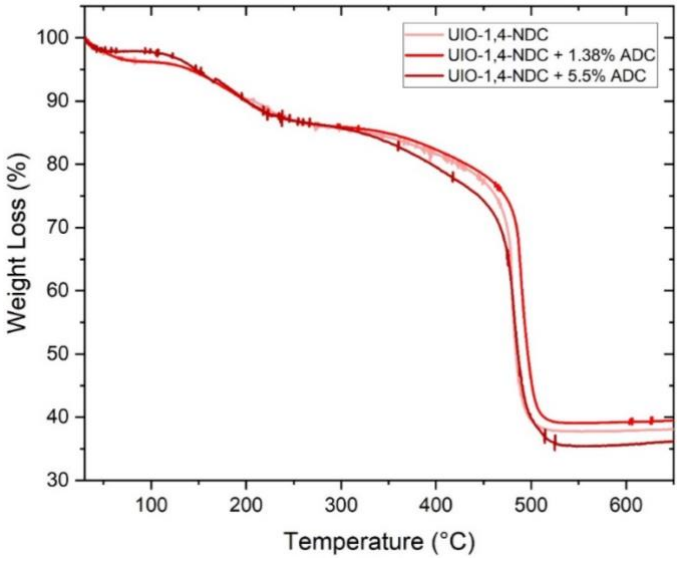

Figure V-44: TGA UIO-1,4-NDC and its doped counterparts.

4.2.4 FT-IR experiments

As seen in Chapter IV, the FT-IR spectrum of UIO-1,4-NDC is consistent with literature[12]. We can see from Figure V-45 that the spectrum of the doped and undoped versions of UIO-1,4-NDC are identical meaning that at such a low doping percentage the doping is undetectable by FT-IR experiments.

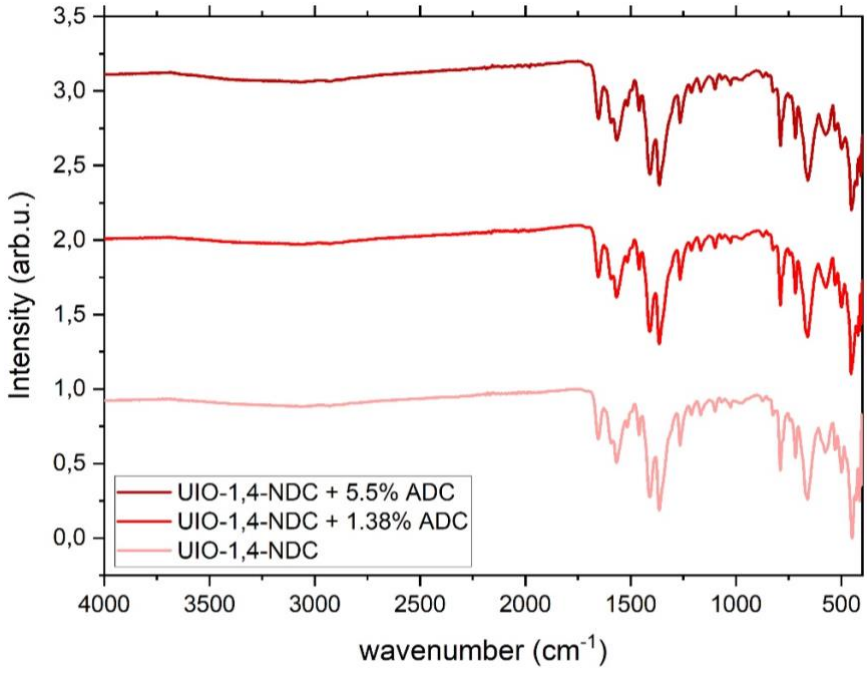

Figure V-45: Showing FT-IR results for UIO-1,4-NDC and its doped counterparts.

4.3 Photophysical characterisation

4.3.1 Excitation and Emission spectra

We can see in Figure V-46 that the emission of UIO-1,4-NDC is centered on the emission of a 10^{-5} M solution of its ligand (1,4-NDC) in DMF. We can also observe that by doping UIO-1,4-NDC with a small percentage of ADC ligand (1.38% ADC or 5.5% ADC), we have shifted the emission to around 440 nm and 450 nm for UIO-1,4-NDC + 1.38% ADC and UIO-1,4-NDC + 5.5% ADC respectively. This centres the emission of both doped UIO-1,4-NDC between the ADC ligand in DMF and the ADC solid ligand. This might be due to the powdered nature of the UIOs. The UIO-1,4-NDC + 5.5% ADC emits at a slightly higher wavelength than the UIO-1,4-NDC + 1.38% ADC as seen with MOF-5 and UIO-66. Note that a similar energy transfer between both ligands as explained for IRMOF-7 is expected for this MOF due to the overlap of the emission and excitation spectra of the ligands (see Appendix Figure 5).

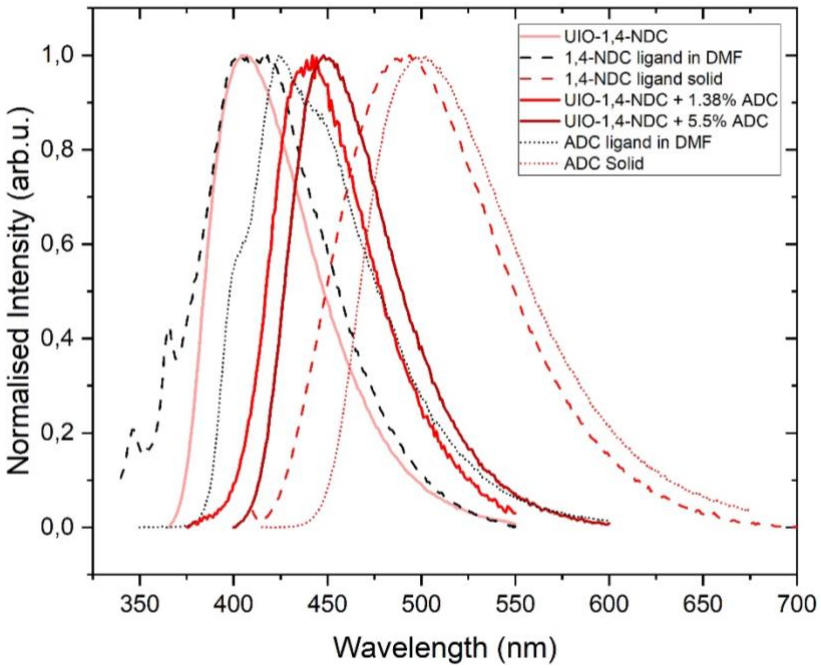

Figure V-46: Emission spectrum of UIO-1,4-NDC and its doped counterparts (solid lines), BDC ligand in DMF (dashed black line), BDC ligand solid (dashed red line), ADC ligand in DMF (dotted black line) and ADC ligand solid (dotted red line).

4.3.2 TCSPC

Figure V-47 reveals the fluorescence decay profile of UIO-1,4-NDC with 339 nm excitation diode and doped UIO-1,4-NDC with a 368 nm excitation diode since the fluorescence is centred on the ADC ligand. By fitting this decay curve with a third-order exponential fit, we can calculate the fluorescence lifetime components, their respective weights, and an average fluorescence lifetime. The results are shown in Table V-11 together with the coefficient of determination (R-Square / COD) of the fit. We can see that the average fluorescence lifetimes of the two doped UIO-1,4-NDC are similar. We can also observe an increase in the fluorescence lifetimes of the doped UIO-1,4-NDC compared to the undoped UIO-1,4-NDC (similar to what we have seen for MOF-5 and UIO-66) meaning this is slightly more inconvenient for coincidence detection since faster fluorescence lifetimes are desired. The lifetime is only slightly higher than the desired 3 ns ideal for coincidence detection.

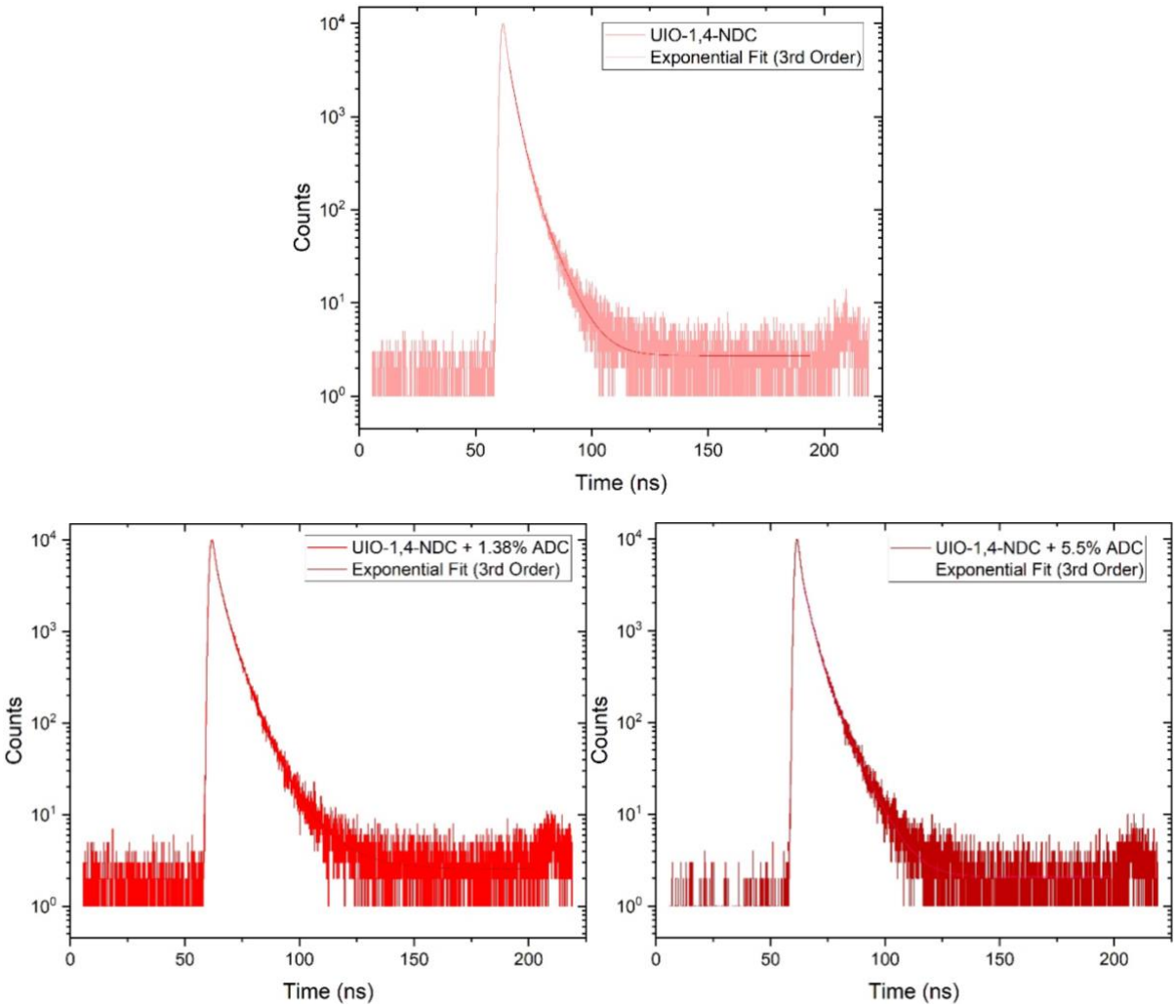

Figure V-47: Showing the TCSPC results of UIO-1,4-NDC and its doped counterparts.

Table V-11: Showing the calculated fluorescence lifetime of UIO-1,4-NDC and its doped counterparts.

MOF	**Diode λ_{ex} (nm)**	**λ_{em}**	**τ_1 (ns)**	**τ_2 (ns)**	**τ_3 (ns)**	**<τ> (ns)**	**R-Square (COD)**
UIO-1,4-NDC	339	405	2.9 (79.7%)	7.1 (17.0%)	0.5 (3.3%)	3.5	0.9994
UIO-1,4-NDC + 1.38% ADC	368	440	5.9 (52.7%)	2.6 (43.4%)	12.8 (3.9%)	4.7	0.9994
UIO-1,4-NDC + 5.5% ADC	368	430	3.2 (70.0%)	7.7 (27.2%)	0.4 (3.8%)	4.3	0.9994

4.4 Radioactive gas bench test

4.4.1 ^{85}Kr

Figure V-48 shows the results from ^{85}Kr gas detection. We can observe here that the photon count rate for UIO-1,4-NDC increased from 98 s^{-1} to 106 s^{-1} for UIO-1,4-NDC + 1.38% ADC. This relays to only a 8% increase in the photon count with a 1.38% ADC doping which is similar to what was obtained with UIO-66 (9% increase) and significantly lower than what was obtained with the doping of MOF-5 with 1.38% ADC (52% increase). Further increasing the doping percentage to 5.5% ADC decreases the photon count to 84 s^{-1} which is very close to the blank. We can observe that even though the number of photons emitted by UIO-1,4-NDC approaches that of our microspheres of polystyrene, all the MOFs presents in Figure V-48 have a relatively mediocre performance compared to this reference microspheres material. We can conclude here that the doping strategy has not worked as well in boosting the performance of UIO-1,4-NDC as it has done for MOF-5, as we have also seen for UIO-66. This might be due to the powdered UIO-1,4-NDC geometry compared to MOF-5 where too much of the photons produced was trapped due to the opacity of the powder.

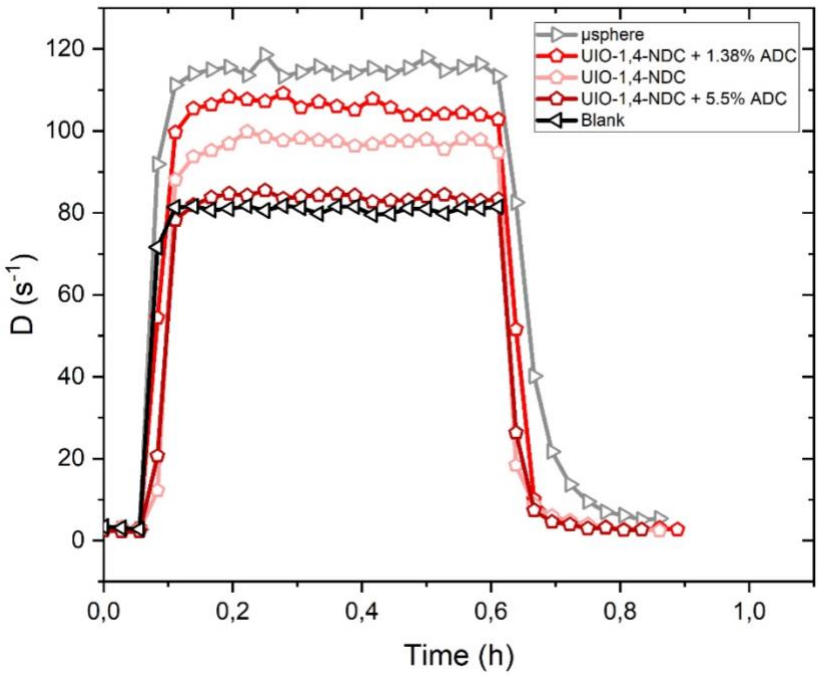

Figure V-48: Showing ^{85}Kr detection results for UIO-1,4-NDC and its doped counterparts.

5. Comparison and discussion

5.1 Radioluminescence experiments

The RL experiments for the multitude of doped MOF are reported in the Appendix Figures 10-13. The scintillation yield of each MOF (undoped and doped) are compared to that of an anthracene crystal in Figure V-49.

Aside from summarising the scintillation yield of the MOFs presented here, Table V-12 also lists the emission wavelength obtained from PL and RL experiments. One blatant observation is that for every MOF (except IRMOF-7), the doping strategy reduced the difference between the PL and RL emission wavelengths.

For MOF-5 and UIO-66, we can observe and increase in the scintillation yield upon doping with 1.38% ADC. When further doping up to 5.5% ADC, we can notice a decrease in the scintillation yield. For MOF-5, this is consistent with what we have observed with the photoluminescence light yield experiments with the integrating sphere in section 1.3.3 of this chapter. We can notice that our doping strategy does not drastically increase the scintillation yield, as we would expect since it did considerably increase the performance of MOF-5 for ^{85}Kr detection. One possible explanation is that since we only have one ADC every 24 units cells or MOF-5 + 1.38% ADC, we are faced with the problem of bound excitons within the lattice as theorised by A. Kshirsagar *et al.*[15].

The highest scintillation yield in this chapter is attributed to IRMOF-7. This material has shown in Chapter III, no porosity and is therefore very dense. This promotes interactions π-π interactions. We can prove this via an increase in the difference between the RL and PL emission wavelength and an increase in the scintillation yield as we increase the doping percentage.

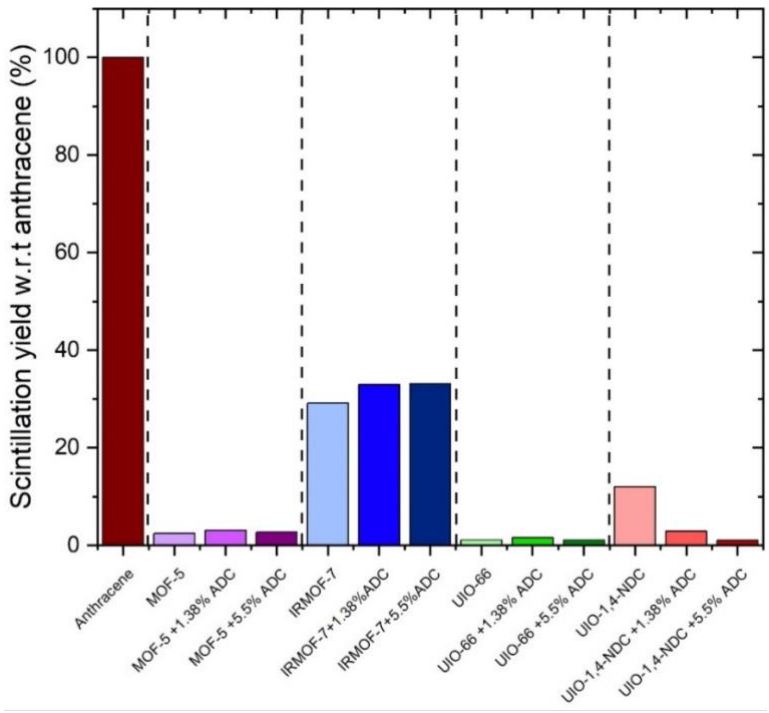

Figure V-49: Illustrating the percentage scintillation yield of each undoped and doped MOF with respect to an anthracene crystal.

Table V-12: Comparing the maximum wavelength of emission of the PL experiments with the RL experiments of activated undoped and doped MOFs and showing the scintillation yields of each MOF calculated via radioluminescence experiments.

	PL λ_{em} (nm)	RL λ_{em} (nm)	Scintillation yield w.r.t Anthracene (%)	Scintillation Yield (ph·MeV^{-1})
Anthracene Single Crystal	-	450	100	15000
MOF-5	358	420	2.5	367
MOF-5 + 1.38% ADC	429	434	3.0	456
MOF-5 + 5.5% ADC	429	431	2.7	407
IRMOF-7	412	418	29.1	4369
IRMOF-7 + 1.38%ADC	427	452	32.9	4935
IRMOF-7 + 5.5%ADC	432	448	33.1	4967
UIO-66	365	405	1.1	158
UIO-66 + 1.38% ADC	432	452	1.6	233
UIO-66 + 5.5% ADC	438	460	1.1	158
UIO-1,4-NDC	405	433	12.0	1803
UIO-1,4-NDC + 1.38% ADC	442	450	2.9	429
UIO-1,4-NDC + 5.5% ADC	448	457	1.0	156

5.2 ^{85}Kr radioactive gas bench test

5.2.1 Photon count rate

Figure V-50 shows the photon count rate of all the MOFs discussed in this chapter doped with 1.38% ADC when detecting a 10 kBq or 76 Bq·cm^{-3} of ^{85}Kr gas. The MOFs doped with 1.38% ADC are the only ones reported here for clarity as they are the best performing for ^{85}Kr detection in this chapter. The average of each plateau was calculated and subtracted from the average plateau of the blank measurement to obtain the true photon count rate produced by the MOF only. The results are summarised in Table V-13 for all the MOFs presented in this chapter and the best results are presented in bold.

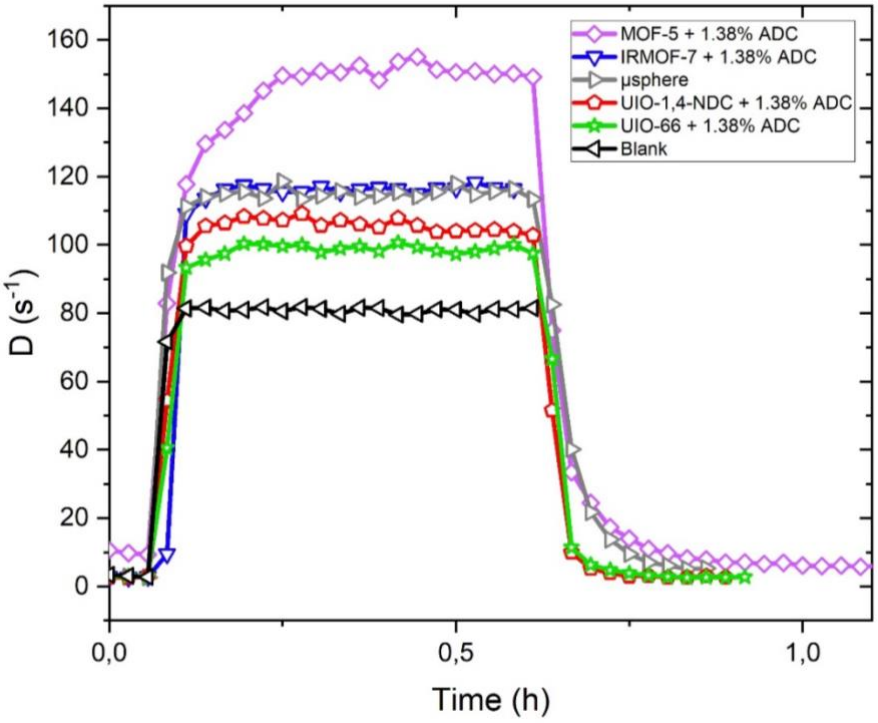

Figure V-50: Comparing the photon count rate of each MOF doped with 1.38% ADC for the detection of 10 kBq of 85Kr.

Table V-13: Showing the plateau average for MOF in this chapter and the µsphere for the 40 ns coincidence windows.

	Effective D in cps (CW-40 ns)
µspheres	34
MOF-5	18
MOF-5 + 1.38 % ADC	**70**
MOF-5 + 5.5 % ADC	15
IRMOF-7	4
IRMOF-7 + 1.38 % ADC	36
IRMOF-7 + 5.5 % ADC	7
UIO-66	11
UIO-66 + 1.38 % ADC	18
UIO-66 + 5.5 % ADC	12
UIO-1,4-NDC	17
UIO-1,4-NDC + 1.38 % ADC	25
UIO-1,4-NDC + 5.5 % ADC	3

Table V-13 summarises that the MOF that produced the higher net photon count rate in the presence of ^{85}Kr is MOF-5 + 1.38 % ADC. We have seen that MOF-5 + 1.38% ADC was reported with a high BET surface area and had a shifted emission wavelength upon doping onto the anthracene which was compatible with the PMTs in the experimental setup. The photoluminescence yield of this MOF was also seen to be higher than its undoped counterpart. This might account for the good results shown here.

We can calculate from the net photon count rate of MOF-5 + 1.38% ADC the primary detection efficiency ε_D using Equation V-2 below.

$$\varepsilon_D = \frac{D}{A_V \times V}$$

Equation V-2

where D is the net photon count (MOF count – blank), A_V is the injected volumic activity and V is the volume cavity of the sample holder (values available in Table V-14). This calculation yields to an ε_D value of 185% for MOF-5 + 1.38% ADC which is above 100% thereby providing evidence of a concentration effect of the radioactive gas within the pores of the MOF. ^{85}Kr therefore interacts with the pores of our MOF and this creates a local radioactive gas concentration higher to our injected one.

This ε_D needs to be corrected by estimating the true volume available to the gas since the MOF occupied a specific volume in the sample holder cavity. With the knowledge of the MOFs' mass, we put inside the cavity (161 mg) and the theoretical density of our MOFs being 0.2[16] we can evaluate the percentage of the occupied volume by MOF-5 + 1.38% ADC at 40.0%. As MOFs are porous architectures, this volume must be further corrected by the percentage of the void present in these architectures. This correction was calculated using lattice parameters and experimental pore size, obtained by BET, to obtain a percentage of the MOF actually occupied by matter. The value is 52% for MOF-5 + 1.38% ADC giving us a final volume occupied by the MOF of 20.8%. This percentage can be used to be deduce the corrected volume, V_c.

The true activity of radioactive gas that interacts directly with the MOF should also be calculated. By performing MCNP-6 simulation[17] we estimated the percentage of beta that interacts with our system. Our MOF is not very dense, therefore, there is a possibility that beta escapes and does not interact with our scintillating MOF. The simulation provides us with a 99.7% proportion of beta that interacts and deposits at least 1 keV inside the MOF. Therefore, only 0.3% of the beta from ^{85}Kr decay are not seen by our system, so the corrected volumetric activity, A_{V_c}, is comparable to the uncorrected one. Using Equation V-3 and the corrected values, we calculated a corrected detection efficiency, of 234%. This further validates our assumption of the local concentration of radioactive gases within the pores of our MOF.

$$\varepsilon_c = \frac{D}{A_{V_c} \times V_c}$$

Equation V-3

These calculations are summarised in Table V-14 below.

Table V-14: Summarising the calculations for the corrected detection efficient of 10 kBq of ^{85}Kr detection with MOF-205.

MOF	Net D (s^{-1})	A_V ($Bq \cdot cm^{-3}$)	V (cm^3)	ε_D (%)	ε_c (%)
MOF-5 + 1.38% ADC	70	75.7	0.5	185	234

The ε_c efficiency calculated here are not yet true efficiency measurements as several parameters such as scintillation yields, transparency of the media, or nonlinearity of the scintillator are not considered. These effects are however negligible in the case of ^{85}Kr because of its relatively high beta spectrum, hence are not explored here.

6. Chapter Conclusion

In this chapter we demonstrated the synthesis of doped versions of MOF-5, UIO-66 and UIO-1,4-NDC. Unfortunately, the same was not concluded for doped IRMOF-7 which showed very poor similarities in the structural characterisation compared to literature. We have proven by structural characterisation that they were indeed the targeted MOFs. However, a relationship between doping and surface area could not be determined with certainty.

We investigated the effect of doping on their photophysical properties where we concluded that doping a MOF with a small amount of a highly fluorescent ligand not only shifts the wavelength of emission but also increases its photoluminescence yield. We also evaluated a doping threshold above which self-absorption from the ADC limits the photoluminescence light yield. We have also noticed slightly slower fluorescence lifetimes for the doped MOFs compared to the undoped ones. These results validate our doping strategy to boost the fluorescence and scintillation yield, which is of interest for the MOF community in general, irrespective of their performance for radioactive gas detection.

We demonstrated via the RL experiment a relatively small but significant increase in the scintillation yield of our MOF when doped with 1.38% of ADC. Just like in PL experiments, we observed a decrease upon increasing the doping percentage due to self-absorption from the ADC.

Due to this approach, we proved that MOF-5 doped at 1.38% ADC was an efficient scintillators for the detection of ^{85}Kr. This is due to its high surface area and shifted emission wavelength in the correct range for the PMT, as well as the incorporated ADC ligand having a better photoluminescence yield than the previous BDC ligand. By comparing the performance of doped MOF-5 with that of the doped UIO-66 and UIO-1,4-NDC we were able to conclude that the doping strategy is far more effective on single crystal morphology like MOF-5 rather than powdered forms like the UIOs for the purpose of radioactive gas detection. We have also shown the limitation of the doping strategy by demonstrating that doping at higher percentages (5.5% ADC in this case) does not further increase the photoluminescence yield or the performance of our MOF as a scintillator for ^{85}Kr detection. On the contrary, the efficiency of a highly doped MOF as scintillator is dampened by self-absorption. Therefore, low doping percentages are preferred for boosting scintillating properties of MOFs.

MOF-5 + 1.38% ADC has a higher photon count rate than our best candidate in other chapter III, MOF-205 and a lower photon count rate than our best performing MOF from Chapter IV, UIO-67.

We also proved that the detection of ^{222}Rn and ^{3}H were possible with MOF-5 + 1.38% ADC even though the performance of MOF-5 + 1.38% ADC is less efficient than that of MOF-205 for ^{3}H detection.

These results validate partially the doping strategy for boosting the performance of MOFs as scintillators, especially for MOFs with millimetric single crystal morphology. Moving towards the same morphology for the different MOFs might help us for a better comparison.

REFERENCES

1. Taniguchi, M. & Lindsey, J. S. Database of Absorption and Fluorescence Spectra of >300 Common Compounds for use in PhotochemCAD. *Photochem Photobiol* **94**, 290–327 (2018).

2. Yaghi, O. M., Li, G. & Li, H. Selective binding and removal of guests in a microporous metal–organic framework. *Nature* **378**, 703–706 (1995).

3. Gangu, K. K., Maddila, S. & Jonnalagadda, S. B. The pioneering role of metal-organic framework-5 in ever-growing contemporary applications - a review. *RSC Adv* **12**, 14282–14298 (2022).

4. Huong, T. T. T., Thanh, P. N., Huynh, N. T. X. & Son, D. N. Metal – organic frameworks: State-of-the-art material for gas capture and storage. *VNU J. Sci.: Math. – Phys.* **32**, 67–85 (2016).

5. Healy, C. *et al.* The thermal stability of metal-organic frameworks. *Coord Chem Rev* **419**, 213388 (2020).

6. Perego, J. *et al.* Highly luminescent scintillating hetero-ligand MOF nanocrystals with engineered Stokes shift for photonic applications. *Nat Commun* **13**, 1–10 (2022).

7. Trepte, K. & Schwalbe, S. Systematic Analysis of Porosities in Metal-Organic Frameworks. 1–9 (2019).

8. Chapon, A., Pigrée, G., Putmans, V. & Rogel, G. Optimization of liquid scintillation measurements applied to smears and aqueous samples collected in industrial environments. *Results Phys* **6**, 50–58 (2016).

9. Schaate, A. *et al.* A Novel Zr-Based Porous Coordination Polymer Containing Azobenzenedicarboxylate as a Linker. *Eur. J. Inorg. Chem* 790–796 (2012).

10. Ambroz, F., Macdonald, T. J., Martis, V. & Parkin, I. P. Evaluation of the BET theory for the characterization of meso and microporous MOFs. *Small Methods* **2**, 1–17 (2018).

11. Ali-Ahmad, A., Hamieh, T., Roques-Carmes, T., Hmadeh, M. & Toufaily, J. Effect of Modulation and Functionalization of UiO-66 Type MOFs on Their Surface Thermodynamic Properties and Lewis Acid–Base Behavior. *Catalysts* **13**, (2023).

12. Xu, W., Dong, M., Di, L. & Zhang, X. A facile method for preparing uio-66 encapsulated ru catalyst and its application in plasma-assisted co2 methanation. *Nanomaterials* **9**, 10–13 (2019).

13. Butova, V. V. *et al.* Modulator effect in UiO-66-NDC (1, 4-naphthalenedicarboxylic acid) synthesis and comparison with UiO-67-NDC isoreticular metal-organic frameworks. *Cryst Growth Des* **17**, 5422–5431 (2017).

14. He, Y. *et al.* UiO-66-NDC (1,4-naphthalenedicarboxilic acid) as a novel fluorescent probe for the selective detection of Fe3+. *J Solid State Chem* **285**, 121206 (2020).

15. Kshirsagar, A. R., Blase, X., Attaccalite, C. & Poloni, R. Strongly Bound Excitons in Metal–Organic Framework MOF-5: A Many-Body Perturbation Theory Study. *J Phys Chem Lett* **12**, 4045–4051 (2021).

16. Sim, J. *et al.* Gas adsorption properties of highly porous metal–organic frameworks containing functionalized naphthalene dicarboxylate linkers. *Journal of the Chemical Society. Dalton Transactions* **43**, 18017–18024 (2014).

17. Mauree, S. *et al.* Detection of Radioactive Gas with Scintillating MOFs. *Adv Funct Mater* (2023) doi:10.1002/adfm.202302877.

Conclusions and Perspectives

Conclusions and Perspectives

Conclusions

This thesis aimed to determine whether the outstanding surface area and fluorescence of MOFs could be combined to produce a scintillating porous material for detecting radioactive gases such as ^{85}Kr, ^{222}Rn and ^{3}H.

To complete such an objective, one first had to build strong foundations of ionising radiation and its interaction with matter, specifically photoluminescence mechanisms. An extensive literature review of MOFs and their synthesis was exposed here, focusing on fluorescent and scintillating MOFs.

The different structural and photophysical characterisation techniques were explained in Chapter II. The homemade gas bench test experiment was also detailed together with the Triple-to-Double Coincidence ratio detection system.

In total 16 MOFs were synthesized and fully characterized. We separate them in three sections; pure Zn based MOFs, pure Zr based MOFs, and ligand doped MOFs. For each MOF we gave an identity card of their structural, photo-physical, and radio-physical characterizations.

In Chapter III we demonstrated the successful synthesis of millimetric single crystals of MOF-5, IRMOF-9 and MOF-205. Unfortunately, the same cannot be said for IRMOF-7, whose characterisation was not on par with literature. The size of the single crystals synthesised here are amongst the biggest discussed in the literature. We were able to confirm our hypothesis that the emission of the MOFs presented here is centred on the emission of their respective ligands. The MOFs were all tested for ^{85}Kr detection, whereby MOF-5, IRMOF-9 and MOF-205 have exhibited an emission of photons in the presence of ^{85}Kr. MOF-5 showed mediocre results (poorer than our reference microsphere material) due to its low scintillation yield and relatively low emission wavelength. We also demonstrated the reproducibility of our system with three consecutive cycles and demonstrated a linear relationship of the photon count with respect to the injected volumic activity of ^{85}Kr. From these results, we could determine our system's decision threshold to be at 3.03 $Bq \cdot cm^{-3}$ and a limit of detection at 6.07 $Bq \cdot cm^{-3}$.

Chapter IV aimed to explore Zr-based MOFs, which are known to be more stable towards humidity. The synthesis of Zr-based MOFs represented a complex challenge. A modulated synthesis method was developed to create a competition between the modulator and the ligand in the MOF. We demonstrated that we could go from a non-crystalline product to a crystalline MOF using this method. The crystal size for UIO-67 was of the order of 100 µm, which is amongst the biggest reported in the literature for Zr-based MOFs. The MOFs in this chapter were all tested for ^{85}Kr detection. All of them produced photons in the presence of ^{85}Kr. Relatively poor results were obtained with UIO-66 and UIO-1,4-NDC.

We have implemented in the last chapter an innovative doping strategy which demonstrated that by doping an existing MOF with only 1.38% or 5.5% ADC, we were able not only to shift the emission of the MOF towards more appropriate wavelengths for the gas detection experiment in coincidence but also considerably boost the scintillation yield. The best-performing doped MOF for ^{85}Kr detection was MOF-5 + 1.38% ADC. We demonstrated with the ^{85}Kr detection experiment, photoluminescence and radioluminescence light yield experiments that, increasing the doping percentage to 1.38% increases the scintillation yield but further increasing to 5.5% ADC decreases the light yield and, hence, the number of photons produced for the gas detection experiment.

Table 1 is a summarises the result obtained for ^{85}Kr detection for the 16 MOFs studied in this manuscript together with the respective specific surface area (SSA), RL yield and maximum PL emission wavelength to help us determine the properties and relationship that mostly affect the performance towards ^{85}Kr detection. The effective D values reported so far were normalised with respect to the mass of MOF used in the scintillating vial and the exact activity injected for each experiment for an accurate comparison (see Appendix Tables 1-3). The table below is listed from the best performing MOF to the least with regards to the D/mass/activity values.

*Table 1: Summarising all MOFs tested for ^{85}Kr detection listed from best performing to least performing according to the D/mass/activity values (coincidence window 40 ns) accompanied by the specific surface area (SSA), RL yield and the maximum PL emission wavelength. * - very little mass for this MOF (see Appendix Table 1), a – NIMBE, b – UNIMIB and c – ILV measurements.*

MOF	D/mass/activity ($s^{-1}\cdot g^{-1}\cdot kBq^{-1}$)	SSA ($m^2\cdot g^{-1}$)	RL yield ($ph\cdot MeV^{-1}$)	PL λ_{em} (nm)
MOF-5 + 5.5 % ADC*	42.8	3444[b]	407	429
MOF-5 + 1.38% ADC	41.9	3752[b]	456	429
MOF-205	33.6	5390[a]	4001	390
UIO-67	31.0	2670[a]	3966	365
CAU-24	24.8	1008[a]	3057	390
IRMOF-9	22.6	902[b]	867	430
UIO-1,4-NDC + 1.38 % ADC	11.3	976[c]	429	442
UIO-66 + 1.38 % ADC	9.9	928[a]	233	432
IRMOF-7 + 1.38 % ADC	9.0	0[b]	4935	427
UIO-1,4-NDC	8.8	760[c]	1803	405
UIO-66	7.9	860[a]	158	365

MOF-5	7.5	3360[b]	367	358
UIO-66 + 5.5 % ADC	6.8	940[a]	158	438
IRMOF-7 + 5.5 % ADC	3.2	0[b]	4967	432
UIO-1,4-NDC + 5.5 % ADC	1.5	739[c]	156	448
IRMOF-7	1.0	0[b]	4369	412

We can observe that MOF-5 + 5.5% ADC is the first to be reported in this table, however not a lot of this MOF was available to perform the experiment since the synthesis yielded a small amount of MOF. The mass of this MOF is extremely small and incomparable to the other ones (see Appendix Table 1). As this result is to be taken with cautious, we have decided to disregard this MOF as a good candidate for our comparison study.

Our best performing MOF for ^{85}Kr detection is hence MOF-5 + 1.38% ADC. It has the 2nd largest surface area reported and an ideal wavelength of emission with respect to the PMTs. Nevertheless, we notice a relatively poor performance in the RL experiments, which, as explained in Chapter V, maybe due to difficulties in excitons mobility in the MOF-5 lattice.

By comparing the D/mass/activity values with the SSA, we clearly notice a trend of increasing ^{85}Kr detection performance with increasing SSA. However, some exceptions are worth mentioning. For example, MOF-5 has one of the highest surface areas, but this is not enough to counterbalance its poor photophysical properties, i.e. emission at a low wavelength and relatively poor RL/scintillation yield.

MOF-205, UIO-67 and CAU-24 are good performers across all boards with good results for ^{85}Kr detection, high SA and excellent scintillation yields from the RL experiments. Even though MOF-205 present a remarkable stability toward moisture for a Zn based MOF, the two other might be better candidate for a real atmosphere test. IRMOF-7 and its doped counterparts, which we have determined to be non-porous materials, are the only ones to have an excellent RL performance but a mediocre performance for ^{85}Kr detection. This proves that a material with the best photophysical properties (even an emission in the correct wavelength for coincidence detection) will not be able to perform well for the detection of radioactive gases without porosity.

Table 2 summarised the results from the ^{222}Rn detection. Unlike for 85Kr, a plateau is not obtained for ^{222}Rn detection so the D value reported here was the highest photon count rate achieved in each experiment. We can notice that the performance clearly decreases with decreasing surface area. The poorer result for UIO-67 might be, aside from a lower SA, an emission at a lower wavelength than the required values for the PMT. MOF-205 being the best performing MOF was also used to perform a long ^{222}Rn detection experiment. The results were

used to calculate for the first time the half-life of ^{222}Rn using a MOF. We cannot compare these results to ^{85}Kr detection since not the same ionising radiation is being studied for each MOF.

Table 2: Summarising the MOFs tested for ^{222}Rn detection listed from best performing to least performing according to the D/mass/activity values (coincidence window 40 ns) accompanied by the specific surface area (SSA), RL yield and the maximum PL emission wavelength. a – NIMBE and b – UNIMIB.

MOF	D/mass/activity ($s^{-1}\cdot g^{-1}\cdot kBq^{-1}$)	SSA ($m^2\cdot g^{-1}$)	RL yield ($ph\cdot MeV^{-1}$)	PL λ_{em} (nm)
MOF-205	7368	5390[a]	4001	390
MOF-5 + 1.38% ADC	2850	3752[b]	456	429
UIO-67	2850	2670[a]	3966	365

The detection of ^{3}H was the most challenging due to its low energy beta emission. Since in the detection of ^{85}Kr we were detecting beta particles with higher energy than the beta particles of ^{3}H, the best performing candidates filtered out from the ^{85}Kr detection will potentially have a better performance for ^{3}H detection than the other MOFs presented in Table 1. The results from ^{3}H detection are exposed in Table 3. Our best performing MOF here is MOF-205 with its outstanding surface area and proper emission wavelength for detection in coincidence. We can notice here that our best candidate for ^{85}Kr detection is now the worst performing MOF out of the three for ^{3}H detection. This reinforces the idea known in the field of scintillation of non-linearity of the photon production vs the energy absorbed. Since tritium has such low energy beta radiation, the photon production probability is very low and even more that of detection since the light diffusion and absorption of the MOF will play a crucial role at such low energies. For example, MOF-5 + 1.38% ADC having a slightly yellow tinge compared to the other two (because of the yellow ADC) might affect the light diffusion in the system. Also, as explained in Chapter V an experimental mistake led to the injection of 7 kBq of ^{3}H for UIO-67 compared to 9 kBq for the others, making the results for UIO-67 non comparable because of the non-linearity behaviour which is especially unknown at low energies.

Table 3: Summarising the MOFs tested for ^{3}H detection listed from best performing to least performing according to the D/mass/activity values (coincidence window 40 ns) accompanied by the specific surface area (SSA), RL yield and the maximum PL emission wavelength. a – NIMBE and b – UNIMIB.

MOF	D/mass/activity ($s^{-1}\cdot g^{-1}\cdot kBq^{-1}$)	SSA ($m^2\cdot g^{-1}$)	RL yield ($ph\cdot MeV^{-1}$)	PL λ_{em} (nm)
MOF-205	1.42	5390[a]	4001	390
UIO-67	7,52E-4	2670[a]	3966	365
MOF-5 + 1.38% ADC	6,10E-4	3752[b]	456	429

The detection of ^{3}H was the most challenging due to its low energy beta emission. Since in the detection of ^{85}Kr we were detecting beta particles with higher energy than the beta particles of ^{3}H, the best performing candidates filtered out from the ^{85}Kr detection will potentially have a better performance for ^{3}H detection than the other MOFs presented here.

Across all gases, we can therefore conclude that a balance between surface area/porosity and photophysical properties is required for a MOF to exhibit a good performance for detection in coincidence using the TDCR detection system. This coincidence set up is especially coherent with all the fluorescence decay measured for our MOFs. For longer-lived decay, a wider coincidence window might give even better efficiency results.

Table 1 compares our detection technique with the other technologies used in laboratories and facilities for radioactive gas detection. We can see that our system has already met the expectations for several practical parameters, such as detector mass and operational practicality. Our approach is also amongst the best in terms of measurement time and active volume used. Even though our results are pretty promising and demonstrate that MOFs can be used to detect radioactive gases, our system's limit of detection and decision threshold needs to be improved to compete with existing technologies.

Table 4: Comparison of the leading technologies used for radioactive gas detection versus the one presented in this thesis.

	Liquid scintillation	Proportional gas counter [Air]	Proportional gas counter [Sealed Xe]	Scintillating MOF + RCTD	Laboratory Target
Limit of Detection	0.005 $Bq\cdot cm^3$	0.01 $Bq\cdot cm^3$	0.5 $Bq\cdot cm^3$	6.07 $Bq\cdot cm^3$	1 $Bq\cdot cm^3$
Decision threshold	0.002 $Bq\cdot cm^3$	0.002 $Bq\cdot cm^3$	0.1 $Bq\cdot cm^3$	3.03 $Bq\cdot cm^3$	0.5 $Bq\cdot cm^3$
Measurement time range	1 h – 1 day	20 min – 1 h	> 1 h	1 min – 20 min	1 min

Active volume	1 L	8 L	11 L	0.8 mL	-
Final detector mass	> 100 kg	50 kg	220 kg	800 g	< 1kg
Operational practicality	Offline, fixed, mixed chemical and radioactive waste	Online, fixed	Online, fixed	Online, Portable	Online

Perspectives

Concerning the MOF themselves, a big challenge still lies ahead, that is that of, the morphology of the crystals. The different crystal sizes and some MOFs being in powdered form make the interpretation and comparison between them very complex. The part of the SPARTE project aimed to synthesise centimetric crystals of MOFs where one big crystal could be used in the gas detection system. This would help with light diffusion and make the sample preparation more straightforward and less time-consuming. However, the synthesis of big single crystals of MOFs are reported to be limited at tens of millimetres at best. One alternative could be the new post synthetic "monolith" method to aggregate crystals of MOF to obtain a mono block that retains the microporous properties[1]. One of these studies by P. Albacete et al. are as recent as July 2023[2]. What is especially interesting is that it includes a protocol for UIO-66 (which we have studied in this manuscript) that gives transparent monolith on the centimetre scale.

In terms of optimising the photon production, more doped MOFs could be explored, especially the ones with good performances, such as IRMOF-9, UIO-67 and CAU-24. We believe that for the doped version of MOF-5 and optimum doping percentage is still to be found. More intermediate doping percentages need to be studied between 1.38% and 5.5% as all as below 1.38%.

For this manuscript, we have assumed a non-radiative energy transfer between the main and the additional ligand of a doped MOF. As briefly discussed in Chapter V, the study of more doped MOFs could be accompanied by in-depth TCSPC measurements to determine the contribution of all the ligands to the fluorescence lifetime of each doped MOFs and evaluate if the energy transfer is indeed non-radiative.

MOF-205 having shown outstanding performance for the detection of radioactive gases as well as scintillation yield; one would want to pursue mixed ligand MOFs to make the most of the antenna effect observed in MOF-205. The exploration of CAU-24 with other fluorescent ligands such as ADC, BPDC and NDC has already started to be explored at the laboratory. For example, research for scintillating and selective MOFs could be attempted to separate Radon

from the other gases as it often disturbs the detection of other gases. The separation of Xenon and Krypton and hence detection of one or the other is also of interest.

We propose several steps to improve our detection system in the long run. One such improvement is changing the scintillation vial from the setup illustrated on the left in Figure 1 below to that on the right. This will allow us to limit unwanted phenomena such as Cherenkov for ^{85}Kr detection and the contribution from the excitation of N_2 in air for ^{222}Rn, which complicate the interpretation of the results for the MOF's contribution to the overall photon count. Several attempts were made to produce the cartridge but the glass thickness and strength would not hold being screwed to the TDCR setup.

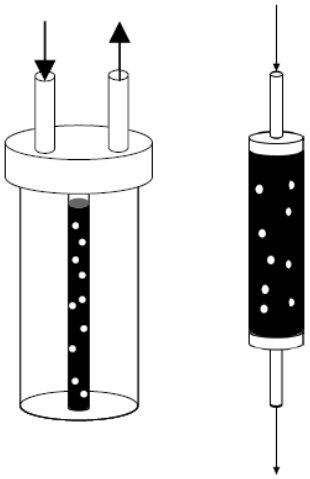

Figure 1: Left – The scintillation vial used for this thesis. Right – the proposed future cartridge setup.

Another objective of improving the gas bench setup is to record the partial pressure's effect on the photon count, which can produce some isotherm, as seen for N_2 adsorption experiments. This might give us an indication of the porosity and surface area with respect to the gas we wish to detect. One could correlate the results from this experiment with traditional BET values.

A final perspective and ideal demonstration would be a practical implementation of the full TDCR + MOF set up in a reprocessing plant ventilation shaft to provide real time measurement of the ^{85}Kr level.

This PhD paved the way to efficient and online detection of radioactive gases, even if 222Rn seems out of reach in term of industrial competition, the other gases do not have a reliable detection solution. We hope that MOFs or other porous materials will help and change the way we deal with radioactive gas in the future.

REFERENCES

1. Hou, J., Sapnik, A. F. & Bennett, T. D. Metal-organic framework gels and monoliths. *Chem Sci* **11**, 310–323 (2020).

2. Albacete, P., Asgari, M., Yang, Y., Al-Shanks, A. N. & Fairen-Jimenez, D. Self-Shaping Monolithic Reticular Materials Ingredients for Success. *Adv Funct Mater* (2023).

Scientific Communication

Publications

Published

- Mauree, S., Villemot, V., Hamel, M., Sabot, B., Pierre, S., Dujardin, C., Belloni, F., Comotti, A., Bracco, S., Perego, J., Bertrand, G. H. V., Detection of Radioactive Gas with Scintillating MOFs. Adv. Funct. Mater. 2023, 33, 2302877. https://doi.org/10.1002/adfm.202302877.

- Villemot, V., Dufour, N., Mauree, S., Sabot, B., Bertrand, G.H.V. and Hamel, M. (2022), From Sintering to Particle Discrimination: New Opportunities in Metal–Organic Frameworks Scintillators. Adv. Photonics Res., 3: 2100259. https://doi.org/10.1002/adpr.202100259.

In Progress

- Effect of ligand doping on fluorescent Metal Organic Framework (MOF) for tuning photo-physical properties.
- A scintillating Metal Organic Framework library for ^{85}Kr detection.

Conferences

- **Oral Presentation**, Metal Organic Frameworks: A novel material for the detection of radioactive gases, 16th International conference on materials chemistry (MC16), Dublin (Ireland), 03-06 July 2023.

- **Oral Presentation**, Scintillating Metal Organic Framework for radioactive gas detection, 2022 French MOFs, COFs and Porous Polymers conference, Montpellier (France), 08-09 June 2022.

- **Oral Presentation**, An efficient and online radioactive gas detection using scintillating Metal Organic Frameworks (MOF), Animma: Nuclear instrumentation and measurement methods, Lucca (Italy), 12-16 June 2023.

- **Poster Presentation,** Metal Organic Frameworks: A new class of scintillators for radioactive gas detection, 16th International Conference on Scintillating Materials & their Applications, Santa Fe (United-States), 19-23 September 2022. (BEST POSTER PRIZE)

- **Poster Presentation**, Metal Organic Framework scintillators for radioactive gas detection, 8th International Conference on Metal-Organic Frameworks and Open Framework, Dresden (Germany), 04-07 September 2022.

- **Poster Presentation,** Scintillating Metal Organic Framework for radioactive gas detection, Doctoral School annual meeting, Saclay (France), Novembre 2021. (BEST POSTER PRIZE)

- Competition of My Thesis in 180 seconds **(MT180s) –** Regional finalist.

List of Figures

List of Tables

Appendix

Appendix Table 1: Mass of MOF and activity of gas used during ^{85}Kr detection.

MOF	Mass / mg	Activity / Bq
MOF-5	234	10250
IRMOF-7	360	11070
MOF-9	200	10180
MOF-205	181	10370
UIO-66	139	10030
UIO-67	251	10020
UIO-1,4-NDC	194	10010
CAU-24	176	10100
MOF-5 + 1.38% ADC	161	10380
MOF-5 + 5.5% ADC	35	10010
IRMOF-7 + 1.38% ADC	338	10790
IRMOF-7 + 5.5% ADC	215	10070
UIO-66 + 1.38% ADC	182	10000
UIO-66 + 5.5% ADC	177	10040
UIO-1,4-NDC + 1.38% ADC	220	10100
UIO-1,4-NDC + 5.5% ADC	187	10050

Appendix Table 2: Mass of MOF an activity of gas used during ^{222}Rn detection.

MOF	Mass / mg	Activity / Bq
MOF-205	123	10066
UIO-67	190	12440
MOF-5 + 1.38% ADC	161	12241

Appendix Table 3: Mass of MOF and activity of gas used during ^{3}H detection.

MOF	Mass / mg	Activity / Bq
MOF-205	160	8910
UIO-67	190	6930
MOF-5 + 1.38% ADC	200	8120

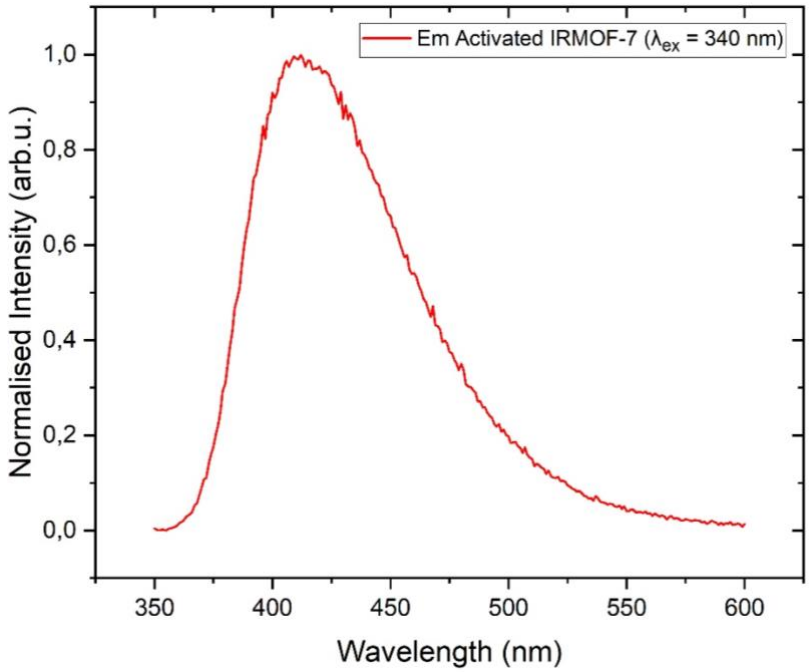

Appendix Figure 1: Illustrating the photoluminescence emission of activated IRMOF-7.

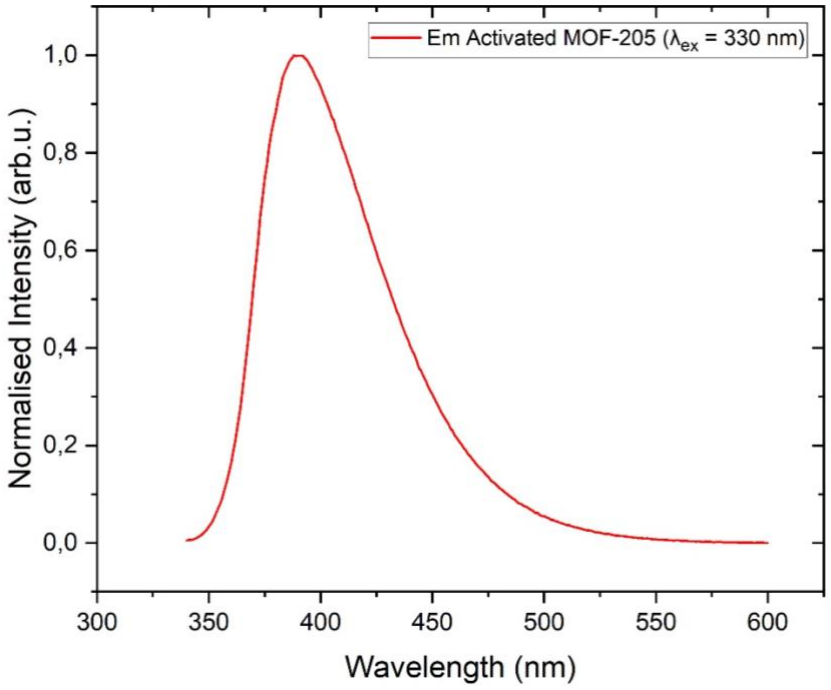

Appendix Figure 2: Illustrating the photoluminescence emission of activated MOF-205.

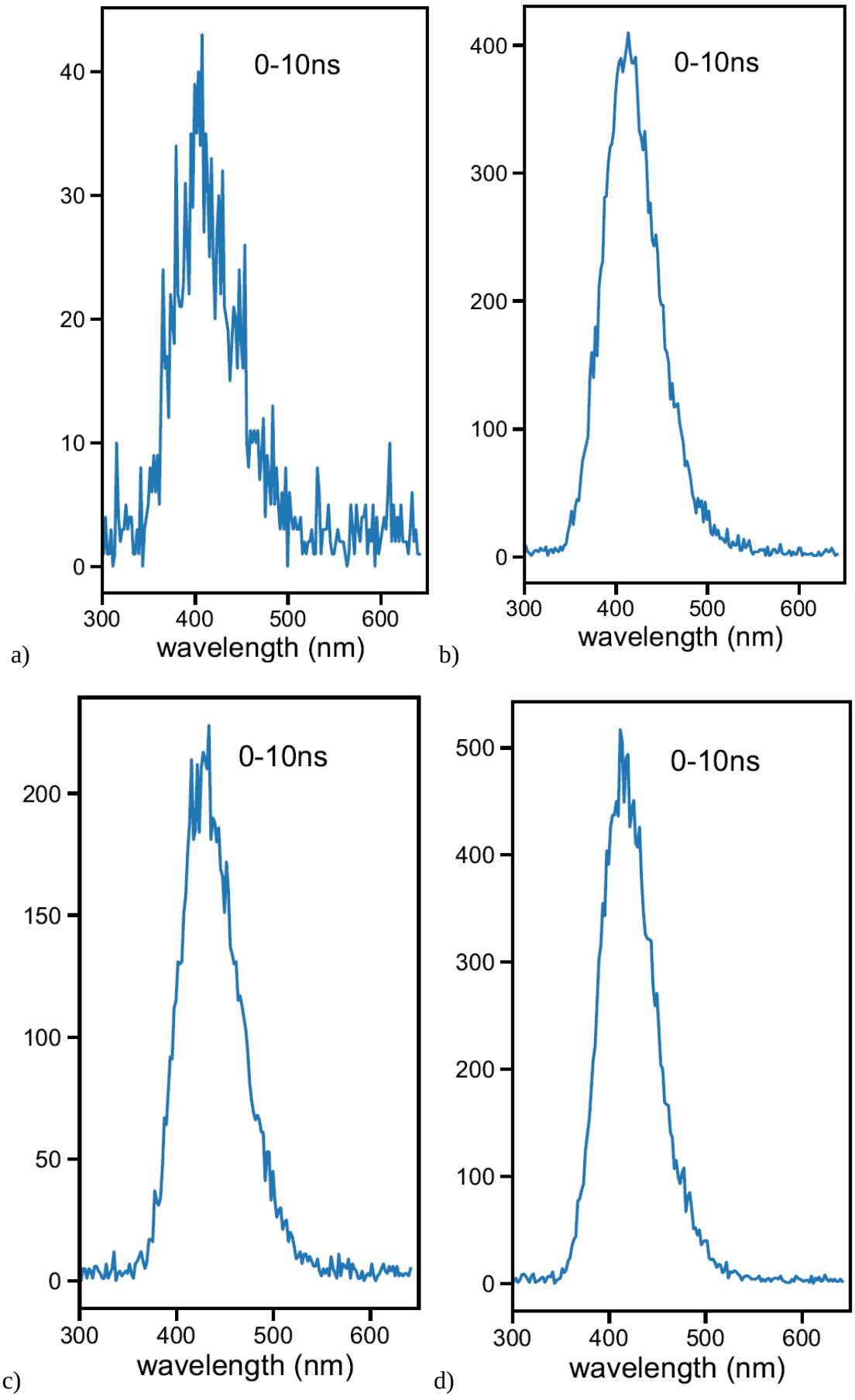

Appendix Figure 3: Showing the RL spectrum for Zr-based MOFs of Chapter IV.

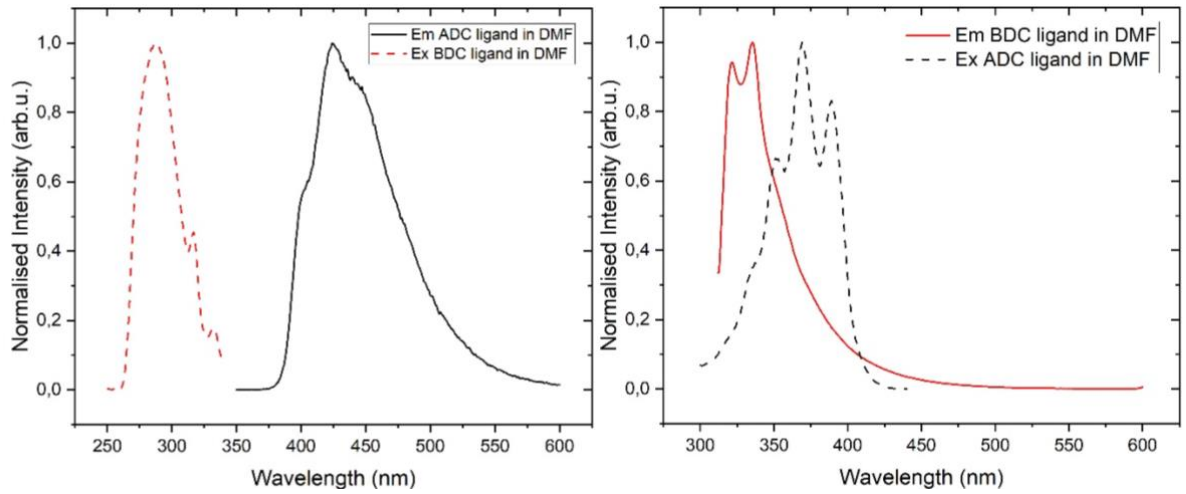

Appendix Figure 4: Showing the overlap of Em-Ex profiled of the ligands in DMF. Left - Ex of BDC ligand and Em of ADC. Right - Ex of ADC ligand and Em of BDC.

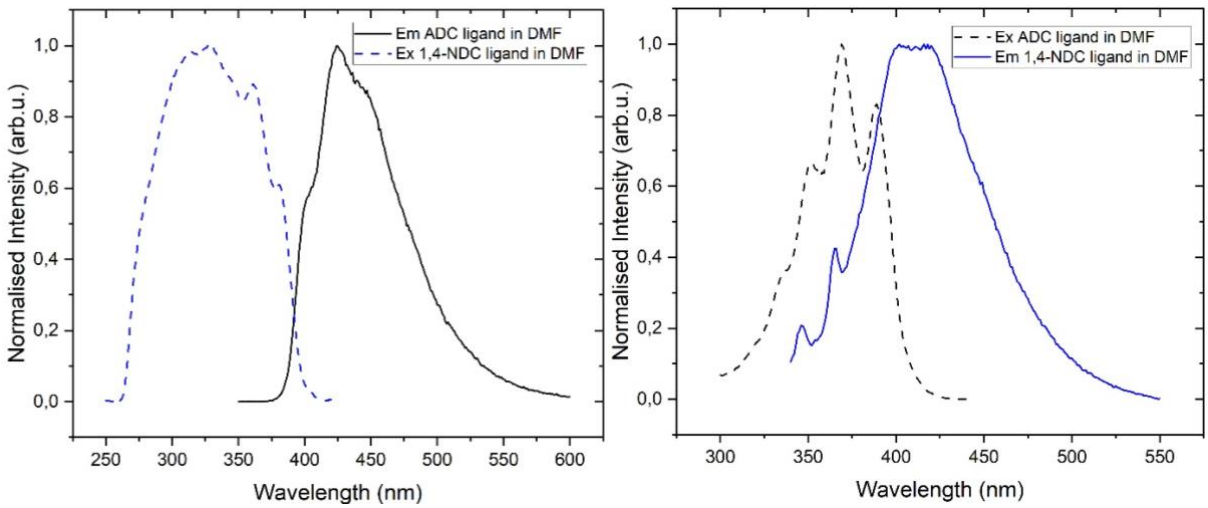

Appendix Figure 5: Showing the overlap of Em-Ex profiled of the ligands in DMF. Left - Ex of 1,4-NDC ligand and Em of ADC. Right - Ex of ADC ligand and Em of 1,4-NDC.

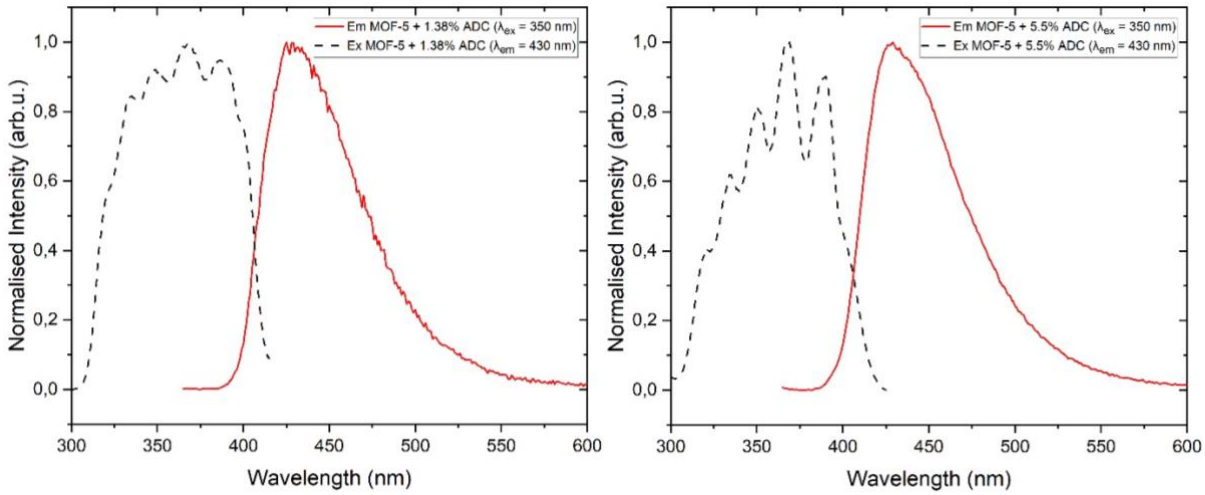

Appendix Figure 6: Illustrating the excitation and emission spectrum of Left – MOF-5 + 1.38% ADC, Right – MOF-5 + 5.5% ADC.

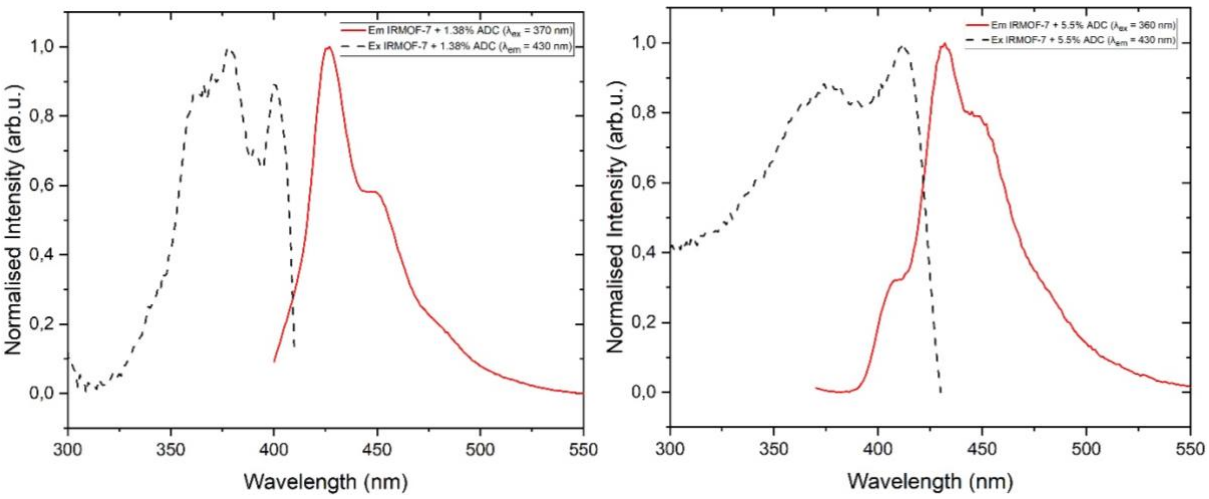

Appendix Figure 7: Illustrating the excitation and emission spectrum of Left – IRMOF-7 + 1.38% ADC, Right – IRMOF-7 + 5.5% ADC.

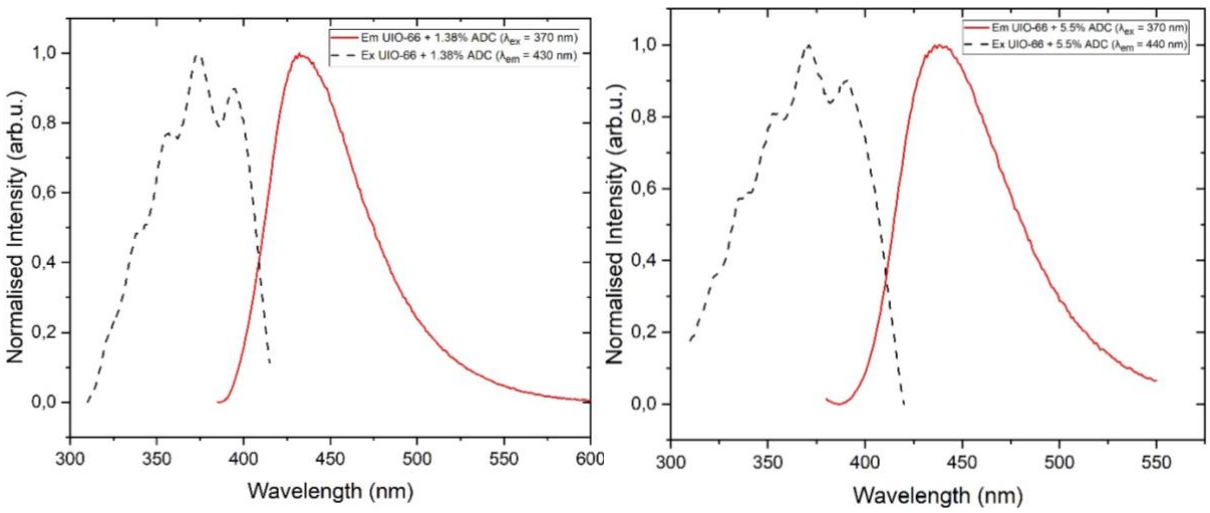

Appendix Figure 8: Illustrating the excitation and emission spectrum of Left – UIO-66 + 1.38% ADC, Right – UIO-66 + 5.5% ADC.

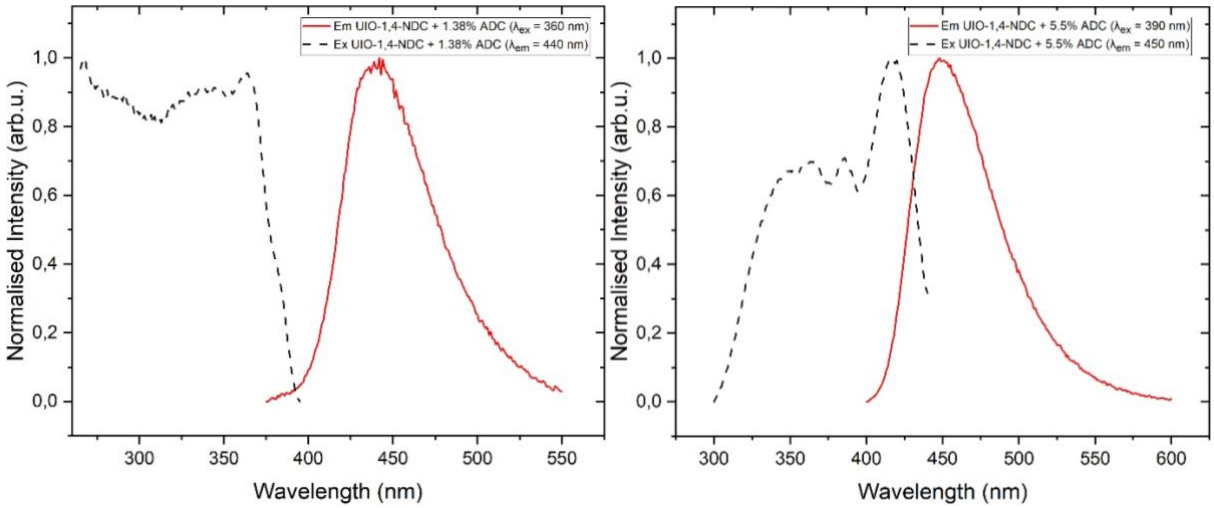

Appendix Figure 9: Illustrating the excitation and emission spectrum of Left – UIO-1,4-NDC + 1.38% ADC, Right – UIO-1,4-NDC + 5.5% ADC.

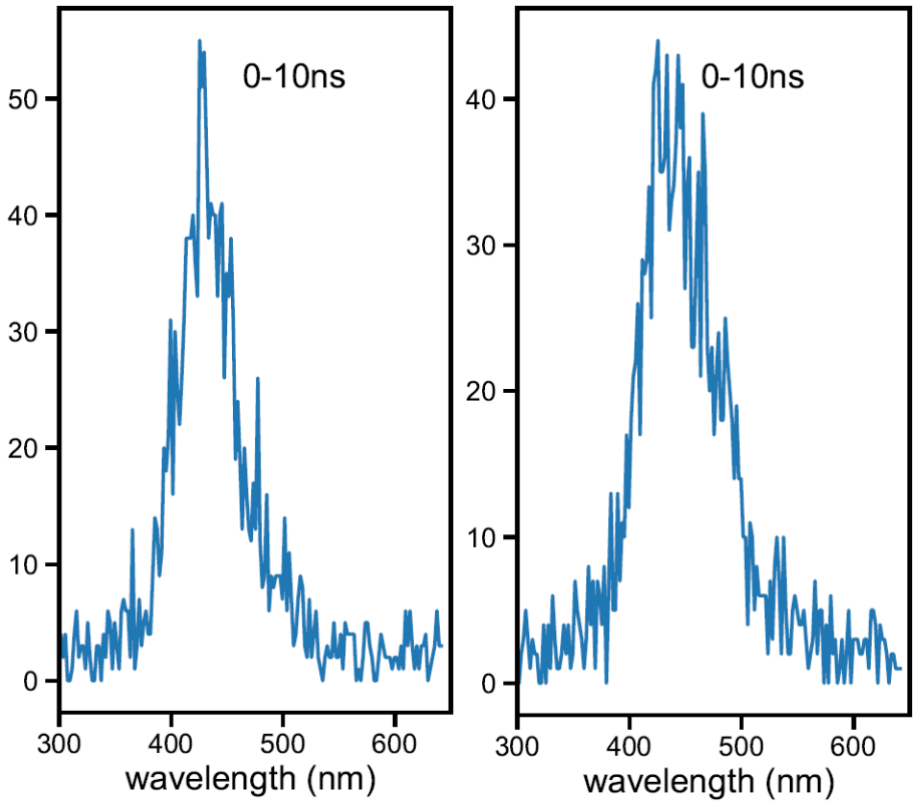

Appendix Figure 10: Showing the RL spectrum for MOF-5 left- 1.38% ADC and right – 5.5% ADC.

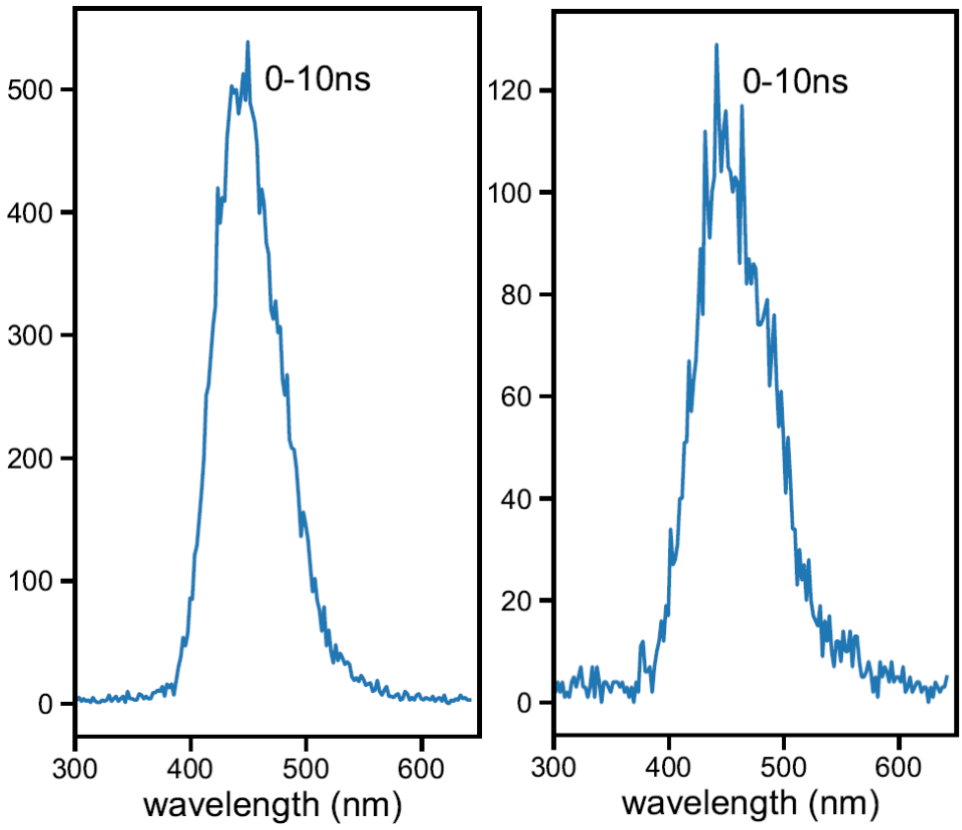

Appendix Figure 11: Showing the RL spectrum for IRMOF-7 left- 1.38% ADC and right – 5.5% ADC.

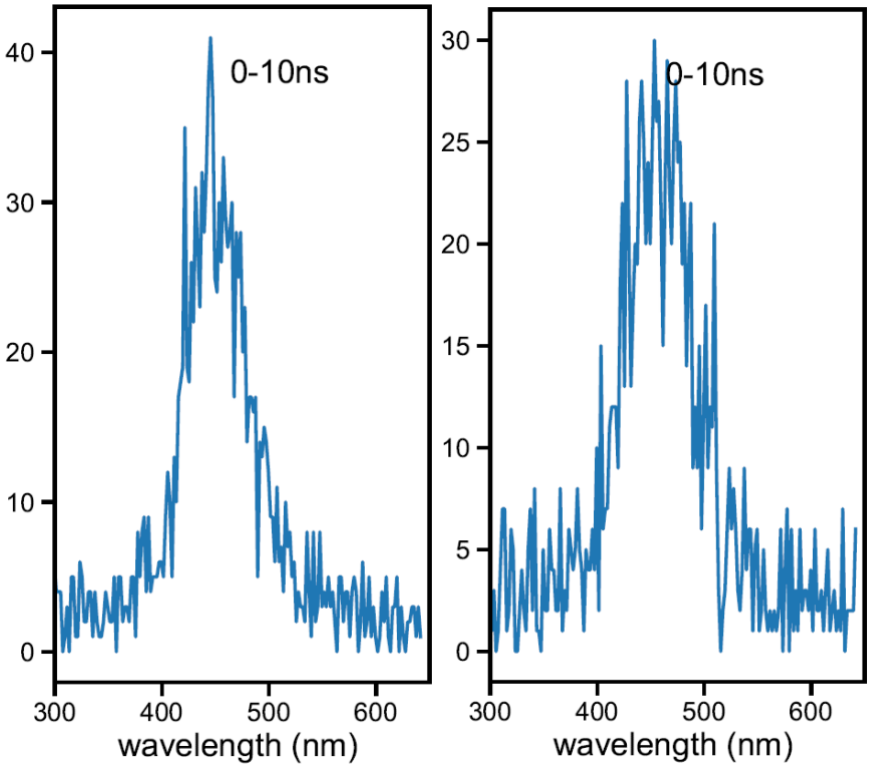

Appendix Figure 12: Showing the RL spectrum for UIO-66 left- 1.38% ADC and right – 5.5% ADC.

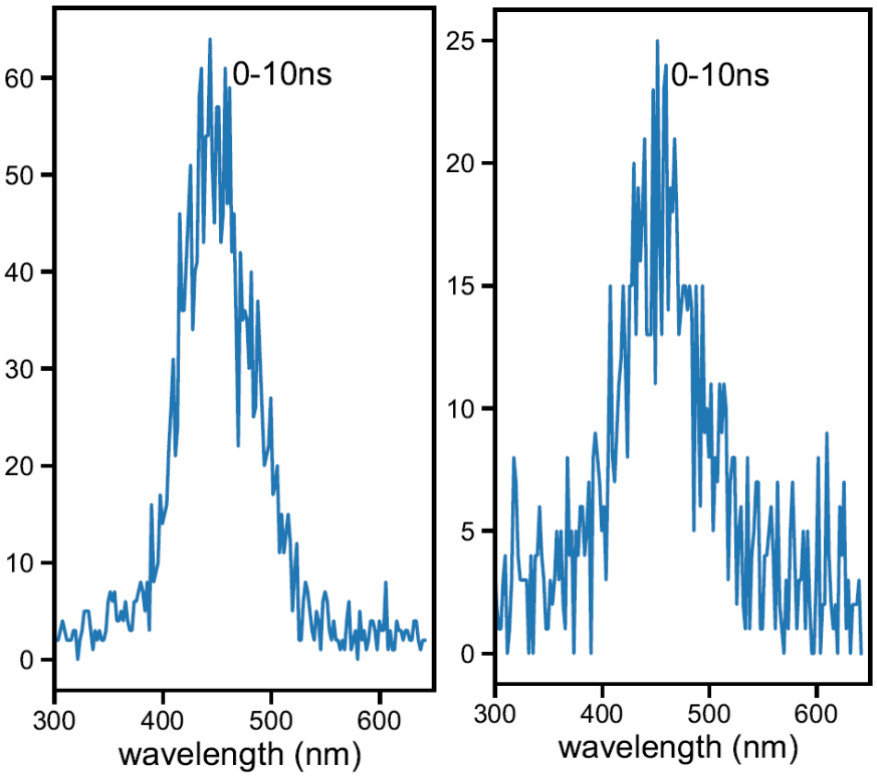

Appendix Figure 13: Showing the RL spectrum for UIO-1,4-NDC left- 1.38% ADC and right – 5